

University of Southampton Research Repository ePrints Soton

Copyright © and Moral Rights for this thesis are retained by the author and/or other copyright owners. A copy can be downloaded for personal non-commercial research or study, without prior permission or charge. This thesis cannot be reproduced or quoted extensively from without first obtaining permission in writing from the copyright holder/s. The content must not be changed in any way or sold commercially in any format or medium without the formal permission of the copyright holders.

When referring to this work, full bibliographic details including the author, title, awarding institution and date of the thesis must be given e.g.

AUTHOR (year of submission) "Full thesis title", University of Southampton, name of the University School or Department, PhD Thesis, pagination

UNIVERSITY OF SOUTHAMPTON

FACULTY OF PHYSICAL AND APPLIED SCIENCES

Electronics and Computer Science

Segmentation of Lungs from Volumetric CT-Scan Images Using Prior Knowledge (Shape and Texture)

by

Wanmu Liu

Thesis for the degree of Doctor of Philosophy

October 2014

Academic Thesis: Declaration Of Authorship

٠,	[please print name]				
	eclare that this thesis and the work presented in it are my own and has been generated by me as the esult of my own original research.				
[tit	le of thesis]				
۱c	onfirm that:				
1.	This work was done wholly or mainly while in candidature for a research degree at this University;				
2.	Where any part of this thesis has previously been submitted for a degree or any other qualification at this University or any other institution, this has been clearly stated;				
3.	Where I have consulted the published work of others, this is always clearly attributed;				
4.	Where I have quoted from the work of others, the source is always given. With the exception of such quotations, this thesis is entirely my own work;				
5.	I have acknowledged all main sources of help;				
6.	Where the thesis is based on work done by myself jointly with others, I have made clear exactly what was done by others and what I have contributed myself;				
7.	Either none of this work has been published before submission, or parts of this work have been published as: [please list references below]:				
Ci a	ned:				
Jig	iicu.				

UNIVERSITY OF SOUTHAMPTON

ABSTRACT

FACULTY OF PHYSICAL AND APPLIED SCIENCES

Electronics and Computer Science

Doctor of Philosophy

SEGMENTATION OF LUNGS FROM VOLUMETRIC CT-SCAN IMAGES USING PRIOR KNOWLEDGE (SHAPE AND TEXTURE)

by Wanmu Liu

This thesis presents a hierarchical segmentation scheme for The segmentation of lungs from volumetric CT images that concerns variational segmentation methods, namely geodesic active surfaces (GAS) and active surfaces without edges (ASWE), a volumetric similarity registration technique, statistical shape modelling using principal component analysis (PCA), and volumetric texture modelling.

GAS and ASWE are 3-D extensions of their 2-D version, geodesic active contours (GAC) and active contours without edges (ACWE). The two models are generalized into a unified framework, referred to as integrated active contours (IAS). Numerical implementation methods are derived for 3-D and the experiments are conducted both in 2-D and 3-D on synthetic and CT images. Global and local properties of active contours/surfaces under different parameter settings are presented and several applications of these models are proposed based on experimental results.

The similarity registration technique aims to find an optimal match between shapes with respect to rotation, scale and translation parameters. In this registration method, PCA is initially employed to calculate the principal axes of shapes. These principal axes are used to obtain a coarse match between shapes to be registered. Then geometric moments are exploited to estimate the isotropic scale parameter. The rotation and translation parameters are estimated by phase correlation techniques which take advantage of the fast Fourier transform (FFT). Experimental results demonstrate that the proposed technique, compared with the standard iterative gradient descent method, is fast, robust in the presence of severe noise, and suitable in registering various types of topologically complex volumetric shapes.

Shape decomposition using PCA is the current state of the art and is widely drawn on in building deformable shape templates. The major problem to be solved in the modelling is to find proper PCA shape parameters that best approximate a novel shape of the same class. A comparison of popular methods for parameter estimation in the literature is presented and a hybrid coarse-to-fine method based on previous works is proposed.

The method achieves satisfactory accuracy over previous works and is validated by a database of lung shapes.

A hierarchical shape-based segmentation method that incorporates GAS, ASWE, similarity registration, and statistical shape modelling is proposed to extract lungs from volumetric low-dose CT images. The method is extensively experimented with a large variety of images including synthetic images with noise and occlusions, low-dose CT images with artificial noise and synthetic tumors, and a low-dose CT database. The results indicate that the method is robust against noise and occlusions.

Last but not least, a novel volumetric texture modelling technique based on isotropic Gaussian Markov random field (IGMRF) is developed and applied to low-dose CT images of lungs. Based on the proposed texture modelling, a hard classification approach is suggested to provide proper initializations for the shape-based segmentation method and enables the segmentation to achieve a higher degree of automation. The method is evaluated by low-dose CT images with synthetic tumors and the low-dose CT database. The experimental results suggest its suitability for offering proper initializations for shape-based segmentation.

Contents

N	omer	ıclatur	re	xxi
A	ckno	wledge	ements	xxvii
1	Intr	oducti	ion	3
	1.1	Lung	Segmentation as An Essential Task	. 3
	1.2	Previo	ous Works on this Issue	. 4
	1.3	Inspira	rations of an Alternative Methodology	. 5
	1.4	Contri	ibutions of this Work	. 7
	1.5	An Ov	verview of the Thesis	. 8
2	Act	ive Co	ontours/Surfaces	9
	2.1	Previo	ous Works	. 9
	2.2	Geode	esic Active Surfaces	. 10
		2.2.1	Classical Snakes in 3-D	. 11
		2.2.2	Implicit Surface Propagation	. 11
		2.2.3	Geodesic Active Surfaces	. 12
	2.3	Active	e Surfaces Without Edges	. 14
		2.3.1	ASWE in A Basic Formulation	. 14
		2.3.2	ASWE in A Level-set Formulation	. 14
	2.4	Integra	rated Active Surfaces	. 15
	2.5	Nume	erical Implementation Details	. 16
	2.6	Exper	rimental Results	. 19
		2.6.1	Active Contours (2-D)	. 19
		2.6.2	Active Surfaces (3-D)	. 22
	2.7	Conclu	usions	. 26
3	Sim	ilarity	Registration of Volumetric Shapes	29
	3.1	Backg	round	. 29
	3.2	Previo	ous Works	. 31
	3.3	Mathe	ematical Preliminaries	. 32
		3.3.1	Unit Quaternions as Representation of Rotations	. 32
		3.3.2	Implicit Representation of Volumetric Shapes	. 33
	3.4	Metho	ods	. 34
		3.4.1	An Initial Transformation Using Principal Axes	. 34
		3.4.2	Scaling	. 36
		3.4.3	Rotation	. 37
		3 4 4	Translation	41

vi CONTENTS

		3.4.5 Si	imilarity Measures for Evaluation of Registration	. 42
	3.5	Experime	ental Results	. 44
		3.5.1 A	n Overview	. 44
		3.5.2 Re	egistration of Topologically Different Shapes	. 44
		3.5.3 A	Comparison with the State-of-Art Methods	. 45
		3.5.4 Pe	erformance Analyses	. 49
		3.	5.4.1 Accuracy vs Efficiency	. 49
		3.	5.4.2 Stability and Robustness Against Noise	. 50
		3.5.5 Ex	xamples of Applications	
			5.5.1 Registration of Reference and Coarsely Segmented Lungs	
		3.	5.5.2 Registration of a Lung Database	
	3.6	Conclusio	ons and Future Works	. 57
4	Stat	tistical M	Iodelling of Lung	5 9
	4.1	Backgrou	ind	. 59
	4.2	Shape De	ecomposition using PCA	. 60
	4.3	An Appro	oximation Technique for Novel Shapes	62
		4.3.1 T	he Previous Works Concerning Shape Modelling	. 62
		4.3.2 A	Novel Hybrid Approximation Technique	63
		4.3.3 Si	imilarity Measures for Evaluation of Modelling	. 64
	4.4	Experime	ental Results	. 66
		4.4.1 Se	everal Intuitive Understandings of the Lung Database	. 66
		4.4.2 T	he Gaussianity of Shapes	. 68
		4.4.3 Le	eventon vs Bresson for Parameter Estimation	. 71
		4.4.4 T	he Proposed Hybrid Shape Modelling Method	. 77
	4.5	Conclusio	ons and Future Works	. 83
5	Aut	omatic S	segmentation of Lungs from Low-dose CT Images	85
	5.1	Backgrou	ınd	. 85
	5.2	Previous	Works	. 87
	5.3	The Prev	vious Theories of Segmentation Using Prior Shapes	. 88
	5.4	A Novel 1	Hierarchical Segmentation Technique	. 92
	5.5	Experime	ental Results	. 94
		5.5.1 A	n Overview	. 94
		5.5.2 T	he Working Conditions of the Proposed Method	. 95
		5.5.3 Sy	ynthetic Images with Occlusions	. 97
		5.5.4 Sy	ynthetic Images with Noise	. 101
		5.5.5 Sy	ynthetic Images with Noise plus Occlusions	. 103
		5.5.6 Lo	ow-dose CT Scans with Artificial Noise	. 104
		5.5.7 Lo	ow-dose CT Scans with Synthetic Tumors	. 106
		5.5.8 A	Database of Low-dose CT Scans	. 113
	5.6	Conclusio	ons and Future Directions	. 117
6	Sha	-	Segmentation Aided by Texture Information	119
	6.1	Inspiration	ons and Introduction	. 119
	6.2		Works	
		6.2.1 G	MRF Texture Modelling	. 120

CONTENTS vii

		6.2.2 Volumetric Texture Modelling	1
	6.3	Mathematical Preliminaries	1
		6.3.1 Markov Random Fields in Volumetric Images	1
		6.3.2 Conditional Gaussian-Markov Random Fields	3
	6.4	The Texture Feature Formulation	5
	6.5	The Probability Images for Segmentation	5
	6.6	Experimental Results	7
		6.6.1 Texture Segmentation and an Automatic Initialization Scheme 12	8
		6.6.2 The Shape-based Segmentation aided by the Initialization Scheme 13	1
	6.7	Conclusions and Future Directions	3
7	Con	nclusions and Future Works 13	7
	7.1	Conclusions	7
	7.2	Future Directions	
A	Ima	age Noise Information 14	1
В	Cas	e Index of the Lung Database 14	3
$\mathbf{R}_{\mathbf{e}}$	efere	nces 14	5

List of Figures

4	resolution computed tomography) scans (coronal plane). (b) The result of segmentation using commercially available software (some airways and vessels fail to be included). (c) The manually corrected result	1.1
	on surface S (the circle in dashes) is implicitly represented by an one-dimension-higher line between two grid points on volume Φ (the square with solid lines). The value change of a point on Φ gives rise to the motion of the point on S . The motion of the point set that constitute S	2.1
11	is deformation	2.2
13	$\max(g(I)) = 0.82$. (e) $g(I)$ when $\xi = 50$ and $\max(g(I)) = 0.97$	
17	increasing	2.3
18	1-D Plots of δ_{ϵ} with $\epsilon = 1, 2, \dots, 15$. Peaks of δ_{ϵ} at 0 reduce with ϵ increasing	2.4
10		2.5
21	$\lambda = 0$ }	
	Top row is the evolution of ACWE. $\{\mu = 10^3, v = 0, \lambda = 1\}$. Middle and bottom rows are the evolution of GAC starting from various initial	2.6
22	contours. $\{\mu = 10^3, v = 0, \lambda = 0\}$	0.7
	Curve evolution on an image of an gradient background: Top row is the evolution of ACWE. $\{\mu = 10^3, v = 0, \lambda = 1\}$. Middle row is the evolution of GAC. $\{\mu = 10^3, v = 0, \lambda = 0\}$. Bottom row is the evolution	2.7
23	of integrated active contours. $\{\mu = 10^2, v = 5 \times 10^2, \lambda = 0.1\}$	
-	contour. (b) The result by ACWE. $\{\mu = 10^3, v = 0, \lambda = 1\}$. (c) Another initial contour in the main airway. (d) The result by GAC. $\{\mu = 10^4, 10^4$	2.8
23	$v = -2 \times 10^3, \ \lambda = 0$	

x LIST OF FIGURES

2.9	The evolution of IAS from initial surfaces till convergence on volumetric HRCT scans. (a) Initial surfaces $(n=0)$: two spheres which reside within left and right lung areas. (b) $n=1$. (c) $n=2$. (d) $n=8$. (e) $n=18$. (f) Converged IAS $(n=31)$. { $\mu=500$, $\nu=0$, $\lambda=1$, $\sigma^2=1$, average time	24
2.10	taken in each iteration $\bar{t} = 9.76s$ }	24
2.10	(f) in figure 2.9 on the coronal plane. $(2)(a)$ -(f) are on axial plane	25
2.11	An enlarged slice image of the segmentation result produced by IAS	25
	(a) Post regularized surfaces of the segmented structures are overlapped on initial surfaces and additional structures detected by GAS are in magenta. $\mu = 500$, $\nu = 0$, $\lambda = 0$, $\sigma^2 = 1$ (b) Another result with increased	
	σ : $\sigma^2 = 3$. Both results are obtained using 3 iterations	26
2.13	Another example of post regularization using GAS. (a) Linearly interpolated lungs from a lower resolution. (b) Result of GAS regularization.	
	$\{\mu = 500, \ \nu = 0, \ \lambda = 0, \ \sigma^2 = 1, \ 17 \text{ iterations with } \bar{t} = 9.63s.\} \dots$	26
3.1	\vec{u}_1 rotates to coincide \vec{u}_3 according to \vec{q}_1 , and the reverse rotation is generated by \vec{q}_1^* . An alternative path is $\vec{u}_1 \to \vec{u}_2 \to \vec{u}_3$, produced by $\vec{q}_2\vec{q}_3$	
	and the path back is according to $\vec{q}_3^* \vec{q}_2^*$	33
3.2	Rotation of a volumetric rigid body can be represented by an axis \vec{a} and	
	an angle $\Delta\theta$, which is equivalent to a unit quaternion	34
3.3	The process of coinciding principal axes of shapes to be registered. Red,	
	green and blue respectively represent the first, second and third principal	26
9.4	axes of shapes	36
3.4	An example of the rotation adjustments. The top row from left to right is respectively the S^2 map, $\mathcal{R}^2_{\vec{a}}$ maps obtained according to \vec{p}_{r_1} , \vec{p}_{r_2} , \vec{p}_{r_3} of the reference '4'. The bottom row from left to right is S^2 map and $\mathcal{R}^2_{\vec{a}}$ maps of the target '4' ordered in the same way. From each $\mathcal{R}^2_{\vec{a}}$ map one quaternion for rotation adjustment is calculated and there are in total	
	three quaternions, namely $\vec{q}_{t_1}, \vec{q}_{t_2}, $ and $\vec{q}_{t_3}. \dots \dots \dots \dots \dots \dots$	39
3.5	The process of fine rotational adjustments. It is sequentially done in a	4.0
2.0	$\vec{p}_{t_1} \rightarrow \vec{p}_{t_2} \rightarrow \vec{p}_{t_3}$ ' manner	40
3.6	Left: the open '4' is fixed while the closed '4' translates in two directions from -128 to 128. Right: the normalized inner products of shapes E_R	40
3.7	(defined in section 3.4.5) under different values of translation The plots of similarity measures while the reference '4' (similar to figure 3.6) translates from -80 to 80 along one direction. Left: Accuracy, overlap, sensitivity, specificity and the normalized inner product. Right: Only accuracy and specificity (their appearances are similar to the other three, however, they are impractical to be used in combination with the	42
	other three.)	43
3.8	The registration of topologically different '4's. (a) The reference shape (a closed '4') and the target shape (an open '4'). (b) The result obtained by	
	the technique proposed here.	45
3.9	The registration of a regular and an irregular shape with different topologies. (a) The reference shape (two linked rings) and the target shape (two	
	linked horseshoes). (b)The result of registration	45

LIST OF FIGURES

3.10	The process of the ICP method registering the reference and the target '4's. (a) The initial poses of the two shapes. (b)-(d) are the intermediate results. (e) The final result	46
3.11	From left to right on the top row are three initial poses chosen here to do the comparison. The corresponding registration results using the ICP method are shown on the bottom row. Particularly, the initial pose shown in the middle on the top row are the result of coinciding the principal axes	
0.40	of shapes.	47
	From left to right are the results of MATLAB registration method under the three initial conditions showed in figure 3.11	48
	figure 3.11	49
	Normalized inner product between shapes (left) and time needed for estimating s_{op} (right) using different values of M	50
	Normalized inner product between shapes after registration (left) and execution time using different bandwidth B (right)	50
3.16	Left: The inner product between shapes when s ranges from 0.60 to 1.20. s_{op} calculated when $M=5$ is 0.93. Right: s_{op} locates on the minimum of E_M , which indicates s_{op} that minimizes E_M also minimizes the inner	E 1
3 17	product	51
0.11	the algorithm and the results presented by three similarity measures	52
3.18	The results of registration presented by the error plot of the three similar-	
	ity measures while the target '4' is affected by increasing level of binary noise ('salt and pepper' noise). The noise levels of HRCT and low-dose	
0.10	CT respectively with SNR=8.68 and SNR=4.07 are pointed out in the plot.	
3.19	Top row: the target '4' contaminated by 30% (SNR=6.45dB), 50% (SNR=4.770% (SNR=3.67dB), and 90% (SNR=2.75dB) level of noise from left to right (viewed from slice). In addition, the formula of SNR calculation can be found in appendix A. Middle row: the target '4' with noises viewed in	8dB),
	3-D. Bottom row: the registration results corresponding to the noise levels.	53
3.20	(a) Overlapping of right lungs to be registered before registration. (b) Another view before registration. (c) Overlapping of right lungs after	
0.01	registration. (d) Another view after registration	53
3.21	(a) Overlapping of left lungs to be registered before registration. (b)	
	Another view before registration. (c) Overlapping of left lungs after registration. (d) Another view after registration	54
3.22	(a) Several examples of overlapped right lungs before registration (center-of-mass alignment) using case 1 as the target shape; (b) Overlapped right lungs after registration. (c) Overlapped left lungs before registration	01
	(center-of-mass alignment). (d) Overlapped left lungs after registration	55
3.23	Difference of E_R before and after registration for both left lungs (left) and right lungs (right)	55
3.24	Difference of E_O before and after registration for both left lungs (left) and right lungs (right)	56
3.25	Difference of E_S before and after registration for both left lungs (left) and	50
0	right lungs (right)	56
3.26	A comparison of the proposed, the ICP and the MATLAB methods for the registration of the lung database leaving case 1 out.	57

xii LIST OF FIGURES

4.1	The process of lung modelling using the hybrid technique	65
4.2	E_{R1} between each case in the database and the average lung of the database. From left to right are the left, right and two lungs	67
4.3	Typical examples of lungs in the database before registration(image size: $128 \times 128 \times 128$). (a), (b) and (c) are respectively case 3, case 15 and case 24	67
4.4	From the top row to the bottom are respectively the variations of the left	07
4.4	lungs influenced by the 1st, 2nd and 3rd eigen-shapes	68
4.5	From the top row to the bottom are respectively the variations of the	UC
1.0	right lungs influenced by the 1st, 2nd and 3rd eigen-shapes	69
4.6	From the top row to the bottom are respectively the variations of two	0.0
1.0	lungs influenced by the 1st, 2nd and 3rd eigen-shapes	70
4.7	From left to right are respectively the plots of eigenvalues of the left, right,	• 0
1.,	and two lungs calculated by PCA	70
4.8	From (1) to (9) are respectively the NPPs of 9 eigenmodes generated from	
	33 cases of the left lungs	71
4.9	From (1) to (9) are respectively the NPPs of 9 eigenmodes generated from	
	33 cases of right lungs	72
4.10	From (1) to (9) are respectively the NPPs of 9 eigenmodes generated from	
	33 cases of two lungs	73
4.11	An overlapped set of 20 ellipses is shown on the left side and the variation	
	of shapes under different α after PCA decomposition is shown by the rest	
	three pictures	73
4.12	The modelling of the set of ellipses using Leventon's and Bresson's meth-	
	ods. (a) The original left-out ellipse from the training set. (b) and (c) are	
	respectively the results given by Leventon's and Bresson's methods. (d)	
	and (e) are the results overlapped with the left-out ellipse	74
4.13	The comparison of the modelling results for the right lungs produced by	
	Leventon's and Bresson's methods	75
4.14	Top row: the PCA modelling results of the left lungs using Leventon's	
	method for case 3, 15 and 24 respectively. Bottom row: the results using	
4.15	Bresson's method. (Novel shapes in green and prior shapes in blue.)	75
4.15	The comparison of the modelling results for the left lungs produced by	70
1 16	Leventon's and Bresson's methods	76
4.10	Top row: the modelling results of the right lungs using Leventon's method for case 3, 15 and 24 respectively. Bottom row: the results using Bresson's	
	method. (Novel shapes in green and prior shapes in blue.)	77
1 17	The comparison of the modelling results for two lungs together produced	11
4.11	by Leventon's and Bresson's methods	78
4 18	Top row: the modelling results of two lungs using Leventon's method for	10
1.10	case 3, 15 and 24 respectively. Bottom row: the results using Bresson's	
	method. (Novel shapes in green and prior shapes in blue.)	79
4.19	The comparison of the modelling results for the left lungs produced by	
	Leventon's and the proposed hybrid method with 10 eigen-shapes and the	
	1st eigen-shape	79
4.20	Top row: the modelling results of the left lungs by the proposed hybrid	
	method using 10 eigen-shapes for case 3, 15 and 24 respectively. Bottom	
	row: the results using the 1st eigen-shape only. (Novel shapes in green	
	and prior shapes in blue.)	80

LIST OF FIGURES xiii

4.21	The comparison of the modelling results for the right lungs produced by Leventon's and the proposed hybrid method with 10 eigen-shapes and the 1st eigen-shape. (Novel shapes in green and prior shapes in blue.)	80
4.22	The comparison of the modelling results for two lungs produced by Leventon's and the proposed hybrid method with 10 eigen-shapes and the 1st eigen-shape	81
4.23		82
4.24	Top row: the modelling results of two lungs together by the hybrid method using 10 eigen-shapes for case 3, 15 and 24 respectively. Bottom row: the results using the 1st eigen-shape only. (Novel shapes in green and prior shapes in blue.)	82
5.1	A comparison of HRCT and low-CT images. The top row presents the slices from HRCT scans and the bottom row the corresponding low-dose CT images from the same subjects. (The HRCT and low-dose CT images for each subject are acquired at different moments, therefore, they do not	
	strictly correspond to each other.)	
5.2	A graphical description of the proposed hierarchical method	93
5.3	The simultaneous segmentation of lungs from volumetric CT images. The middle row gives the evolving surfaces restricted by the prior shape. The top row provides the corresponding prior shape interpretations of the surfaces extracted from the CT images. Bottom row presents typical slice	
5.4	views of the segmentation process	94 96
5.5	The evolution of active surfaces restricted by the prior shape starts inside the ROIs. Top row: the 3-D visualization of the evolution process.	
5.6	Bottom row: the corresponding slice views	96 97
5.7	The segmentation process of a synthesized ellipse image using Leventon's method ($E_{R1} = 0.99$). The top and bottom rows are respectively the 3-D views and slice views.	98
5.8	The segmentation process of a synthesized ellipse image using Tsai's method ($E_{R1} = 0.99$). The top and bottom rows are respectively the 3-D views and slice views.	
5.9	The segmentation of a synthetic image with the first type of occlusion (leakage) using Leventon's, Tsai's and the proposed method. (a1) The 3-D view of the original image overlapped with the initial surfaces for the three method. (a2) The segmentation result by Leventon's method. (a3) The segmentation result by Tsai's method. (a4) The segmentation result by the proposed method. (b1)-(b4) are typical slices corresponding to (a1)-(a4).	

xiv LIST OF FIGURES

5.10	The segmentation of a synthetic image with the second type of occlusion using the three methods. (a1) The 3-D view of the image overlapped with the initial surfaces for the three methods. (a2) The segmentation result by Leventon's method. (a3) The segmentation result by Tsai's method. (a4)	
F 11	The segmentation result by the proposed method. (b1)-(b4) are typical slices corresponding to (a1)-(a4)	. 100
5.11	The segmentation of images with an increasing level of noise using the three methods. (a1)-(a4) are respectively the noisy images of level 1, 4, 7 and 10 with the initial surfaces overlapped. (b1)-(b4) are the 3-D views of the corresponding segmentation results by Leventon's method overlapped with the ground truth. (c1)-(c4) are the results by Tsai's method. (d1)-(d4) are the results by the proposed method	106
5.12	A quantitative evaluation of the three methods in segmentation of the images with increasing levels of noise using E_{R1} and E_{D1} (corresponding to figure 5.11).	
5.13	The segmentation of images with an increasing level of noise plus the second type of occlusion using the proposed method. (a1)-(a4) respectively correspond to noise level 1, 4, 7 and 10 with the initial surfaces overlapped. (b1)-(b4) are the 3-D views of the corresponding results overlapped with	
	the ground truth	. 104
5.14	A quantitative comparison of the proposed method with Leventon's and Tsai's methods for the segmentation of the images with noise plus occlusion using Equand Equation (corresponding to forms 5.12)	10/
5.15	mentation of case 3, 15 and 24 in the experiments of section 5.5.6 and 5.5.7, overlapped with the ground truth (purple) and raw surfaces of the	
5.16	bodies (grey)	. 105
5.17	ground truth	. 106
	respond to noise level 1, 4, 7 and 10. (b1)-(b4) are the noisy images overlapped with the initial surfaces for segmentation. (c1)-(c4) are the corresponding results overlapped with the ground truth	. 107
5.18	The segmentation of the low-dose CT image of case 24 with an increasing level of noise using the proposed methods. (a1)-(a4) respectively correspond to noise level 1, 4, 7 and 10. (b1)-(b4) are the noisy images overlapped with the initial surfaces for segmentation. (c1)-(c4) are the	
5.19	corresponding results overlapped with the ground truth	. 108
	Tsar's methods for the segmentation of the low-dose CT images using E_{R1} and E_{D1} (corresponding to figure 5.16, 5.17 and 5.18). The top, middle	
	and the bottom rows are respectively case 3, 15 and 24	. 109

LIST OF FIGURES xv

5.20	Synthetic tumors of all locations overlapped with the corresponding lungs. (a) and (e) are respectively the left and the right lungs from case 3; (b) and (f) from case 15; (c) and (g) from case 24	. 110
5.21	A comparison of Leventon's, Tsai's and the proposed method for the segmentation of the left lung with a synthetic tumor from case 15. (a) The overlapping of the initial surface (green), the ground truth (purple), the emphasized tumor (cyan) and the raw surfaces of the body (grey). (b), (c) and (d) are respective the results produced by Leventon's, Tsai's	. 110
5.22	Several examples of the segmentation for case 3 with synthetic tumors viewed from typical slices. (a1)-(a4) are several selected conditions of	
5.23	3 with synthetic tumors for both left and right lungs. The case indices of	
5.24	the left and right lungs respectively correspond to figure 5.20 (a) and (e). Several examples of segmentation for the left lungs of case 15 with synthetic tumors viewed from typical slices. (a1)-(a4) are several selected conditions of tumor. (b1)-(b4) are the corresponding results of segmentarious	111
5.25	tation	. 112
5.26	tation	112
5.27	tation	113
5.28	A quantitative evaluation of the proposed method for the segmentation of case 15 and 24 with synthetic tumors for both left and right lungs. The case indices of the left and right lungs of case 15 and 24 respectively	. 114
5.29	correspond to figure 5.20 (b), (f), (c) and (g)	. 114
5.30	the low-dose CT database	. 115
5.31	15 and 24. Top row from left to right are respectively the segmentation results of case 3, 15 and 24 viewed from typical slices. The bottom row	
	are their corresponding 3-D views.	. 116

xvi LIST OF FIGURES

	The quantified results of the proposed method measured by E_{R1} , E_{R2} , E_{D1} and E_{D2} for the segmentation of the low-dose CT database for the left, right and simultaneously two lungs	
6.1	An example of the neighborhood system of voxel \mathbf{i} $(r=1,N=26)$. The	
	indexing through the neighborhood system follows a 'x-y-z' manner	. 122
6.2	A graphical description of the texture feature formulation process	. 126
6.3	Three volumes extracted from low-dose CT scans and the corresponding average PL histograms representing their texture features. (a) A cubic volume from the body with a tip of the left lung. (b) A volume of the left lung with a tip of the heart. (c) A volume of the background with a tip	
	of the body. (d), (e) and (f) are respectively their PL histograms	. 127
6.4	(a), (b) and (c) are respectively a slice from a volumetric CT image, its	
	distance images $(D(\hat{I}_i, \hat{\mathbf{I}}))$ and probability images (P_i)	. 128
6.5	The probability images of case 3 computed using PL histograms that change with an increasing value of k . (a1) The original image slice. (a2)-(a7) respectively correspond to $k = 1$, $k = 2$, $k = 5$, $k = 10$, $k = 20$,	
	k = 50	. 129
6.6	The probability images of case 15 computed using PL histograms that change with an increasing value of k . (b1) The original image slice. (b2)-(b7) respectively correspond to $k = 1$, $k = 2$, $k = 5$, $k = 10$, $k = 20$,	
0.7	k = 50.	. 129
6.7	The probability images of case 24 computed using PL histograms that change with an increasing value of k . (c1) The original image slice. (c2)-(c7) respectively correspond to $k = 1$, $k = 2$, $k = 5$, $k = 10$, $k = 20$,	100
6.8	k = 50. The percentage of volume obtained by the proposed hard classification	. 130
0.8	method overlapped with the ground truth for the whole database	. 130
6.9	The hard classifications (magenta) of low-dose CT images of case 3, 15 and 24, overlapped with the ground truth (purple) and the coarse surfaces	
	of the body (grey)	. 131
6.10	A graphical description of the initialization scheme based on the texture	101
C 11	information	. 131
0.11	The improper initialization leads to failures of the segmentation. (a) The initial surfaces. (b), (c) and (d) are the results respectively produced by Leventon's, Tsai's and the hierarchical segmentation method proposed in	
	*	. 132
6.12	The results of the segmentation using the proposed initialization scheme followed by the shape-based segmentation method introduced in chapter 5 measured by E_{R1} , E_{R2} , E_{D1} and E_{D2} in segmentation of the low-dose CT	
	database for the left, right and simultaneously two lungs. \dots	. 133

LIST OF FIGURES xvii

6.13	Three examples of the supervised texture segmentation of CT images with synthetic tumors using the proposed method. (a1), (b1) and (c1) are respectively the typical slices from case 3, 15 and 24. (a2), (b2) and (c2) are respectively the corresponding soft classifications (probability images). (a3), (b3) and (c3) the overlapping of the hard classification surfaces (magenta), emphasized tumors (cyan) and the coarse surfaces of	
	the bodies (grey)	. 134
6.14	A 3-D visualization of the segmentation process of case 3 with synthetic tumors. (a) The overlapping of the regions extracted by the hard classification method (magenta), the initial surface found by the initialization scheme (green), the synthetic lung tumor (cyan) and the coarse surfaces of the human body (grey). (b)-(d) are the evolution of the shape-based	
		. 135
6.15	The segmentation of case 3 with synthetic tumors for both left and right lungs (corresponding to figure 6.16 and 6.17). The case indices of the left	
6.16	tumors. (a) The overlapping of the regions extracted by the hard classification method (magenta), the initial surface found by the initialization scheme (green), the synthetic lung tumor (cyan) and the coarse surfaces of the human body (grey). (b)-(d) are the evolution of the shape-based	. 135 . 135
6.17	A 3-D visualization of the segmentation process of case 24 with synthetic tumors. (a) The overlapping of the regions extracted by the hard classification method (magenta), the initial surface found by the initialization scheme (green), the synthetic lung tumor (cyan) and the coarse surfaces of the human body (grey). (b)-(d) are the evolution of the shape-based active surfaces.	. 136
6.18	The quantitive results of the segmentation of case 15 and 24 with synthetic tumors for both left and right lungs. The case indices of the left and right lungs of case 15 and 24 respectively correspond to figure 5.20 (b), (f), (c) and (g)	126
	and (g)	. 136

List of Tables

3.1 3.2	Some experimental data concerning registrations performed in this section. The quantified comparison of the ICP, the MATLAB and the proposed registration with respect to accuracy. Pose 1-3 correspond to the three	46
3.3	poses presented on the top left to right in figure 3.11	48
3.4	figure 3.11	48 56
4.1	A comparison of the parameter estimation methods proposed by Leventon et al. (2000) and Bresson et al. (2006) with respect to efficiency. The average time of estimation for each case respectively from the databases of the left, right and two lungs are presented, including the time for learning stage, which is 0.5-0.6s.	76
4.2	A comparison concerning efficiency of the proposed hybrid shape approximation method and Leventon's method. The average time of shape approximation for each case respectively from the databases of the left, right and two lungs are presented, including the time for learning stage, which is 0.5-0.6s	81
5.1	A comparison of the popular theories on the shape-based segmentation problem	91
5.2	A comparison concerning the accuracy and efficiency of Leventon's, Tsai's and the proposed methods for the first type of occlusion (corresponding to figure 5.9).	99
5.3	A comparison concerning the accuracy and the efficiency of Leventon's, Tsai's and the proposed methods for the second type of occlusion (corresponding to figure 5.10).	
5.4	A comparison with respect to the efficiency of Leventon's, Tsai's and the proposed methods for the segmentation of noisy images (corresponding to figure 5.12)	
A.1	Noise information of figure 5.11 and 5.12 demonstrating the experiments in section 5.5.4	142
A.2	Noise information of figure 5.17 demonstrating the experiments in section 5.5.6	142
A.3		

xx LIST OF TABLES

A.4	Noise information of figure 5.18 demonstrating the experiments in sec-	1.40
	tion 5.5.6	142
B.1	The case index of the high resolution CT images referred in chapter $3.$	143
B.2	The case index of the low-dose CT images referred to in chapter 4, 5 and 6	.144

Nomenclature

Abbreviations

ACWE active contours without edges

ASM active shape model

ASWE active surfaces without edges

CF characteristic function

COPD chronic obstructive pulmonary disease

CT computed tomography

EL Euler-Lagrangian (equation)

FFT fast Fourier transform
GAC geodesic active contours
GAS geodesic active surfaces

GMRF Gaussian Markov random field

HRCT high resolution computed tomography

ICP iterative closest point

IGMRF isotropic Gaussian Markov random field

LSE least square estimation MAP maximum a posteriori

MLE maximum likelihood estimation

MRF Markov random field

MRI magnetic resonance imaging
MS Mumford-Shah (functional)
NPP normal probability plot

PCA principal component analysis
PDE partial differential equation
PDF probability density function
PL parameter local (histogram)

ROI region of interest

SDF signed distance function
SSD sum of squared distance
argmax argument of the maximum
argmin argument of the minimum
e.g. exempli gratia, for example

xxii NOMENCLATURE

etc. $et\ cetera$, and so forth et al. $et\ alii$, and the rest i.e. $id\ est$, that is (to say)

Notations for Active Contours/Surfaces

\mathbb{R}^3	3-D vector space over the field of real numbers
Ω	3-D image domain
Ω_{+}	the interior region of closed surfaces
Ω	the exterior region of closed surfaces
A	area of a 3-D surface S
A_{GAS}	area of geodesic active surfaces
D_E	minimum Euclidean distance of a point and S
E_{ASWE}	energy of the functional in the ASWE model
E_{IAS}	energy of the functional in the IAS model
I	image intensity of a pixel/voxel
S	3-D surface
V	volume of region
c_{+}	average value of I in Ω_+
c_{-}	average value of I in Ω_{-}
$ec{n}$	unit inward normal of S
\mathcal{K}	mean curvature of S
\mathcal{K}_{Φ}	mean curvature of Φ
\mathcal{V}	propagation velocity of active surfaces
Φ	3-D level-set function, mostly an SDF
ϕ	2-D level-set function
h	space step used in sampling continuous 3-D functions
Δt	time step of evolving active contours/surfaces
μ	area parameter in the functional of ASWE
ν	volume parameter in the functional of ASWE
λ	image parameter in the functional of ASWE
ξ	image dynamic range reduction factor in $g(\cdot)$ of GAS
ϵ	precision factor for $H(\cdot)_{\epsilon}$ and $\delta(\cdot)_{\epsilon}$
$H(\cdot)$	Heaviside function
$H(\cdot)_{\epsilon}$	numerical approximation of Heaviside function
$g(\cdot)$	transformation of ${\cal I}$ into a weighted (Riemannian) space for GAS
$\delta(\cdot)$	Dirac function
$\delta(\cdot)_{\epsilon}$	numerical approximation of Dirac function
d_t	total derivative with respect to t
∂_p , ∂_q , etc.	partial derivative with respect to p, q

NOMENCLATURE xxiii

${\bf Notations} \ {\bf for} \ {\bf Similarity} \ {\bf Registration}$

\mathbb{S}^3	4-D unit vector space
\mathbb{S}^2	3-D unit vector space
SO(3)	rotation group
$\Omega_{\mathcal{S}^2}$	spherical domain inside the image domain Ω
R	3-D rotation matrix, $det(\mathbf{R}) = 1$
c	centroid of \mathcal{X}
\mathbf{r}	parametrized coordinate of a spherical coordinate system
$\hat{\mathbf{x}}$	parametrized unit coordinate of a sphere
В	bandwidth of an $\mathcal{R}_{\vec{a}}^2$ map (associated with resolution)
E_M	energy of the function that calculates
E_R	normalized inner products of two CFs
E_A, E_O	accuracy, overlap of two CFs
G_r, G_t	geometric moments of $\check{\mathcal{X}}_r,\check{\mathcal{X}}_t$
M	Maximum order of the geometric moments
R	Maximum radius of spherical domain Ω_{S^2}
m	order of the geometric moments
r	radial distance of a spherical coordinate system
s	scale parameter
s_{op}	optimal scale parameter
\vec{a}	rotation axis
\vec{a}_{op}	optimal rotation axis that constitutes \vec{q}_{op}
$\vec{p}_{r_1},\vec{p}_{r_2},\vec{p}_{r_3}$	the first, second and third principal axes of the reference shape
$\vec{p}_{t_1},\vec{p}_{t_2},\vec{p}_{t_3}$	the first, second and third principal axes of the target shape
$ec{q}$	unit quaternion (3-D rotation parameter)
$ec{q}^*$	conjugate of \vec{q} , $\vec{q}\vec{q}^* = (1, 0, 0, 0)$
$ec{q}_p$	quaternion that coincides principal axes of \mathcal{X}_r and \mathcal{X}_t
$\vec{q}_{t_1},\vec{q}_{t_2},\vec{q}_{t_3}$	quaternions calculated using $\vec{p}_{t_1},\vec{p}_{t_2},\vec{p}_{t_3}$
$ec{q}_{op}$	optimal rotation parameter
$ec{T}$	translation parameter
$ec{T}_{op}$	optimal translation parameter
$\mathcal{X}_r,\mathcal{X}_t$	characteristic functions of the reference and the target shapes
$cute{\mathcal{X}_r}$	$\dot{\mathcal{X}}_r(\mathbf{x}) = \mathcal{X}_r(s_{op}\mathbf{R}(\vec{q}_{op})\mathbf{x})$
$reve{oldsymbol{\mathcal{X}}_r},reve{oldsymbol{\mathcal{X}}_t}$	centralized \mathcal{X}_r , \mathcal{X}_t
$ ilde{\mathcal{X}}_r(\hat{\mathbf{x}})$	\mathcal{S}^2 maps of \mathcal{X}_r
$ ilde{\mathcal{X}}_t(\hat{\mathbf{x}})$	\mathcal{S}^2 maps of $\check{\mathcal{X}}_t$
	$\mathcal{R}_{\vec{a}}^2$ maps of $\breve{\mathcal{X}}_r$
$ ilde{\mathcal{X}}_t(extit{ heta}, extit{\phi})$	$\mathcal{R}^2_{ec{a}}$ maps of $ec{\mathcal{X}}_t$
$ ilde{\mathcal{Y}}_r, ilde{\mathcal{Y}}_t$	1-D Fourier transforms of $\mathcal{R}_{\vec{a}}^2$ maps with respect to $\hat{\theta}$

xxiv NOMENCLATURE

Notations for PCA Shape Modelling

 \mathbf{U} $Q \times N$ matrix consists of reshaped mean-offset shapes \mathbf{V}_N $Q \times N$ matrix calculated using singular value decomposition First K columns of \mathbf{V} \mathbf{V}_K similarity registration parameter \mathbf{x}_R Nthe total number of shapes in a training set Kthe number of selected eigen-shapes for modelling normalized inner product of shapes' CFs E_{R1} E_{R2} Dice's coefficient E_{D1} average Euclidean distance of two closed surfaces E_{D2} Hausdorff distance of surfaces width of a narrow band that allows Φ_{mod} to deform b_m PCA shape parameter α PCA shape parameter that reconstructs the i_{th} shape in the training set $oldsymbol{lpha}_i$ α_i the i_{th} element of α the i_{th} shape in a training set Φ_i $\bar{\Phi}$ mean shape of a training set $\vec{\Phi}_i$ a Q dimensional vector reshaped from the i_{th} mean-offset shape $\hat{\Phi}_i$ the i_{th} eigen-shape obtained from PCA shape modelling Φ_{as} SDF of a shape that provides image information Φ_{mod} SDF of prior shape that models novel shapes $\mathcal{T}_{re}(\cdot)$ the operation that reshapes 3-D matrices to vectors $\mathcal{T}_{re}^{-1}(\cdot)$ inverse operation of $\mathcal{T}_{re}(\cdot)$ \mathcal{T}_{sim} similarity transformation $P(\cdot)$ probability of a shape

Notations for Texture Segmentation

\mathbb{Z}^3	3-D integer space
Ω_D	3-D discrete image domain
Ω_{D_l}	3-D local domain of voxel \mathbf{i} , $\Omega_{D_l} = \{\mathbf{i}, \mathcal{N}_{\mathbf{i}}\}$
Ω_{ROI}	domain of region of interest
\mathcal{L}	likelihood of parameter \mathbf{w}_i and σ_i

NOMENCLATURE xxv

$\mathcal{N}_{\mathbf{i}}$	a set of neighborhood voxels of voxel ${\bf i}$
$\hat{\mathbf{I}}$	a set of texture feature vectors sampled from ROI, $\hat{\mathbf{I}} = \{\hat{I}_j\}$
\mathbf{i}_i	the i_{th} neighborhood voxel of voxel ${f i}$
$D(\hat{I}_{\mathbf{i}},\hat{\mathbf{I}})$	the distance between $\hat{I}_{\mathbf{i}}$ and the nearest $\hat{I}_{j} \in \hat{\mathbf{I}}$
P(A B)	probability of A given B
$P_{\mathbf{i}}$	probability of voxel ${\bf i}$ belongs to ROI
$p(\cdot)$	probability density function
$\hat{I}_{\mathbf{i}}$	texture feature vector of voxel \mathbf{i}
$\mathbf{w_i}$	interaction parameter vector of voxel \mathbf{i} and $\mathcal{N}_{\mathbf{i}}$ in GMRF
$\mathbf{w_i}$	interaction parameter of voxel i and \mathcal{N}_i in IGMRF
$\sigma_{\mathbf{i}}$	standard deviation in GMRF/IGMRF

Acknowledgements

I would love to present my sincere gratitude to my supervisors, Dr. Sasan Mahmoodi and Dr. Michael J. Bennett, both of whom are not only knowledgeable and insightful, but also considerate and helpful. They encourage and befriend me. I benefit from their expertise and am fully convinced that without them, I would go nowhere further in my field of research.

My thankfulness to NIHR Southampton Respiratory Imaging Group for supplying the CT image data. The CT data in this work were acquired as a part of a study into the application of imaging to the characterization of the phenotypes of chronic obstructive pulmonary disease (COPD). The study was approved by the Southampton and South West Hampshire local research ethics committee (LREC number: 09/H0502/91) and the University Hospital Southampton NHS Foundation Trust Research and Development Department. The study was conducted in the Southampton NIHR Respiratory Biomedical Research Unit. Also, I would like to thank Chathurika Dharmagunawardhana for kindly providing her MATLAB programs for image texture analysis.

My gratefulness to Wei Liu, Ke Yuan and Xin Liu, who ever since I joined this group, provided all kinds of assistance and advice that made me quickly adapt to this research environment. Many thanks to Tayyaba Azim, Oliver Brend for sharing their research experience through numerous valuable discussions. Furthermore, thanks to all in CSPC group who are kind and intelligent, making the life here a true enjoyment.

Last, but not least, I would like to express my everlasting gratitude to my parents-my mother, Shuhua Zhao, and my father, Zhuang Liu, who have been supporting me financially and spiritually during my study like always. Without them, it would not be possible to be this far.

To my parents...

Publications

Publications based on this work include:

- 1. A Solution to the Similarity Registration Problem for Volumetric Shapes Represented by Characteristic Functions, Lecture Notes in Computer Science: The 9th International Symposium on Visual Computing, 2013, 1144-1158.
- 2. Robust Similarity Registration Technique for Volumetric Shapes Represented by Characteristic Functions, Pattern Recognition, 47 (3) (2014) 1144-1158.

Chapter 1

Introduction

1.1 Lung Segmentation as An Essential Task

Computed tomography (CT) as the standard for pulmonary imaging, has been playing a vital part in lung disease diagnosis since its first introduction in the 1970s. Modern scanner hardware allows CT to provide high spatial resolution and tissue contrast of anatomical structures in the human thorax. Therefore, it is often used follow up both acute and chronic pathological changes ongoing in the parenchyma of the lung. The major applications of CT imaging include providing essential diagnostic information, including lung parenchymal density, airway wall thickness for chronic obstructive lung disease (COPD) study, locating and screening tumors for lung cancer treatment, and determining the necessity of conducting surgeries. By providing the relevant 3-D spatial information, CT enables the doctors to conduct more effective and efficient treatments of all kinds of lung diseases.

While high quality volumetric data at hand benefit diagnostic capabilities, the extraction of the information that lies in the huge amount of data can be a considerable burden. Therefore, accurate segmentation of lungs that involves as little human endeavors as possible is a necessary step that could allow physicians to put more attention into disease analyses. Furthermore, one of the key benefits of accurate segmentation is the reduction in computational cost by limiting the further processing algorithms to only the region of interest (ROI) and hence reducing the number of voxels that have to be processed. Limiting the size of ROIs prevents the analytic algorithms from being corrupted by considering voxels that are outside the ROIs.

However, the segmentation of lungs is not a straightforward task to be accomplished. One of the basic information that one use to perform the task is the intensities of voxels. Healthy lungs are relatively simple to handle, because they are filled by air and mostly dark, while there are still all kinds of bright structures, including small ones including

blood vessels, airway walls, and large ones including arteries, veins. They belong to lung area, yet may be excluded in segmentation (see figure 1.1). Lungs with certain pathological changes, say fibrotic lung diseases and lung cancers, are more difficult to segment, for they have large bright focal areas or brighter regions caused by localized increase in tissue density, which, without expert supervisions, mostly fail to be included in the final segmentation results.

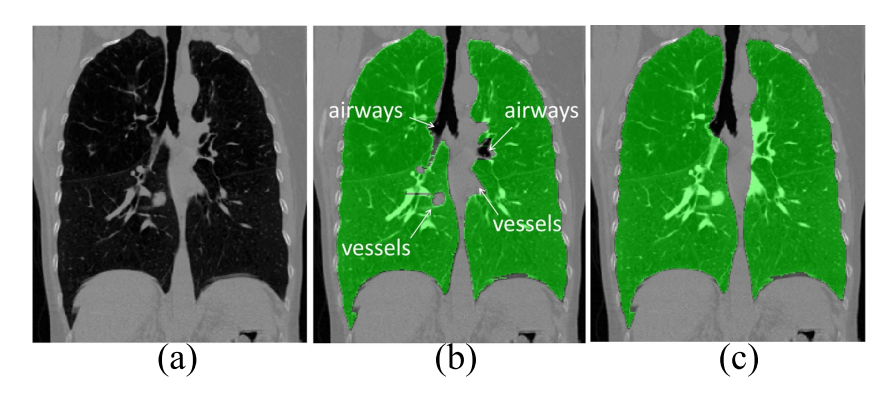


Figure 1.1: An example of lung segmentation. (a) One of the slices from HRCT (high resolution computed tomography) scans (coronal plane). (b) The result of segmentation using commercially available software (some airways and vessels fail to be included). (c) The manually corrected result.

1.2 Previous Works on this Issue

Several early approaches are introduced by Keller et al. (1981); Hedlund et al. (1982); Hoffman et al. (1983); Hoffman and Ritman (1985); Hoffman (1985); Denison et al. (1986); Kalender et al. (1991). The work of Denison et al. (1986) involves manual tracing of lung boundaries naturally provided by large contrast between lung areas and chest walls. However, this is performed slice by slice, which is laborious and dependent on observers. Keller et al. (1981); Hedlund et al. (1982); Kalender et al. (1991) also provide 2-D based methods that detect edges of left and right lungs. Hoffman et al. (1983); Hoffman and Ritman (1985); Hoffman (1985) proposed 3-D region growing method, which starts with selected seed points and gradually includes voxels by manually set criteria. Other than Denison et al. (1986), the above approaches are semi-automatic and allow manual editing of segmentation results.

Later Brown et al. (1997); Hu et al. (2001); Shojaii et al. (2005) proposed fully automatic methods to solve this problem. Brown et al. (1997) employed anatomical knowledge to guide the segmentation, making it more robust in presence of pathological changes in lungs. This method also provides an architecture to separate tracheobronchial tree, chest wall and mediastinum. Hu et al. (2001) combined thresholding and morphological processing to accomplish segmentation and smoothing operation. Shojaii et al. (2005)

applied watershed transform to segmenting lungs and a post perfection scheme is used to cover some parts that belong to lung areas yet fail to be included.

Recent focus on this topic is to perform segmentation on pathologically changed lungs. Semi-automatic approach was proposed by Kockelkorn et al. (2010), which employs user interaction and pre-calculated compact regions with homogeneous texture for lungs with severe diseases. The work of Pu et al. (2008) aims at including lung nodules into the final segmentation results. Hua et al. (2011) proposed a graph-search algorithm combining intensity, gradient, boundary smoothness and rib information.

More interestingly, an active shape model (ASM) was introduced by Sun et al. (2012) to perform lung segmentation in presence of cancers. This method exploits extracted rib information to guide a lung shape model obtained from a training set using principal component analysis (PCA) to lung areas and optimal boundaries of lungs can be found with limited freedom of deformation. This is a segmentation scheme that employs prior knowledge (shapes) into segmentation and presents excellent results.

1.3 Inspirations of an Alternative Methodology

While existing automatic or semi-automatic methods for lung segmentation involve decades of efforts, admittedly, the most ideal results are produced under supervision of human experts (mostly radiologists). Experts recognize ROIs in images from observation to interpretation based on their knowledge through years of training. Taking lung segmentation for an example, the most outstanding features of the lungs are their colors (voxel intensities) and shapes, and then, by a closer look the intensities of the voxels of lungs follow a textural pattern. Therefore, it is interesting to mathematically model these types of knowledge and algorithmically apply them into forming an automatic segmentation approach.

Bresson et al. (2006) presented an interesting method employing shape knowledge using level-set functions (see figure 1.2), taking advantage of the developments of several research fields, including variational image segmentation model (active contours), similarity/affine registration, and deformable shape template building based on PCA. The recognition of voxel intensities is performed by active contours and their evolutions are also restricted by a deformable shape template through registration. This method simulates human recognition process and it is shown promising results in the extraction of ROIs of specific shape class.

The formulation of this idea is analogous to that of Sun et al. (2012), however, the two works has major differences with respect to the style of solution. The work of Bresson et al. (2006) is a general variational model and presents mathematically sound optimizations of energy functionals, while Sun et al. (2012) employed grid point-based empirical

methods specifically for high resolution CT (HRCT) images. The optimizations are given by derived partial differential equations (PDEs) which have well established numerical solutions using level-set functions proposed by Osher and Sethian (1988). The level-set functions have long been considered superior in numerical implementation over control points for their pixel-wise precision, sub-pixel resolution and natural handling of topology (splitting and merging) which gives rise to simultaneous segmentation of multiple objects (Malladi et al., 1994, 1995; Caselles et al., 1997a; Chan and Vese, 2001; Vese and Chan, 2002; Kimmel and Bruckstein, 2003). A more significant advantage of level-set functions is their convenience of extension into higher dimensions, making it possible to get rid of control points selection process. See figure 1.2 for examples of point-based and level-set representations of a lung surface.

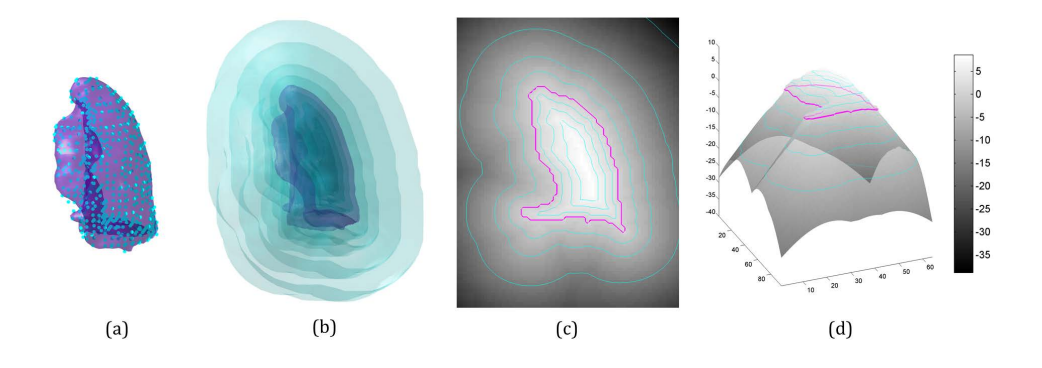


Figure 1.2: (a) Point-based representations of a lung surface. (b) A 3-D view of the level-set representations. (c) One typical slice (2-D) of the level-set function. (d) The level-set surface.

Based on the above discussion, the idea proposed by Bresson et al. (2006) is adopted in the formulation of the methodology for the segmentation of lungs from volumetric CT images. However, a full extension of Bresson's method into 3-D is not necessary because deriving PDEs is not the only path to solve the segmentation problem, for example, similarity registration and statistical shape modelling. PDEs are, more often than not, accompanied by delicate and iterative numerical schemes under various conditions of use in image processing (various conditions refer to image resolutions, noise levels, dynamic ranges etc.). Therefore, if possible, the solutions should be simplified for better robustness and efficiency especially in volumetric images, where one increase in dimensionality incurs hundreds of times larger data. The iterative schemes are supposed to be employed only when they are fully necessary after appropriate evaluations.

1.4 Contributions of this Work

The major contribution of the thesis here is that, it presents a hierarchical methodology of a high degree of automation that introduces prior knowledge (both shape and texture) into the segmentation of lungs from volumetric CT images. The method is also suitable for the segmentation of general volumetric images, say ultra-sound and MRI (magnetic resonance imaging). It fundamentally consists of four models: variational segmentation method, namely active contours/surfaces, a similarity registration technique, PCA modelling of lung shapes and lung texture segmentation. Each of models are investigated into details to effectively exploit their advantages in the segmentation process. Therefore, the contributions of the thesis can be considered in four aspects:

Firstly, active contours/surfaces models including geodesic active contours (GAC), active contours without edges (ACWE), geodesic active surfaces (GAS) and active surfaces without edges (ASWE) are introduced and their numerical implementation schemes based on a level-set formulation for 3-D case is derived from 2-D. Experiments are conducted for both 2-D and 3-D to demonstrate their global and local properties under various parameter settings.

Secondly, the similarity registration technique provides a fast and robust solution to the volumetric shape alignment problem over traditional iterative gradient descent methods. The technique aims to find an optimal match between shapes represented by characteristic functions with respect to scale, rotation and translation parameters. The theories behind the technique involve PCA for a coarse match, geometric moments for scale estimation, and correlation techniques for rotation and translation calculation. Extensive experimental results are given to show the capability of the method. It can register shapes of various topologies and with severe noise, and can achieve successful registration under arbitrary initializations. Also, it eliminates iterations and exploits the Fourier transform. This technique not only offers a solid foundation for deformable shape template building and the shape-based segmentation scheme, but contributes to automatic initialization of segmentation as well. To clarify, the role played by PCA in this technique is to find principal axes of shapes for a coarse match, but not for statistical modelling.

Thirdly, a deformable shape template for the lungs is built up based on PCA. Previous theories (Leventon et al., 2000; Bresson et al., 2006) on this topic are introduced and based on these theories, a hybrid shape modelling technique is proposed for better accuracy and efficiency. Multiple analyses of the shape features of the lungs are presented to validate the feasibility of employing the PCA shape parameter estimation schemes. Comparisons of the hybrid scheme and previous works are presented both theoretically and experimentally. The proposed hybrid shape approximation technique is shown to be suitable for modelling of shapes of lungs.

Last but not least, a supervised texture segmentation method based on Isotropic Gaussian Markov Random Field (IGMRF) is presented for volumetric CT images. It provides proper initializations for the segmentation based on shapes. The distribution of interior voxels of lung regions distinguishes the lung from other parts in the CT images. Parameters estimated from the IGMRF are used to form parameter local (PL) histograms, which exhibit satisfactory discriminative power of textures. By texture modelling and segmentation, the majority of the lung volume can be extracted and thus a proper initialization is provided for the shape-based segmentation.

1.5 An Overview of the Thesis

Before proceeding to details, the organization of this thesis is given here for an overview: chapter 2 introduces the theory of active contours/surfaces and several applications of this model to both 2-D and 3-D images; a novel registration technique is then proposed in chapter 3 with its feasibility to solve this problem validated; chapter 4 investigates into PCA modelling of lungs, performing analyses of the lung shape class and proposes a novel hybrid modelling method; With essential techniques ready, chapter 5 describes a hierarchical scheme incorporating these techniques to achieve a satisfactory segmentation of volumetric images in presence of large amount of noise and various types of occlusions; in addition to the prior shape, a volumetric texture segmentation method to employ texture information as prior knowledge is given in chapter 6; Finally, chapter 7 concludes the thesis and proposes several future directions for this research topic.

Chapter 2

Active Contours/Surfaces

2.1 Previous Works

Kass et al. (1988) first introduced the idea of active contours (snakes) into the field of image segmentation. Classical active contours are explicitly presented in an Euler-Lagrange equation deduced from an energy functional that basically consists of two parts: internal energy and external energy. The internal energy serves to control the geometric properties of the contours and the external energy are mostly exerted by the target image. In an attempt to minimize the energy functional, the associated Euler-Lagrange equation which controls the motion of the contours is derived. When the contours achieve its steady state, local minima of the image, mostly lines and edges, are detected. Its 3-D version is proposed by Terzopoulos et al. (1988) and this methodology was later applied effectively into medical image segmentation in the forms of topology-adaptive snakes (t-snakes) (Montagnat and Delingette, 2000b; McInerney and Terzopoulos, 2000), Eigen-snakes (Toledo et al., 2000a,b), 3-D parametric active surface (Montagnat and Delingette, 2000a), deformable tubular model (Yim et al., 2001).

Novel models of a similar style were proposed by Caselles et al. (1993) and Malladi et al. (1994, 1995) based on the theory of curve evolution and geometric flows. In these models, the contours evolve in a velocity that constrains two terms, one relates to the regularity of the contour and the other pushes the contours towards the boundary of the image. However, stopping condition has to be chosen properly, for the geometric models are given in the form of curve evolution equation, but not an energy minimization one. The numerical implementation of the geometric models is hugely facilitated by the level-set based method (Osher and Sethian, 1988), in which 2-D curves are embedded into a 3-D surface (often a signed distance function). Thus, automatic handling of the curve topologies makes it possible for several objects to be detected simultaneously without prior knowledge.

Caselles et al. (1997a) generalized a particular case of classical snakes into finding a geodesic curve in a Riemannian space with a metric derived from the image. This means that boundary detection in this sense, becomes finding a geodesic curve that has the minimal length in Riemannian space. The framework is similar to the geometric active contours, however, the geodesic active contour model is intrinsic and non-parametric, also, unlike geometric active contours, no stopping term has to be chosen, for the curve becomes static when it reaches the steepest area of the boundary. Moreover, it is capable of detecting objects with sharper corners compared to geometric active contours.

While the above models are more or less dependent on image gradient to detect boundaries, Chan and Vese (2001) presents a region feature based image segmentation model. The contours in this model are described as the interface of two regions: inside and outside on a finite domain of the image. The image force that drives the contour is derived from minimizing the respective variance of a specified term, say pixel intensity, inside and outside the contour, therefore the steady state of contour indicates that both the areas inside and outside of the contour achieve maximal similarity with respect to the specified term. This model is a reduced form of Mumford-Shah (MS) functional (Mumford and Shah, 1989), referred to as the minimal partition problem. However, the implementation of this model is different from previous ones. The embedment of the contours into the signed distance function (SDF) is achieved along with derivation of the associated Euler-Lagrange equation, or in other words, the curve evolution equation of this model is in essence an SDF evolution equation and thus achieves better numerical stability.

Kimmel and Bruckstein (2003) put both geodesic active contours and active contours without edges into the one curve evolution equation along with an optimal edge integration term which is generalized as an equivalence with the zeros crossings of the image Laplacian. Later, this unified work was referred to as integrated active contours by Sagiv et al. (2006), in which, the methodology appeared to be capable of detecting objects with interior boundaries in a background of gradually attenuating illumination, which may be the case in medical images. This was also applied into the segmentation of thin and tree like structure such as blood vessels, in the volumetric CT images (Holtzman-Gazit et al., 2006).

2.2 Geodesic Active Surfaces

This model proposed by Caselles et al. (1997b) is an extension of GAC (Caselles et al., 1997a) into 3-D. GAC mathematically connects two edge detection approaches, classical snakes (Kass et al., 1988) and geometric curve propagations (Caselles et al., 1993; Malladi et al., 1994, 1995), making itself benefit from both models.

2.2.1 Classical Snakes in 3-D

Let $S(p,q):[0,1]\times[0,1]\to\mathbb{R}^3$ represent a parametric 3-D surface and $I:\Omega\to\mathbb{R}$ an image, where $S=(x(p,q),y(p,q),z(p,q))^{\mathrm{T}}$ and Ω is bounded open set of \mathbb{R}^3 denoting the image domain. Let $\hat{\Omega}=[0,1]\times[0,1]$, the energy functional introduced by Terzopoulos et al. (1988) is given as

$$E_{snk}(S) = \int_{\hat{\Omega}} \left[\mu_1 |\partial_p S|^2 + \mu_2 |\partial_q S|^2 + \mu_3 |\partial_{pp} S|^2 + \mu_4 |\partial_{pq} S|^2 + \mu_5 |\partial_{qq} S|^2 + \lambda |\nabla I| \right] dp dq$$
(2.1)

where μ_i and λ are positive constants. The first and second order derivatives of S are to regularize the curve (internal energy). The first order derivatives control elasticity and the second bending. The deformation of S are also affected by gradients of I (external energy), which attracts S to image boundaries. Given a set of constant parameters, S evolves to minimize E_{snk} . Trade-off between surface smoothness and proximity to object edges is manually adjusted and topology is dealt with using specific schemes.

2.2.2 Implicit Surface Propagation

Malladi et al. (1995) proposed an implicit 3-D surface propagation for segmentation. S in this model is embedded into an one-dimension-higher volume and propagates according to the mean curvature and geometric features of I. The advantage of the embedment is that it uses value changes of voxels to represent deformation of S (see figure 2.1), and thus vastly facilitates the numerical implementation.

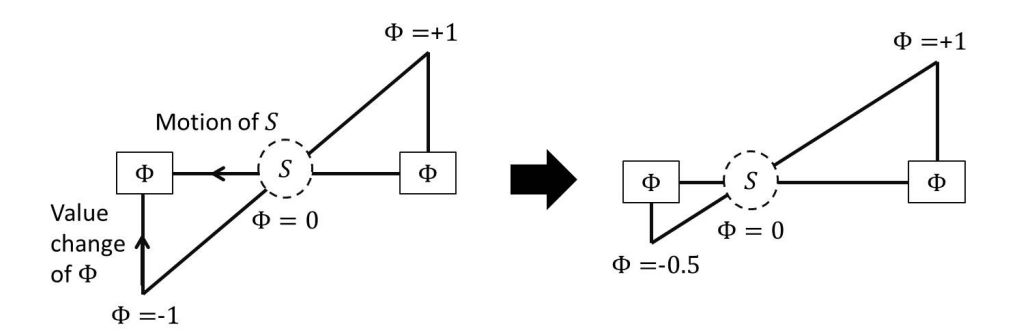


Figure 2.1: A 1-D demonstration of the motion of S when embedded into Φ . A point on surface S (the circle in dashes) is implicitly represented by an one-dimension-higher line between two grid points on volume Φ (the square with solid lines). The value change of a point on Φ gives rise to the motion of the point on S. The motion of the point set that constitute S is deformation.

Let $\Phi(\mathbf{x}): \Omega \to \mathbb{R}$ be a volumetric level-set function, where $\mathbf{x} = (x, y, z)^{\mathrm{T}}$ and in this sense $S = {\mathbf{x} : \Phi = 0}$. Mostly Φ is preferred to be a signed distance function. The

explicit surfaces propagate according to the following motion equation:

$$\partial_t S = \vec{n} \mathcal{V} \tag{2.2}$$

where \mathcal{V} is the propagation velocity and \vec{n} is the unit inward normal of S. Replacing \vec{n} by $\nabla \Phi/|\nabla \Phi|$, the implicit surface propagation equation proposed by Osher and Sethian (1988) is

$$d_{t}\Phi = \partial_{t}\Phi + \partial_{x}\Phi\partial_{t}x + \partial_{y}\Phi\partial_{t}y + \partial_{z}\Phi\partial_{t}z$$

$$= \partial_{t}\Phi + \nabla\Phi \cdot \partial_{t}S$$

$$= \partial_{t}\Phi + \nabla\Phi \cdot (\mathcal{V}\vec{n})$$

$$= \partial_{t}\Phi + \mathcal{V}(\nabla\Phi \cdot \frac{\nabla\Phi}{|\nabla\Phi|})$$

$$= \partial_{t}\Phi + \mathcal{V}|\nabla\Phi| = 0$$
(2.3)

Therefore, the motion equation of Φ is $\partial_t \Phi = -|\nabla \Phi| \mathcal{V}$. In the work of Malladi et al. (1995), Φ evolves according to

$$\partial_t \Phi = |\nabla \Phi| \left[g(I) \left(\nabla \cdot \frac{\nabla \Phi}{|\nabla \Phi|} + \nu \right) \right]$$
$$= |\nabla \Phi| g(I) (\mathcal{K}_{\Phi} + \nu) \tag{2.4}$$

Here $\mathcal{K}_{\Phi} = \nabla \cdot (\nabla \Phi/|\nabla \Phi|)$ is twice the mean curvature (sum of the two principal curvatures) of the zero level set of Φ and $g(I) = 1/(1 + (|\mathcal{G}*\nabla I|/\xi)^2)$, where \mathcal{G} is the Gaussian filter that smooths the image and ξ is used to normalize the smoothed image gradients. ξ is necessary due to the fact that HRCT data have high dynamic range (0-3000) which may cause numerical instability of GAS (g(I)) that corresponds to different values of ξ is given in figure 2.2). Therefore ξ is chosen so that g(I) is smooth enough to let GAS perform well. At ideal edges in the image, where $\nabla I = \infty$, and therefore g(I) = 0, Φ stops evolving. This can also be considered as manually intervened mean curvature motion equation that stops at edges of image during its evolution that minimizes the Euclidean area of zero level surface S. ν here serves to minimize the volume of inside region of S when $\nu < 0$ and when $\nu > 0$, it acts as balloon force that dilates S.

2.2.3 Geodesic Active Surfaces

Caselles et al. (1997a) generalized classical snakes and geometric curve propagation into finding a minimal path in a given Riemannian space. This model is extended to 3-D in the work of Caselles et al. (1997b). In 3-D, while surface-propagation-based model minimizes the Euclidean area $A = \int_S da$, where $da = |\partial_p S \times \partial_q S| dp dq$ is the area

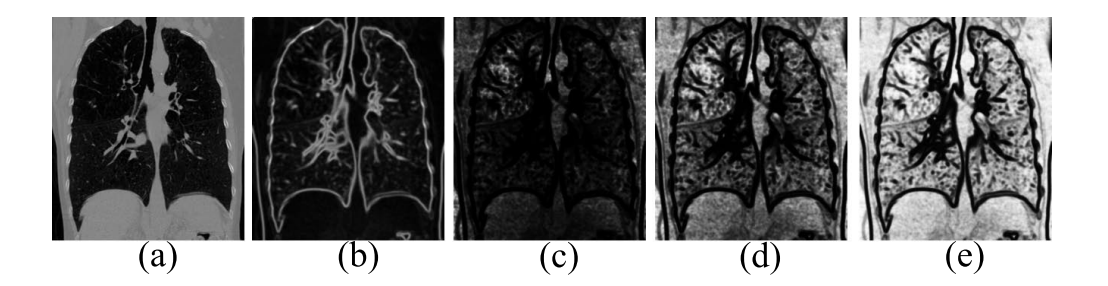


Figure 2.2: (a) One slice of HRCT scans. (b) Smoothed gradient image of the slice. (c) g(I) when $\xi = 1$ and $\max(g(I)) = 0.01$. (d) g(I) when $\xi = 20$ and $\max(g(I)) = 0.82$. (e) g(I) when $\xi = 50$ and $\max(g(I)) = 0.97$.

element of S, the GAS minimizes a weighted area:

$$A_{GAS} = \int_{S} g(S) \, \mathrm{d}a \tag{2.5}$$

Image gradients are naturally embedded into the above functional. The corresponding Euler-Lagrange equation is given as

$$\partial_t S = \vec{n} \left[g(I) \mathcal{K} - \nabla g(I) \cdot \vec{n} \right]$$
 (2.6)

where $\mathcal{K} = \nabla \cdot \vec{n}$ is twice the mean curvature (sum of two principal curvatures) of the explicit surface S. Motion of S naturally stops at image edges. Bring $\vec{n} = \nabla \Phi / |\nabla \Phi|$ into the above equation, level-set formulation of GAS is

$$\partial_{t}\Phi = |\nabla\Phi| \left[g(I)\mathcal{K}_{\Phi} + \nabla g(I) \cdot \frac{\nabla\Phi}{|\nabla\Phi|} \right]$$

$$= |\nabla\Phi|g(I)\nabla \cdot \left(\frac{\nabla\Phi}{|\nabla\Phi|}\right) + \nabla g(I) \cdot \nabla\Phi$$

$$= |\nabla\Phi|\nabla \cdot \left(g(I)\frac{\nabla\Phi}{|\nabla\Phi|}\right)$$
(2.7)

GAS is closely related to surface propagation model of Malladi et al. (1995) and a general GAS model includes the constant speed term:

$$\partial_t \Phi = |\nabla \Phi| \left[\nabla \cdot (g(I) \frac{\nabla \Phi}{|\nabla \Phi|}) + \nu g(I) \right]$$
(2.8)

The constant speed term is optional, however, in practice, properly choosing the value of ν and the stopping term g(I) gives rise to a much faster convergence. Superior to its predecessors, the GAS model is capable of detecting thinner and sharper structures while keeping its smoothness, since it provides an optimal balance between object boundary presentation and surface regularity. Furthermore, in the level-set framework, surfaces naturally split and merge, therefore multiple objects could be detected simultaneously without specially designed topology handling schemes.

2.3 Active Surfaces Without Edges

While most traditional methods employ image gradients for edge detection, Chan and Vese (2001) proposed a region-feature-based segmentation technique which involves no image gradients.

2.3.1 ASWE in A Basic Formulation

Let Ω_+ be an open subset of Ω and denote the inside region of a closed-form surface S, therefore $S = \partial \Omega_+$, and let $\Omega_- = \Omega \setminus \bar{\Omega}_+$ denote the outside region of S. In 2-D, the general idea proposed by Chan and Vese (2001) is to find a curve that makes the pixels of the region inside and outside the curve achieve the most homogeneity respectively. In 3-D, it can be mathematically presented in the following functional:

$$E_{ASWE} = \mu A(S) + \nu V(\Omega_{+}) + \lambda_{+} \int_{\Omega_{+}} |I - c_{+}|^{2} d\mathbf{x} + \lambda_{-} \int_{\Omega_{-}} |I - c_{-}|^{2} d\mathbf{x}$$
 (2.9)

The first and second term respectively denote the Euclidean area of S and the volume of Ω_+ and these two terms (internal energy) ensure the smoothness of S. The area term takes the form $A = \int_S da$. Constants c_+ and c_- are the averages of region Ω_+ and region Ω_- dependent on S. When E_{ACWE} is minimized, the variances both inside and outside S become the minimal.

2.3.2 ASWE in A Level-set Formulation

The level-set function Φ can represent surface S, region Ω_+ and region Ω_- by

$$\begin{cases} S = \partial \Omega_{+} = \{ \mathbf{x} \in \Omega : \Phi(\mathbf{x}) = 0 \} \\ \Omega_{+} = \{ \mathbf{x} \in \Omega : \Phi(\mathbf{x}) > 0 \} \\ \Omega_{-} = \{ \mathbf{x} \in \Omega : \Phi(\mathbf{x}) < 0 \} \end{cases}$$

However, unlike GAS, in which the level-set formulation is exploited in the surface evolution equation, ASWE, however, embeds Φ into the energy functional represented by equation 2.9. Using the Heaviside function H and its one-order derivative Dirac function δ_0

$$H(\Phi) = \begin{cases} 1 & \text{if } \Phi \ge 0\\ 0 & \text{if } \Phi < 0 \end{cases}, \qquad \delta_0(\Phi) = d_{\Phi}H(\Phi)$$
 (2.10)

the terms in equation 2.9 are expressed in the level-set formulation:

$$A(S) = A(\Phi = 0) = \int_{\Omega} |\nabla H(\Phi)| \, d\mathbf{x} = \int_{\Omega} \delta_0(\Phi) |\nabla \Phi| \, d\mathbf{x}$$
 (2.11)

$$V(\Omega_{+}) = \int_{\Omega} H(\Phi) \, d\mathbf{x} \tag{2.12}$$

$$\int_{\Omega_{+}} |I - c_{+}|^{2} d\mathbf{x} = \int_{\Omega} |I - c_{+}|^{2} H(\Phi) d\mathbf{x}$$
(2.13)

$$\int_{\Omega_{-}} |I - c_{-}|^{2} d\mathbf{x} = \int_{\Omega} |I - c_{-}|^{2} (1 - H(\Phi)) d\mathbf{x}$$
 (2.14)

Then equation 2.9 could be written as

$$E_{ASWE} = \int_{\Omega} \left[\mu \delta(\Phi) |\nabla \Phi| + \nu H(\Phi) + \lambda_{+} |I - c_{+}|^{2} H(\Phi) + \lambda_{-} |I - c_{-}|^{2} (1 - H(\Phi)) \right] d\mathbf{x}$$
 (2.15)

where c_+ and c_- are

$$c_{+}(\Phi) = \frac{\int_{\Omega} IH(\Phi) \, d\mathbf{x}}{\int_{\Omega} H(\Phi) \, d\mathbf{x}}$$
 (2.16)

$$c_{-}(\Phi) = \frac{\int_{\Omega} I(1 - H(\Phi)) \, d\mathbf{x}}{\int_{\Omega} (1 - H(\Phi)) \, d\mathbf{x}}$$
(2.17)

It is assumed in these two equations that $\int_{\Omega} H(\Phi) d\mathbf{x} > 0$ and $\int_{\Omega} (1 - H(\Phi)) d\mathbf{x} > 0$, that is, both the inside and outside volumes of surface S exist in Ω .

Assuming that c_+ and c_- are constants, the Euler-Lagrangian (EL) equation that minimizes E_{ASWE} is derived as

$$\partial_t \Phi = \delta_0(\Phi) \left[\mu \nabla \cdot \left(\frac{\nabla \Phi}{|\nabla \Phi|} \right) + \nu - \lambda_+ |I - c_+|^2 + \lambda_- |I - c_-|^2 \right]$$
 (2.18)

This model is region-feature-based, therefore it has a greater robustness than image-gradient-based model to noise and is able to achieve a faster convergence. Moreover, the initialization of this model does not affect final segmentation, which is not the case in previous models.

2.4 Integrated Active Surfaces

Holtzman-Gazit et al. (2006) put GAS and ASWE into one unified framework. The functional is given as

$$E_{IAS} = \mu A_{GAS} + \lambda E_{ASWE}$$

$$= \mu \int_{S} g(S) da + \lambda \left(\int_{\Omega_{+}} |I - c_{+}|^{2} d\mathbf{x} + \int_{\Omega_{-}} |I - c_{-}|^{2} d\mathbf{x} \right)$$
(2.19)

The Euclidean area term $A = \int_S da$ in the original ASWE model is replaced by a geodesic area term. By adjusting μ and λ , the GAS term could act both as a regularizing term or the main driving force in the surface evolution. Furthermore, it can be noted that the region parameter in the IAS model becomes a single λ rather than λ_+ and λ_- in the ASWE model. The reason is that in the current literature, it is the general practice to set $\lambda_+ = \lambda_-$, therefore in the unified IAS model, they are replaced by one λ . The corresponding surface evolution equation in the explicit form is deduced as follows:

$$\partial_t S = \vec{n} \left[\mu \left(g\mathcal{K} - \nabla g \cdot \vec{n} \right) - \lambda \left(|I - c_+|^2 - |I - c_-|^2 \right) \right]$$
 (2.20)

Then it is put into the level-set formulation for simpler implementation:

$$\partial_t \Phi = |\nabla \Phi| \left[\mu \nabla \cdot (g(\mathbf{x}) \frac{\nabla \Phi}{|\nabla \Phi|}) - \lambda \left(|I - c_+|^2 - |I - c_-|^2 \right) \right]$$
 (2.21)

However, a more preferable form is to combine Φ into the IAS energy functional, just like the work by Sagiv et al. (2006):

$$E_{IAS} = \int_{\Omega} \left[\mu g(\mathbf{x}) \delta(\Phi) |\nabla \Phi| + \nu H(\Phi) + \lambda |I - c_+|^2 H(\Phi) + \lambda |I - c_-|^2 (1 - H(\Phi)) \right] d\mathbf{x} \quad (2.22)$$

The associated EL equation is

$$\partial_t \Phi = \delta_0(\Phi) \left[\mu \nabla \cdot (g(\mathbf{x}) \frac{\nabla \Phi}{|\nabla \Phi|}) + \nu - \lambda |I - c_+|^2 + \lambda |I - c_-|^2 \right]$$
 (2.23)

This equation is a unified and stable model of all the active surface models described above. By setting λ to zero, and adding a stopping term $g(\mathbf{x})$ to ν , the model becomes geodesic active surfaces that can be used for local optimization. If the global detection of edges is needed, the ASWE term could be turned on, in which case the term A_{GAS} serves only to regularize the curve. Therefore, this model is proposed to be used as driving force of prior shape in segmentation of volumetric CT images.

2.5 Numerical Implementation Details

The level-set function Φ is intended to be a signed distance function (SDF) which satisfies $|\nabla \Phi| = 1$ given a closed surface S. In fact, SDFs could be represented by Lipschitz functions defined as

$$\Phi(\mathbf{x}) = \begin{cases}
0, & \mathbf{x} \in S, \\
D_E(\mathbf{x}, S), & \mathbf{x} \in \Omega_+, \\
-D_E(\mathbf{x}, S), & \mathbf{x} \in \Omega_-,
\end{cases}$$
(2.24)

where D_E is the minimum Euclidean distance between surface S and each point in Ω . Ω_+ and Ω_- respectively represent regions inside and outside S. The fast Euclidean distance transform proposed by Maurer Jr et al. (2003) is employed here to initialize and to reinitialize Φ .

Since the ideal form of Heaviside function H and Dirac function δ_0 does not exist in numerical implementation, they are to take approximated forms. The approximations proposed by Chan and Vese (2001) are adopted here and $H(\Phi)$ becomes

$$H_{\epsilon}(\Phi) = \frac{1}{2} + \frac{1}{\pi} \arctan(\frac{\Phi}{\epsilon})$$
 (2.25)

 $\delta_0(\Phi)$ becomes

$$\delta_{\epsilon}(\Phi) = \frac{\epsilon}{\pi(\Phi^2 + \epsilon^2)} \tag{2.26}$$

These approximations (see figure 2.3 and figure 2.4) allow calculation of speed on all level sets of Φ and thus makes equation 2.23 a global minimizer of Φ . Moreover, a narrow band of zero level set with bandwidth $[-\epsilon, \epsilon]$ plays the major part and evolutions of other level sets outside the narrow band are significantly repressed. This in practice delivers greater numerical stability, due to the fact that the zero level set of Φ is of much greater significance than other level sets.

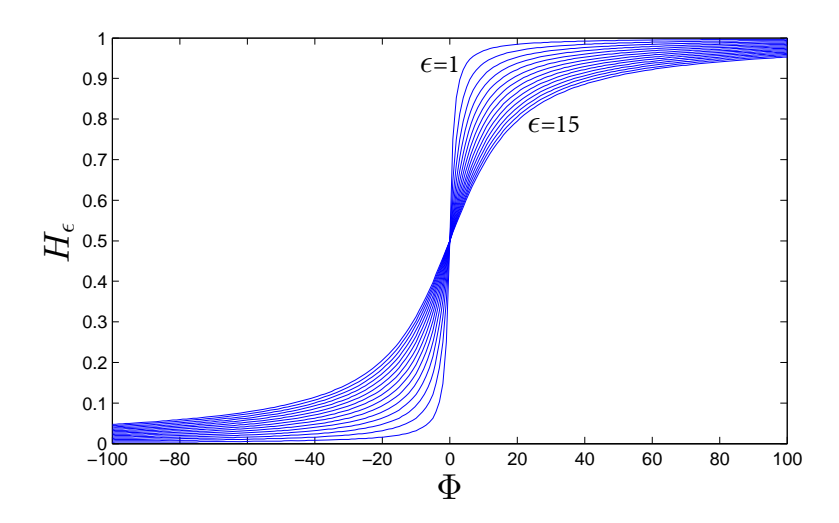


Figure 2.3: 1-D Plots of H_{ϵ} with $\epsilon = 1, 2, \dots, 15$. H_{ϵ} becomes smoother with ϵ increasing.

The discretization of equation 2.23 requires special numerical schemes. It is to be explained in section 2.6.1 that a direct discretization would give rise to numerical instability. Therefore, a superior scheme, namely the semi-finite implicit difference scheme introduced by Vese and Chan (2002), is adopted here and is extended to 3-D. Let $h = \Delta x = \Delta y = \Delta z$ be the space step, Δt the time step, $(x_i, y_j, z_k) = (ih, jh, kh)$

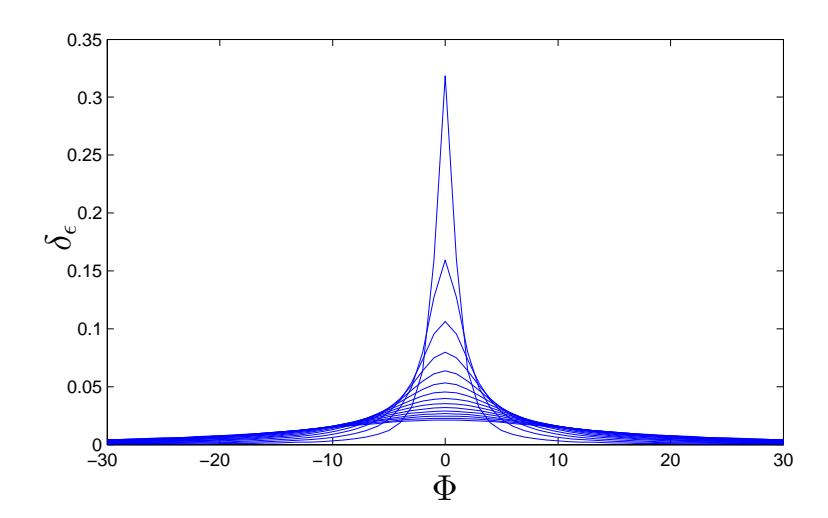


Figure 2.4: 1-D Plots of δ_{ϵ} with $\epsilon = 1, 2, \dots, 15$. Peaks of δ_{ϵ} at 0 reduce with ϵ increasing.

the grid points and $\Phi^n_{(i,j,k)} = \Phi(x_i,y_j,z_k;n\Delta t)$ an approximation of $\Phi(\mathbf{x};t)$, where $1 \leq i,j,z \leq N$. Let

$$D_{i+} = \frac{g(i+1,j,k)}{\sqrt{\left(\frac{\Phi_{(i+1,j,k)}^{n} - \Phi_{(i,j,k)}^{n}}{h}\right)^{2} + \left(\frac{\Phi_{(i,j+1,k)}^{n} - \Phi_{(i,j-1,k)}^{n}}{2h}\right)^{2} + \left(\frac{\Phi_{(i,j,k+1)}^{n} - \Phi_{(i,j,k-1)}^{n}}{2h}\right)^{2}}},$$

$$D_{i-} = \frac{g(i-1,j,k)}{\sqrt{\left(\frac{\Phi_{(i,j,k)}^{n} - \Phi_{(i-1,j,k)}^{n}}{h}\right)^{2} + \left(\frac{\Phi_{(i-1,j+1,k)}^{n} - \Phi_{(i-1,j-1,k)}^{n}}{2h}\right)^{2} + \left(\frac{\Phi_{(i-1,j,k+1)}^{n} - \Phi_{(i-1,j,k-1)}^{n}}{2h}\right)^{2}}},$$

$$D_{j+} = \frac{g(i,j+1,k)}{\sqrt{\left(\frac{\Phi_{(i+1,j,k)}^{n} - \Phi_{(i-1,j,k)}^{n}}{2h}\right)^{2} + \left(\frac{\Phi_{(i,j+1,k)}^{n} - \Phi_{(i,j,k)}^{n}}{h}\right)^{2} + \left(\frac{\Phi_{(i,j+1,k)}^{n} - \Phi_{(i,j,k+1)}^{n}}{2h}\right)^{2}}},$$

$$D_{j-} = \frac{g(i,j-1,k)}{\sqrt{\left(\frac{\Phi_{(i+1,j-1,k)}^{n} - \Phi_{(i-1,j-1,k)}^{n}}{2h}\right)^{2} + \left(\frac{\Phi_{(i,j,k)}^{n} - \Phi_{(i,j-1,k)}^{n}}{h}\right)^{2} + \left(\frac{\Phi_{(i,j-1,k+1)}^{n} - \Phi_{(i,j-1,k-1)}^{n}}{2h}\right)^{2}}},$$

$$D_{k+} = \frac{g(i,j,k+1)}{\sqrt{\left(\frac{\Phi_{(i+1,j,k)}^{n} - \Phi_{(i-1,j,k)}^{n}}{2h}\right)^{2} + \left(\frac{\Phi_{(i,j+1,k)}^{n} - \Phi_{(i,j-1,k)}}^{n}}{2h}\right)^{2} + \left(\frac{\Phi_{(i,j+1,k)}^{n} - \Phi_{(i,j-1,k)}}^{n}}{h}\right)^{2} + \left(\frac{\Phi_{(i,j,k-1)}^{n} - \Phi_{(i,j,k)}}^{n}}{h}\right)^{2}},$$

$$D_{k-} = \frac{g(i,j,k-1)}{\sqrt{\left(\frac{\Phi_{(i+1,j,k-1)}^{n} - \Phi_{(i-1,j,k-1)}}^{n}}{2h}\right)^{2} + \left(\frac{\Phi_{(i,j+1,k-1)}^{n} - \Phi_{(i,j-1,k-1)}}^{n}}{2h}\right)^{2} + \left(\frac{\Phi_{(i,j+1,k-1)}^{n} - \Phi_{(i,j,k-1)}}^{n}}{h}\right)^{2} + \left(\frac{\Phi_{(i,j,k-1)}^{n} - \Phi_{(i,j,k-1)}}^{n}}{h}\right)^{2}}.$$

and

$$D = 1 + \frac{\mu \Delta t}{h^2} \delta_{\epsilon}(\Phi_{i,j,k}^n) (D_{i+} + D_{i-} + D_{j+} + D_{j-} + D_{k+} + D_{k-})$$
 (2.27)

Finally, $\Phi_{(i,j,k)}^{n+1}$ is updated by

$$\Phi_{(i,j,k)}^{n+1} = \frac{1}{D} \left\{ \Phi_{(i,j,k)}^n + \frac{\mu \Delta t}{h^2} \delta_{\epsilon}(\Phi_{(i,j,k)}^n) \left[D_{i+} \Phi_{(i+1,j,k)}^n + D_{i-} \Phi_{(i-1,j,k)}^n + D_{j+} \Phi_{(i,j+1,k)}^n + D_{j-} \Phi_{(i,j-1,k)}^n + D_{k+} \Phi_{(i,j,k+1)}^n + D_{k-} \Phi_{(i,j,k-1)}^n \right] + \Delta t \delta_{\epsilon}(\Phi_{(i,j,k)}^n) \left[\nu g_{(i,j,k)} - \lambda (I_{(i,j,k)} - c_+)^2 + \lambda (I_{(i,j,k)} - c_-)^2 \right] \right\}$$
(2.28)

where

$$c_{+}(\Phi_{(i,j,k)}^{n}) = \frac{\sum_{i,j,k=1}^{N} I_{(i,j,k)} H_{\epsilon}(\Phi_{(i,j,k)}^{n})}{\sum_{i,j,k=1}^{N} H_{\epsilon}(\Phi_{(i,j,k)}^{n})}$$
(2.29)

$$c_{-}(\Phi_{(i,j,k)}^{n}) = \frac{\sum_{i,j,k=1}^{N} I_{(i,j,k)}(1 - H_{\epsilon}(\Phi_{(i,j,k)}^{n}))}{\sum_{i,j,k=1}^{N} (1 - H_{\epsilon}(\Phi_{(i,j,k)}^{n}))}$$
(2.30)

2.6 Experimental Results

The 2-D active contours here provides several intuitive understanding of their properties in various types of images, e.g. natural handling of curve topologies, different features of local active contours (geodesic active contours) and global active contours (active contours without edges). The experiments concerning active surfaces present applications of the model to volumetric CT images to demonstrate their characteristics in 3-D. Following the previous works, the parameters involved in the active contour/surface models are chosen to well present the experimental results.

2.6.1 Active Contours (2-D)

Sample images of figure 2.5, figure 2.6 and figure 2.7, are images of size 256×256 and figure 2.8 is one of the 512×512 HRCT slice images provided by NIHR Southampton Respiratory Biomedical Research Unit. For computation convenience, following the work of Chan and Vese (2001) and Kimmel (2003), all experiments are conducted by setting $\Delta t = \epsilon = h = 1$, and by 5×5 Gaussian smoothing filter with $\sigma = 1$. The values of μ , ν and λ are given in the captions of the corresponding figures.

Firstly, the problem of selecting the numerical implementation schemes is addressed here. A direct discretization scheme of ASWE is given as follows: let h be the space step, Δt the time step, $(x_i, y_i) = (ih, jh)$ the grid points and $\phi_{i,j}^n = \phi(x_i, y_i, n\Delta t)$ an approximation of $\phi(x, y, t)$ (the 2-D version of $\Phi(x, y, z, t)$), where $1 \leq i, j \leq N$. The

finite differences can be presented by

$$D_x^- \phi_{i,j} = \phi_{i,j} - \phi_{i-1,j}, D_x^+ \phi_{i,j} = \phi_{i+1,j} - \phi_{i,j}$$
$$D_y^- \phi_{i,j} = \phi_{i,j} - \phi_{i,j-1}, D_y^+ \phi_{i,j} = \phi_{i,j+1} - \phi_{i,j}$$

Then a direct discretization scheme is

$$\phi_{i,j}^{n+1} = \phi_{i,j}^{n} + \Delta t \delta_{\epsilon}(\phi_{i,j}^{n}) \left[\frac{\mu}{h^{2}} D_{x}^{-} \left(\frac{g_{i,j} D_{x}^{+} \phi_{i,j}^{n}}{\sqrt{\left(\frac{D_{x}^{+} \phi_{i,j}^{n}}{h}\right)^{2} + \left(\frac{\phi_{i,j+1}^{n} - \phi_{i,j-1}^{n}}{2h}\right)^{2}}} \right) + \frac{\mu}{h^{2}} D_{y}^{-} \left(\frac{g_{i,j} D_{y}^{+} \phi_{i,j}^{n}}{\sqrt{\left(\frac{\phi_{i+1,j}^{n} - \phi_{i-1,j}^{n}}{2h}\right)^{2} + \left(\frac{D_{y}^{+} \phi_{i,j}^{n}}{h}\right)^{2}}} \right) - \upsilon - \lambda (I_{i,j} - c_{+}(\phi_{i,j}^{n}))^{2} + \lambda (I_{i,j} - c_{-}(\phi_{i,j}^{n}))^{2}} \right]$$

$$(2.31)$$

where c_- , c_+ becomes

$$c_{-}(\phi_{i,j}^{n}) = \frac{\sum_{i,j=1}^{N} I_{i,j} H_{\epsilon}(\phi_{i,j}^{n})}{\sum_{i,j=1}^{N} H_{\epsilon}(\phi_{i,j}^{n})}$$

$$c_{+}(\phi_{i,j}^{n}) = \frac{\sum_{i,j=1}^{N} I_{i,j} (1 - H_{\epsilon}(\phi_{i,j}^{n}))}{\sum_{i,j=1}^{N} j = 1(1 - H_{\epsilon}(\phi_{i,j}^{n}))}$$
(2.32)

Figure 2.5 illustrates the curve evolution using a direct discretization scheme. It can be observed according to the top two lines that, with $\lambda=1$, boundaries of the sample image, including sharp, smooth, exterior and interior ones, are accurately detected with arbitrary initialization. However, the bottom row of figure 2.5, with $\lambda=0$, which means the curve is supposed to be GAC, exhibits numerical instability. Therefore, a superior numerical approximation scheme proposed by Vese and Chan (2002) is employed to overcome this situation.

 $\phi_{i,j}^{n+1}$ is then computed as follows:

Let

$$D_{i+} = \frac{g_{i+1,j}}{\sqrt{\left(\frac{\phi_{i+1,j}^n - \phi_{i,j}^n}{h}\right)^2 + \left(\frac{\phi_{i,j+1}^n - \phi_{i,j-1}^n}{2h}\right)^2}}}$$

$$D_{i-} = \frac{g_{i-1,j}}{\sqrt{\left(\frac{\phi_{i,j}^n - \phi_{i-1,j}^n}{h}\right)^2 + \left(\frac{\phi_{i-1,j+1}^n - \phi_{i-1,j-1}^n}{2h}\right)^2}}}$$

$$D_{j+} = \frac{g_{i,j+1}}{\sqrt{\left(\frac{\phi_{i+1,j}^n - \phi_{i-1,j}^n}{2h}\right)^2 + \left(\frac{\phi_{i,j+1}^n - \phi_{i,j}^n}{h}\right)^2}}}$$

$$D_{j-} = \frac{g_{i,j-1}}{\sqrt{\left(\frac{\phi_{i+1,j-1}^n - \phi_{i-1,j-1}^n}{2h}\right)^2 + \left(\frac{\phi_{i,j}^n - \phi_{i,j-1}^n}{h}\right)^2}}}$$
(2.33)

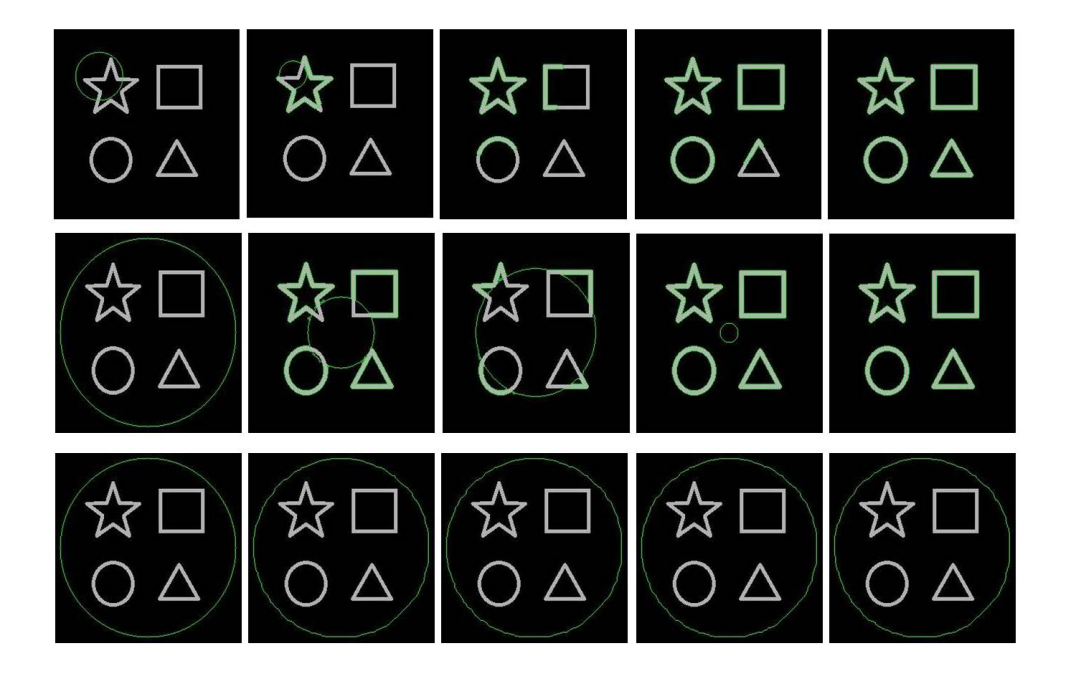


Figure 2.5: Curve evolution using a direct discretization scheme. Top and middle rows are the evolutions of ACWE. $\{\mu=10^3, v=0 \text{ and } \lambda=1\}$. Bottom row is the evolution of GAC (numerical instability). $\{\mu=10^3, v=0 \text{ and } \lambda=0\}$.

and

$$D = 1 + \frac{\mu \Delta t}{h^2} \delta_{\epsilon}(\phi_{i,j}^n) (D_{i+} + D_{i-} + D_{j+} + D_{j-})$$
(2.34)

finally

$$\phi_{i,j}^{n+1} = \frac{1}{D} \left[\phi_{i,j}^n + \frac{\mu \Delta t}{h^2} \delta_{\epsilon} (D_{i+} \phi_{i+1,j}^n + D_{i-} \phi_{i-1,j}^n + D_{j+} \phi_{i,j+1}^n + D_{j-} \phi_{i,j-1}^n) + \Delta t \delta_{\epsilon} (\phi_{i,j}^n) (-g_{i,j} v - \lambda (I_{i,j} - c_+(\phi_{i,j}^n))^2 + \lambda (I_{i,j} - c_2(\phi_{i,j}^n))^2) \right]$$
(2.35)

Figure 2.6 presents the results achieve by the superior numerical scheme. The middle and bottom rows of figure 2.6 indicate the effectiveness of the numerical scheme and the curve with $\lambda = 0$, which is GAC, is capable of detecting local sharp boundaries.

Figure 2.7 presents the evolution of IAS in 2-D in the image with a gradient illumination background. The top row of the figure indicates that the curve captures the global features of the image and fails to distinguish the circle from background. By setting μ to a very high value, enabling the geodesic term play the major part, the curve only detects the outer boundary, not coinciding with the result showed in Sagiv et al. (2006), in which, the integrated active contours achieve accurate detection of both interior and exterior boundaries. However, by setting v (the area minimization parameter) to a high

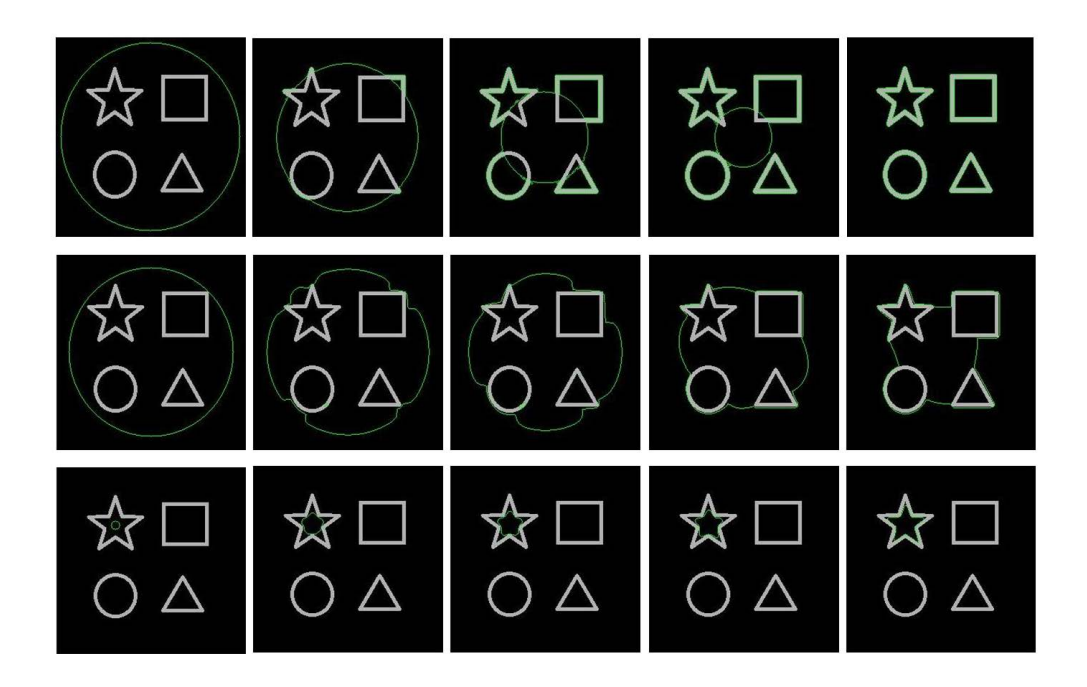


Figure 2.6: The curve evolution using the scheme proposed by Vese and Chan (2002). Top row is the evolution of ACWE. $\{\mu = 10^3, v = 0, \lambda = 1\}$. Middle and bottom rows are the evolution of GAC starting from various initial contours. $\{\mu = 10^3, v = 0, \lambda = 0\}$.

value, such result can be achieved, as is showed by the bottom row of figure 2.7. It should be noted that this result could be achieved by employing ACWE only.

Figure 2.8 is an example of lung 2-D slice segmentation. On the first line with ACWE term on, the large airway boundaries and the thin structures in the image are detected, however, small airway walls are too vague compared to other parts, say bones and vessels, to be regarded by the ACWE term as objects. The second line is the result of using only the GAC term and it could be observed that strong local edges are detected. The third line shows the effect of the constant speed term (balloon speed), which drives the curve to fill up the whole airway lumen. In addition, by sole GAC term, the curve is incapable of expanding, for the evolution equation is to minimize the geodesic length. Therefore, for accurate detection, the sum of perimeter of targeted objects boundaries should be less than or not too much more than that of the initial curve.

2.6.2 Active Surfaces (3-D)

This section gives some results of basic experiments associated with IAS. Recall that IAS consist of two parts: GAS and ASWE. IAS involve several parameters that control the weights of different terms: μ controls the geodesic area, ν the balloon force (the volume parameter), λ the ASWE term and σ the variance of Gaussian kernels that smooths images. Moreover, there are other parameters that remain constant in all the

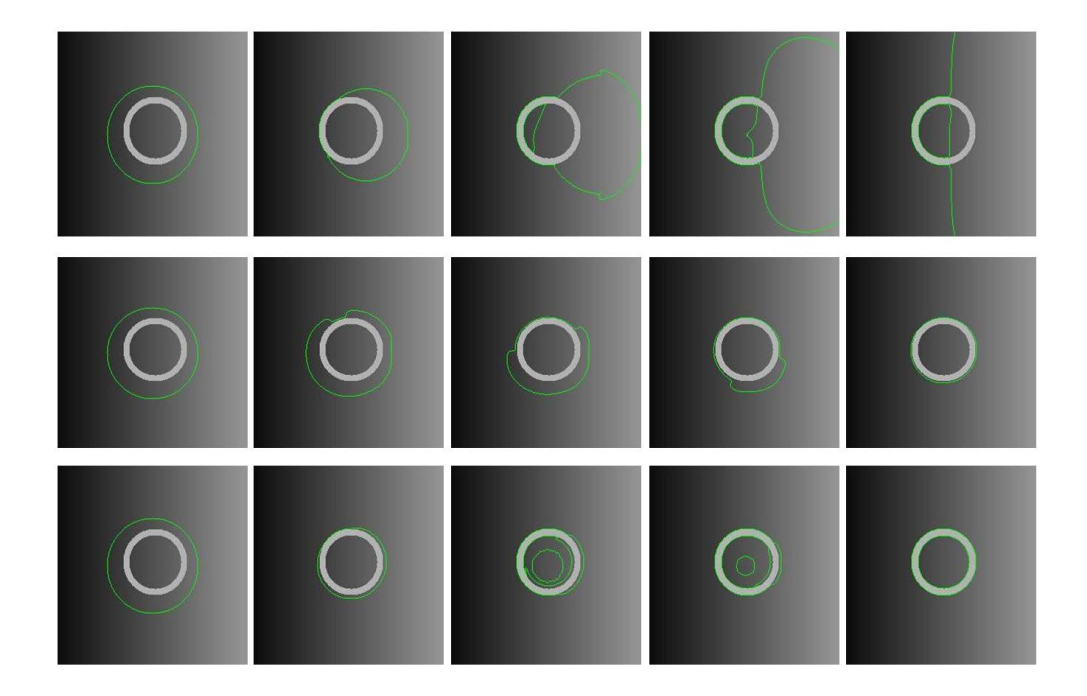


Figure 2.7: Curve evolution on an image of an gradient background: Top row is the evolution of ACWE. $\{\mu=10^3, v=0, \lambda=1\}$. Middle row is the evolution of GAC. $\{\mu=10^3, v=0, \lambda=0\}$. Bottom row is the evolution of integrated active contours. $\{\mu=10^2, v=5\times10^2, \lambda=0.1\}$.

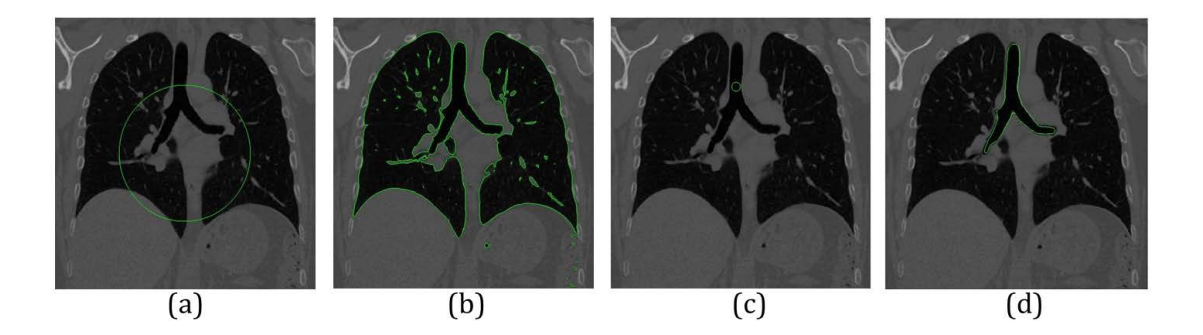


Figure 2.8: An example of segmentation of a slice from the lung data. (a) An initial contour. (b) The result by ACWE. $\{\mu=10^3,\ v=0,\ \lambda=1\}$. (c) Another initial contour in the main airway. (d) The result by GAC. $\{\mu=10^4,\ v=-2\times10^3,\ \lambda=0\}$.

experiments: $h = \epsilon = \Delta t = 1$, $\xi = 50$ (recall that ξ is a parameter that normalizes image gradients, see section 2.2.2) and the size of Gaussian kernel used here is $7 \times 7 \times 7$. The resolution of HRCT scans is reduced from $512 \times 512 \times 592$ to $256 \times 256 \times 296$ to save memory.

Figure 2.9 demonstrates the process of IAS evolving in volumetric HRCT scans. The initial surfaces are manually chosen. Multiple structures in the medical data are detected including lung surfaces, large airways, main blood vessels and some other dark areas beneath lungs. IAS does well in automatic handling of topologies, however, it is

insufficient to accurately extract lungs because the information employed for segmentation are simply voxel intensities and image gradients. More constraints are necessary to obtain well-segmented lungs automatically. In addition, dark regions outside the body in the image are masked. An enlarged slice image of the segmentation result is presented by figure 2.11.

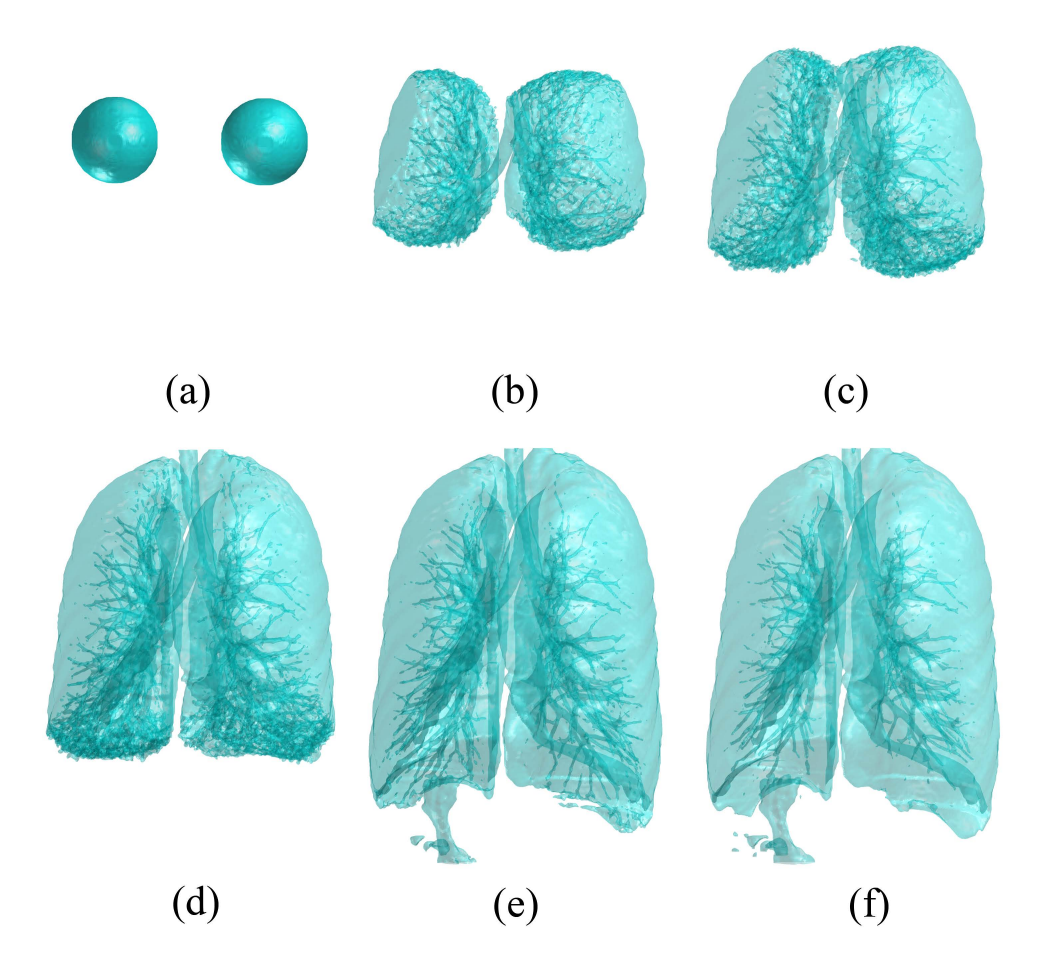


Figure 2.9: The evolution of IAS from initial surfaces till convergence on volumetric HRCT scans. (a) Initial surfaces (n=0): two spheres which reside within left and right lung areas. (b) n=1. (c) n=2. (d) n=8. (e) n=18. (f) Converged IAS (n=31). $\{\mu=500,\ \nu=0,\ \lambda=1,\ \sigma^2=1,\ \text{average time taken in each iteration } \bar{t}=9.76s\}$

When $\lambda=0$, IAS becomes in fact GAS whose evolution is quite slow from manually chosen initial surfaces, a superior scheme is to use GAS for post regularization and detection of local boundaries. Figure 2.12 gives an example. The results are obtained using shape in figure 2.9(f) as initial surfaces by setting λ to 0. GAS does well in local regularization given a segmented shape from the image. More thin structures are detected and smoothed.

Figure 2.13 presents another application of GAS. Figure 2.13(a) shows the lungs linearly interpolated from $128 \times 128 \times 198$ to $256 \times 256 \times 296$. There is boundary information

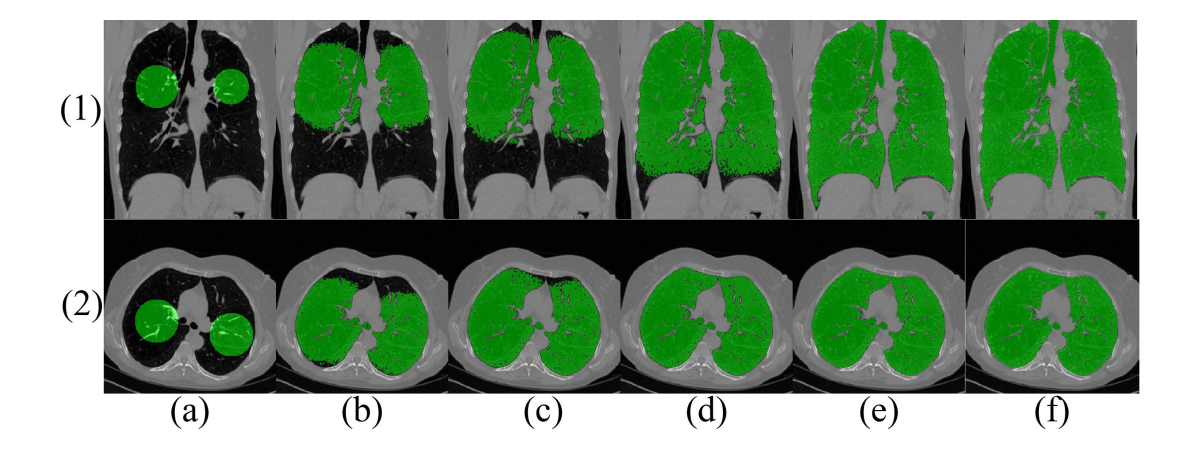


Figure 2.10: Selected slices that present evolution of IAS. (1)(a)-(f) correspond to (a)-(f) in figure 2.9 on the coronal plane. (2)(a)-(f) are on axial plane.

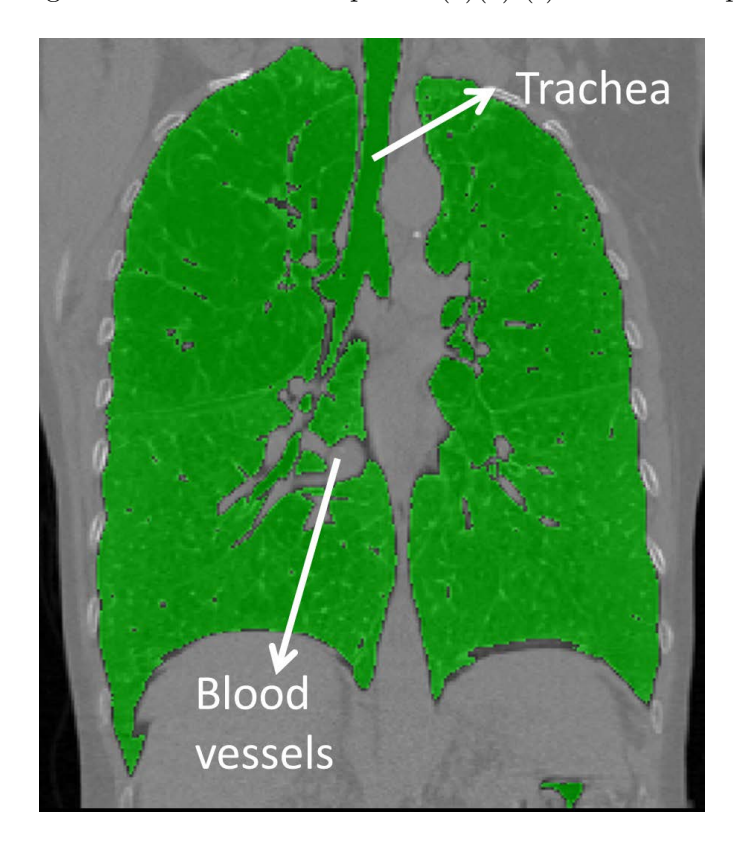


Figure 2.11: An enlarged slice image of the segmentation result produced by IAS.

loss and the lung surfaces are inaccurate. A better interpolation scheme, say cubic interpolation, could be chosen for a nicer shape, however, the accuracy is not ensured, for it is not based on image information. GAS regularization delivers a satisfactory result and it could be considered, in this application, as image-based interpolation. This is very useful in future scheme of lung extraction using prior-shape-based active surfaces. General lung shapes could be extracted from lower resolution volumetric medical image

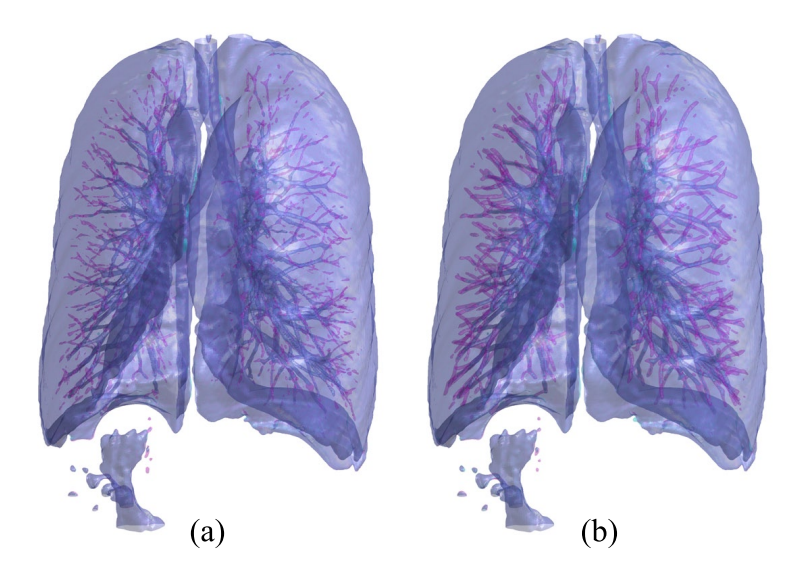


Figure 2.12: (a) Post regularized surfaces of the segmented structures are overlapped on initial surfaces and additional structures detected by GAS are in magenta. $\mu = 500$, $\nu = 0$, $\lambda = 0$, $\sigma^2 = 1$ (b) Another result with increased σ : $\sigma^2 = 3$. Both results are obtained using 3 iterations.

for memory and time efficiency, then GAS regularization is performed on original image for better boundary accuracy.

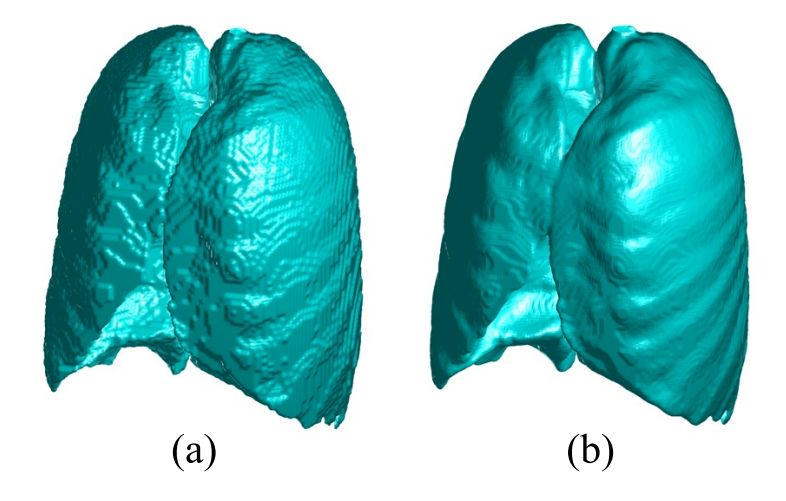


Figure 2.13: Another example of post regularization using GAS. (a) Linearly interpolated lungs from a lower resolution. (b) Result of GAS regularization. $\{\mu = 500, \nu = 0, \lambda = 0, \sigma^2 = 1, 17 \text{ iterations with } \bar{t} = 9.63s.\}$

2.7 Conclusions

Variational feature extraction models, namely active contours/surfaces, are considered to be advanced image segmentation methods and discussed in detail in this chapter.

They are associated with mathematical optimization problems and naturally smoothed by internal force during evolution for image segmentation. Experiments are conducted both for 2-D and 3-D cases and the results suggest that active contours/surfaces model is capable of automatically detecting regions and boundaries of images and its local and global properties can be adjusted by various parameter settings. It also requires superior numerical implementation scheme to work properly.

However, internal force is insufficient for an accurate lung segmentation under influence of bright vessels and dark airways, as is shown by experimental results in section 2.6. Therefore, prior knowledge (prior shape) is necessary for an accurate segmentation and the next step is to incorporate the prior shape model into the process of segmentation.

Chapter 3

Similarity Registration of Volumetric Shapes

3.1 Background

In the previous chapter, it is shown that the active surface models fail to produce accurate segmentation of lungs from CT images. Therefore introducing shape template into active surfaces, known as the shape-based image segmentation method is necessary. Particularly for shape-based image segmentation problem, shape registration is essential because, as discussed in section 1.3, it enables the deformable shape template to contribute to the evolution of the active contours/surfaces. This gives the shape-based segmentation method a greater robustness against noise and occlusions as is pointed out in the works of Leventon et al. (2000), Tsai et al. (2003) and Bresson et al. (2006). Furthermore, shape registration benefits a variety of research fields, such as statistical shape study, shape-based image segmentation, 3-D modelling of real world objects, which give rise to all kinds of registration techniques. Before a certain registration technique is developed, four aspects need to be taken into account:

1. Shape representations: The raw data acquired at hand may well differ in various research fields, and they are intended to be well suited for application purposes. For example, in real world object modelling, popular representations include range data (Li et al. (2011), Gelfand et al. (2005), Lucchese et al. (2002)), and point sets (Chen et al. (2010), Breitenreicher and Schnörr (2010)), while in shape-based image segmentation (Spiegel et al. (2009),Sun et al. (2012)), parametric surfaces and signed distance functions (SDFs,Osher and Sethian (1988)) are frequently used for curve/surface evolutions. In medical imaging, shapes are often represented by characteristic functions (CFs) which serve as mask to emphasize regions of interest.

- 2. Expected results of registration: In 3-D object modelling, a sequence of partial views represented by range data are to be registered for acquisition of a full 3-D object. This process involves matching of common regions of surfaces. In shape-based image segmentation and statistical shape modelling, registration to find a suitable match of two entire shapes.
- 3. Degrees of precision: In fact, registration precision is closely associated with given degrees of freedom. Rigid transformation (Breitenreicher and Schnörr (2010), Gelfand et al. (2005), Besl and McKay (1992)) involves rotation and translation and similarity registration further includes scale, while non-rigid transformation allow local deformation to achieve a greater matching. One can choose proper degrees of freedom according to the registration problem at hand. For example, entire shape or surface may be sufficiently matched by rigid transformation, however, more sophisticated modelling such as facial expression modelling or heart ventricle motion tracking involve non-rigid transformation (Huang et al. (2006)).
- 4. Similarity/Dissimilarity measure of registration: Most frequently used measure is sum of squared distance/difference (SSD) between either explicit corresponding points or functions that used to represent shapes without explicit correspondence. Novel measures used in recent years include information theoretic measure between probability distribution functions estimated from point sets or signed distance functions (Chen et al. (2010), Huang et al. (2006), Wang et al. (2002)) and kernel correlation of point sets entropy (Tsin and Kanade (2004)). There are all kinds of measures to choose from, however, the measure should be well suited for the representations of shapes to achieve a satisfying result for registration.

The method proposed here is intended to be applied to two areas of research: statistical shape study of volumetric shapes and shape-based volumetric image segmentation. Considering the four aspects given above, the method could be described as follows:

- 1. It concerns shapes represented by CFs. Anatomical structures acquired from medical images are mostly volumetric and characteristic functions that denote the regions of interest in a straightforward way. Also, in shape-based image segmentation, regions inside the reference shapes and the target areas of images are to be maximized, where CFs are a representation with simplicity.
- 2. It registers two entire shapes. In statistical modelling of volumetric shapes, one entire shape in volumetric image could be obtained through manual or computer-aided segmentation, which does not involve matching partial views (range data) together. The same goes with shape-based image segmentation, the target areas are intact shapes and they are to be registered with model shapes at hand.
- 3. It handles similarity registration that involves isometric scale, rotation and translation. Similarity registration is a precursor to statistical modelling of volumetric shapes.

Furthermore, in the shape-based image segmentation, the first step to bring reference shape to segmentation process is similarity registration before any local deformation.

4. It employs region-based similarity measures between shapes. Region-based similarity measures between CFs denote the volume of homogeneous region of shapes. In statistical modelling of volumetric shapes, we focus more on the region features rather than the boundaries. With regard to the volumetric image segmentation, although it is ideal to achieve both region and boundary accuracy, the final results one would expect first are accurate regions. It should be pointed out that the registration is performed using all voxels inside shapes to be registered.

Furthermore, the reason for particularly choosing similarity registration in this thesis is that it is the general practice in the literature (Tsai et al., 2003; Bresson et al., 2006) to employ this type of registration in shape-based medical image segmentation. Also, in the case of this thesis, when CT images are acquired from various patients, it is can be assumed that the regions of lungs inside the CT images to have three individual differences, which are the volumes, the poses and the position. They corresponds to the three parameters in the similarity registration technique, which are scale, rotation and translation. Let us now proceed to review several previous works that concern this topic.

3.2 Previous Works

The method frequently used in similarity registration is gradient descent optimization of shapes represented by SDFs. The shape-based segmentation method proposed in Chen et al. (2002) involves rigid registration in 2-D using a variational frame work. It handles registration by optimizing a proposed functional that iteratively registers the evolving contours to rigid shapes represented by level-set functions. Similar works are done in Tsai et al. (2003) and Bresson et al. (2006), who applied rigid/affine registration to statistical modelling of shapes and image segmentation process. Also, in Paragios et al. (2003), similarity registration is used as a pre-alignment technique for non-rigid registration. These works commonly choose SSD as the measure for similarity between shapes, which also suffers local minima problem. Alternatively, it is proposed in Huang et al. (2006) to maximize mutual information between SDFs of shapes and the method performs well in finding a global maximum.

The methods proposed in Al-Huseiny et al. (2010); Mahmoodi et al. (2012) have a close relationship with the works done in this work. The calculations of rotation and translation parameters are related to standard correlation problems and scale parameter is computed using geometric moments of shapes. Experiments show that they have good robustness against occlusions, noise and topological differences. However, these methods

are based on 2D and shapes are represented by SDFs, while the method proposed in this work employs CFs as shape representation and designed for volumetric shapes.

Another method that concerns this topic is the iterative closed point (ICP) method introduced in Besl and McKay (1992) that solves general rigid registration problem (concerning rotation and translation). This method, at each iteration, finds the closest points on the surface of target shape to that of the reference shape and optimizes rotation and translation. Results indicate that it is suitable for a variety of representations of shapes including point sets, parametric surfaces and implicit surfaces represented by level-set functions. The ICP method performs well in local optimization, however, when the poses of shapes to be registered have large differences, it may fall into local minima. Another disadvantage is that it is claimed to be slow. Accelerated ICP methods were later proposed in Rusinkiewicz and Levoy (2001); Granger and Pennec (2006); Segal et al. (2009).

In recent years, the Laplace-Beltrami spectra employed as shape descriptors in Reuter et al. (2009, 2006); Reuter (2010); Rustamov (2007) could be used to perform analyses of shapes regardless of their poses and scale. Our method has some similarities with these works. In the calculations of rotation and scale parameters, shapes are transformed into other representations. However, these works aim at evaluating similarity between shapes without registration for shape retrieval from databases and quality assessment of data that represent surfaces and volumes.

3.3 Mathematical Preliminaries

3.3.1 Unit Quaternions as Representation of Rotations

Unit quaternions are used as mathematical representation of rotation of three dimensional rigid shapes. A unit quaternion is a four vector $\vec{q} \in \mathbb{S}^3$, where $\mathbb{S}^3 = \{\mathbf{h} \in \mathbb{R}^4 : ||\mathbf{h}|| = 1\}$ ($||\cdot||$ is the Euclidean norm). \mathbb{S}^3 represents a unit sphere in 4-D Euclidean space, frequently referred to as unit 3-sphere. A volumetric rigid body could be considered as a set of 3-D vectors, and rotation of a vector set about a fixed axis is a linear transform and performed by a 3×3 matrix, denoted by \mathbf{R} with $\det(\mathbf{R}) = 1$. It is explained well in Diebel (2006) that one unit quaternion \vec{q} generates one rotation matrix \mathbf{R} through the equation given in the footnote¹.

A unit quaternion in representation of rotation, consists of a scalar part and a vector part, namely $\vec{q} = (\eta, \vec{v})$. It has a counterpart known as the 'conjugate', denoted by

$$\mathbf{R}(\vec{q}) = \begin{pmatrix} q_0^2 + q_1^2 - q_2^2 - q_3^2 & 2(q_1q_2 - q_0q_3) & 2(q_1q_3 + q_0q_2) \\ 2(q_1q_2 + q_0q_3) & q_0^2 + q_2^2 - q_1^2 - q_3^2 & 2(q_2q_3 - q_0q_1) \\ 2(q_1q_3 - q_0q_2) & 2(q_2q_3 + q_0q_1) & q_0^2 + q_3^2 - q_1^2 - q_2^2 \end{pmatrix}$$

¹Assuming that $\vec{q} = (q_0, q_1, q_2, q_3),$

 $\vec{q}^* = (\eta, -\vec{v})$. Multiplication of quaternions follows the formula below:

$$\vec{q}_1 \vec{q}_2 = (\eta_1 \eta_2 - \vec{v}_1 \cdot \vec{v}_2, \ \eta_1 \vec{v}_2 + \eta_2 \vec{v}_1 + \vec{v}_1 \times \vec{v}_2) \tag{3.1}$$

where '.' is the dot product of vectors and 'x' the cross product. However, this multiplication is non-commutative. In particular, $\vec{q}\vec{q}^*=(1,0,0,0)$, which corresponds to a 3×3 identity matrix. This means that while \vec{q} generates a rotation, \vec{q}^* generates a corresponding inverse rotation. Multiplication of a set of unit quaternions in a particular order, namely $\vec{q}=\vec{q}_1\vec{q}_2\cdots\vec{q}_N$, could produce one unique rotation and the corresponding inverse rotation could be produced by $\vec{q}^*=\vec{q}_N^*\cdots\vec{q}_2^*\vec{q}_1^*$ (see figure 3.1 for an example).

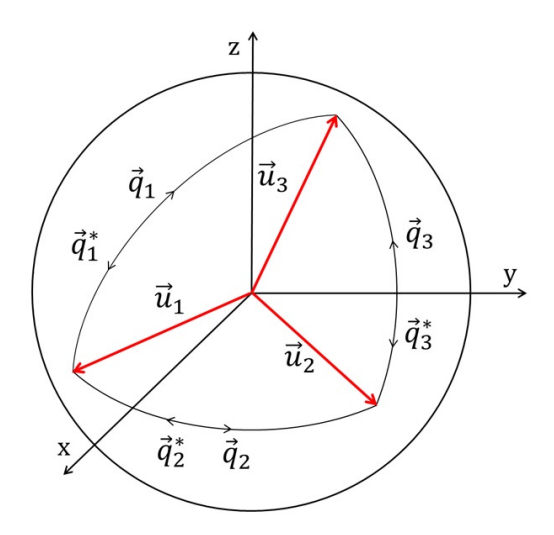


Figure 3.1: \vec{u}_1 rotates to coincide \vec{u}_3 according to \vec{q}_1 , and the reverse rotation is generated by \vec{q}_1^* . An alternative path is $\vec{u}_1 \to \vec{u}_2 \to \vec{u}_3$, produced by $\vec{q}_2\vec{q}_3$ and the path back is according to $\vec{q}_3^*\vec{q}_2^*$.

More intuitively, a unit quaternion consists of an axis $\vec{a} \in \mathbb{S}^2$, where $\mathbb{S}^2 = \{\hat{\mathbf{x}} \in \mathbb{R}^3 : ||\hat{\mathbf{x}}|| = 1\}$, and an angle $\Delta\theta \in \mathbb{R}$, making $\vec{q}(\vec{a}, \Delta\theta) = (\cos(\Delta\theta/2), \vec{a}^{\mathrm{T}}\sin(\Delta\theta/2))$. Vector \vec{a} and angle $\Delta\theta$ are considered as the axis and angle of rotation, following the right handle rule. It could be observed that when $\Delta\theta = 4n\pi$, $\vec{q} = (1, 0, 0, 0)$, which means keeping the current pose, and $\vec{q}(\vec{a}, \Delta\theta) = \vec{q}^*(\vec{a}, -\Delta\theta)$, which simply means that rotations about axis \vec{a} by $\Delta\theta$ and by $-\Delta\theta$ are inverse to each other.

3.3.2 Implicit Representation of Volumetric Shapes

Let $\Omega \subset \mathbb{R}^3$ be bounded and represent the image domain, and $\mathcal{X}_r(\mathbf{x}) : \Omega \to \mathbb{R}$ and $\mathcal{X}_t(\mathbf{x}) : \Omega \to \mathbb{R}$ denote the characteristic functions (CFs) of reference shapes and target

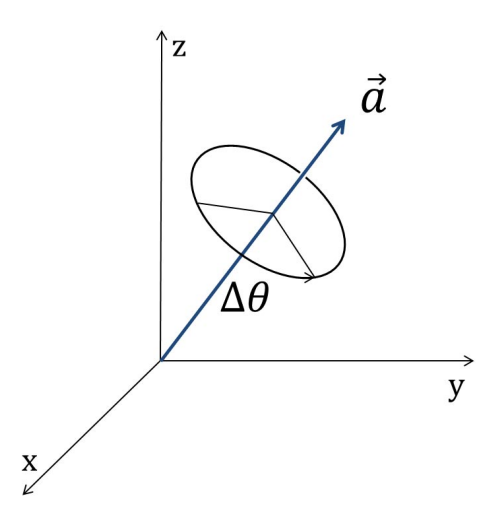


Figure 3.2: Rotation of a volumetric rigid body can be represented by an axis \vec{a} and an angle $\Delta\theta$, which is equivalent to a unit quaternion.

shapes. These functions are defined as

$$\mathcal{X}(\mathbf{x}) = \begin{cases} 1, & \mathbf{x} \in \Omega_+, \\ 0, & \mathbf{x} \in \Omega_-, \end{cases}$$
 (3.2)

where Ω_+ and Ω_- respectively represent domains inside and outside shapes. The surfaces of shapes are implicit and of less importance in this work.

This is a convenient representation especially in medical imaging, which mostly requires masks that emphasize region of interest (ROI). Furthermore, it is non-parametric and naturally handle shape topologies, which could be associated with signed distance functions (SDFs) that facilitate deformation and statistical study of shapes. In later experiments, we show that it is, furthermore, a statistically robust representation that is insensitive to outliers.

3.4 Methods

3.4.1 An Initial Transformation Using Principal Axes

It is frequently assumed that in the similarity registration of two shapes, the reference shape is scaled, rotated and translated to match the target shape. To facilitate calculations of registration parameters, principal component analysis (PCA) is used here to find a coarse match of shapes.

Let $\mathbf{c} \in \mathbb{R}^3$ denote the centroid of \mathcal{X} in the initial Cartesian coordinate system. \mathbf{c} is calculated by

$$\mathbf{c} = \frac{\int_{\Omega} \mathbf{x} \mathcal{X}(\mathbf{x}) \, d\mathbf{x}}{\int_{\Omega} \mathcal{X}(\mathbf{x}) \, d\mathbf{x}}$$
(3.3)

Then 3×3 symmetric covariance matrix Σ could therefore be obtained from

$$\Sigma = \frac{\int_{\Omega} (\mathbf{x} - \mathbf{c}) (\mathbf{x} - \mathbf{c})^{\mathrm{T}} \mathcal{X}(\mathbf{x}) \, d\mathbf{x}}{\int_{\Omega} \mathcal{X}(\mathbf{x}) \, d\mathbf{x}}$$
(3.4)

 Σ_r and Σ_t respectively for reference and target shapes could be computed using the above equation. We then calculate respective three eigenvectors of Σ_r and Σ_t , denoted by $\mathbf{P}_r = (\vec{p}_{r_1}, \vec{p}_{r_2}, \vec{p}_{r_3})$ and $\mathbf{P}_t = (\vec{p}_{t_1}, \vec{p}_{t_2}, \vec{p}_{t_3})$. The eigenvectors are ordered according to their eigenvalues, i.e. the first eigenvector corresponds to the largest eigenvalue (see figure 3.3). These three eigenvectors are referred to in this work as the first, second and third principal axes. $\mathcal{X}_r(\mathbf{x})$ is then translated and rotated so that \mathbf{P}_r is coincided with \mathbf{P}_t , and \mathbf{P}_t is used as the axes of the new Cartesian coordinates. This rotation is generated by \vec{q}_p , which is calculated by three steps:

Step 1: Calculating \vec{q}_{p_1} that coincides the first principal axis,

$$\begin{split} & \Delta \theta_{p_1} = \cos^{-1}(\vec{p}_{r_1} \cdot \vec{p}_{t_1}), \\ & \vec{a}_{p_1} = (\vec{p}_{r_1} \times \vec{p}_{t_1}) / \sin(\Delta \theta_{p_1}), \\ & \vec{q}_{p_1} = (\cos(\Delta \theta_{p_1}/2), \ \vec{a}_{p_1}^{\mathrm{T}} \sin(\Delta \theta_{p_1}/2)), \end{split}$$

Step 2: Calculating \vec{q}_{p_2} that coincides the second principal axis,

$$\begin{split} & \Delta \theta_{p_2} = \cos^{-1}(\mathbf{R}(\vec{q}_{p_1}) \vec{p}_{r_2} \cdot \vec{p}_{t_2}), \\ & \vec{a}_{p_2} = (\mathbf{R}(\vec{q}_{p_1}) \vec{p}_{r_2} \times \vec{p}_{t_2}) / \sin(\Delta \theta_{p_2}), \\ & \vec{q}_{p_2} = (\cos(\Delta \theta_{p_2}/2), \ \vec{a}_{p_2}^{\mathrm{T}} \sin(\Delta \theta_{p_2}/2)), \end{split}$$

Step 3: Calculating \vec{q}_p by quaternion multiplication of \vec{q}_{p_1} and \vec{q}_{p_1} , $\vec{q}_p = \vec{q}_{p_1} \vec{q}_{p_2}$,

In certain cases the third principal axes may be inverse to each other after the coinciding, however, this would not affect the final result, because the third principal axes are statistically of less significance. $\mathcal{X}_r(\mathbf{x})$ and $\mathcal{X}_t(\mathbf{x})$ are thus brought into the new coordinate system i.e.:

$$\ddot{\mathcal{X}}_r(\mathbf{x}) = \mathcal{X}_r(\mathbf{R}(\vec{q}_p)(\mathbf{x} + \mathbf{c}_r)),$$
(3.5)

$$\overset{\sim}{\mathcal{X}}_t(\mathbf{x}) = \mathcal{X}_t(\mathbf{x} + \mathbf{c}_t),$$
(3.6)

where \mathbf{c}_r and \mathbf{c}_t are the respective centroids of CFs. Figure 3.3 presents a general process of coinciding shapes' principal axes.

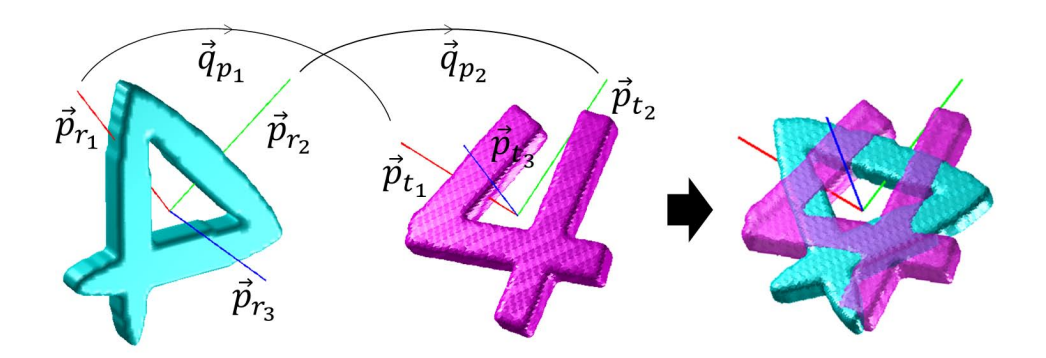


Figure 3.3: The process of coinciding principal axes of shapes to be registered. Red, green and blue respectively represent the first, second and third principal axes of shapes.

3.4.2 Scaling

Geometric moments of CFs are employed here to calculate scale difference of shapes. Let $s \in (0, +\infty)$ denote the scale parameter. We start with considering a simple case that the target shape is the scaled version of the reference shape, therefore, their CFs are related to each other with respect to s by the following equation:

$$\ddot{\mathcal{X}}_t(\mathbf{x}) = \ddot{\mathcal{X}}_r(s\mathbf{x}) \tag{3.7}$$

The geometric moments of $\breve{\mathcal{X}}_r(\mathbf{x})$ and $\breve{\mathcal{X}}_t(\mathbf{x})$ are given as

$$G_r(m) = \int_{\Omega} ||\mathbf{x}||^m \breve{\mathcal{X}}_r(\mathbf{x}) \, d\mathbf{x}, \qquad (3.8)$$

$$G_t(m) = \int_{\Omega} ||\mathbf{x}||^m \check{\mathcal{X}}_t(\mathbf{x}) \, d\mathbf{x}, \tag{3.9}$$

where m = 0, 1, 2, ..., M is the degree of the moments and $||\cdot||$ is the Euclidean norm. Substituting equation 3.7 to equation 3.9, assuming $\mathbf{\acute{x}} = s\mathbf{x}$, we have

$$G_{t}(m) = \int_{\Omega} ||\mathbf{x}||^{m} \check{\mathcal{X}}_{r}(s\mathbf{x}) \, d\mathbf{x}$$

$$= \int_{\Omega} \frac{||\mathbf{\acute{x}}||^{m}}{s^{m}} \check{\mathcal{X}}_{r}(\mathbf{\acute{x}}) \, \frac{d\mathbf{\acute{x}}}{s^{3}}$$

$$= \frac{1}{s^{m+3}} \int_{\Omega} ||\mathbf{\acute{x}}||^{m} \check{\mathcal{X}}_{r}(\mathbf{\acute{x}}) \, d\mathbf{\acute{x}}$$

$$= \frac{1}{s^{m+3}} G_{r}(m)$$
(3.10)

The logarithms of both sides hold the equality:

$$\ln G_t(m) = \ln \frac{1}{s^{m+3}} G_r(m) \tag{3.11}$$

However, shapes to be registered have differences in practice, therefore we minimize the squared difference of both sides. Let E_M be the sum of the scale error with degree m given by

$$E_{M} = \sum_{m=0}^{M} \left| \ln G_{t}(m) - \ln \frac{1}{s^{m+3}} G_{r}(m) \right|^{2}$$

$$= \sum_{m=0}^{M} \left| (m+3) \ln s + \ln \frac{G_{t}(m)}{G_{r}(m)} \right|^{2}$$
(3.12)

Finally, the optimal scale parameter s_{op} is estimated by minimizing E_M :

$$s_{op} = \operatorname*{argmin}_{s} E_{M} \tag{3.13}$$

3.4.3 Rotation

An optimal rotation could be represented by a unit quaternion \vec{q}_{op} which consists of a unit vector \vec{a}_{op} and an angle $\Delta\theta_{op}$ (explained in section 3.3.1). For convenience to find \vec{a}_{op} and $\Delta\theta_{op}$, $\check{\mathcal{X}}_r(\mathbf{x})$ and $\check{\mathcal{X}}_t(\mathbf{x})$ are mapped to a spherical coordinate system. Let $\Omega_{\mathcal{S}^2} \subset \mathbb{R} \times \mathbb{S}^2$ denote a spherical domain inside image domain Ω , and $\Omega_{\mathcal{S}^2}$ is bounded with radius R. Then $\check{\mathcal{X}}_r(\mathbf{x})$ and $\check{\mathcal{X}}_t(\mathbf{x})$ are respectively represented by $\check{\mathcal{X}}_r(\mathbf{r}): \Omega_{\mathcal{S}^2} \to \mathbb{R}$ and $\check{\mathcal{X}}_t(\mathbf{r}): \Omega_{\mathcal{S}^2} \to \mathbb{R}$, where $\mathbf{r} = (r, \hat{\mathbf{x}}(\theta, \varphi))^{\mathrm{T}}$ ($\hat{\mathbf{x}} = (\cos(\theta)\sin(\varphi), \sin(\theta)\sin(\varphi), \cos(\varphi))^{\mathrm{T}}$). Moreover, $r \in [0, R]$, $\theta \in [0, 2\pi)$, and $\varphi \in [0, \pi]$.

Radial variable r contains scale difference between the shapes to be registered, therefore to remove its impact on calculating rotation angle of the two CFs, we integrate the CFs over variable r, i.e.:

$$\tilde{\mathcal{X}}_r(\hat{\mathbf{x}}(\theta,\varphi)) = \int_0^R \breve{\mathcal{X}}_r(\mathbf{r})r^2 \,\mathrm{d}r,\tag{3.14}$$

$$\tilde{\mathcal{X}}_t(\hat{\mathbf{x}}(\theta,\varphi)) = \int_0^R \check{\mathcal{X}}_t(\mathbf{r}) r^2 dr,$$
 (3.15)

This indeed could be intuitively considered as projecting the CFs of shapes on to a parametric unit sphere centered by their centroids, referred to in this work as S^2 maps (see figure 3.4). The problem becomes to maximize the inner product of the two S^2

maps:

$$\vec{q}_{op} = \underset{\vec{q}}{\operatorname{argmax}} \int_{\mathbb{S}^{2}} \tilde{\mathcal{X}}_{t}(\hat{\mathbf{x}}) \tilde{\mathcal{X}}_{r}(\mathbf{R}(\vec{q})\hat{\mathbf{x}}) \, d\hat{\mathbf{x}}$$

$$= \underset{\vec{q}}{\operatorname{argmax}} \left\langle \tilde{\mathcal{X}}_{t}(\hat{\mathbf{x}}), \tilde{\mathcal{X}}_{r}(\mathbf{R}(\vec{q})\hat{\mathbf{x}}) \right\rangle$$
(3.16)

 \vec{q}_{op} calculated from this term is not affected by scale of shapes according to the following lemma

Lemma 3.1. The optimal rotation parameter \vec{q}_{op} calculated using equation 3.16 is scale invariant.

Proof. Since $s\mathbf{x} = sr\hat{\mathbf{x}}$, $\check{\mathcal{X}}(s\mathbf{x})$ (rescaled version of $\check{\mathcal{X}}(\mathbf{x})$) could be given in $\Omega_{\mathcal{S}^2}$ as $\check{\mathcal{X}}(sr,\hat{\mathbf{x}})$. Assuming that $\dot{r} = sr$, the \mathcal{S}^2 map of rescaled $\check{\mathcal{X}}(\mathbf{r})$, denoted by $\check{\mathcal{X}}_s(\hat{\mathbf{x}})$, satisfies:

$$\tilde{\mathcal{X}}_{s}(\hat{\mathbf{x}}) = \int_{0}^{R} \check{\mathcal{X}}(sr, \hat{\mathbf{x}}) r^{2} dr$$

$$= \int_{0}^{R} \check{\mathcal{X}}(\acute{r}, \hat{\mathbf{x}}) \frac{\acute{r}^{2}}{s^{2}} d\frac{\acute{r}}{s}$$

$$= \frac{1}{s^{3}} \int_{0}^{R} \check{\mathcal{X}}(\acute{r}, \hat{\mathbf{x}}) \acute{r}^{2} d\acute{r}$$

$$= \frac{1}{s^{3}} \tilde{\mathcal{X}}(\hat{\mathbf{x}}) \tag{3.17}$$

Let $\check{\mathcal{X}}_{rs}$ and $\check{\mathcal{X}}_{ts}$ be rescaled versions of $\check{\mathcal{X}}_r$ and $\check{\mathcal{X}}_t$ respectively using s_r and s_t , therefore, the equation below holds:

$$\left\langle \tilde{\mathcal{X}}_{ts}(\hat{\mathbf{x}}), \tilde{\mathcal{X}}_{rs}(\mathbf{R}(\vec{q})\hat{\mathbf{x}}) \right\rangle = \frac{1}{(s_r s_t)^3} \left\langle \tilde{\mathcal{X}}_t(\hat{\mathbf{x}}), \tilde{\mathcal{X}}_r(\mathbf{R}(\vec{q})\hat{\mathbf{x}}) \right\rangle$$
 (3.18)

According to the above equation, rescaling of CFs causes the correlation term in equation 3.16 to multiply a constant $(\frac{1}{(s_r s_t)^3})$. Therefore, \vec{q}_{op} that maximizes $\langle \tilde{\mathcal{X}}_t(\hat{\mathbf{x}}), \tilde{\mathcal{X}}_r(\mathbf{R}(\vec{q})\hat{\mathbf{x}}) \rangle$ also maximizes $\langle \tilde{\mathcal{X}}_{ts}(\hat{\mathbf{x}}), \tilde{\mathcal{X}}_{rs}(\mathbf{R}(\vec{q})\hat{\mathbf{x}}) \rangle$. \vec{q}_{op} calculated using equation 3.16 is thus scale invariant.

In fact, equation 3.16 is a spherical cross correlation problem described in Gutman et al. (2008) and Kostelec and Rockmore (2003) as to find $\vec{q}_{op} \in SO(3)^2$ that maximizes $\langle \tilde{\mathcal{X}}_t(\hat{\mathbf{x}}), \tilde{\mathcal{X}}_r(\mathbf{R}(\vec{q})\hat{\mathbf{x}}) \rangle$. Solution to this problem is given in these works using fast Fourier transform (FFT) on SO(3). However, there is no need to go that far to solve our problem. Next, we present a solution which is suited in our case.

 $^{^2}SO(3) = {\vec{q} \in \mathbb{R}^4 : ||\vec{q}|| = 1}$ is a group of unit quaternions.

The unit sphere is mapped onto a bounded plane with coordinates θ and φ , referred to in this work as an $\mathcal{R}^2_{\vec{a}}$ map. The reason for using ' \vec{a} ' as a subscript is that an $\mathcal{R}^2_{\vec{a}}$ map is generated according to a chosen rotation axis \vec{a} . Different choices of rotation axis \vec{a} generate different $\mathcal{R}^2_{\vec{a}}$ maps. In our case, three maps are generated according to the three principal axes \vec{p}_{t_1} , \vec{p}_{t_2} and \vec{p}_{t_3} (see figure 3.4).

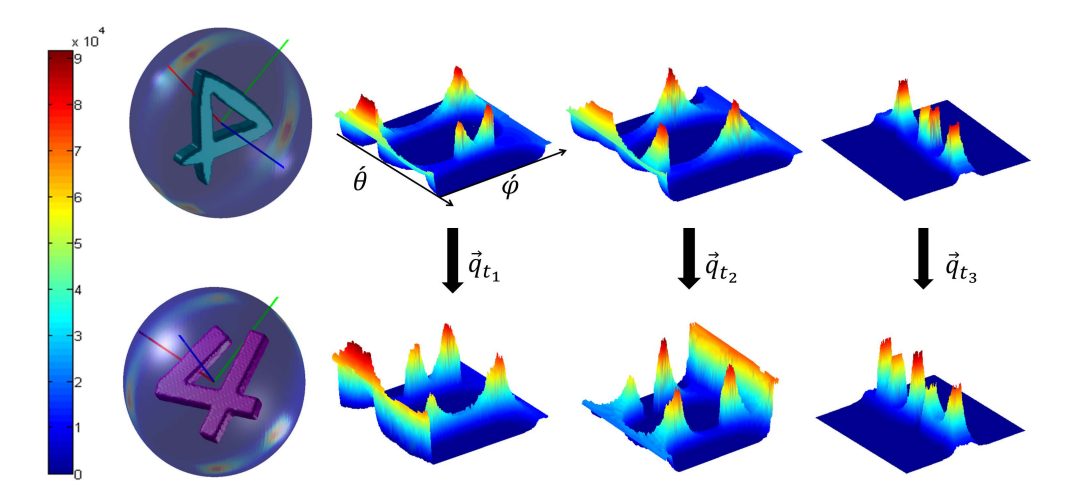


Figure 3.4: An example of the rotation adjustments. The top row from left to right is respectively the S^2 map, $\mathcal{R}^2_{\vec{a}}$ maps obtained according to \vec{p}_{r_1} , \vec{p}_{r_2} , \vec{p}_{r_3} of the reference '4'. The bottom row from left to right is S^2 map and $\mathcal{R}^2_{\vec{a}}$ maps of the target '4' ordered in the same way. From each $\mathcal{R}^2_{\vec{a}}$ map one quaternion for rotation adjustment is calculated and there are in total three quaternions,namely \vec{q}_{t_1} , \vec{q}_{t_2} , and \vec{q}_{t_3} .

Thus, $\tilde{\mathcal{X}}_r(\mathbf{R}(\vec{q}(\vec{a},\Delta\theta))\hat{\mathbf{x}}(\theta,\varphi)) \cong \tilde{\mathcal{X}}_r(\acute{\theta}-\Delta\theta,\acute{\varphi}))$, namely, rotations of an \mathcal{S}^2 map around an axis \vec{a} could be represented by simple shifts of the corresponding $\mathcal{R}^2_{\vec{a}}$ map along its $\acute{\theta}$ -axis. Assume that the 1-D Fourier transform of $\tilde{\mathcal{X}}_r(\acute{\theta},\acute{\varphi})$ and $\tilde{\mathcal{X}}_t(\acute{\theta},\acute{\varphi})$ with respect to $\acute{\theta}$ a respectively $\tilde{\mathcal{Y}}_r(\omega_{\acute{\theta}},\acute{\varphi})$ and $\tilde{\mathcal{Y}}_t(\omega_{\acute{\theta}},\acute{\varphi})$, namely

$$\tilde{\mathcal{Y}}_r(\omega_{\acute{\theta}}, \acute{\varphi}) = \int_0^{2\pi} \tilde{\mathcal{X}}_r(\acute{\theta}, \acute{\varphi}) e^{-i\omega_{\acute{\theta}}} d\acute{\theta}$$
(3.19)

$$\tilde{\mathcal{Y}}_t(\omega_{\acute{\theta}}, \acute{\varphi}) = \int_0^{2\pi} \tilde{\mathcal{X}}_t(\acute{\theta}, \acute{\varphi}) e^{-i\omega_{\acute{\theta}}} d\acute{\theta}$$
(3.20)

According to the shift property of the Fourier transform and Parseval's theorem, we have

$$\int_{0}^{\pi} \int_{0}^{2\pi} \tilde{\mathcal{X}}_{t}(\dot{\theta}, \dot{\varphi}) \overline{\tilde{\mathcal{X}}_{r}(\dot{\theta} - \Delta \theta, \dot{\varphi})} \sin(\dot{\varphi}) \, \mathrm{d}\dot{\theta} \, \mathrm{d}\dot{\varphi}$$

$$= \int_{0}^{\pi} \int_{-\infty}^{+\infty} \tilde{\mathcal{Y}}_{t}(\omega_{\dot{\theta}}, \dot{\varphi}) \overline{\tilde{\mathcal{Y}}_{r}(\omega_{\dot{\theta}}, \dot{\varphi}) e^{-i\omega_{\dot{\theta}}\Delta \theta}} \sin(\dot{\varphi}) \, \mathrm{d}\omega_{\dot{\theta}} \, \mathrm{d}\dot{\varphi}$$

$$= \int_{0}^{\pi} \int_{-\infty}^{+\infty} \tilde{\mathcal{Y}}_{t}(\omega_{\dot{\theta}}, \dot{\varphi}) \overline{\tilde{\mathcal{Y}}_{r}(\omega_{\dot{\theta}}, \dot{\varphi})} e^{i\omega_{\dot{\theta}}\Delta \theta} \sin(\dot{\varphi}) \, \mathrm{d}\omega_{\dot{\theta}} \, \mathrm{d}\dot{\varphi} \tag{3.21}$$

Since $\tilde{\mathcal{X}}_r$ is a real function, $\overline{\tilde{\mathcal{X}}_r(\acute{\theta} - \Delta\theta, \acute{\varphi})} = \tilde{\mathcal{X}}_r(\acute{\theta} - \Delta\theta, \acute{\varphi})^3$. Then the optimal rotation angle by rotating around a fixed common axis \vec{a}_0 could be obtained by

$$\Delta\theta_{op}(\vec{a}_0) = \underset{\Delta\theta}{\operatorname{argmax}} \int_0^{\pi} \int_{-\infty}^{+\infty} \tilde{\mathcal{Y}}_t(\omega_{\acute{\theta}}, \acute{\varphi}) \overline{\tilde{\mathcal{Y}}_r(\omega_{\acute{\theta}}, \acute{\varphi})} e^{i\omega_{\acute{\theta}}\Delta\theta} \sin(\acute{\varphi}) \, \mathrm{d}\omega_{\acute{\theta}} \, \mathrm{d}\acute{\varphi}$$
(3.22)

Thus, fine rotational angles are adjusted sequentially around all three principal axes using equation 3.22. The order of adjustments is from the first principal axis to the third (see figure 3.5). Finally \vec{q}_{op} could be obtained by:

$$\vec{q}_{op} = \vec{q}_p \vec{q}_{t_1} \vec{q}_{t_2} \vec{q}_{t_3}, \tag{3.23}$$

where \vec{q}_p is the quaternion that coincides principal axes of shapes (see section 3.4.1) and \vec{q}_{t_1} , \vec{q}_{t_2} , \vec{q}_{t_3} are respectively the quaternions calculated using equation 3.22 for the three principal axes \vec{p}_{t_1} , \vec{p}_{t_2} and \vec{p}_{t_3} .

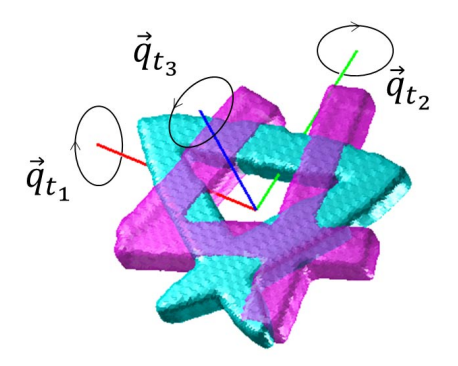


Figure 3.5: The process of fine rotational adjustments. It is sequentially done in a ' $\vec{p}_{t_1} \to \vec{p}_{t_2} \to \vec{p}_{t_3}$ ' manner.

It should be pointed out that in implementation, one $\mathcal{R}^2_{\vec{a}}$ map is directly calculated from CFs of shapes, and the other two maps are then computed from the first map. One can simply transform CFs of shapes into a spherical coordinate system with axes $r - \theta - \phi'$ and calculate sum of all voxels along the r-axis. The coordinate of each point on an $\mathcal{R}^2_{\vec{a}}$ map can be represented by a unit three vector and these vectors could be used to calculate where the value of the current point should be assigned when 'rotating' the $\mathcal{R}^2_{\vec{a}}$ map. The notion of \mathcal{S}^2 map serves only as an intuition to explain the theory, however, it is not used in implementation.

The accuracy of rotation adjustments is determined by the number of sample points (resolution) of an $\mathcal{R}_{\vec{a}}^2$ map. Bandwidth B is used here to denote the sample density and π/B and $\pi/2B$ respectively represent the sample intervals of $\acute{\theta}$ and $\acute{\varphi}$. Therefore, there

 $^{3\}overline{\tilde{\mathcal{X}}_r}$ is the complex conjugate of $\tilde{\mathcal{X}}_r$

are in total $4B^2$ points on an $\mathcal{R}^2_{\vec{a}}$ map. This convention could be found in Kostelec and Rockmore (2003). More about bandwidth B is discussed in section 3.5.

3.4.4 Translation

Using the calculated scale and rotation parameters, \vec{q}_{op} and s_{op} , we obtain $\acute{\mathcal{X}}_r(\mathbf{x}) = \mathcal{X}_r(s_{op}\mathbf{R}(\vec{q}_{op})\mathbf{x})$. The problem is now to maximize the inner product of the CFs that represent the two shapes:

$$\vec{T}_{op} = \underset{\vec{T}}{\operatorname{argmax}} \int_{\Omega} \mathcal{X}_{t}(\mathbf{x}) \dot{\mathcal{X}}_{r}(\mathbf{x} - \vec{T}) d\mathbf{x}$$

$$= \underset{\vec{T}}{\operatorname{argmax}} \left\langle \mathcal{X}_{t}(\mathbf{x}), \dot{\mathcal{X}}_{r}(\mathbf{x} - \vec{T}) \right\rangle \tag{3.24}$$

where $\vec{T} \in \mathbb{R}^3$ denotes the translation parameter. 3-D Spacial Fourier transform of \mathcal{X}_t and $\hat{\mathcal{X}}_r$ are respectively

$$\mathcal{Y}_t(\boldsymbol{\omega}) = \int_{\Omega} \mathcal{X}_t(\mathbf{x}) e^{-i\boldsymbol{\omega} \cdot \mathbf{x}} \, d\mathbf{x}$$
 (3.25)

$$\dot{\mathcal{Y}}_r(\boldsymbol{\omega}) = \int_{\Omega} \dot{\mathcal{X}}_r(\mathbf{x}) e^{-i\boldsymbol{\omega} \cdot \mathbf{x}} \, \mathrm{d}\mathbf{x}$$
(3.26)

where $\omega \in \mathbb{R}^3$ is the spatial frequency vector. According to shift property of Fourier transform and Parseval's theorem, the following equation holds:

$$\left\langle \mathcal{X}_{t}(\mathbf{x}), \dot{\mathcal{X}}_{r}(\mathbf{x} - \vec{T}) \right\rangle = \int_{\mathbb{R}^{3}} \mathcal{Y}_{t}(\mathbf{x}) \overline{\dot{\mathcal{Y}}_{r}(\mathbf{x})} e^{i\boldsymbol{\omega} \cdot (-\vec{T})} \, d\boldsymbol{\omega}$$
$$= \int_{\mathbb{R}^{3}} \mathcal{Y}_{t}(\mathbf{x}) \overline{\dot{\mathcal{Y}}_{r}(\mathbf{x})} e^{i\boldsymbol{\omega} \cdot \vec{T}} \, d\boldsymbol{\omega}$$
(3.27)

 $\dot{\mathcal{Y}}_r(\boldsymbol{\omega})$ and $\mathcal{Y}_t(\boldsymbol{\omega})$ are respectively the 3-D spatial Fourier transform of $\dot{\mathcal{X}}_r(\mathbf{x})$ and $\mathcal{X}_t(\mathbf{x})$. Therefore, the optimal translation parameter \vec{T}_{op} could be computed using

$$\vec{T}_{op} = \underset{\vec{T}}{\operatorname{argmax}} \int_{\mathbb{R}^3} \mathcal{Y}_t(\boldsymbol{\omega}) \overline{\dot{\mathcal{Y}}_r(\boldsymbol{\omega})} e^{i\boldsymbol{\omega}\cdot\vec{T}} d\boldsymbol{\omega}, \qquad (3.28)$$

Although calculations of rotation and scale are independent, translation optimization relies on how well the rotation and scale are estimated, namely \vec{T}_{op} varies with s_{op} and \vec{q}_{op} .

The normalized inner products of shapes to be registered under different values of translation parameters are demonstrated in figure 3.6. Two typical directions of translation in [-128,128] are selected and two local maximum adjacent to the global peak could be observed on the right side of figure 3.6. It is important to note that the method proposed here is not affected by these local maxima. Further experiments addressing

this issue could be found in section 3.5. Although the calculations of rotation and scale are independent, translation optimization relies on how well the rotation and scale are estimated, namely \vec{T}_{op} varies with s_{op} and \vec{q}_{op} .

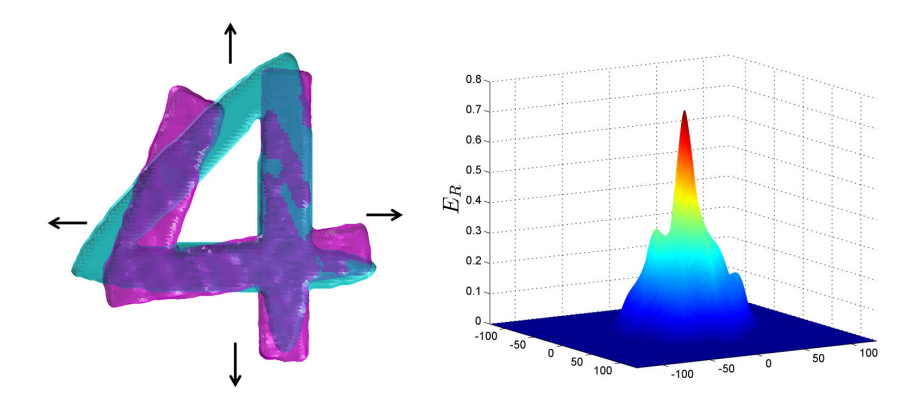


Figure 3.6: Left: the open '4' is fixed while the closed '4' translates in two directions from -128 to 128. Right: the normalized inner products of shapes E_R (defined in section 3.4.5) under different values of translation.

3.4.5 Similarity Measures for Evaluation of Registration

After the shapes are registered using the method proposed here, some similarity/disimilarity measures are supposed to be chosen for the evaluation of registration results. Several measures regarding region similarity in Silva et al. (2012) are adopted here to achieve this task. Namely, normalized inner product, accuracy, overlap, sensitivity and specificity.

1. The normalized inner product of CFs of shapes denoted by E_R :

$$E_R = \int_{\Omega} \frac{\mathcal{X}_t(\mathbf{x}) \mathcal{X}_r(s_{op} \mathbf{R}(\vec{q}_{op}) \mathbf{x} - \vec{T}_{op})}{||\mathcal{X}_t(\mathbf{x})||_2 ||\mathcal{X}_r(s_{op} \mathbf{R}(\vec{q}_{op}) \mathbf{x} - \vec{T}_{op})||_2} d\mathbf{x}$$
(3.29)

where $||\cdot||_2$ is the \mathbf{L}^2 -norm of CFs⁴.

The normalized inner product between shapes represented by CFs measures the volume of homogeneous region inside shapes. This measure is equivalent to the similarity angle presented in Silva et al. (2012) and is suitable to measure similarity not only between two shapes, but also among a group of shapes. One of the issues in statistical shape modelling is to decide which sample shape is to be used as a standard. Normalized inner product is used to compare the registration results comparable when different shapes are chosen as the standard (examples are given in section 3.5.5.2).

 $^{|\}mathcal{X}| |\mathcal{X}|_2 = \left(\int_{\Omega} |\mathcal{X}|^2 d\mathbf{x} \right)^{\frac{1}{2}}$

2. Let us denote accuracy, overlap, sensitivity and specificity, respectively by E_A , E_O , E_S , E_{SP} :

$$E_A = \frac{V_1 + V_2}{V} \tag{3.30}$$

$$E_O = \frac{V_1}{V_1 + V_3 + V_4} \tag{3.31}$$

$$E_S = \frac{V_1}{V_1 + V_3} \tag{3.32}$$

$$E_{SP} = \frac{V_2}{V_2 + V_4} \tag{3.33}$$

where V stands for the volume of the image domain, V_1 the volume of common region of both shapes, V_2 the volume outside both regions of shapes, V_3 the volume of region inside \mathcal{X}_t but outside \mathcal{X}_r , and V_4 the volume of the region inside \mathcal{X}_r but outside \mathcal{X}_t . Two of the four measures, namely, E_O and E_S would be used in the experiments due to the fact that E_A and E_{SP} are too close to 1 (between 0.995 and 1). A primary comparison of the similarity measures can be found in figure 3.7.

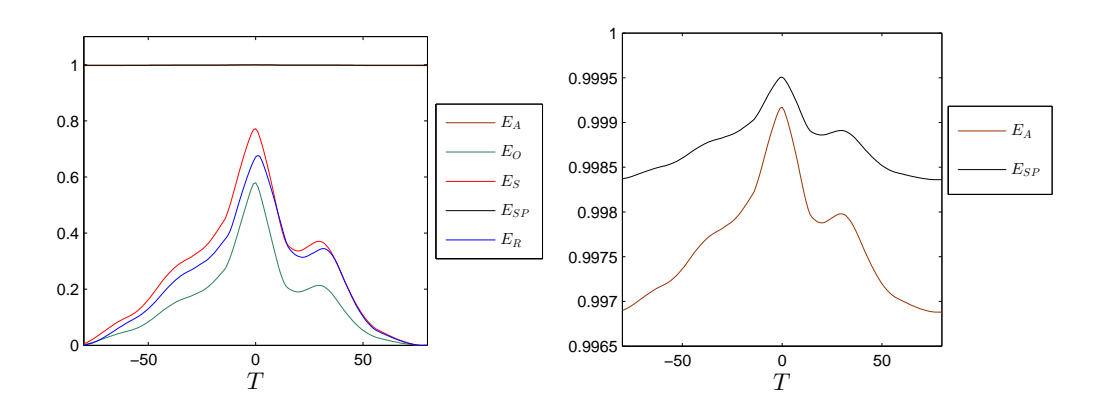


Figure 3.7: The plots of similarity measures while the reference '4' (similar to figure 3.6) translates from -80 to 80 along one direction. Left: Accuracy, overlap, sensitivity, specificity and the normalized inner product. Right: Only accuracy and specificity (their appearances are similar to the other three, however, they are impractical to be used in combination with the other three.)

In shape-based image segmentation, especially ROI extraction, region accuracy is of greater significance than boundary accuracy. Therefore, similarity registration used in the segmentation process should maximize the homogeneous region between the reference shape and internal area of evolving surfaces. In previous methods, such as ICP, the sum of squared difference or distance (SSD) between explicit corresponding points on shapes' surfaces is used as the measure, which is dependent on the accuracy of locating corresponding points and can be largely affected by noise and initial poses.

3.5 Experimental Results

3.5.1 An Overview

A series of experiments is presented here to show the performance of the proposed technique. Initially, synthetic shapes with various topologies are registered as a primary test stage to show the method proposed here is able to deal with relatively difficult shapes. A comparison is then presented between our method and the classical ICP method to show that our method barely suffers from traditional local minima problem. Next, several performance analyses are given here to show accuracy, efficiency, stability and robustness of our method. In addition, the performance analyses mainly concern scale and rotation parameters, which are the major part of the method proposed here. Lastly, we give two examples for the applications of the method: registration in shape-based image segmentation and in statistical modelling of shapes. Shapes of lungs involved in this stage are mask images. The case index of the lung database which includes the patients' IDs and the disease states is provided by table B.1 in appendix B.

The method proposed here is implemented using MATLAB 2012b (MathWorks, Inc.) on a PC station with a 2.67 GHz Xeon processor and 12 GB RAM. Reference shapes are in cyan (light color), target shapes in magenta (deep color) and for visualization purposes, only the surface of the shapes are shown here.

3.5.2 Registration of Topologically Different Shapes

Some primary experiments are presented here to show the method proposed here works with shapes with complex topologies. Figure 3.8 demonstrates the registration of topologically different '4's extended from 2D image. By feature points corresponding method, the number of feature points involved may well be different, due to their difference in Euler characteristic numbers. Such a difference in the number of feature points makes the additional handling of the topology more difficult, while such a difference has no impact on the technique proposed here.

A more complex case of registering two shapes with various topologies is presented in figure 3.9. The reference shape is two linked symmetric rings whereas the target shape consists of two unsymmetric horseshoes with some manually added clutters. However, such a topological variation and the clutters have no impact on the technique proposed here.

Some data concerning registration are provided in table 3.1, including Image size, approximate scopes of shapes, maximum degree of moments M, bandwidth B (this parameter is explained in the last paragraph of section 3.4.3), the execution time t of our algorithm and registration parameters.

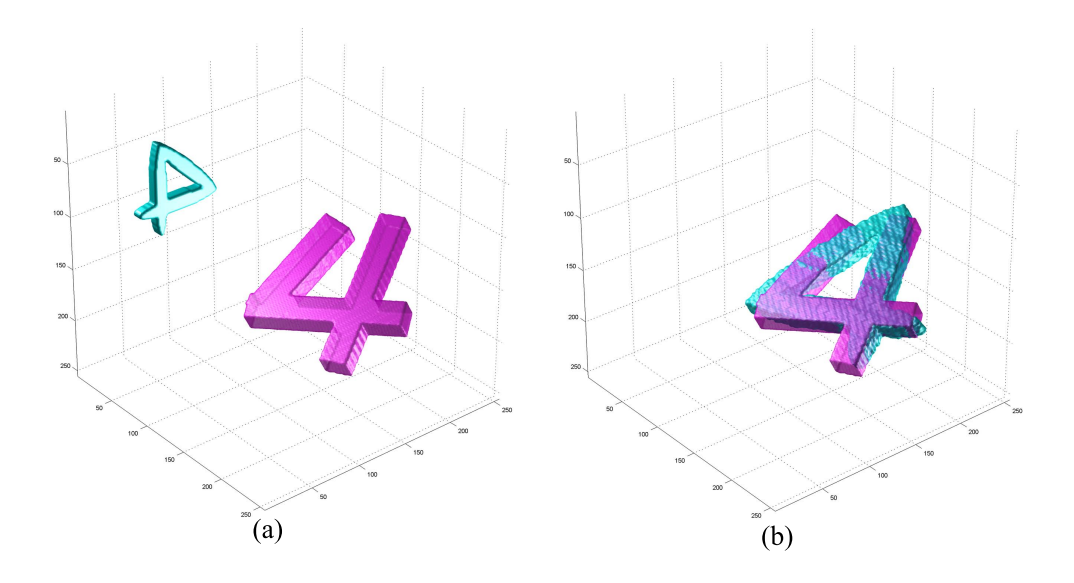


Figure 3.8: The registration of topologically different '4's. (a) The reference shape (a closed '4') and the target shape (an open '4'). (b) The result obtained by the technique proposed here.

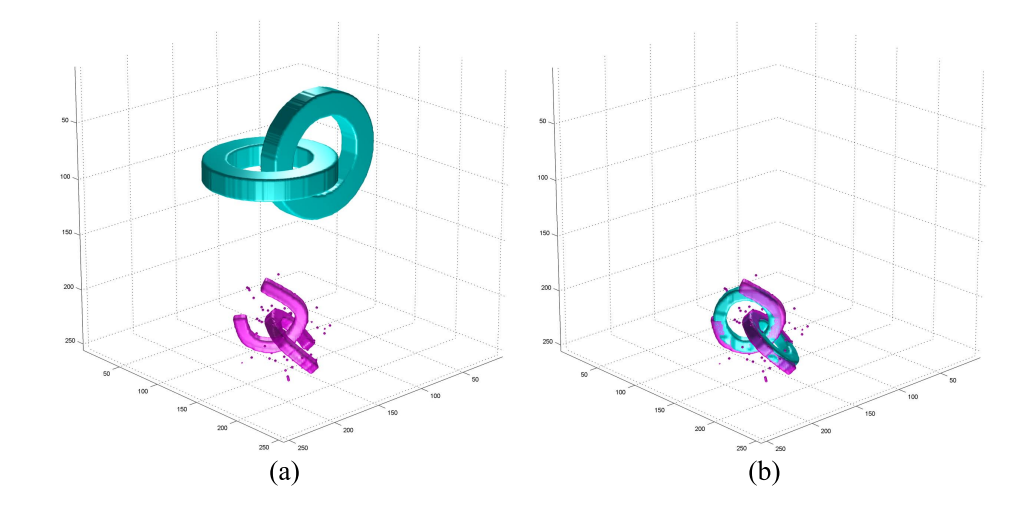


Figure 3.9: The registration of a regular and an irregular shape with different topologies. (a) The reference shape (two linked rings) and the target shape (two linked horseshoes). (b)The result of registration.

3.5.3 A Comparison with the State-of-Art Methods

The classical ICP method (Besl and McKay, 1992) is implemented to compare with the technique proposed here. According to the work of Besl and McKay (1992), firstly the centroids of both reference and the target shapes are calculated and by mapping the centroids, the reference shape is shifted to coarsely match the target shape. Then the centroid of the target shape is used as the center of rotation for the reference shape. An SDF is calculated using the CF of the target shape and for each iteration, the distance values on the surface voxels of the reference shape are extracted to calculate

Shape types	'4's	Linked rings and horse shoes
Image size	$256 \times 256 \times 256$	$256 \times 256 \times 256$
Reference shape size	$80 \times 80 \times 10$	$120 \times 120 \times 170$
Target shape size	$150 \times 150 \times 20$	$60 \times 60 \times 90$
\overline{M}	5	5
B	128	128
t	3.55s	5.43s
s_{op}	1.85	0.47
$ec{q}_{op}$	(-0.66, 0.38, -0.65, -0.03)	(0.52, 0.70, -0.02, 0.50)
$ec{T}_{op}$	$(89, 102, -93)^{\mathrm{T}}$	$(104, 96, -96)^{\mathrm{T}}$

Table 3.1: Some experimental data concerning registrations performed in this section.

the quaternion for the current rotation using equation 25 in the work of Besl and McKay (1992). Figure 3.10 demonstrates of the registration process performed by the ICP method.

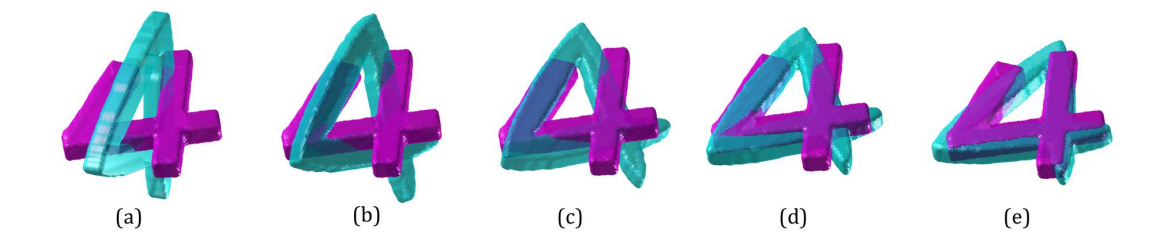


Figure 3.10: The process of the ICP method registering the reference and the target '4's. (a) The initial poses of the two shapes. (b)-(d) are the intermediate results. (e) The final result.

The ICP method is able to handle the registration of shapes in a variety of representations and in the case of CFs, only the boundary voxels are considered in the calculations. Also, shapes represented by CFs could be viewed as a particular type of image (mask image), therefore the similarity image registration algorithm available in MATLAB is used here to do the comparison. The size of the target '4' is reduced here for comparison the purposes and the reference '4' is rescaled using calculated s_{op} . One major purpose of this comparison is to address the local minima issue that affects most registration methods. Three typical initial poses of the reference '4' shown on the top row of figure 3.11 are used here to register the two shapes.

The left column of figure 3.11 demonstrates that ICP method falls into a local minimum using the first initial pose with $E_R = 0.60$. The second initial pose is the result of coinciding the principal axes, which is suggested in Besl and McKay (1992). However, the ICP method falls into the same local minimum with $E_R = 0.60$. Finally, we manually adjust the pose of the reference '4', which is shown on the right column of figure 3.11,

and the ICP method gives an accurate result with $E_R = 0.73$. This also indicates that the ICP method does well in registering shapes of various topologies with appropriate initial poses.

Regarding the execution time (which can be found in table 3.3), the ICP method takes 16.01s (50 iterations) from the pose on top left in figure 3.11, 11.79s (31 iterations) for the top middle in figure 3.11 and 11.31s (29 iterations) for the top right in figure 3.11 (. In fact, the volumetric implementation of the ICP method is generally efficient, because there is no need for calculation of corresponding closest points during each iteration once the preprocessing (calculating Euclidean distance map, which takes on average 4.8s) is done. Average 0.225s for each iteration is mostly spent on extracting boundary voxels and rotation. In contrast, our algorithm takes 1.33s (B=128) to calculate rotation parameter given arbitrary initial pose.

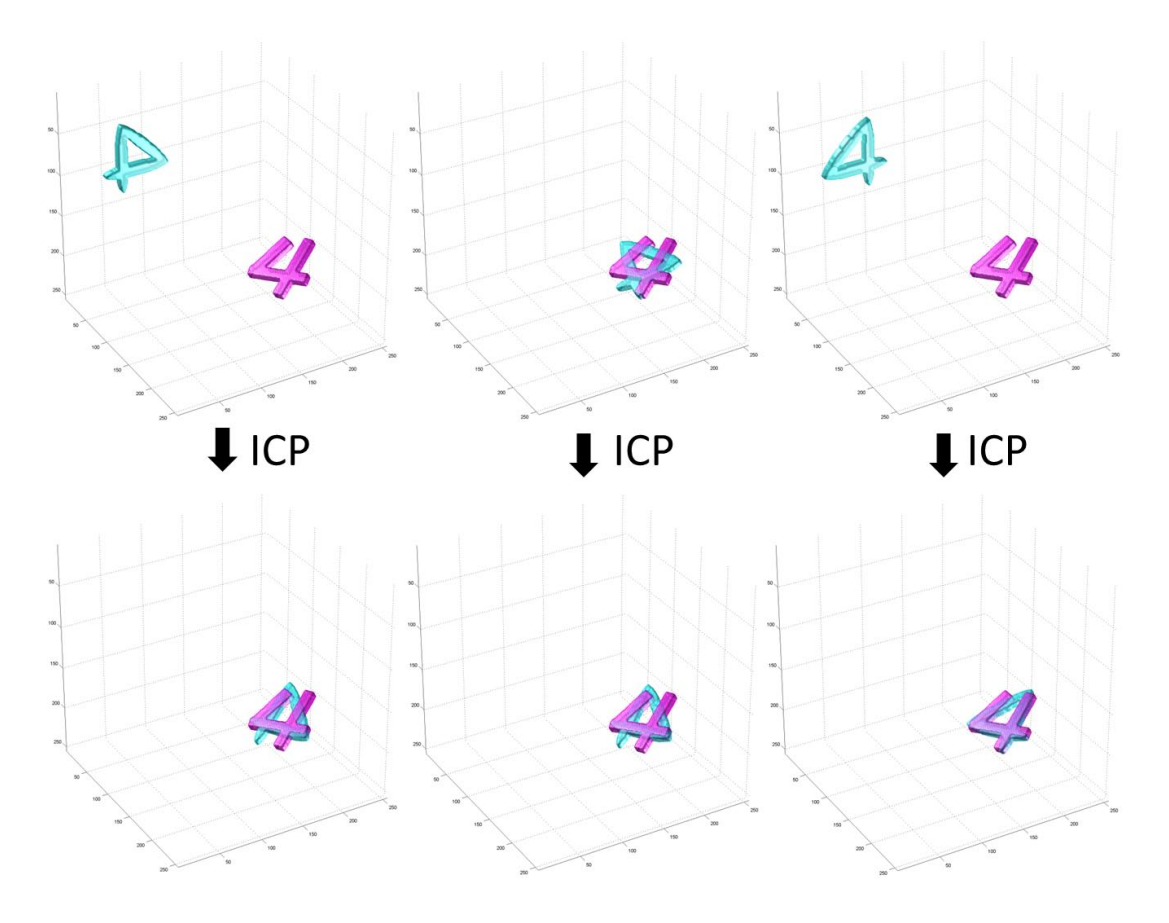


Figure 3.11: From left to right on the top row are three initial poses chosen here to do the comparison. The corresponding registration results using the ICP method are shown on the bottom row. Particularly, the initial pose shown in the middle on the top row are the result of coinciding the principal axes of shapes.

Figure 3.12 presents the results of registration using the MATLAB registration algorithm corresponding to the three initial poses in figure 3.11. Figure 3.12 left and right indicate

that the method falls into local minima with $E_R = 0.24$ and $E_R = 0.57$ respectively, while figure 3.12 middle gives a correct result of the registration with $E_R = 0.75$. However, the execution time needed from left to right are respectively 83.11s, 109.81s and 103.90s (see table 3.3). Admittedly, the image registration method is not specifically designed for shape registration and fails in certain conditions.

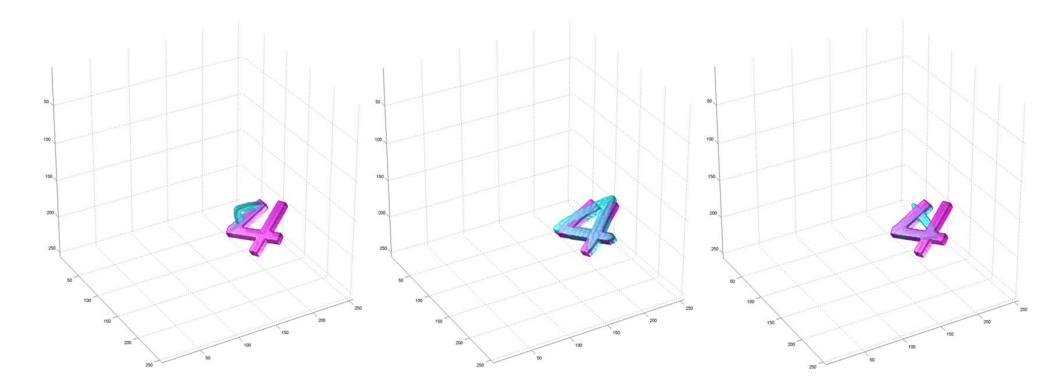


Figure 3.12: From left to right are the results of MATLAB registration method under the three initial conditions showed in figure 3.11.

The registration results for all three initial poses using our method are shown in figure 3.13. Only one picture is given here because the results achieved by our method are the same for all three initial poses with $E_R = 0.75$. In addition, the ICP method handles translation by simply coinciding the centroids of shapes to be registered, which may not be optimal. The quantified comparison of the ICP, the MATLAB and the proposed registration results regarding accuracy and efficiency are repectively given in table 3.2 and table 3.3.

	ICP	MATLAB	Proposed
Pose 1: E_R	0.60	0.24	0.75
Pose 2: E_R	0.61	0.75	0.75
Pose 3: E_R	0.73	0.57	0.75

Table 3.2: The quantified comparison of the ICP, the MATLAB and the proposed registration with respect to accuracy. Pose 1-3 correspond to the three poses presented on the top left to right in figure 3.11.

	ICP	MATLAB	Proposed
Pose 1: T	16.01s	83.11s	1.34s
Pose 2: T	11.79s	109.81s	1.33s
Pose 3: T	11.31s	103.90s	1.34s

Table 3.3: The quantified comparison of the ICP, the MATLAB and the proposed registration with respect to efficiency (T represents execution time). Pose 1-3 correspond to the three poses presented on the top left to right in figure 3.11.

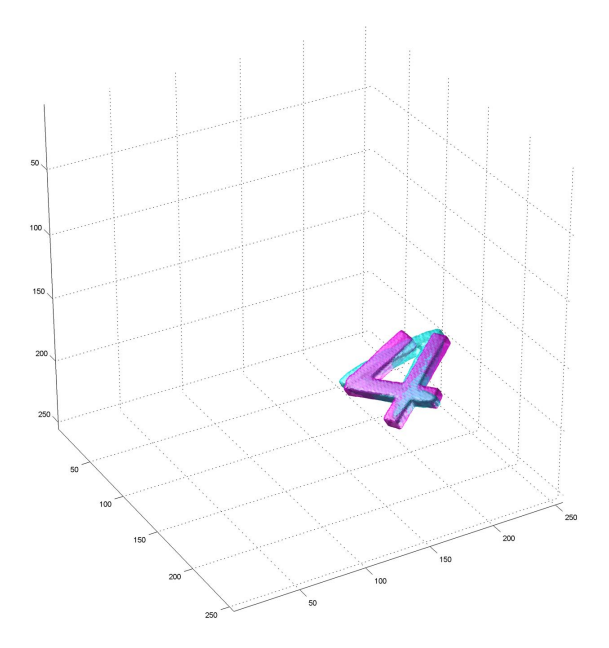


Figure 3.13: The registration result of our method using the three initial poses in figure 3.11.

In addition, the intermediate result after coinciding the principal axes given on the top middle image in figure 3.11 suggests that PCA provides only a coarse match of the two shapes and further fine adjustments are necessary.

3.5.4 Performance Analyses

Two aspects of the technique are given to analyse its performance: one is accuracy and efficiency, and the other is stability. The reference shape and the target shape chosen for the analyses in this section are the same in section 3.5.3, namely, two volumetric '4's. The major parts of the method proposed here are the calculations of scale and rotation parameters, therefore, extensive analyses are performed for these two parameters.

3.5.4.1 Accuracy vs Efficiency

Different values of M and B are chosen to demonstrate their impacts upon accuracy and efficiency of the proposed technique.

Figure 3.14 presents the relationship among similarity measures, execution time and M. In the computation of the similarity measures, a fixed large bandwidth (B=256) is used and the corresponding \vec{T}_{op} is recalculated when M is changed. As observed from figure 3.14, the increase of M does not significantly change the value of those similarity measures and only prolongs the time needed for scale estimation. Therefore, lower degrees of geometric moments are sufficient to estimate s.

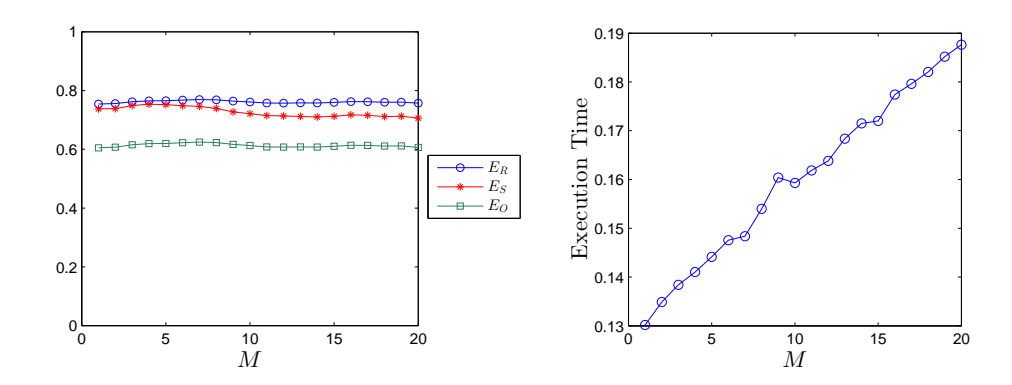


Figure 3.14: Normalized inner product between shapes (left) and time needed for estimating s_{op} (right) using different values of M.

Figure 3.15 demonstrates the relationship among the similarity measures, execution time and bandwidth B. Trade-off between accuracy and efficiency with respect to bandwidth could be observed from the plot on the left in figure 3.15. The inner product increases as bandwidth becomes larger, while more time is needed for numerical computations. Again, M is fixed and \vec{T}_{op} is recalculated for the computation of similarity measures.

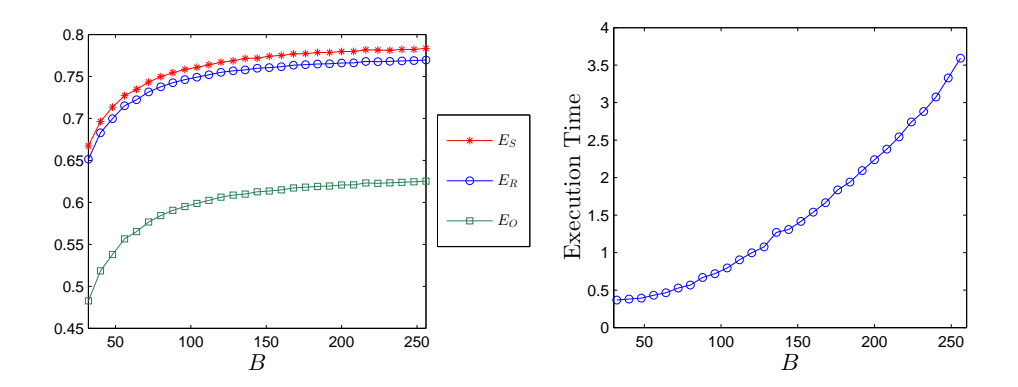


Figure 3.15: Normalized inner product between shapes after registration (left) and execution time using different bandwidth B (right).

3.5.4.2 Stability and Robustness Against Noise

In this section, the stability of the proposed algorithm is to be shown with respect to scale calculations. Furthermore, we present a noise test to prove the robustness against initial poses and noise.

The similarities between CFs of shapes are given in figure 3.16 when the reference shape is rescaled by using s ranging from 0.60 to 1.20. s_{op} calculated using the proposed technique is located in the peak area of the curves of the similarity measures. This suggests that minimizing the scale similarity measure in equation 3.12 based on the geometric moments

of CFs, is numerically equivalent to maximizing the similarity measures with respect to s. However, as shown in figure 3.16 (left), there are fluctuations around the peak area of the curves. This is in fact caused by numerical errors. One reason is that for each manually chosen s, optimal values for \vec{q} and \vec{T} are recalculated. Another reason is that the rescaling of the reference shape is implemented by a simple nearest-neighbor interpolation algorithm. Boundary accuracy of shapes is therefore not ensured.

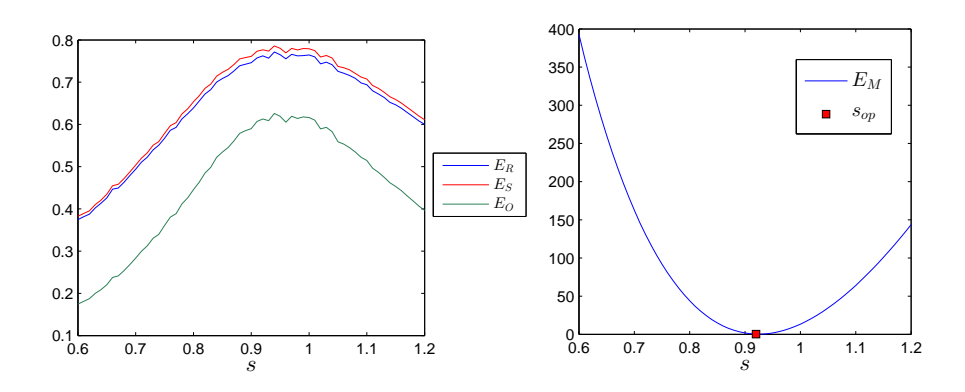


Figure 3.16: Left: The inner product between shapes when s ranges from 0.60 to 1.20. s_{op} calculated when M=5 is 0.93. Right: s_{op} locates on the minimum of E_M , which indicates s_{op} that minimizes E_M also minimizes the inner product.

Figure 3.17 shows the stability of the algorithm while the target shape is placed in a variety of poses. Every time the target '4' is in a new pose, the algorithm is used to register the reference '4' to the target. The group of quaternions that pose the target '4' is acquired by extracting the surface coordinates of a 4-D ball with the radius of 8 in a 4-D array (744 poses in total), and thus the poses are equally distributed in SO(3). As demonstrated in figure 3.17, the reference '4' follows well while the target is in various poses. However, little local fluctuations could be observed. These are mainly caused by the fact that while volumetric shape rotates, the number of voxels contained in the shape varies a little due to the nearest-neighbor interpolation.

The result of the noise analysis is presented in figure 3.18. Using the same initial poses for shapes to be registered, the reference shape is to be registered to the target shape contaminated by binary noise ('salt and pepper' noise). The noise is generated inside the target shape 10 times at each level which ranges from 10% to 90%. For each level, the mean and variance of similarity measures are computed and these results are presented in figure 3.18. As observed from figure 3.18, the means of similarity measures decrease with the increasing level of noise while the standard deviations remain very low, which indicates that our method is stable in presence of excessive noise. Figure 3.19 gives several examples of volumetric '4' with different levels of noise. It can be observed that high levels of noise (70% and 90%) cause severe topological defects of the target shape, while the method proposed here can still achieve accurate results.

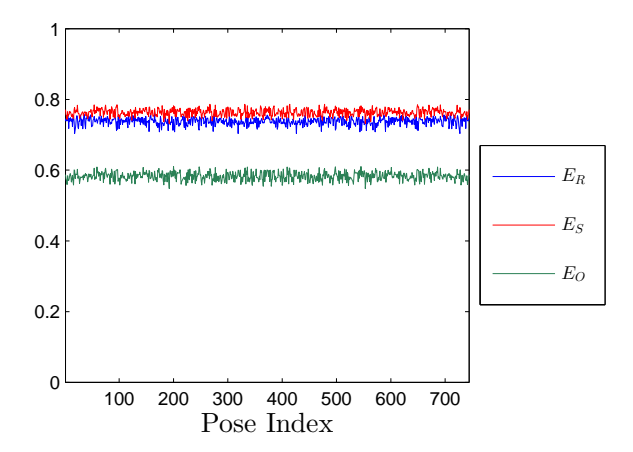


Figure 3.17: Target shape with 744 poses (equally distributed in SO(3)) chosen to test the algorithm and the results presented by three similarity measures.

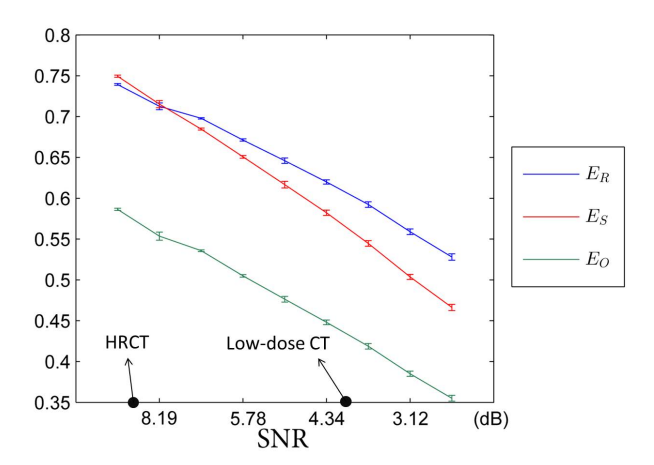


Figure 3.18: The results of registration presented by the error plot of the three similarity measures while the target '4' is affected by increasing level of binary noise ('salt and pepper' noise). The noise levels of HRCT and low-dose CT respectively with SNR=8.68 and SNR=4.07 are pointed out in the plot.

3.5.5 Examples of Applications

3.5.5.1 Registration of Reference and Coarsely Segmented Lungs

Figure 3.20 and figure 3.21 demonstrate the registrations of reference lungs and coarsely segmented lungs. The coarsely segmented lungs are obtained by thresholding HRCT (high resolution computed tomography) scans and finding the largest 18-connected region. The reference and the target lungs are from two subjects. In respective registrations of the left and the right lungs, the other irrelevant half is masked out. As observed from figure 3.20 and figure 3.21, the method proposed here is barely affected by non-trivial noises (main airways outside and vessels inside).

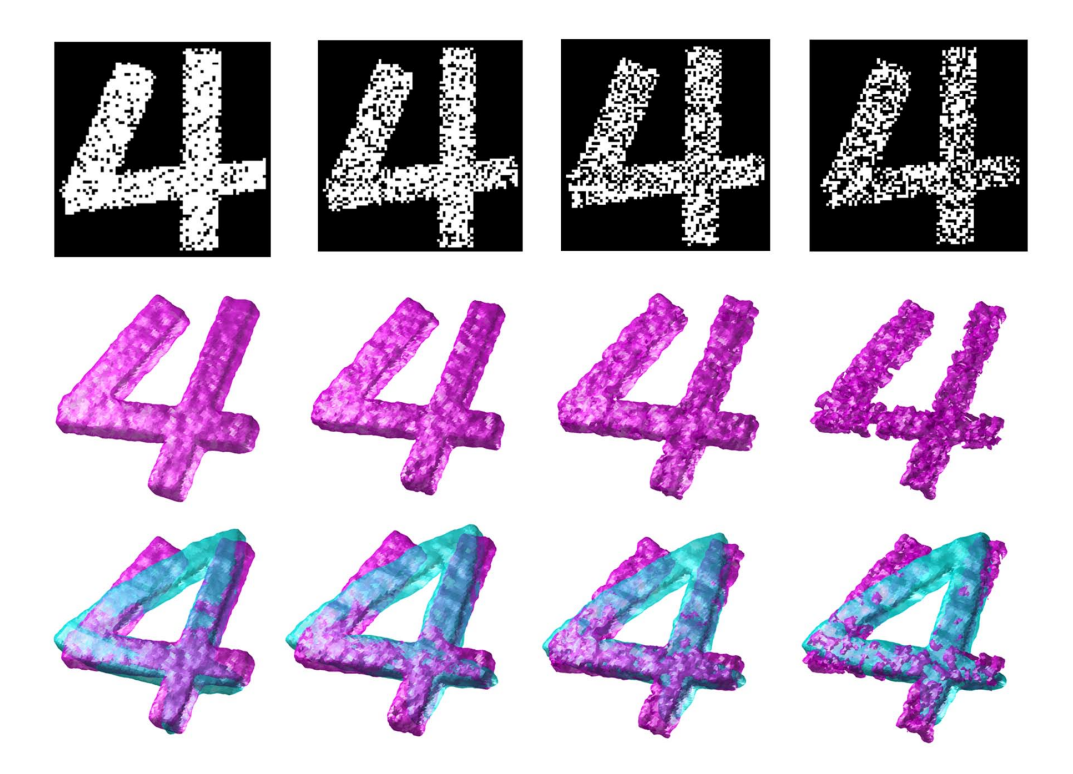


Figure 3.19: Top row: the target '4' contaminated by 30% (SNR=6.45dB), 50% (SNR=4.78dB), 70% (SNR=3.67dB), and 90% (SNR=2.75dB) level of noise from left to right (viewed from slice). In addition, the formula of SNR calculation can be found in appendix A. Middle row: the target '4' with noises viewed in 3-D. Bottom row: the registration results corresponding to the noise levels.

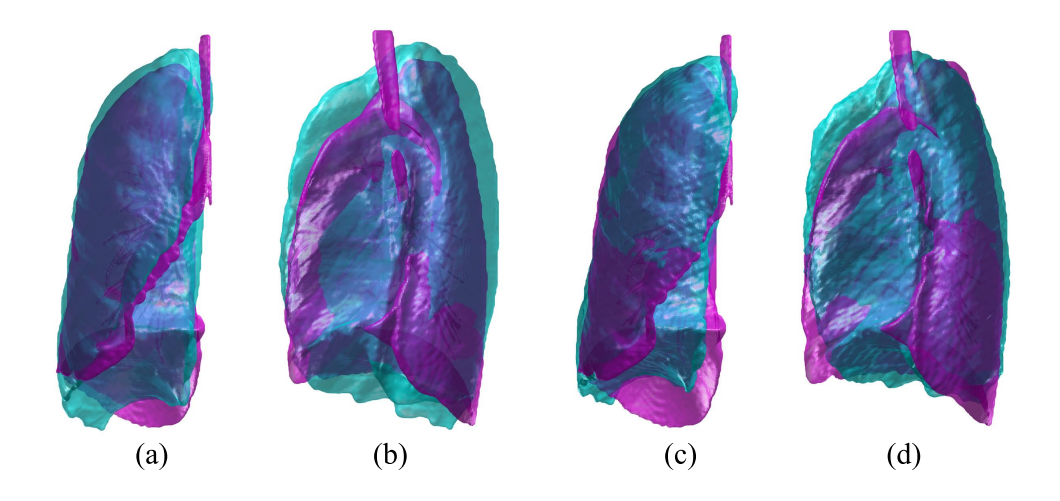


Figure 3.20: (a) Overlapping of right lungs to be registered before registration. (b) Another view before registration. (c) Overlapping of right lungs after registration. (d) Another view after registration.

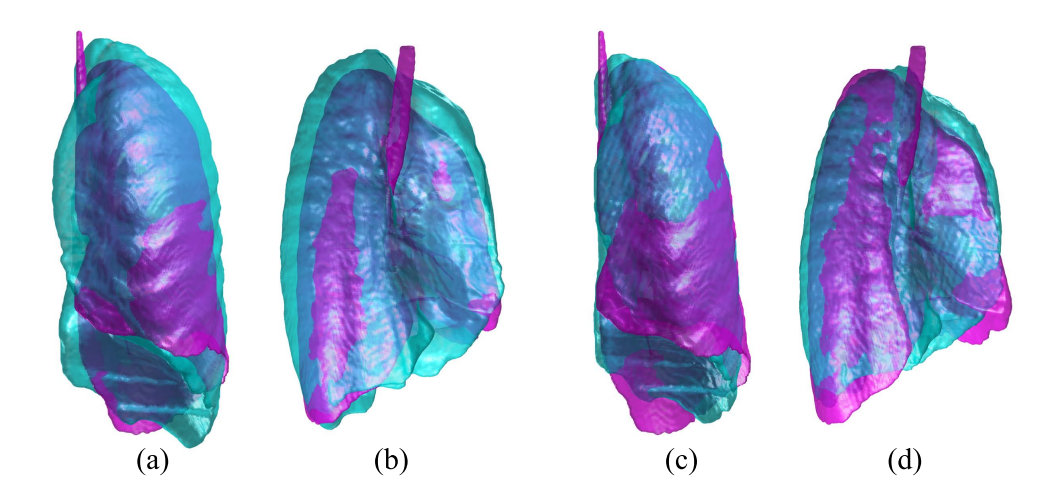


Figure 3.21: (a) Overlapping of left lungs to be registered before registration. (b) Another view before registration. (c) Overlapping of left lungs after registration. (d) Another view after registration.

3.5.5.2 Registration of a Lung Database

In this section, our method is applied to volumetric lungs in a lung data base. The lung database consists of respectively 35 left and right lungs (70 lungs in total). This database covers a range of disease states, including spanning healthy, healthy smoker, mild COPD (chronic obstructive pulmonary disease) and moderate COPD.

Lungs in this database are manually segmented from HRCT images with resolution reduced by half to save memory (from approximately $512 \times 512 \times 700$ to $256 \times 256 \times 350$) under expert supervision to ensure acceptable qualities and they are all represented by 3-D binary arrays (discrete CFs). Furthermore, due to the fact that the coarse lung data are provided in various numbers of slices (ranging from 545 to 714), the process of adjusting all of the cases ready to be registered includes extension of 3-D arrays to the size of $350 \times 350 \times 350$ and alignment of these lungs using their centers of mass.

'Leave-one-out' scheme is employed here to perform the test: each lung is regarded as target while the other 34 lungs are reference shapes. There are 35 targets respectively for the group of right lungs and left lungs. The total number of registrations is therefore 2380. Several results of lung registration are visualized and presented in figure 3.22.

Figure 3.23, figure 3.24 and figure 3.25 demonstrate a global view of the database registration. We here use ΔE_R , ΔE_O and ΔE_S , which are respectively the difference of E_R , E_O and E_S before and after registration using our method. It could be observed from these error plots that the majority of the almost all values of means are above zero, while under certain conditions the algorithm did not deliver correct results. The percentage of successful cases of registration is presented in table 3.4 with respect to each similarity

measure for both left and right lungs. It should be noted that we strictly consider registrations with the difference of similarity measures before and after registration above 0 as successful cases, while failed cases have the differences very close to 0.

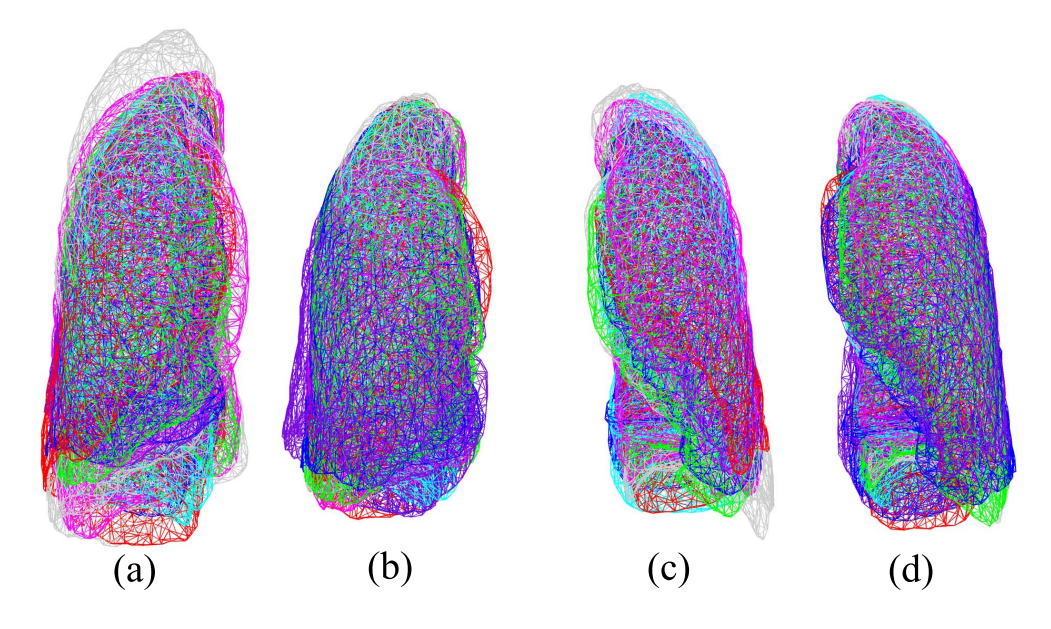


Figure 3.22: (a) Several examples of overlapped right lungs before registration (center-of-mass alignment) using case 1 as the target shape; (b) Overlapped right lungs after registration. (c) Overlapped left lungs before registration (center-of-mass alignment). (d) Overlapped left lungs after registration.

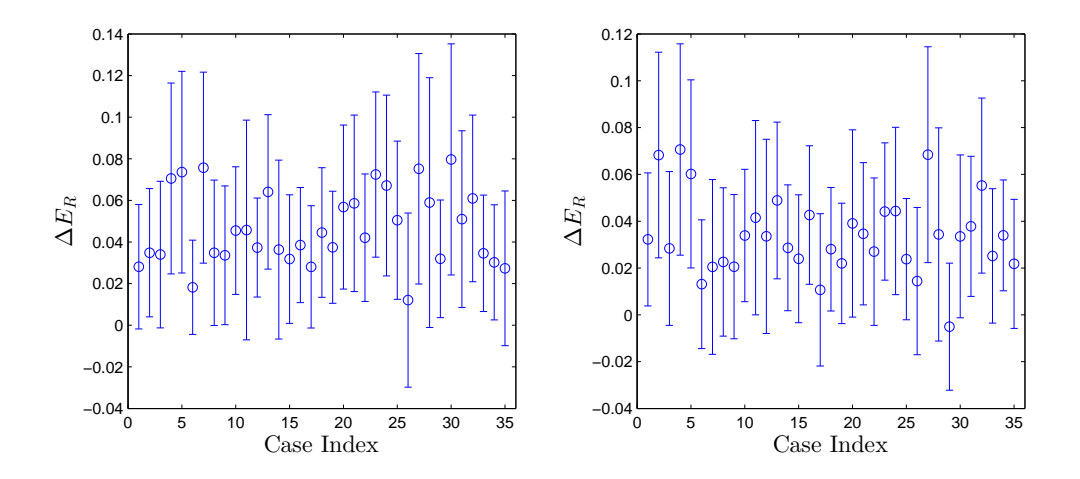


Figure 3.23: Difference of E_R before and after registration for both left lungs (left) and right lungs (right).

A comparison among the proposed, the ICP and the MATLAB methods is presented in figure 3.26. Case 1 is regarded as the target shape while the other 34 lungs the reference shapes. It can be observed that the ICP and the MATLAB methods fall into local minima for most of cases and in contrast, the proposed method produced better results than the two methods.

8

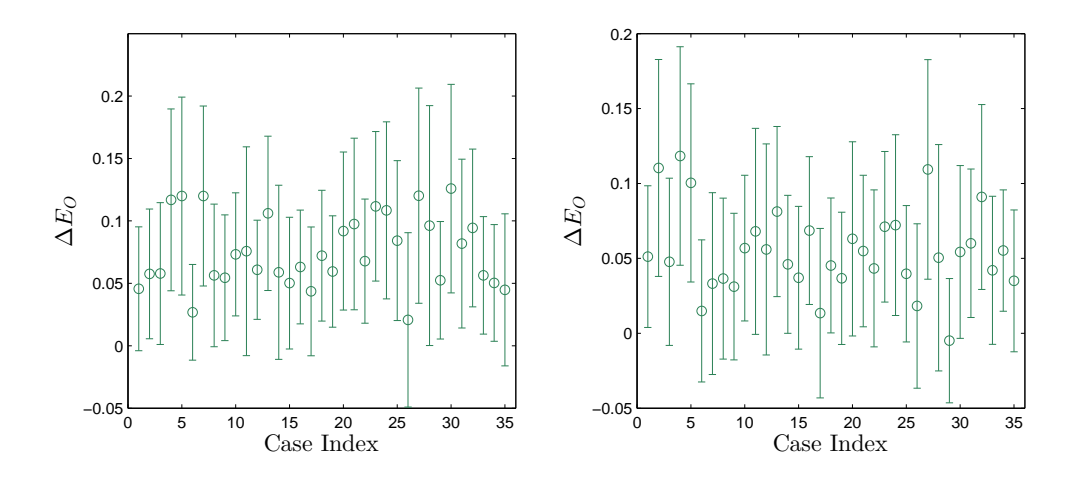


Figure 3.24: Difference of E_O before and after registration for both left lungs (left) and right lungs (right).

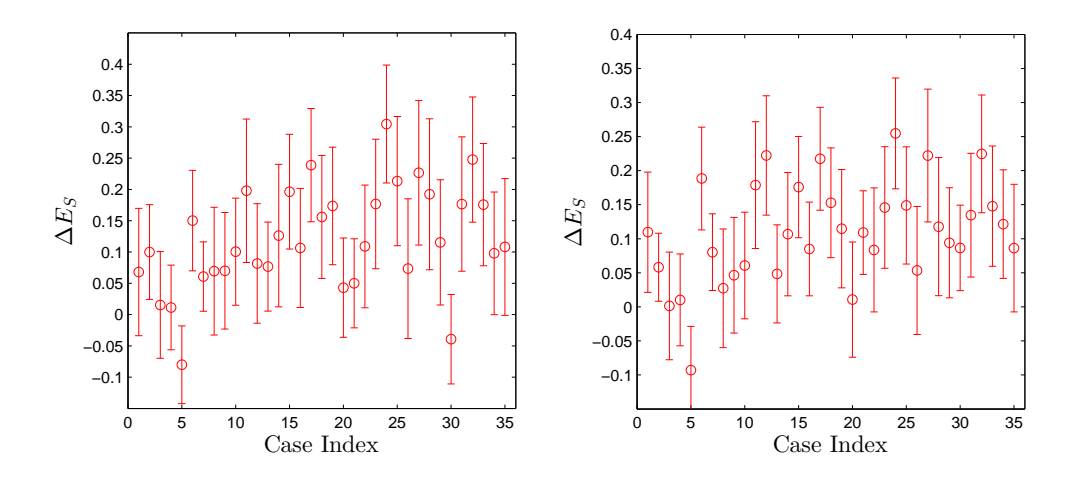


Figure 3.25: Difference of E_S before and after registration for both left lungs (left) and right lungs (right).

Similarity			
Measures	ΔE_R	ΔE_O	ΔE_S
Left lungs	84.45%	83.03%	84.07%
Right lungs	90.84%	90.25%	89.71%

Table 3.4: The percentage of successful cases of registration with respect to each similarity measure for both left and right lungs.

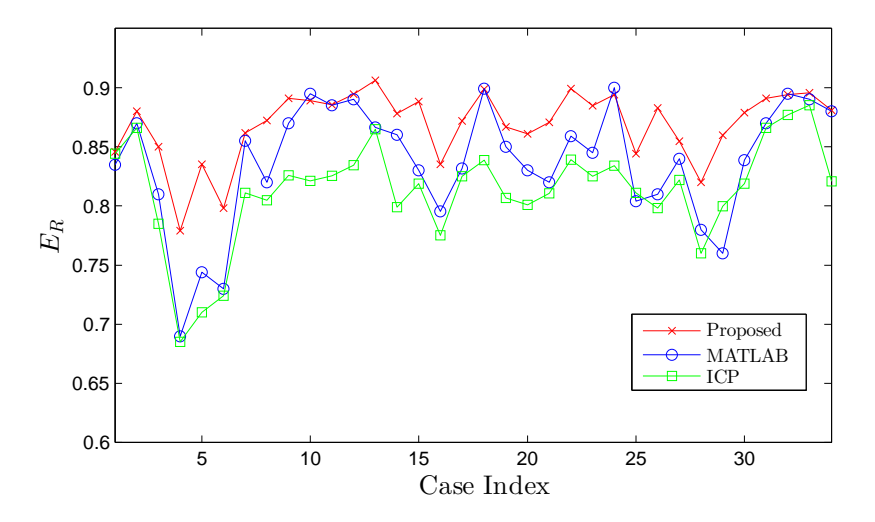


Figure 3.26: A comparison of the proposed, the ICP and the MATLAB methods for the registration of the lung database leaving case 1 out.

3.6 Conclusions and Future Works

This chapter proposes a robust and fast registration technique of two volumetric shapes represented by CFs. PCA is employed to find principal axes associated with each shape. These principal axes provide a rotation and translation invariant transformation which largely facilitates the calculation of rotation parameters. Geometric moments are first employed to estimate scale parameter. Rotation and translation parameters are then calculated by maximizing corresponding phase correlation terms, which take the advantage of FFT and make the method proposed here efficient.

We validate the method through three stages of experiments: primary tests that concern registration of topologically different synthetic shapes, performance analyses that demonstrate accuracy, efficiency and stability of the method, and applications that show practical use of the method. Experimental results suggest that our method is able to register shapes with various topologies, robust to noise and initial poses, and efficient. However, a limitation of our work is that the ground truth (the true values of the registration parameters) of our lung database is not available. Nevertheless, successful registrations can be verified by examining ΔE_R , ΔE_O and ΔE_S over the entire database.

Regarding future directions, first, it is interesting to extend the method to perform non-rigid registration. Second, the method is to be incorporated into shape-based volumetric image segmentation which involves statistical modelling of training set and iterative registration during the segmentation process. This will allow us to have further understandings of the registration method proposed here. Last but not least, it will further improve the quality of the work to relate the noise levels presented in figure 3.18 and figure 3.19 to CT images.

Chapter 4

Statistical Modelling of Lung

4.1 Background

Statistical modelling is a powerful method of understanding and interpreting shapes from the real world. It provides explicit shape invariants and a parametrization of the degrees of freedom in a training set. The most popular application of shape modelling is the extraction of regions of specific shape classes from images. As discussed in section 1.3, the shape-based image segmentation method brings an deformable shape template to contribute to the evolution of the active contours/surfaces. With the active contours/surfaces and the similarity registration technique investigated respectively in chapter 1 and chapter 3, the purpose of this chapter is to build up a deformable shape template of the human lungs.

Major styles of shape modelling differ in the representation of shapes. Early model proposed by Cootes et al. (1992) and shapes involved in the modelling are represented by explicit curves and therefore, proper control points need to be selected based on human expertise. The disadvantage is that when the training set of shapes is large, manual labelling of control points can be highly laborious. Leventon et al. (2000) achieves modelling of shapes in a level-set formulation (mostly SDFs), which grants more topological freedom and seamless combination with active contours/surfaces for segmentation (Tsai et al., 2003; Bresson et al., 2006).

When a shape class requires modelling, it is usually of rich variations. The ultimate goal of shape modelling is to estimate novel shapes of the same class. An accurate approximation of a novel shape enormously facilitates the later stage of segmentation. PCA (principal component analysis) has long been drawn on for shape modelling shapes, however, PCA works well only when a training set of shapes has a Gaussian distribution (Leventon et al., 2000; Bresson et al., 2006). The suitability of PCA for modelling shapes of human lungs represented by SDFs remains a question. This chapter presents

the discussion on this issue and also, inspired by the works of Leventon et al. (2000) and Bresson et al. (2006), introduces a novel hybrid lung modelling scheme. The proposed scheme achieves improved accuracy of lung modelling over previous works.

4.2 Shape Decomposition using PCA

Assuming that $\{\Phi_1, \Phi_2, \dots, \Phi_N\}$ is an aligned training set of N shapes represented by SDFs, the mean shape $\bar{\Phi}$ can be calculated by

$$\bar{\Phi} = \frac{1}{N} \sum_{i=1}^{N} \Phi_i \tag{4.1}$$

Then the mean-offset shapes are calculated by subtracting the mean shape $\bar{\Phi}$ from $\Phi_1, \Phi_2, \dots, \Phi_N$ and these shapes are reshaped to form a $Q \times N$ matrix (Q is the total number of voxels that consist shape Φ_i) represented by

$$\mathbf{U} = (\vec{\Phi}_1, \vec{\Phi}_2, \vec{\Phi}_3, \cdots, \vec{\Phi}_N) \tag{4.2}$$

For representation convenience, let us denote the operation that reshapes 3-D matrix to a vector by $\mathcal{T}_{re}(\cdot)$ and its inverse operation by $\mathcal{T}_{re}^{-1}(\cdot)$:

$$\vec{\Phi}_i = \mathcal{T}_{re}(\Phi_i - \bar{\Phi}) \tag{4.3}$$

By the employing eigen-decomposition of the covariance matrix UU^{T}/N , we have

$$\frac{1}{N}\mathbf{U}\mathbf{U}^{\mathrm{T}} = \mathbf{V}_{Q}\Sigma_{Q}\mathbf{V}_{Q}^{\mathrm{T}} \tag{4.4}$$

The problem now is to calculate the $Q \times Q$ unitary matrix¹ \mathbf{V}_Q and Σ_Q , whose columns are respectively eigenvectors and eigenvalues of the $Q \times Q$ matrix $\mathbf{U}\mathbf{U}^{\mathrm{T}}/N$. The value of Q in this work is extremely large, roughly 10^6 , far exceeds that of N. Furthermore, only the first N columns of the diagonal matrix Σ_Q have real values and the rest are all zeros (Leventon, 2000). This also indicates only the first N columns of \mathbf{V}_Q are relevant to shape modelling. Therefore, to reduce the computational cost, Leventon (2000) proposed to use the eigenvectors and eigenvalues of $\mathbf{U}^{\mathrm{T}}\mathbf{U}/N$ of size $N \times N$ to calculate those of $\mathbf{U}\mathbf{U}^{\mathrm{T}}/N$. The eigen-decomposition of $\mathbf{U}^{\mathrm{T}}\mathbf{U}/N$ is

$$\frac{1}{N}\mathbf{U}^{\mathrm{T}}\mathbf{U} = \mathbf{W}_{N}\Sigma_{N}\mathbf{W}_{N}^{\mathrm{T}} \tag{4.5}$$

 $[\]overline{^1}$ A unitary matrix satisfy $\mathbf{V}\mathbf{V}^* = \mathcal{I}$, where \mathbf{V}^* is the conjugate transpose of \mathbf{V} and \mathcal{I} the identity matrix. When \mathbf{V} is a real matrix, $\mathbf{V}^T = \mathbf{V}^{-1}$.

where Σ_N is an $N \times N$ matrix consisting of the first N rows and columns of Σ_Q . \mathbf{W}_N and Σ_N can be readily calculated and then the first N columns of \mathbf{V}_Q , denoted by \mathbf{V}_N can be calculated by

$$\mathbf{V}_N = \mathbf{U}\mathbf{W}_N \hat{\Sigma} \tag{4.6}$$

where $\hat{\Sigma}$ is an $N \times N$ diagonal matrix that normalizes each column of $\mathbf{U}\mathbf{W}_N$ to become a unit vector. Thus \mathbf{V}_N and $\Sigma_N = \operatorname{diag}(\sigma_1^2, \sigma_2^2, \cdots, \sigma_N^2)$ are calculated, where σ_i^2 represents the eigenvalue of the corresponding eigenvector.

By recovering the eigenvectors of Q dimensions back to 3-D matrix, we have a set of eigen-shapes represented by $\{\hat{\Phi}_1, \hat{\Phi}_2, \cdots, \hat{\Phi}_N\}$ and $\mathbf{V}_N = (\mathcal{T}_{re}(\hat{\Phi}_1), \mathcal{T}_{re}(\hat{\Phi}_2), \cdots, \mathcal{T}_{re}(\hat{\Phi}_N))$. It should be pointed out that the importance of the eigen-shapes decreases as the subscript increases.

Let $K \leq N$ be the number of selected eigen-shapes and the shape approximation Φ_{mod} can be calculated using

$$\Phi_{mod}(\boldsymbol{\alpha}) = \bar{\Phi} + \mathcal{T}_{re}^{-1}(\mathbf{V}_K \boldsymbol{\alpha})$$

$$= \bar{\Phi} + \sum_{i=1}^K \alpha_i \hat{\Phi}_i$$
(4.7)

where \mathbf{V}_K consists of the first K columns of \mathbf{V} and $\boldsymbol{\alpha} = (\alpha_1, \alpha_2, \dots, \alpha_K)^T$ is the shape parameter vector that controls the contribution of each eigen-shape. One can choose a proper value of K for a desired shape approximation up to N. Thus, each shape in the training set can be represented by a unique $\boldsymbol{\alpha}_i$ that can be calculated by

$$\alpha_i = \mathbf{V}_K^{\mathrm{T}} \vec{\Phi}_i \tag{4.8}$$

An N by N matrix \mathbf{A} is used here to represent a specific training set:

$$\mathbf{A} = (\boldsymbol{\alpha}_1, \boldsymbol{\alpha}_2, \cdots, \boldsymbol{\alpha}_N) \tag{4.9}$$

The columns of **A** are α_i used to represent shapes in the training set, while the rows of **A** are eigen-modes corresponding to eigen-shapes.

It is convenient to assume that the distribution of shapes is Gaussian, and therefore, in a Q dimensional space, the probability of a certain shape in the training set can be

written as:

$$P(\boldsymbol{\alpha}_{i}) = \frac{1}{\sqrt{(2\pi)^{N}|\Sigma_{N}|}} \exp\left(-\frac{1}{2}\mathcal{T}_{re}(\boldsymbol{\Phi}_{i} - \bar{\boldsymbol{\Phi}})^{\mathrm{T}}(\frac{1}{N}\mathbf{U}\mathbf{U}^{\mathrm{T}})^{-1}\mathcal{T}_{re}(\boldsymbol{\Phi}_{i} - \bar{\boldsymbol{\Phi}})\right)$$

$$= \frac{1}{\sqrt{(2\pi)^{N}|\Sigma_{N}|}} \exp\left(-\frac{1}{2}\vec{\boldsymbol{\Phi}}^{\mathrm{T}}(\frac{1}{N}\mathbf{U}\mathbf{U}^{\mathrm{T}})^{-1}\vec{\boldsymbol{\Phi}}\right)$$

$$= \frac{1}{\sqrt{(2\pi)^{N}|\Sigma_{N}|}} \exp\left(-\frac{1}{2}\vec{\boldsymbol{\Phi}}^{\mathrm{T}}(\mathbf{V}_{N}\Sigma_{N}\mathbf{V}_{N}^{\mathrm{T}})^{-1}\vec{\boldsymbol{\Phi}}\right)$$

$$= \frac{1}{\sqrt{(2\pi)^{N}|\Sigma_{N}|}} \exp\left(-\frac{1}{2}\vec{\boldsymbol{\Phi}}^{\mathrm{T}}\mathbf{V}_{N}\Sigma_{N}^{-1}\mathbf{V}_{N}^{\mathrm{T}}\vec{\boldsymbol{\Phi}}\right)$$

$$= \frac{1}{\sqrt{(2\pi)^{N}|\Sigma_{N}|}} \exp\left(-\frac{1}{2}\boldsymbol{\alpha}_{i}^{\mathrm{T}}\Sigma_{N}^{-1}\boldsymbol{\alpha}_{i}\right)$$

$$(4.10)$$

when the first K eigen-shapes are selected to reconstruct the shapes in the training set, Σ_N in the above equation is replaced by Σ_K and α_i is naturally a K dimensional vector.

4.3 An Approximation Technique for Novel Shapes

4.3.1 The Previous Works Concerning Shape Modelling

There are currently two methods exist in the literature for shape approximation in a level-set formulation. One is proposed by Leventon et al. (2000) and the other by Bresson et al. (2006). Let us assume that a novel shape is represented by Φ_{as} which can be a noisy surface extracted from images or a shape acquired from any source in a level set formulation. The shape approximation in the work of Leventon et al. (2000) is first to calculate the shape parameter vector $\boldsymbol{\alpha}$ as described in section 4.2:

$$\alpha = \mathbf{V}_K^{\mathrm{T}} \mathcal{T}_{re} (\Phi_{as} - \bar{\Phi}) \tag{4.11}$$

Then the Φ_{as} can be interpreted in the statistical space provided by PCA as

$$\Phi_{mod} = \bar{\Phi} + \mathcal{T}_{re}^{-1}(\mathbf{V}_K \boldsymbol{\alpha}) \tag{4.12}$$

The accuracy of this approximation technique is decided by the number of the eigenshapes. Undoubtedly a better accuracy incurs a greater computational cost. However, the growing number of eigenvectors is unable to insure an infinite increase in accuracy and therefore, a 'proper' number K should be chosen to balance accuracy and efficiency through experiments. Furthermore, this approximation method is under the assumption that the registration parameters including scale, rotation and translation are well estimated and shape distribution is Gaussian.

The method proposed by Bresson et al. (2006) follows a strict variational frame work which starts with an objective functional for shape modelling:

$$E_{shape}(\mathbf{x}_R, \boldsymbol{\alpha}, \Phi_{as}) = \int_{\Omega} \Phi_{mod}^2(\mathbf{x}_R, \boldsymbol{\alpha}) |\nabla \Phi_{as}| \delta(\Phi_{as}) \, d\mathbf{x}$$
 (4.13)

 \mathbf{x}_R (similarity registration parameter, $\mathbf{x}_R = (s, \vec{q}, \vec{T})$) and Φ_{as} are two variables that optimize energy E_{shape} other than α compare to Leventon's model. Φ_{as} provides novel shape information and is often acquired from images in the shape-based image segmentation. Equation 4.13 is to find the optimal \mathbf{x}_R and α that minimize the squared distance between Φ_{mod} and Φ_{as} . On the other hand, Φ_{as} is not static. It also evolves as a geodesic flow to approach shape model Φ_{mod} . This is a coarse-to-fine process of shape approximation from global to local. The solution to this functional requires three motion equations derived from equation 4.13:

$$d_{t}\mathbf{x}_{R} = -2\int_{\Omega} \Phi_{mod} \langle \Phi_{mod}, \nabla_{\mathbf{x}_{R}} \mathcal{T}_{sim} \rangle |\nabla \Phi_{as}| \delta(\Phi_{as}) d\mathbf{x}$$
(4.14)

$$d_t \boldsymbol{\alpha} = -2 \int_{\Omega} \Phi_{mod} \nabla_{\boldsymbol{\alpha}} \Phi_{mod} |\nabla \Phi_{as}| \delta(\Phi_{as}) d\mathbf{x}$$
(4.15)

$$\partial_t \Phi_{as} = \delta(\Phi_{as}) \left[\nabla \cdot (\Phi_{mod}^2 \frac{\nabla \Phi_{as}}{|\nabla \Phi_{as}|}) \right]$$
(4.16)

In equation 4.14, $\mathcal{T}_{sim}(\mathbf{x}) = s\mathbf{R}\mathbf{x} + \vec{T}$ represents the similarity transformation. In an iterative manner, from equation 4.14 to equation 4.16, Φ_{mod} and Φ_{as} are updated to minimize E_{shape} . It should be pointed out that equation 4.15 for shape parameter estimation works well also under a Gaussian assumption.

4.3.2 A Novel Hybrid Approximation Technique

Following the works of Leventon et al. (2000) and Bresson et al. (2006), a hybrid approximation technique is built up for shape modelling in 3-D. Before introducing the technique, some inspirations will be presented in the following paragraphs.

The idea behind method proposed by Bresson et al. (2006) is an optimization process and mathematically sound, however, iterations, which are computationally costly, take place in each step of the shape approximation. Considering equation 4.14, the solution to the registration problem, in 3-D, the term $\nabla_{\mathbf{x}_R} \mathcal{T}_{sim}$ has seven degrees of freedom if using similarity transformation. One update of \mathbf{x}_R requires simultaneous calculations of seven equations which incur huge computational cost.

Concerning equation 4.15, under a Gaussian assumption where $\alpha \in [-3\sigma_1, 3\sigma_1] \times [-3\sigma_2, 3\sigma_2] \times \cdots \times [-3\sigma_K, 3\sigma_K]$, it is not necessary to employ iterative method to acquire α when the result produced by equation 4.12 is satisfactory.

As for equation 4.16, evolution of geodesic flow which starts with Φ_{as} compromise the original information contained in the surface. It is proposed here to start the evolution with Φ_{mod} , let Φ_{mod} deform to approach the shape of Φ_{as} , while the neighbourhood band of deformation is limited. In this way, E_{shape} would still be minimized while the novel shape information Φ_{as} is kept for optimal description from knowledge base $\Phi_{mod}(\mathbf{x}_R, \boldsymbol{\alpha})$.

Based on the above discussion, the idea proposed by Bresson et al. (2006) is employed here while reducing its computational cost in 3-D. The novel technique for shape registration introduced in chapter 3 and Leventon's method for shape parameter estimation would be applied here. Therefore, the minimization of energy E_{shape} can be achieved in three steps:

Step 1: Calculate $\mathbf{x}_R = (s, \vec{q}, \vec{T})$ and register Φ_{as} to Φ_{mod} using the method introduced in chapter 3.

Step 2: Calculate α and update Φ_{mod} using the equations blow:

$$\alpha = \mathbf{V}_K^{\mathrm{T}} \mathcal{T}_{re} (\Phi_{as} - \bar{\Phi}) \tag{4.17}$$

$$\Phi_{mod} = \bar{\Phi} + \mathcal{T}_{re}^{-1}(\mathbf{V}_K \boldsymbol{\alpha}) \tag{4.18}$$

Step 3: Start with Φ_{mod} acquired in step 2, evolve Φ_{mod} using the equation blow:

$$\partial_t \Phi_{mod} = \delta(\Phi_{mod}) \left[\nabla \cdot (\Phi_{as}^2 \frac{\nabla \Phi_{mod}}{|\nabla \Phi_{mod}|}) \right]$$
 (4.19)

 Φ_{as}^2 is a squared SDF and replaces g(I) in standard formulation of geodesic flow (see equation 2.8). Another difference of this work with that of Bresson et al. (2006) other than registration is that, the geodesic flow starts with Φ_{mod} , and Φ_{as} provides novel shape information without getting involved in surface deformation. The only freedom that Φ_{as} has is similarity transformation. These three steps from coarse to fine use the knowledge base (shape model) to describe new observed information (novel shape). In step 3, the geodesic flow evolves on a narrow band of a 3 voxel width, denoted by $b_m = 3$. The narrow band is built using the method proposed by Sethian (2001). The width of the narrow band b_m controls the flexibility of the lung model. Higher value of b_m would bring in more noise into the segmentation results and lower value, $b_m = 1$ or $b_m = 2$ would reduce the accuracy of segmentation. Figure 4.1 depicts the modelling process using the proposed hybrid technique.

4.3.3 Similarity Measures for Evaluation of Modelling

The hybrid technique for shape modelling follows the formulation proposed by Bresson et al. (2006) and inherits its stability in theory. The term that the work of Bresson et al. (2006) minimizes is the sum of squared distance of shapes' boundaries. However,

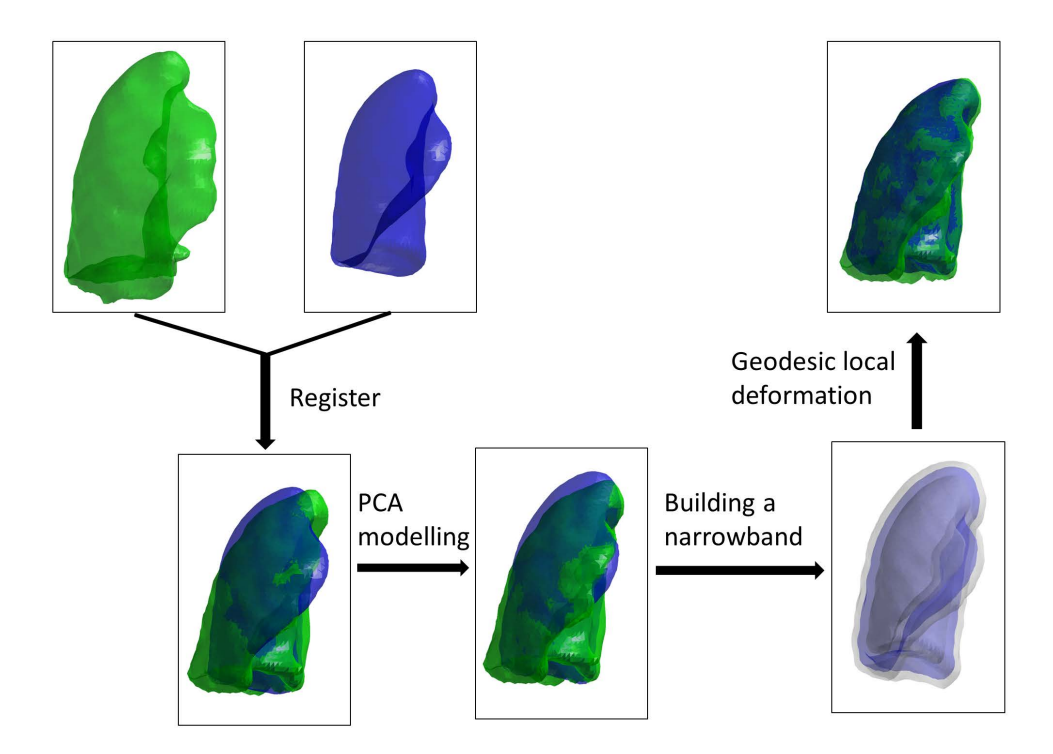


Figure 4.1: The process of lung modelling using the hybrid technique.

more similarity measures should be chosen to achieve a comprehensive and quantitative evaluation of the technique. Here, four measures are adopted to perform the task, two for region similarity and the other two for surface distance.

1. The normalized inner product of shapes' CFs (characteristic functions introduced in chapter 3) can be written as

$$E_{R1} = \int_{\Omega} \frac{\mathcal{X}_{mod} \mathcal{X}_{as}}{||\mathcal{X}_{mod}||_2 ||\mathcal{X}_{as}||_2} \, d\mathbf{x}$$

$$(4.20)$$

where $\mathcal{X}_{mod} = H(\Phi_{mod})$ and $\mathcal{X}_{as} = H(\Phi_{as})$ ($H(\cdot)$ is the Heaviside function). This measure is chosen in accordance with similarity registration to further indicate whether this term can be maximized in the modelling process.

2. Another region similarity measure used here is Dice's coefficient:

$$E_{R2} = \frac{2 \int_{\Omega} \mathcal{X}_{mod} \mathcal{X}_{as} \, d\mathbf{x}}{||\mathcal{X}_{mod}||_2 + ||\mathcal{X}_{as}||_2}$$
(4.21)

This measure is recently used in the work of Sun et al. (2012) to indicate the similarity of regions for lung segmentation. Therefore, it is also employed in our evaluation.

3. The average Euclidean distance of two closed surfaces represented by SDFs can be written as

$$E_{D1} = \frac{\int_{\Omega} |\Phi_{mod}| |\nabla \Phi_{as}| \delta(\Phi_{as}) \, d\mathbf{x}}{\int_{\Omega} |\nabla \Phi_{as}| \delta(\Phi_{as}) \, d\mathbf{x}}$$
(4.22)

The measure is equivalent to E_{shape} in equation 4.13. When the modelling process reach a steady state, the area of the zero level set of Φ_{as} becomes a constant. Therefore, minimizing E_{D1} would also minimizes E_{shape} .

4. Hausdorff distance of surfaces is presented by

$$E_{D2} = \max(|\Phi_{mod}(\Phi_{as} = 0)|) \tag{4.23}$$

Hausdorff distance is the maximum distance between two surfaces. It is a most popular measure to evaluate experimental results in medical image segmentation.

4.4 Experimental Results

A set of experiments are conducted and presented in this section. Firstly, an intuitive sense of the lung database is presented to gain some basic understanding of the lung shapes decomposed by PCA. Secondly, a Gaussianity demonstration of shapes will be given to validate the applications of Leventon's and Bresson's methods to the lung database. Then, a comparison between the PCA parameter estimation schemes of the two methods is performed to the show their equivalence. Lastly, the proposed hybrid method for shape modelling is compared to the two previous methods to show the advantage with respect to accuracy and efficiency.

The database of mask images of lungs used in this section are segmented under expert supervision from a database of low-dose thoracic CT scans of 33 cases with size $128 \times 128 \times 128$ provided by NIHR Southampton Respiratory Biomedical Research Unit. The case index of the lung database which includes the patients' IDs and the disease states is provided by table B.2 in appendix B. It is considered in this work that this database consists of three classes of lungs, which are the left, right and two lungs together. All three classes of lungs participate the experiments. The original mask images of lungs are of the same size as the low-dose CT scans and after registration using the method proposed in chapter 3, their sizes are reduced. The left and right lungs are represented by $96 \times 64 \times 96$ matrices and the two lungs by $96 \times 96 \times 96$ matrices. They are all transformed into SDFs for modelling using the fast Euclidean distance transform algorithm proposed by Maurer Jr et al. (2003) just as section 2.5.

4.4.1 Several Intuitive Understandings of the Lung Database

This section provides several fundamental understandings of PCA decomposition of the lung database. Three classes of lungs, namely the left, right and two lungs together are involved here. Two lungs can topologically be considered as one shape of two parts. They are interesting to investigate in shape modelling because the shapes we use for the

experiments in this study are represented by SDFs, which have long been deemed to be advantageous over contour/surface representations with respect to handling topologies.

Figure 4.2 presents E_{R1} between each case in the training set with their average shape. Considering left, right and two lungs are of different shape class, three plots are generated to offer a basic sense of the training set. It can be observed that E_{R1} has relatively large variations which indicates that the database has a good degree of versatility.

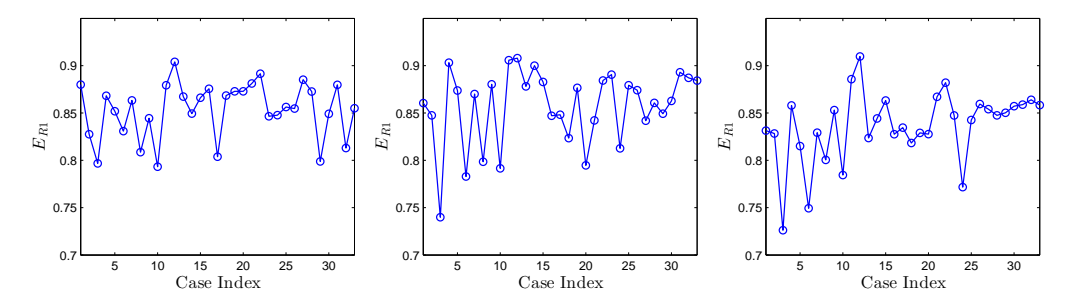


Figure 4.2: E_{R1} between each case in the database and the average lung of the database. From left to right are the left, right and two lungs.

Several typical examples of the lungs in the database are given in figure 4.3. From left to right are respectively case 3, 15 and 24. Case 3 (figure 4.3(a)) in figure 4.2 has lowest similarity with the averages lungs in all three classes. The shapes appear to be much shorter than average and the distance between two lungs are quite large. Case 15 (figure 4.3(b)) represents a normal condition and most individuals have shapes of lungs as these. Case 24 (figure 4.3(c)) is another extreme. It is among the most dissimilar ones and it is tall and thin.

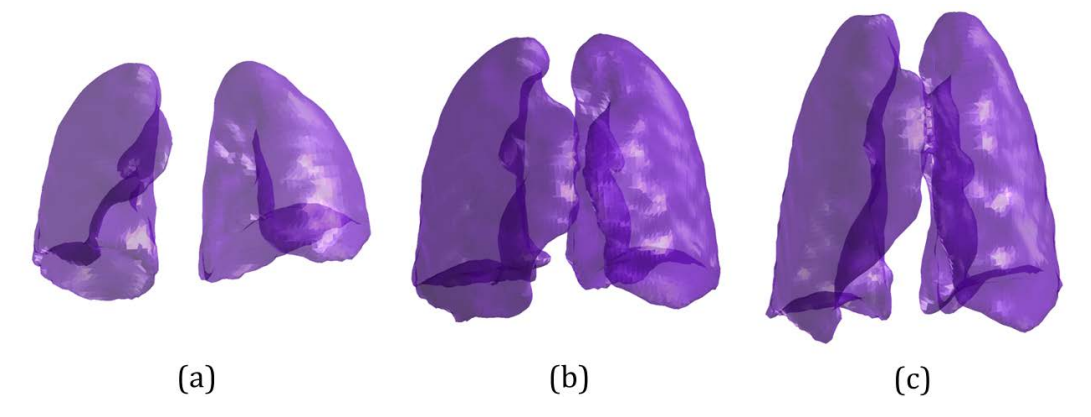


Figure 4.3: Typical examples of lungs in the database before registration(image size: $128 \times 128 \times 128$). (a), (b) and (c) are respectively case 3, case 15 and case 24.

Figure 4.4 shows the variations of the left lung under several typical values of $\alpha = (\alpha_1, \alpha_2, \alpha_3, ..., \alpha_K)$. The first eigen-shape is of chief importance and it can be observed from the first row of figure 4.4 that the negative value of α_1 stretches the lung, making it taller and the positive value expand the lung, making it shorter. The second and third eigen-shapes exert similar effects.

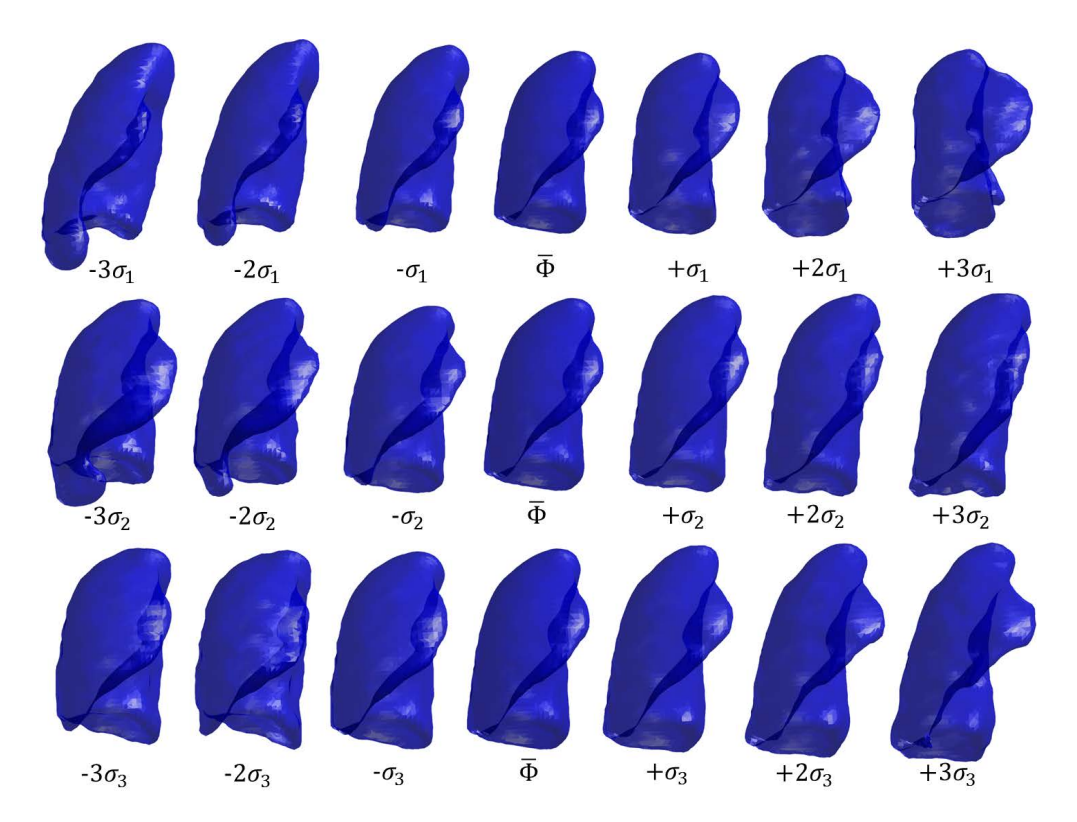


Figure 4.4: From the top row to the bottom are respectively the variations of the left lungs influenced by the 1st, 2nd and 3rd eigen-shapes.

Figure 4.5 demonstrates the variations of the right lung in different parameter settings. Different from the left lungs, the value of σ_1 has an inverse effect on the variations. The second eigen-shape is mainly affecting the bottom contours of the right lungs and the third affects some local corners.

The variations of two lungs altogether under various parameter settings can be found in figure 4.6. The most interesting part is the topological changes. The two lungs merge into each other when α is large enough. This is the advantage of SDFs representations of shapes. Topology changes are naturally handled without incurring specific schemes.

Figure 4.7 gives the plot of eigenvalues in PCA decomposition of lungs. It can be seen from the plots that number of the significant eigen-shapes goes no further than the first 10 respectively for each lung class. Therefore, more detailed analysis in the next sections will involve only the first 10 eigen-shapes.

4.4.2 The Gaussianity of Shapes

In the PCA modelling of shapes, it is assumed that shapes represented by α have a Gaussian distribution (see section 4.2). Here, normal probability plot (NPP, Chambers et al. (1983)) is used to carry out the Gaussianity test on the lung database of 33 cases.

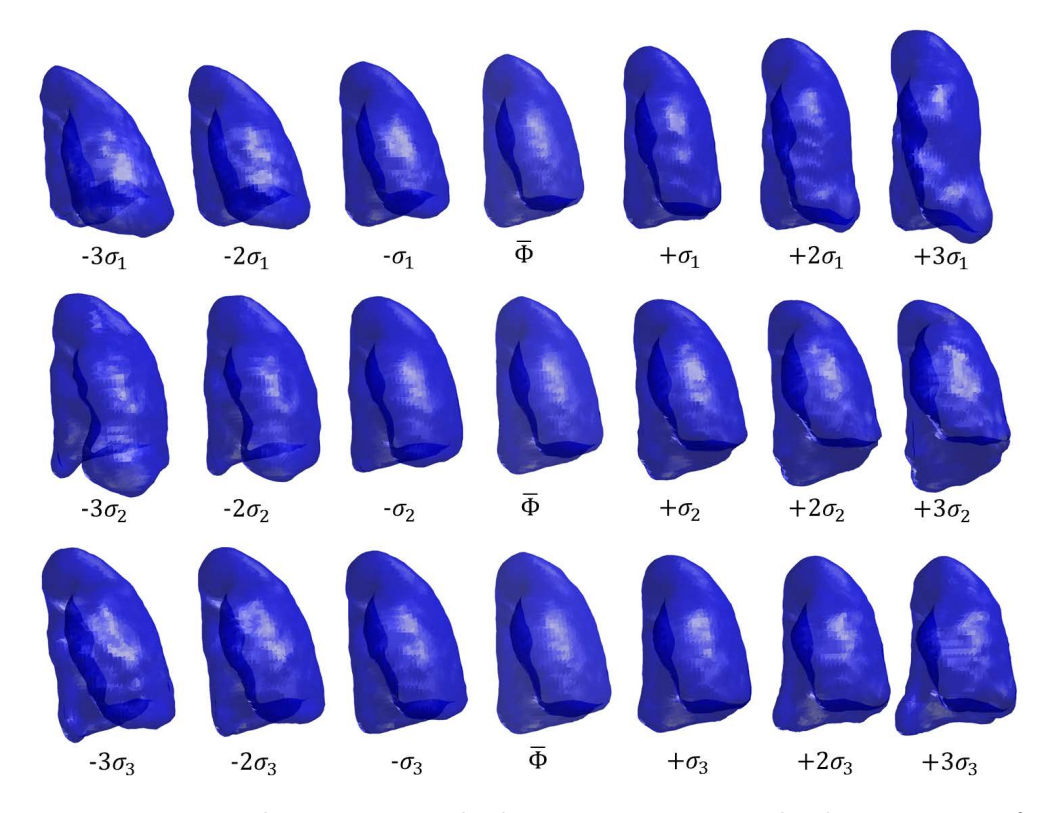


Figure 4.5: From the top row to the bottom are respectively the variations of the right lungs influenced by the 1st, 2nd and 3rd eigen-shapes.

Figure 4.8 presents the NPPs of several eigenmodes of the left lungs in the database. There are in total 33 eigenmodes generated after PCA is performed, while the first 9 are selected and shown here for exemplary purpose. It can be observed from the figure that most of plots follow straight lines, which indicates the validity of the Gaussian assumption of the left lung shapes. However there are several special cases. Anomalies appear in the 4th, 7th and 8th eigenmode and locally there are outliers. If the Gaussian assumption is still being used, the quality of the modelling result should be examined to judge whether the left lung would still belong to 'lung class' when $\alpha_3 \in (-3\sigma_3, 3\sigma_3)$. Furthermore, the modelling process mostly involves multiple eigenmodes. They are probably capable of compensating for each other and achieve a satisfactory result. The next section (section 4.4.3) will provide proof of this assumption.

The NPPs of eigenmodes of the right lungs are presented by figure 4.9. The right lungs have a more stable Gaussian distribution than left lungs. Only the NPP of the 3rd eigenmode shown in figure 4.9(3) fluctuates greater than others and there are 6 points away from the straight line. The most likely reason for the more stable Gaussian distribution of the right lungs over the left lungs is that the shapes of left lungs are largely affected by the presence of the heart (anatomically, the left lungs envelop the hearts). While individuals are holding their breath during image acquisition process and generally keeping the shapes of the lungs fixed, there is no stopping of the cardiac motions.

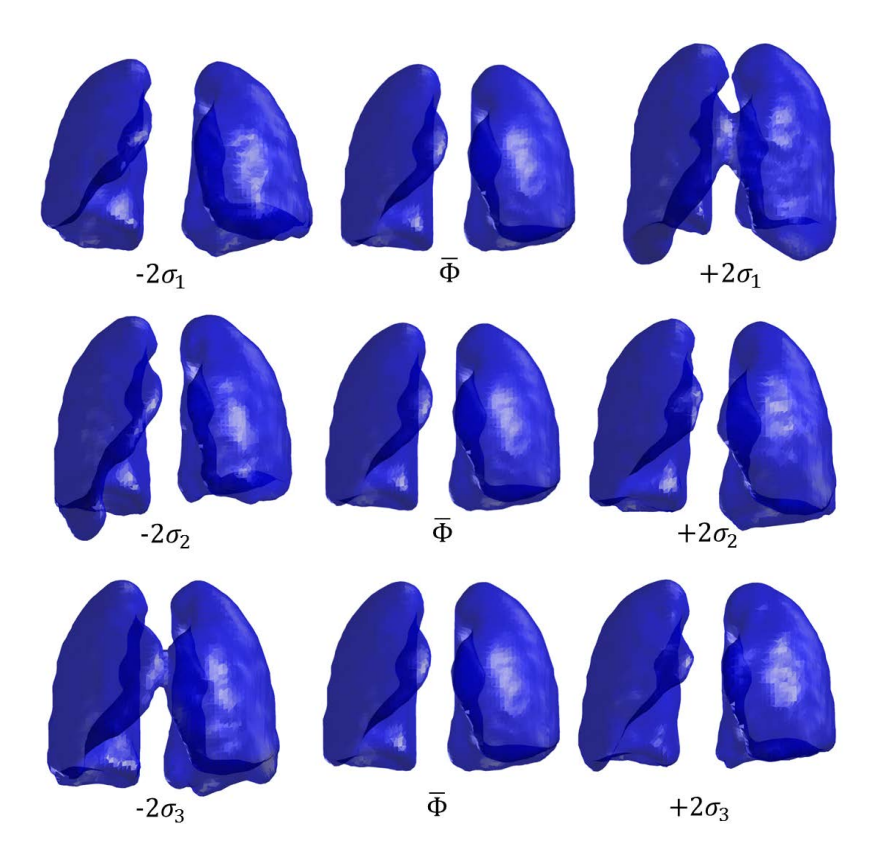


Figure 4.6: From the top row to the bottom are respectively the variations of two lungs influenced by the 1st, 2nd and 3rd eigen-shapes.

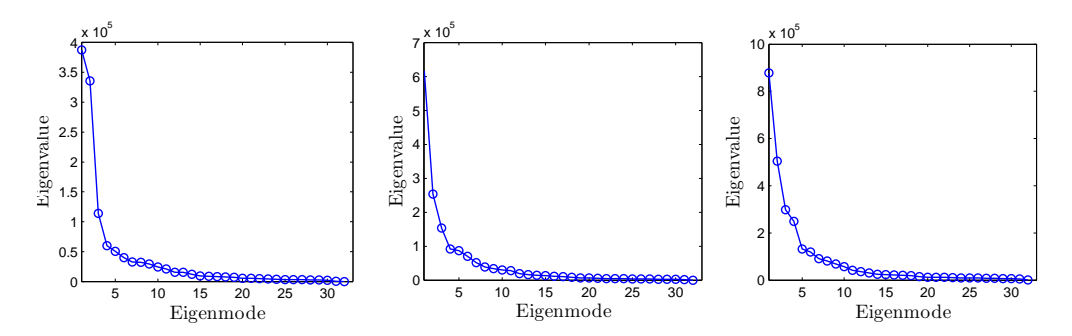


Figure 4.7: From left to right are respectively the plots of eigenvalues of the left, right, and two lungs calculated by PCA.

Figure 4.10 demonstrates NPPs of two lungs. Two lungs involve relative positioning from each other. It is reasonable to assume that the distance between the left and right lungs varies in individual case. While interestingly, there are less anomalies than single lung modellings. This indicates that the individual relative positioning of two lungs can be tolerated in the modelling process and they can be regarded as one shape of two parts topologically. This result in addition suggests the prospect of simultaneous modelling of two lungs and further to this, the simultaneous segmentation of two lungs.

In summary, based on the NPPs for the eigenmodes of the left, right and two lungs, the Gaussian assumption is valid. Therefore, both methods proposed by Leventon et al.

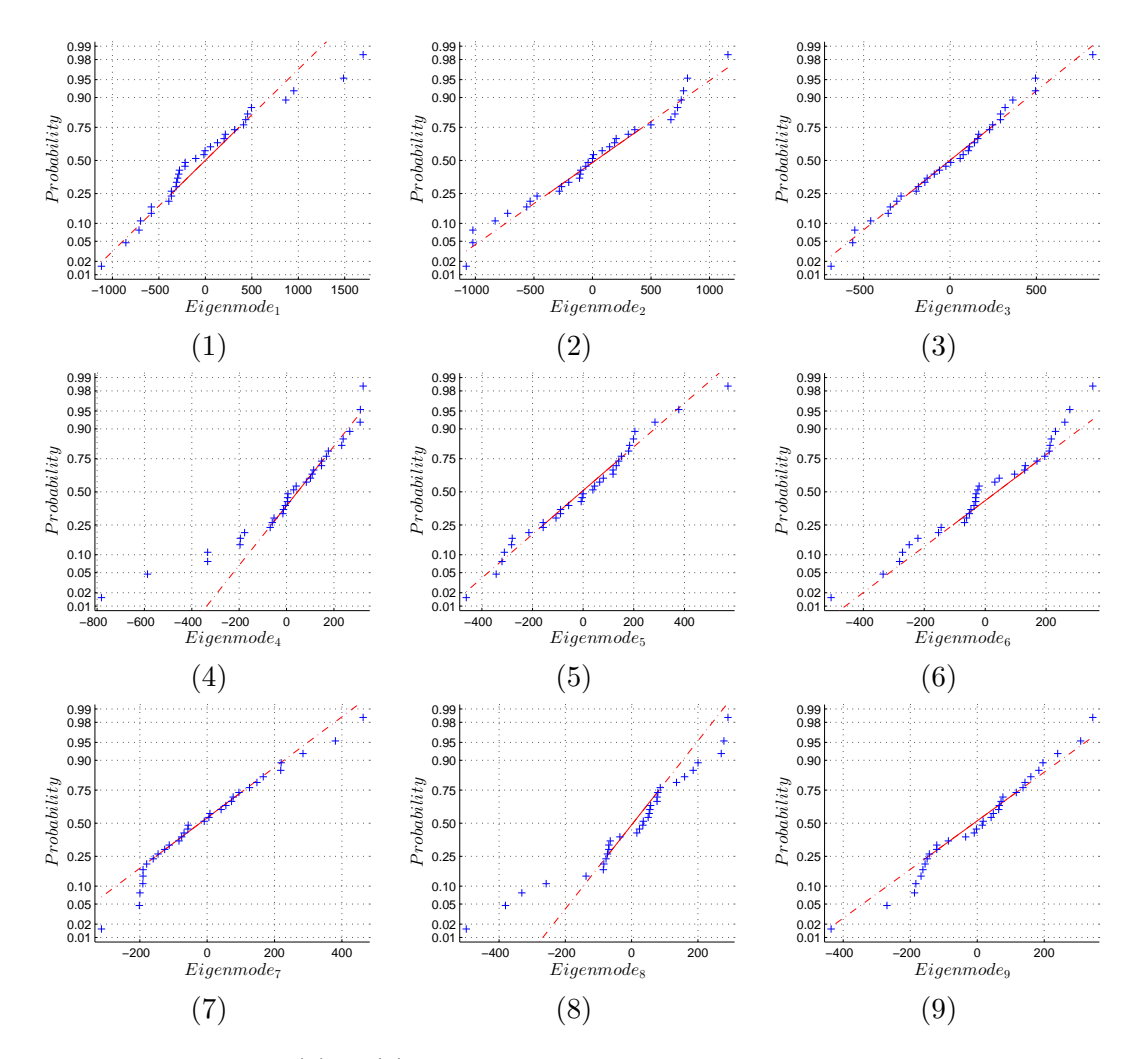


Figure 4.8: From (1) to (9) are respectively the NPPs of 9 eigenmodes generated from 33 cases of the left lungs.

(2000) and Bresson et al. (2006) can be used for modelling of lungs.

4.4.3 Leventon vs Bresson for Parameter Estimation

This section focuses on the accuracy of estimation of the shape parameter α . The methods proposed by Leventon et al. (2000) and Bresson et al. (2006) both have advantages. Leventon's method calculates α directly given a novel shape under Gaussian assumption, however, theoretically there is no insuring any of the basic similarity measure (region or surface) is to be optimized (either minimized or maximized) between the model and novel shapes. Bresson's method derives a motion equation (see equation 4.15) from the function of the sum of squared distance between shapes, while the method is iterative and computationally costly. Next, in lung modelling (both for single and two lungs modelling), a comparison of these two methods will be demonstrated.

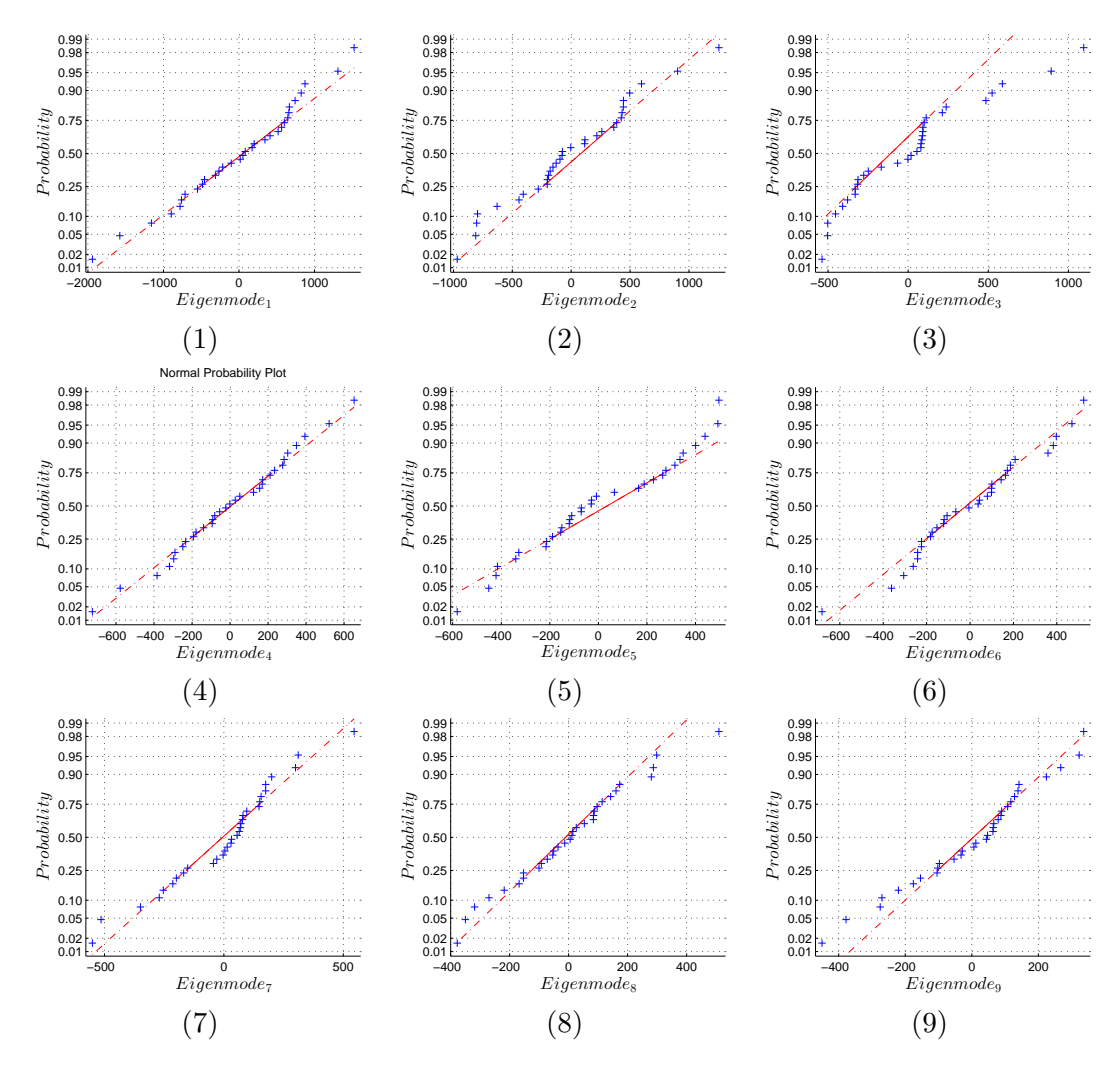


Figure 4.9: From (1) to (9) are respectively the NPPs of 9 eigenmodes generated from 33 cases of right lungs.

One thing to clarify is that this section does not present a complete comparison between Leventon's and Bresson's ideas in modelling. Only the estimation of α from Bresson's method is used here for a comparison. Bresson's method also include geodesic flows for local adjustment, which would be further discussed in the next section (section 4.4.4). Furthermore, the modelling involves the first 10 eigen-shapes only. As is presented figure 4.7 in section 4.4.1, beyond the first 10, the eigenvalues occupy a small minority, therefore, 10 would be sufficient for the comparison purpose.

The implementation validations of Leventon's and Bresson's methods are presented in figure 4.11 and figure 4.12 following the work of Bresson et al. (2006). 20 synthesized ellipses are used here to perform the validation. Figure 4.11 presents the result of PCA decomposition of the 20 ellipses and the variation of the shapes under various values of α . Figure 4.12 shows the results of modelling a novel ellipse left out from the training set using both Leventon's and Bresson's methods. It can be observed that the ellipse is

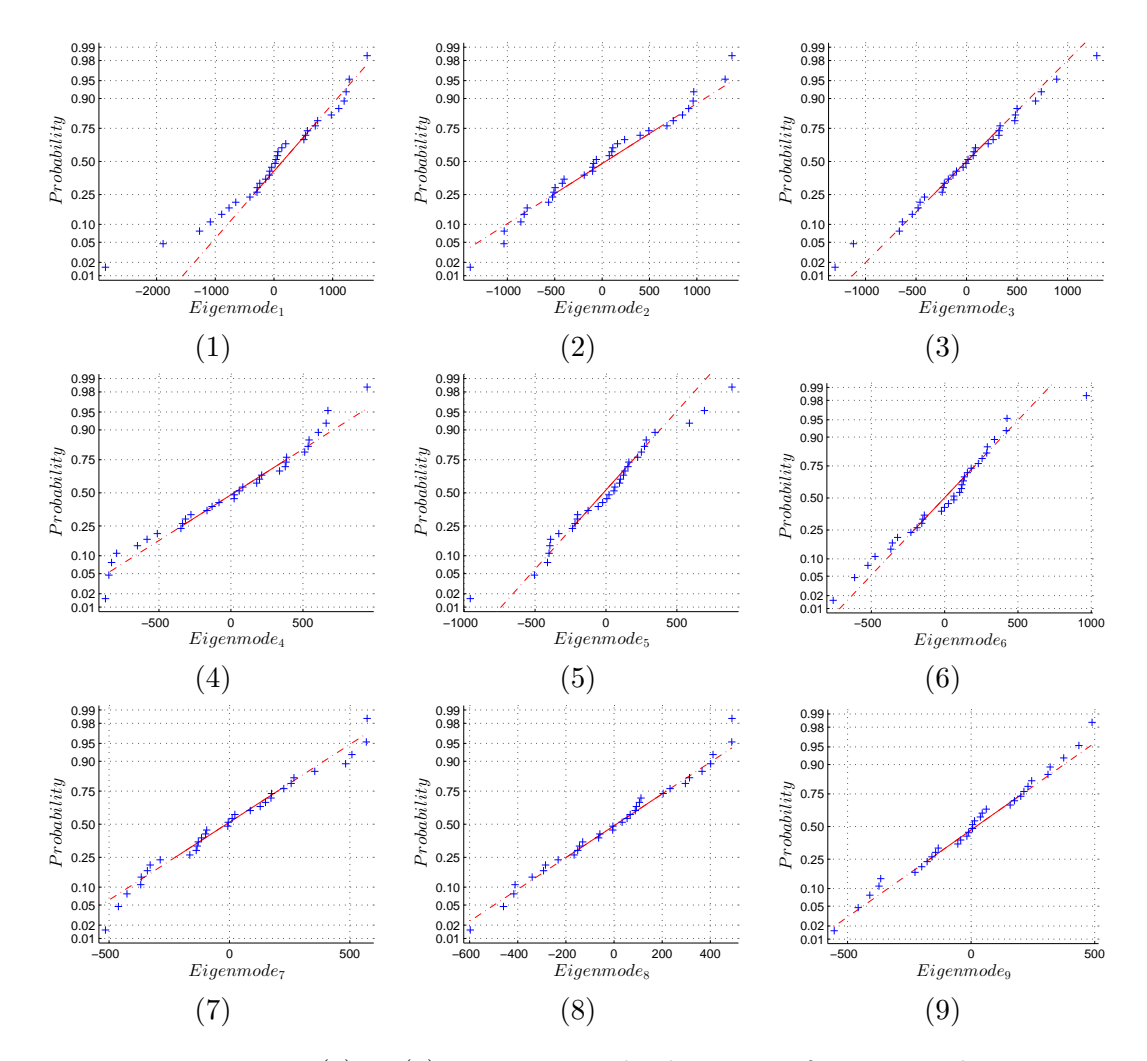


Figure 4.10: From (1) to (9) are respectively the NPPs of 9 eigenmodes generated from 33 cases of two lungs.

correctly modelled by both methods and thus the implementations of both methods are validated.

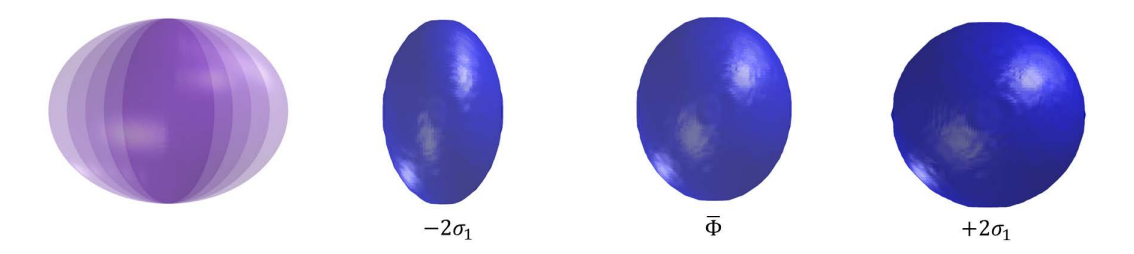


Figure 4.11: An overlapped set of 20 ellipses is shown on the left side and the variation of shapes under different α after PCA decomposition is shown by the rest three pictures.

Figure 4.13 presents the comparison of modelling the left lungs by Leventon et al. (2000) and Bresson et al. (2006) using the four similarity measures, which are E_{R1} (normalized inner product of shape's CFs), E_{R2} (Dice's coefficient), E_{D1} (average Euclidean

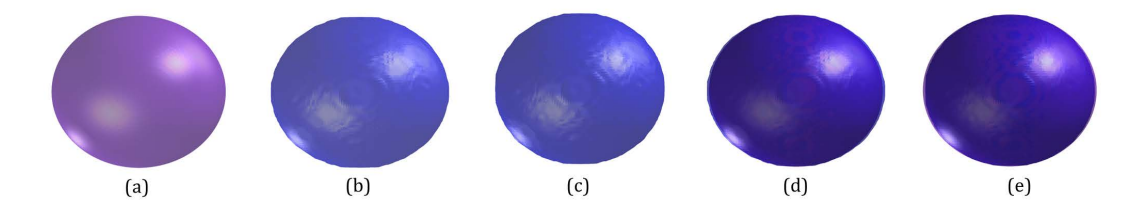


Figure 4.12: The modelling of the set of ellipses using Leventon's and Bresson's methods. (a) The original left-out ellipse from the training set. (b) and (c) are respectively the results given by Leventon's and Bresson's methods. (d) and (e) are the results overlapped with the left-out ellipse.

distance), and E_{D2} (Hausdorff distance). Please refer to section 4.3.3 for more details. The natural differences of individuals in the database give rise the the fluctuation of the modelling accuracy. Furthermore, a leave-one-out scheme is utilized here, which means each shape to be modelled is novel to the database. There is a limitation for the database to describe the novel shape. Leventon's method in the case of left lungs delivers slightly better results on average. It should be taken into account that the results of Bresson's method are dependent on precisions of numerical implementation. The evolution equation (equation 4.15) minimizes sum of squared distance of surfaces represented by SDFs and is largely affected by the numerical approximation of the Dirac function δ . The approximation scheme for δ is same as section 2.5. For numerical stability, ϵ should not be too small and it is reasonable to expect there can be 1 voxel of fluctuation in the approximation. Therefore, considering the numerical defects, Bresson's method produces similar results as Leventon's. Some examples of modelling using the two methods are given in figure 4.14.

Figure 4.15 shows the comparison of modelling the right lungs by the two methods. By observation the modelling results of the right lung using the two methods are quite close to each other. The most significant differences are showed figure 4.15(4) which is Hausdorff distance. It should be pointed out that the term that Bresson's method minimizes is the sum of squared distance of two surfaces while the Hausdorff distance is maximum distance. In certain cases, the distance of local areas may well be enlarged to compensate the minimization of the global average distance. (See figure 4.16 for some examples.)

Figure 4.17 suggests similar results of modelling for two lungs by the two methods. The accuracy is reduced by a degree compared to modelling of single lungs, due to the fact that two lungs altogether possess greater variations than any single one. (See figure 4.18 for some examples.)

As for the efficiency of the two methods, a comparison can be found in table 4.1. The iterative solution to the parameter estimation problem proposed by Bresson et al. (2006) consumes much longer time than the solution given by Leventon et al. (2000).

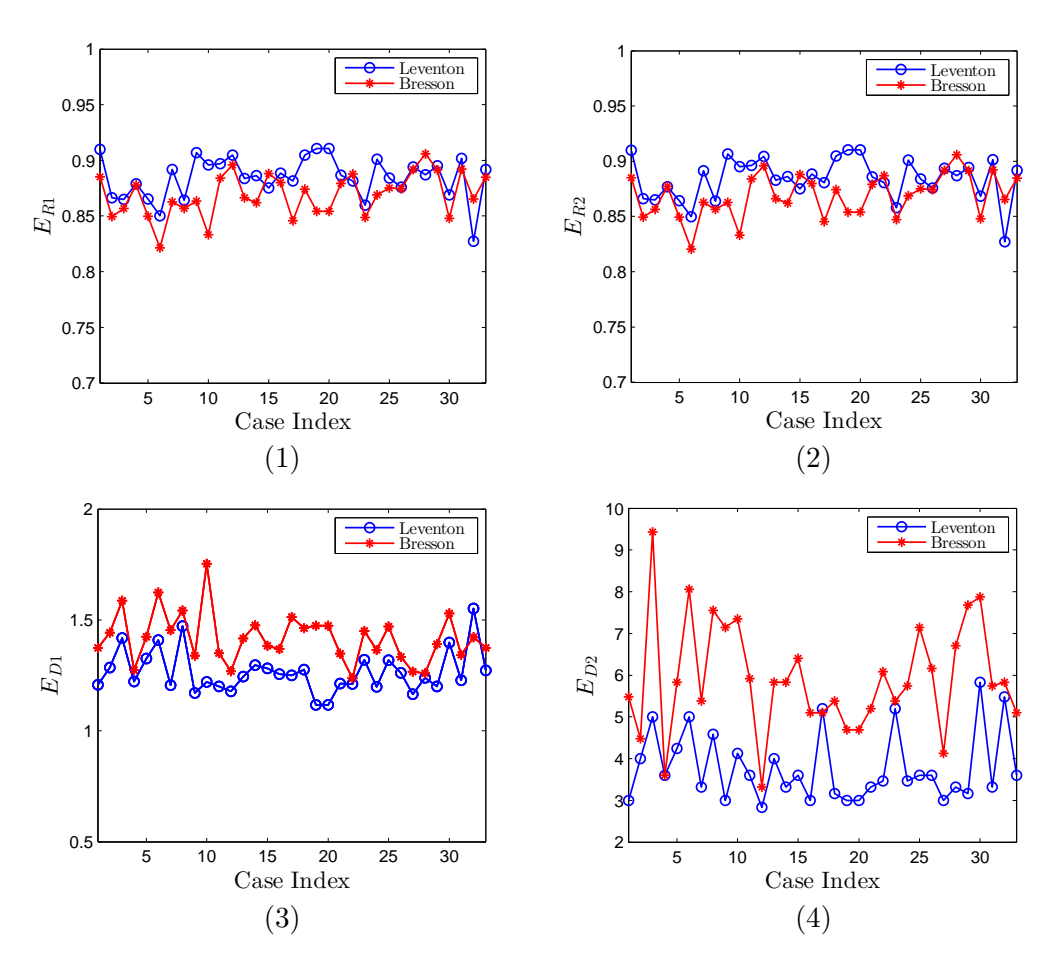


Figure 4.13: The comparison of the modelling results for the right lungs produced by Leventon's and Bresson's methods.

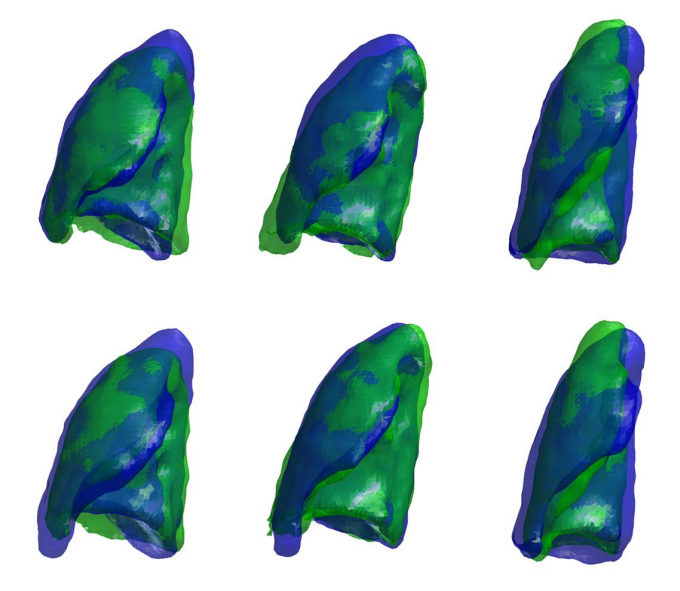


Figure 4.14: Top row: the PCA modelling results of the left lungs using Leventon's method for case 3, 15 and 24 respectively. Bottom row: the results using Bresson's method. (Novel shapes in green and prior shapes in blue.)

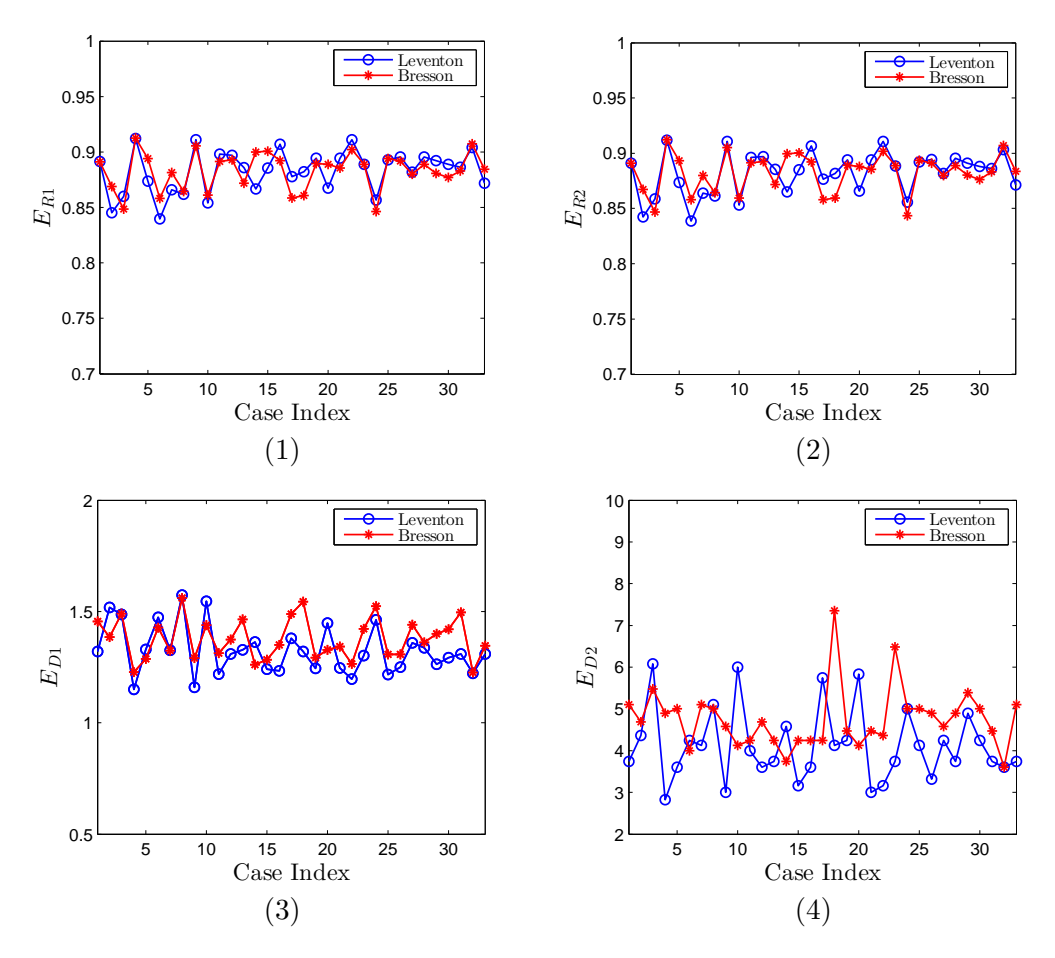


Figure 4.15: The comparison of the modelling results for the left lungs produced by Leventon's and Bresson's methods.

Lung class	Left	Right	Two
Leventon et al. (2000)	2.06s	2.09s	4.71s
Bresson et al. (2006)	21.54s	21.36s	28.96s

Table 4.1: A comparison of the parameter estimation methods proposed by Leventon et al. (2000) and Bresson et al. (2006) with respect to efficiency. The average time of estimation for each case respectively from the databases of the left, right and two lungs are presented, including the time for learning stage, which is 0.5-0.6s.

In summary, this section on the whole indicates both methods proposed by Leventon et al. (2000) and Bresson et al. (2006) produce 'close-to-equivalent' results. It is claimed in the work of Bresson et al. (2006) that their method is a variational formulation of Leventon's method. This claim is thus validated in this experiment. In practice, it is better to use Leventon's approximation of shape parameter α because it incurs less computational cost than Bresson's while producing similar (sometimes better) results.

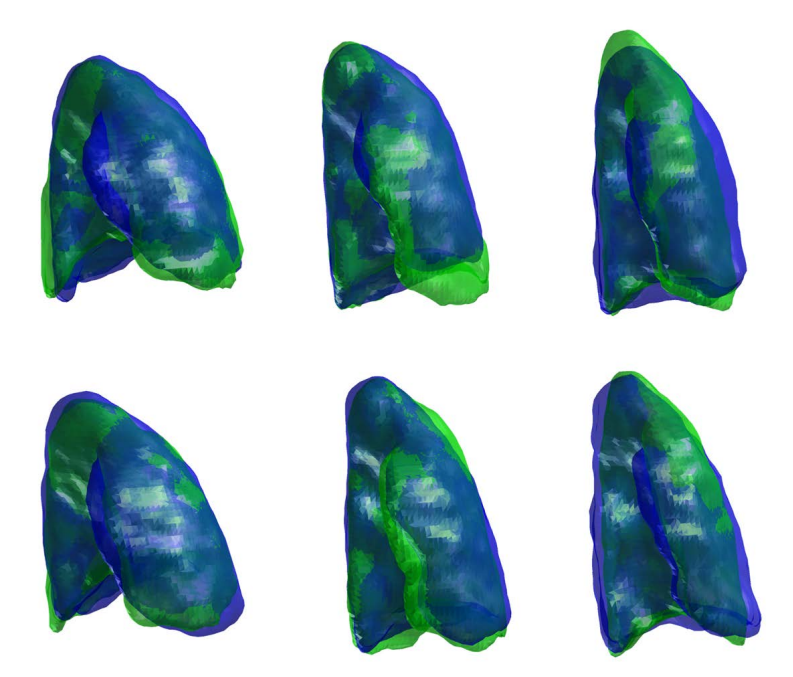


Figure 4.16: Top row: the modelling results of the right lungs using Leventon's method for case 3, 15 and 24 respectively. Bottom row: the results using Bresson's method. (Novel shapes in green and prior shapes in blue.)

4.4.4 The Proposed Hybrid Shape Modelling Method

In section 4.3.2, a hybrid shape approximation scheme is introduced. Based on the formulation of Bresson et al. (2006) and incorporating the registration method proposed in chapter 3, it follows a coarse-to-fine process to model a novel shape which is left out from the database. Technically the hybrid method achieves the same result as the modelling in the work of Bresson et al. (2006), however, two steps are replaced by more efficient techniques which involves no iterations, which are similarity registration and estimation of α .

This section addresses the accuracy of the hybrid scheme for shape modelling and presents a comparison with Leventon's modelling method. While the similarity registration is not the centre of interest and it is proven in the last section (section 4.4.3) that the parameter estimation methods of Leventon and Bresson are generally equivalent, the major concern of this section is to show the advantage of adding a geodesic flow in addition to PCA modelling.

Figure 4.19 demonstrates the left lung modelling results of the hybrid and Leventon's methods. A huge improvement can be observed from the plots with respect to accuracy and stability (fluctuation between cases). 'Hybrid10' means the modelling involves 10 eigen-shapes in the process and 'Hybrid1' employs the 1st eigen-shape only. While figure 4.21(4) indicates greater difference, the other three suggests that both the results produced by 'Hybrid10' and 'Hybrid1' are similar to each other in a more global view.

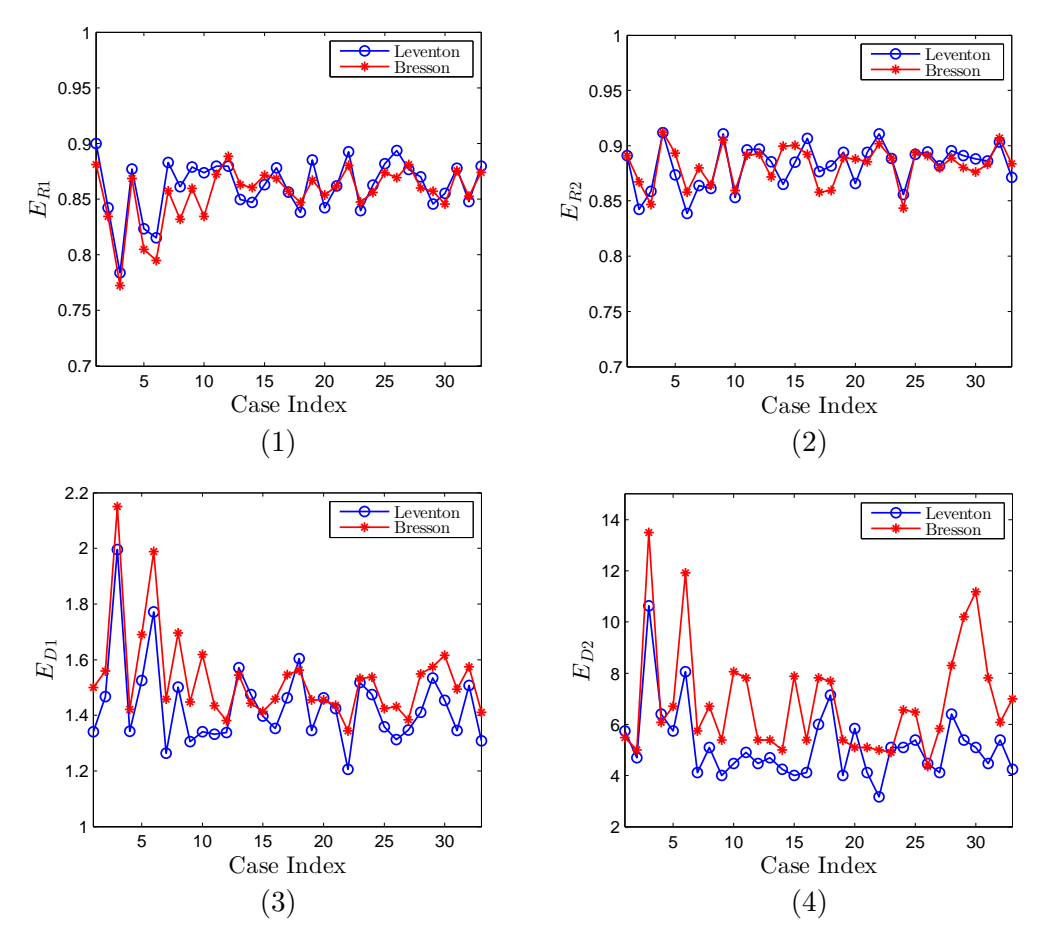


Figure 4.17: The comparison of the modelling results for two lungs together produced by Leventon's and Bresson's methods.

It is claimed in the work of Bresson et al. (2006) that with geodesic flow following the PCA modelling, only the 1st eigen-shape is sufficient and thus this claim is valid in our case. Some examples of the shape approximation are provided in figure 4.20.

Figure 4.21 and figure 4.22 present the comparison of the two methods respectively for the right and two lungs. The results again indicate the improvements of the modelling quality and the similarity of the modelling using 10 and the 1st eigen-shape. The geodesic flow can in fact be understood as a local non-rigid voxel-wise registration and contributes a lot in following local variations of the novel shapes where the database is unable to reach. Figure 4.23 and figure 4.24 respectively provide some examples of modelling for the right and two lungs.

Table 4.2 provides the comparison with respect to the efficiency of Leventon's and the proposed hybrid methods. The proposed method takes roughly 1 second longer than Leventon's with the databases of lung shapes at hand.

In summary, adding geodesic flow after PCA modelling process significantly improves

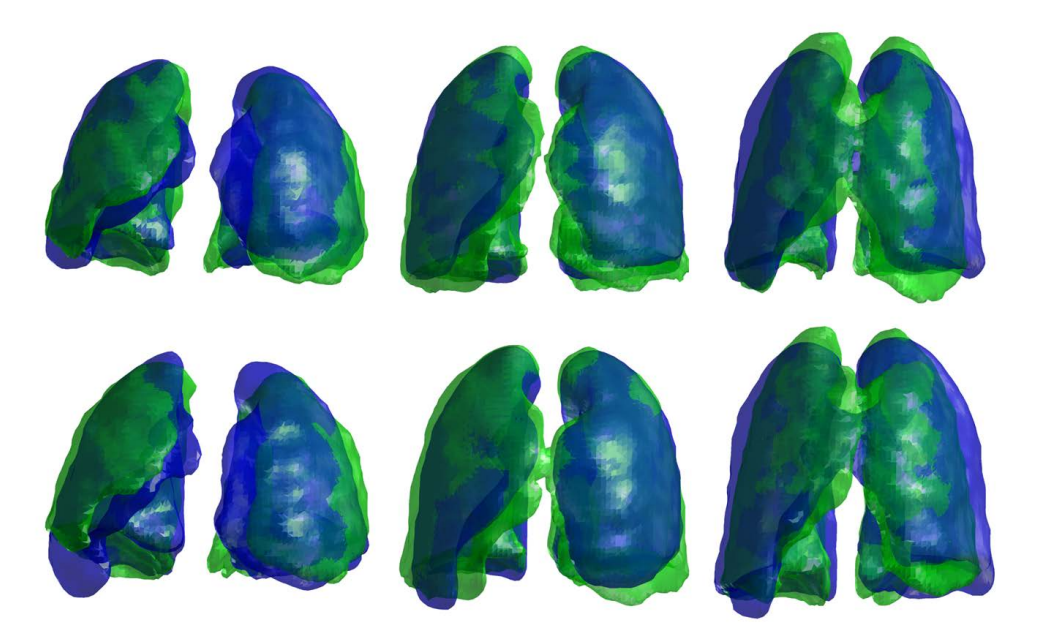


Figure 4.18: Top row: the modelling results of two lungs using Leventon's method for case 3, 15 and 24 respectively. Bottom row: the results using Bresson's method. (Novel shapes in green and prior shapes in blue.)

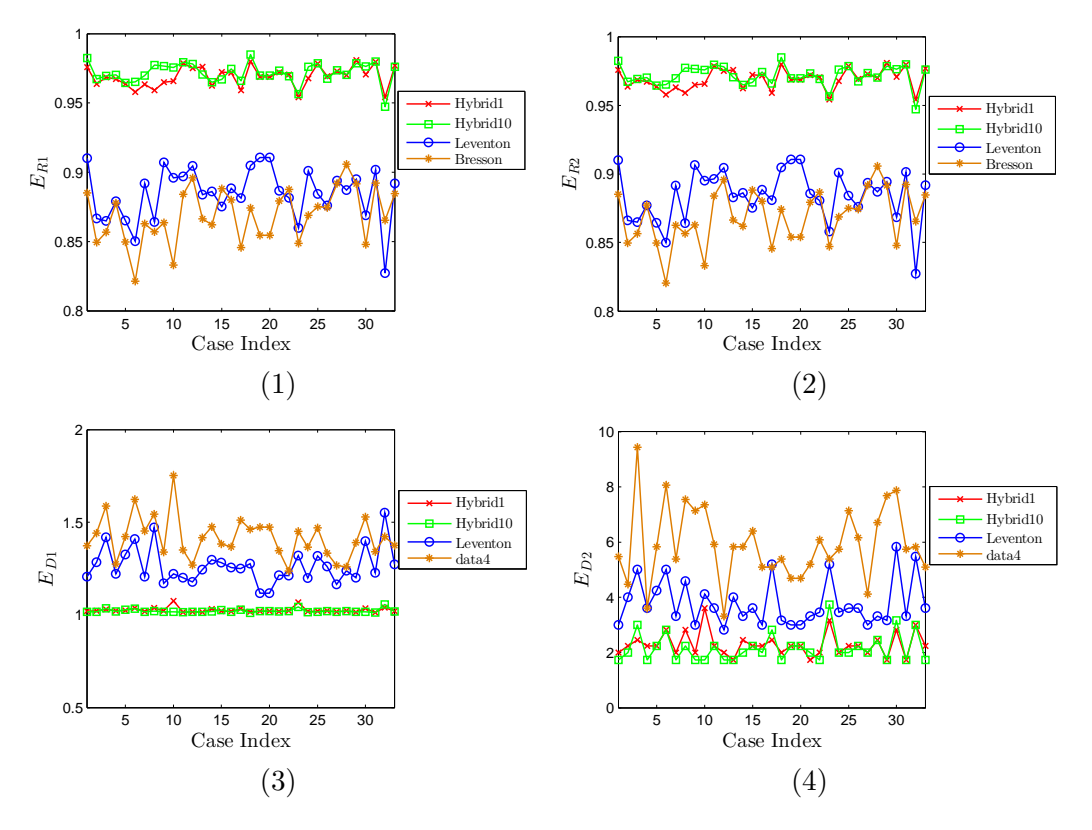


Figure 4.19: The comparison of the modelling results for the left lungs produced by Leventon's and the proposed hybrid method with 10 eigen-shapes and the 1st eigen-shape.

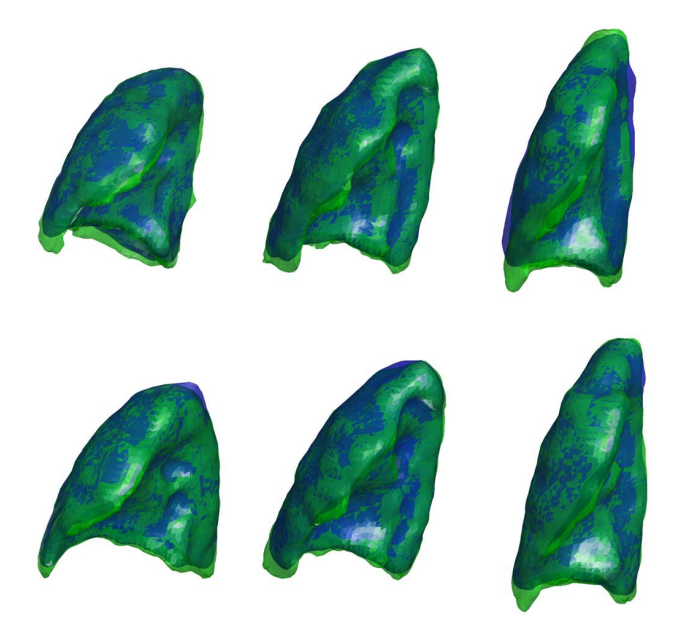


Figure 4.20: Top row: the modelling results of the left lungs by the proposed hybrid method using 10 eigen-shapes for case 3, 15 and 24 respectively. Bottom row: the results using the 1st eigen-shape only. (Novel shapes in green and prior shapes in blue.)

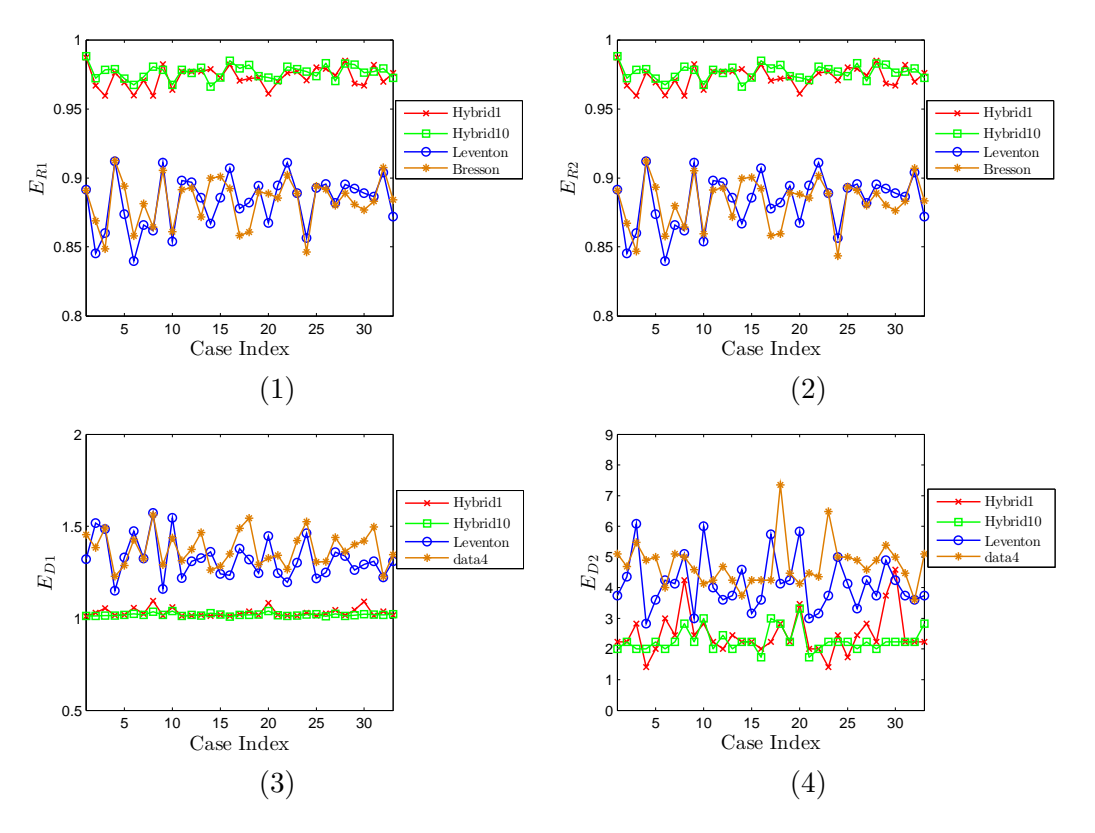


Figure 4.21: The comparison of the modelling results for the right lungs produced by Leventon's and the proposed hybrid method with 10 eigen-shapes and the 1st eigen-shape. (Novel shapes in green and prior shapes in blue.)

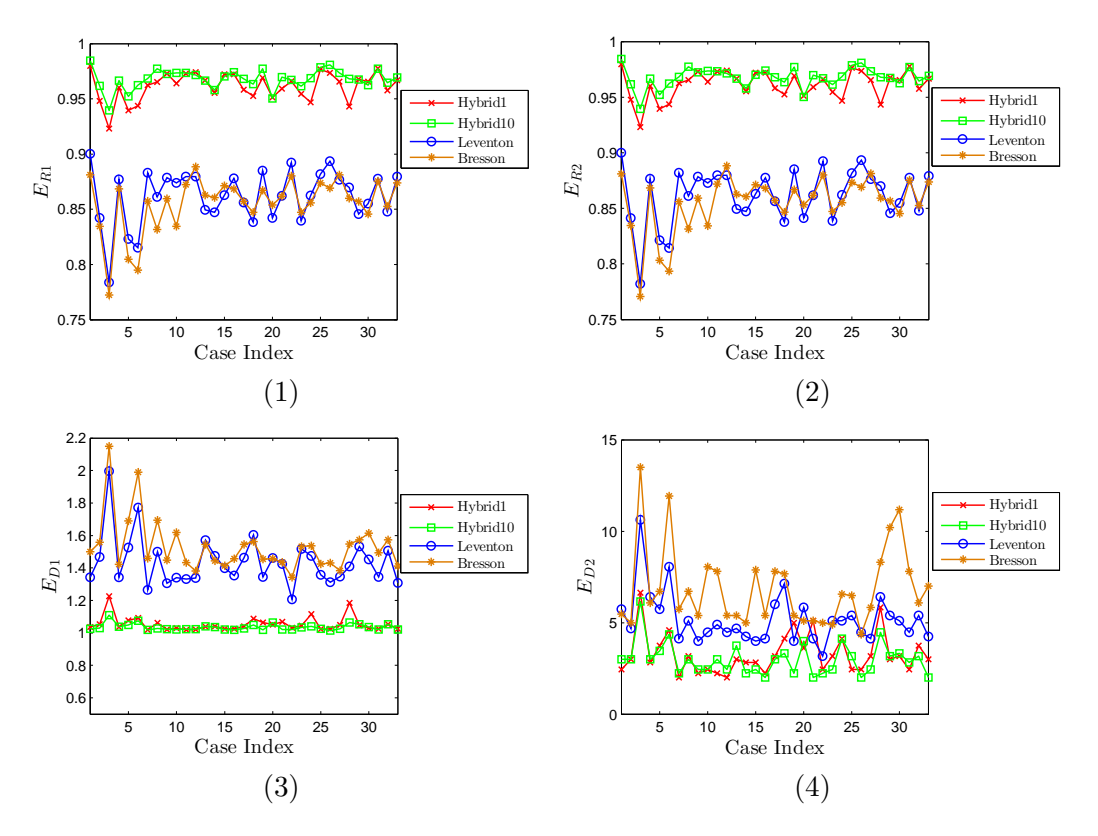


Figure 4.22: The comparison of the modelling results for two lungs produced by Leventon's and the proposed hybrid method with 10 eigen-shapes and the 1st eigen-shape.

Lung class			
Proposed	3.27s	3.31s	5.48s
Leventon	2.06s	2.09s	4.71s

Table 4.2: A comparison concerning efficiency of the proposed hybrid shape approximation method and Leventon's method. The average time of shape approximation for each case respectively from the databases of the left, right and two lungs are presented, including the time for learning stage, which is 0.5-0.6s.

the modelling accuracy. The geodesic flow can be understood as a local non-rigid voxel-wise registration. It can also greatly reduce the number of eigen-shapes from multiple to only one involved in PCA modelling process and thus reduce the computational cost. Statistical methods perform well in general classification, in other words, PCA modelling is capable of insuring the modelling result of a novel shape to be a shape of 'lung' class, however, it has limitations to achieve a better local accuracy when the training set has not a shape that is very close to the novel shape to be modelled.

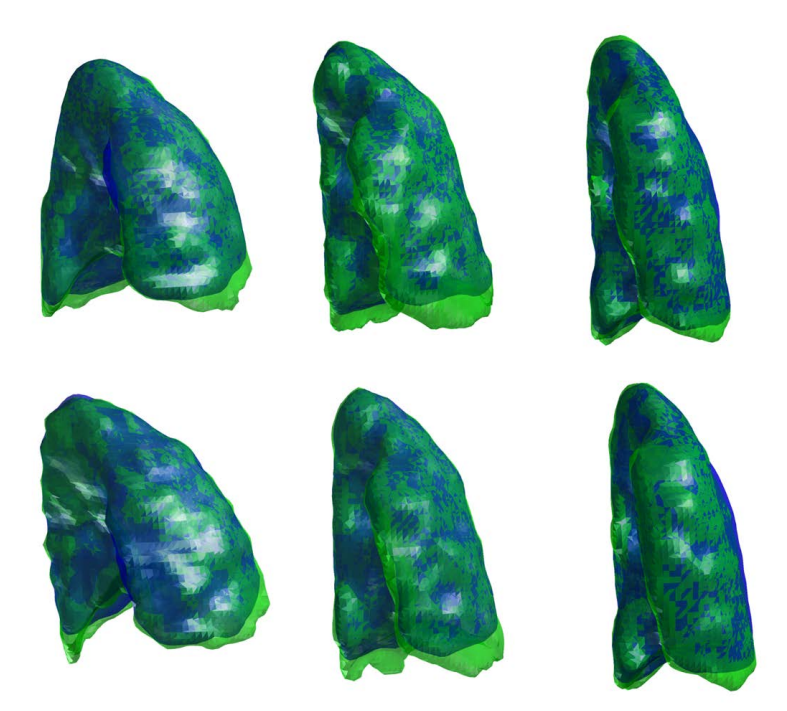


Figure 4.23: Top row: the modelling results of the right lungs by the hybrid method using 10 eigen-shapes for case 3, 15 and 24 respectively. Bottom row: the results using the 1st eigen-shape only. (Novel shapes in green and prior shapes in blue.)

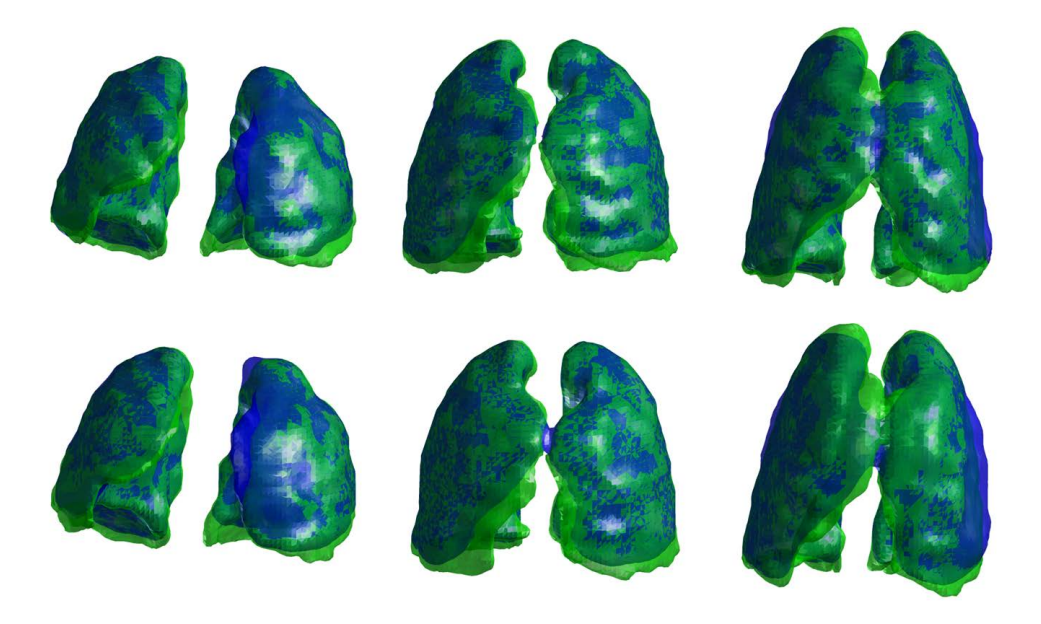


Figure 4.24: Top row: the modelling results of two lungs together by the hybrid method using 10 eigen-shapes for case 3, 15 and 24 respectively. Bottom row: the results using the 1st eigen-shape only. (Novel shapes in green and prior shapes in blue.)

4.5 Conclusions and Future Works

This chapter firstly presents a review of two popular methods in the literature, one proposed by Leventon et al. (2000) and the other by Bresson et al. (2006). Based on the two methods and the similarity registration technique introduced in chapter 3, a hybrid modelling scheme is proposed and improves the accuracy and efficiency of novel shape approximation.

Extensive experiments based on a lung database consisting of the left, right and two lungs together, which are in total 99 shapes, are carried out. Firstly, the Gaussinity of 'lung' shapes are validated to justify the combination of Leventon's and Bresson's methods. Then it is experimentally proven that the estimation methods of the PCA shape parameter α by both Leventon et al. (2000) and Bresson et al. (2006) have equivalence. Furthermore the geodesic flow following PCA modelling enormously improves local accuracy and remarkably reduce the number of eigen-shapes involved.

The hybrid method proposed here eliminates two iterative processes (similarity registration and PCA parameter estimation) and reinforced by geodesic flow, the number of eigen-shapes in PCA modelling is reduce from 10 to 1. The method inherits the accuracy of Bresson's method and the efficiency of Leventon's method. It should be pointed out that the method can be assured to work well when the training set of shapes satisfy a Gaussian distribution.

Chapter 5

Automatic Segmentation of Lungs from Low-dose CT Images

5.1 Background

The most popular trend of developing CT imaging technique is to improve the spatial resolution that enables more detailed anatomical structures to be revealed. While this is one way of advancement, in recent years, CT imaging is jointly used with single photon emission computed tomography (SPECT), known as SPECT-CT, to serve as a powerful tool in lung disease diagnosis. SPECT is a functional imaging technique that reveals the physiological and biochemical processes ongoing in the human bodies, however, its spatial resolution is significantly lower than other types of medical imaging techniques like CT and MRI. This means that the locations of the disease given by the SPECT technique is less accurate than those provided by CT and MRI. SPECT-CT takes advantage of both imaging methods, therefore, it is capable of associating the functional images with the corresponding anatomical pulmonary structures, which largely facilitates diagnostic procedures, surgical planning, radiation therapy, cancer staging, etc.

For a SPECT-CT machine, the CT scanner and the SPECT scanner are put together to perform the acquisition of the SPECT and CT images simultaneously. In this way, the biochemical impacts of the disease can be located more accurately than a stand-alone SPECT machine. However, the CT scanners on the SPECT-CT machines provides lower resolution images than those on the CT machines, due to the fact that the voltage can be applied on the CT scanners on a SPECT-CT machine is lower than that of the CT machines. The lower the voltage, the less the radiation of the X-ray, therefore the less resolution of the acquired images (more details of CT imaging principles can be found on the book written by Hsieh (2009)).

The CT images acquired using SPECT-CT involve lower dose of radiation from the scanners and are of lower spatial resolution and noisier than HRCT (see figure 5.1). These CT images are referred to in this work as low-dose CT images. The process of scanning takes longer time to complete, which increases the tissue densities compared to HRCT images obtained during full inhalation of each subject. Moreover, longer time of acquisition process incurs an extra amount of noise caused by breathing and cardiac motions. Therefore, it is a more challenging task to segment low-dose CT images than HRCT images.

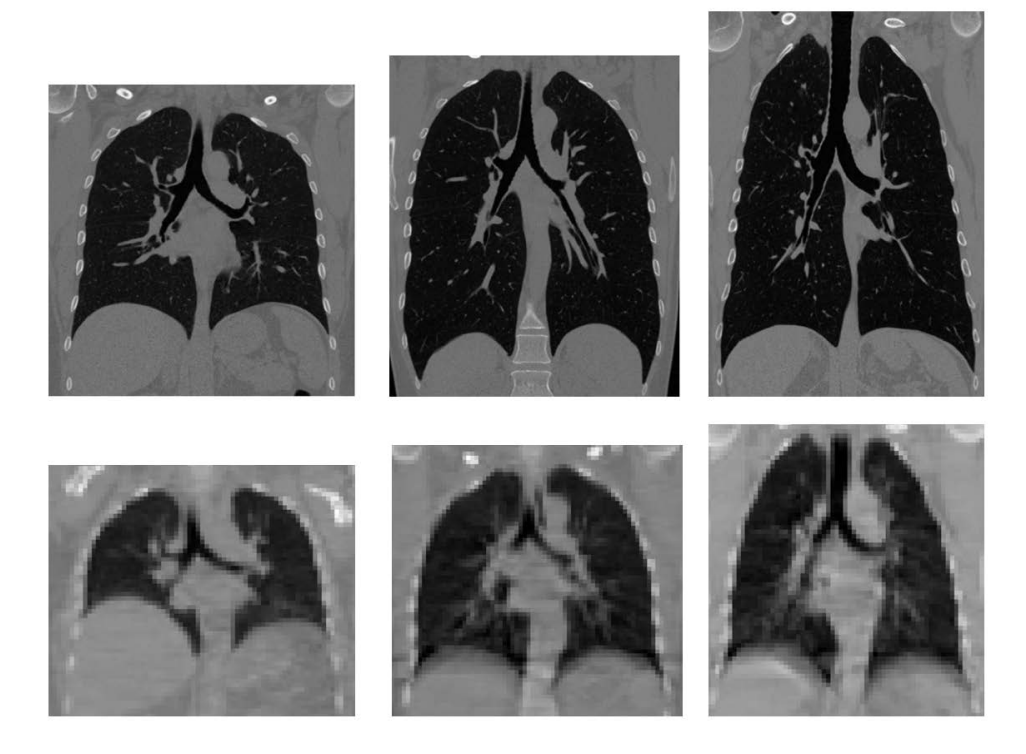


Figure 5.1: A comparison of HRCT and low-CT images. The top row presents the slices from HRCT scans and the bottom row the corresponding low-dose CT images from the same subjects. (The HRCT and low-dose CT images for each subject are acquired at different moments, therefore, they do not strictly correspond to each other.)

In section 1.3, the shape-based segmentation as an alternative methodology is proposed to solve the lung segmentation problem, therefore, this chapter introduces a hierarchical volumetric image segmentation technique that combines the methods proposed in the former chapters (chapter 2, 3 and 4), including active surfaces, similarity registration and statistical modelling of lungs.

Introducing shape information into image segmentation follows a progressive manner, from the early deformable shape template building (Cootes et al., 1992) to the recent global-to-local segmentation scheme in a variational framework (Bresson et al., 2006). A

review of previous methods is presented as follows to introduce the ongoing development of research concerning this topic.

5.2 Previous Works

Explicit prior shape model is first proposed by Cootes et al. (1992). PCA is utilized in this model to decompose a set of shapes and then to give a parametric description of these shapes in an explicit representation (control point sets). This model was built into a segmentation technique referred to as ASM (Cootes et al., 1994) to capture brain ventricles in 3-D magnetic resonance (MR) data sets and heart ventricles in echo-cardiogram sequences. The prior shape in this method adjusts itself to adjacent features in the greyscale medical images. Later Hamarneh and Gustavsson (2000) combined parametric snakes introduced by Kass et al. (1988) and prior shape model to segment left heart ventricles in ultrasound images. Snakes act as the force that guides the prior shape to the target in the image and the prior shape in its turn constrains the motion of the snakes to prevent them from being attracted by irrelevant edges elsewhere in the image. Also Cremers et al. (2002) used the Mumford-Shah functional (Mumford and Shah, 1989), which maximizes regional homogeneities, as the force that drives prior shapes.

Another popular style of segmentation methods are based on the shapes implicitly represented by level-sets, first introduced by Osher and Sethian (1988). Level-set formulation is non-parametric and naturally handles topological changes. Segmentation methods base on level-sets frequently employ implicit active contours as the driving force. The advantage is that while active contours attracted by external forces exerted by image features, it is naturally regularized by inner force during evolution.

Chen et al. (2002) proposed to put boundary-based geodesic active contours (GAC) (Caselles et al., 1997a) and rigid prior shape into one equation. Prior shapes constrain motions of GAC in a partial differential equation (PDE) through similarity registration (scale, rotation and translation) during curve evolution. Leventon et al. (2000) also uses GAC, however, the prior shapes becomes deformable in their work and the two models accomplish the segmentation in separated stages. One is as usual curve evolution, while the other is estimation of maximum a posteriori (MAP), which seeks to find the optimal parameters that deform and transform the prior shape, making it best match a given curve at a certain iteration.

Tsai et al. (2003) applied a reduced form of the Mumford-Shah functional, namely active contours without edges (ACWE) introduced by Chan and Vese (2001), as the driving force of prior shapes to medical image segmentation. This method performs segmentation both 2-D and 3-D, and is robust in the presence of a considerable amount of noise and occlusions. Another approach based on region features is proposed by Rousson et al.

(2004), which exploits texture information. A unified framework is proposed by Bresson et al. (2006), which integrates region features, boundary optimization, statistical shape modelling and registration (similarity and affine) together into one energy functional. This integration functions well in the segmentation of brain ventricles in noisy data obtained from magnetic resonance imaging (MRI). While most statistical prior shape modelling assumes the training set to has a Gaussian distribution, Cremers et al. (2006) proposed one that benefits from non-parametric density estimators modelling arbitrary distributions. Also the proposed segmentation algorithm employs intrinsic registration that removes iterative optimization of explicit pose parameters.

5.3 The Previous Theories of Segmentation Using Prior Shapes

In this section, several popular theories of shape-based segmentation methods are explained in details. They mark the major advancements of this methodology. Also, the description of these theories facilitates the introduction of a novel hierarchical technique to be proposed in the next section (section 5.4) for the segmentation of lungs from volumetric CT images.

Leventon et al. (2000) proposed a pioneering shape-based image segmentation method applied to the medical imagery. PCA is initially performed on a set of training shapes represented by SDFs to obtain a deformable shape model controlled by parameter α as described in section 4.2. Then, guided by geodesic active contours/surfaces, the statistical shape prior achieves the segmentation following a MAP framework that leads to the motion equation:

$$\phi_{ac}(t+1) = \phi_{ac}(t) + \lambda_1(\phi_{mod}(t) - \phi_{ac}(t)) + \lambda_2|\nabla\phi|\left[\nabla\cdot(g(I)\frac{\nabla\phi}{|\nabla\phi|}) + \nu g(I)\right]$$
(5.1)

This is a linear coupling of the deformable shape model and GAC (geodesic active contours) that detects edges in the image to be segmented. The segmentation process requires the initial contours to be located inside the ROIs. Registration participates the segmentation process, however, the parameters involved are only rotation and translation. Scale is not addressed. Possibly the images to be segmented have already been aligned and thus scale differences from individuals are minimized.

Another thing to be noted is that examples given by Leventon et al. (2000) also share the same feature that the interior area of ROIs have a relatively stable intensity. This feature is friendly to GAC as no local intensity pitfalls would hamper the evolution of the contours to detect the correct boundaries. While in the interior areas of the lung images, where the intensity of the voxels has relatively large variations, the GAC model only is probably insufficient.

Chen et al. (2002) presented a mathematically sound method that combines GAC, similarity registration and rigid prior shape. The method aims at minimizing the following energy functional:

$$E_{chen} = \int_{\Omega} \left[g(I) + d^2(\phi_{ac}(\mathcal{T}_{sim}(\mathbf{x})), \phi_{mod}) \right] |\nabla \phi_{ac}| \delta(\phi_{ac}) \, d\mathbf{x}$$
 (5.2)

where $\mathcal{T}_{sim}(\mathbf{x}) = s\mathbf{R}\mathbf{x} + \vec{T}$ (also mentioned in equation 4.14) and d^2 is the squared distance between the active contours and shape model. The solution to this functional is given by two motion equations:

$$\partial_t \phi_{ac} = \delta_0(\phi_{ac}) \left[\nabla \cdot (g(I) \frac{\nabla \phi_{ac}}{|\nabla \phi_{ac}|}) \right]$$
 (5.3)

$$d_t \mathbf{x}_R = -\int_{\Omega} d\langle d, \nabla_{\mathbf{x}_R} \mathcal{T}_{sim} \rangle |\nabla \phi_{ac}| \delta(\phi_{ac}) d\mathbf{x}$$
(5.4)

The existence of a solution to equation 5.2 is proven in this work, theoretically insuring the stability of this method.

In fact, d^2 is equivalent to the term $\phi_{mod}^2(\phi_{as}=0)$ in equation 4.13, therefore equation 5.4 in finding the similarity registration parameter follows the same manner as equation 4.15. The difference is that Bresson et al. (2006) add α , the PCA shape parameter into the equation, allowing ϕ_{mod} to deform in the statistical space provided by a training set.

Tsai et al. (2003) introduced a method that combines similarity registration, ACWE (active contours without edges), and PCA modelling of shapes. This method employs a functional derived from the one proposed by Chan and Vese (2001) which is a reduced form of the MS (Mumford-Shah) functional (please refer to equation 2.15, 2.16 and 2.17 for more details):

$$E_{ACWE} = \int_{\Omega} (I - c_{+})^{2} H(\phi_{ac}) \, d\mathbf{x} + \int_{\Omega} (I - c_{-})^{2} H(-\phi_{ac}) \, d\mathbf{x}$$

$$= -2 \int_{\Omega} [Ic_{+} H(\phi_{ac}) + Ic_{-} H(-\phi_{ac})] \, d\mathbf{x} + \int_{\Omega} [(I^{2} + c_{+}^{2}) H(\phi_{ac})$$

$$+ (I^{2} + c_{-}^{2}) H(-\phi_{ac})] \, d\mathbf{x}$$

$$= -2 \left[c_{+} \int_{\Omega} IH(\phi_{ac}) \, d\mathbf{x} + c_{-} \int_{\Omega} IH(-\phi_{ac}) \, d\mathbf{x} \right] + \left[c_{+}^{2} \int_{\Omega} H(\phi_{ac}) \, d\mathbf{x} \right]$$

$$+ c_{-}^{2} \int_{\Omega} H(-\phi_{ac}) \, d\mathbf{x} + \int_{\Omega} I^{2} \, d\mathbf{x}$$

$$= -\left[c_{+}^{2} \int_{\Omega} H(\phi_{ac}) \, d\mathbf{x} + c_{-}^{2} \int_{\Omega} H(-\phi_{ac}) \, d\mathbf{x} \right] + \int_{\Omega} I^{2} \, d\mathbf{x}$$

$$= -\left[c_{+}^{2} \int_{\Omega} H(\phi_{ac}) \, d\mathbf{x} + c_{-}^{2} \int_{\Omega} H(-\phi_{ac}) \, d\mathbf{x} \right] + \int_{\Omega} I^{2} \, d\mathbf{x}$$

$$= -\left[c_{+}^{2} \int_{\Omega} H(\phi_{ac}) \, d\mathbf{x} + c_{-}^{2} \int_{\Omega} H(-\phi_{ac}) \, d\mathbf{x} \right] + \int_{\Omega} I^{2} \, d\mathbf{x}$$

$$= -\left[c_{+}^{2} \int_{\Omega} H(\phi_{ac}) \, d\mathbf{x} + c_{-}^{2} \int_{\Omega} H(-\phi_{ac}) \, d\mathbf{x} \right] + \int_{\Omega} I^{2} \, d\mathbf{x}$$

$$= -\left[c_{+}^{2} \int_{\Omega} H(\phi_{ac}) \, d\mathbf{x} + c_{-}^{2} \int_{\Omega} H(-\phi_{ac}) \, d\mathbf{x} \right] + \int_{\Omega} I^{2} \, d\mathbf{x}$$

$$= -\left[c_{+}^{2} \int_{\Omega} H(\phi_{ac}) \, d\mathbf{x} + c_{-}^{2} \int_{\Omega} H(-\phi_{ac}) \, d\mathbf{x} \right] + \int_{\Omega} I^{2} \, d\mathbf{x}$$

$$= -\left[c_{+}^{2} \int_{\Omega} H(\phi_{ac}) \, d\mathbf{x} + c_{-}^{2} \int_{\Omega} H(-\phi_{ac}) \, d\mathbf{x} \right] + \int_{\Omega} I^{2} \, d\mathbf{x}$$

$$= -\left[c_{+}^{2} \int_{\Omega} H(\phi_{ac}) \, d\mathbf{x} + c_{-}^{2} \int_{\Omega} H(-\phi_{ac}) \, d\mathbf{x} \right] + \int_{\Omega} I^{2} \, d\mathbf{x}$$

$$= -\left[c_{+}^{2} \int_{\Omega} H(\phi_{ac}) \, d\mathbf{x} + c_{-}^{2} \int_{\Omega} H(\phi_{ac}) \, d\mathbf{x} \right] + \int_{\Omega} I^{2} \, d\mathbf{x}$$

$$= -\left[c_{+}^{2} \int_{\Omega} H(\phi_{ac}) \, d\mathbf{x} + c_{-}^{2} \int_{\Omega} H(\phi_{ac}) \, d\mathbf{x} \right] + \int_{\Omega} I^{2} \, d\mathbf{x}$$

$$= -\left[c_{+}^{2} \int_{\Omega} H(\phi_{ac}) \, d\mathbf{x} + c_{-}^{2} \int_{\Omega} H(\phi_{ac}) \, d\mathbf{x} \right] + \int_{\Omega} I^{2} \, d\mathbf{x}$$

The term $\int_{\Omega} I^2 d\mathbf{x}$ is a constant regardless of ϕ_{ac} . Therefore, assuming that the inside area of ϕ_{ac} : $A_+ = \int_{\Omega} H(\phi_{ac}) d\mathbf{x}$, outside area: $A_- = \int_{\Omega} H(-\phi_{ac}) d\mathbf{x}$, sum of the intensity inside ϕ_{ac} : $I_+ = \int_{\Omega} IH(\phi_{ac}) d\mathbf{x}$ and sum of the intensity outside: $I_- = \int_{\Omega} IH(-\phi_{ac}) d\mathbf{x}$,

equation 5.5 can be rewritten as

$$E_{tsai} = -(c_{+}^{2}A_{+} + c_{-}^{2}A_{-})$$

$$= -\left(\frac{I_{+}^{2}}{A_{+}} + \frac{I_{-}^{2}}{A_{-}}\right)$$
(5.6)

This equation omits the length and area terms in the original work of Chan and Vese (2001) and thus requires no special numerical schemes. The solution to this energy functional is found by a gradient decent method:

$$\alpha(t+1) = \alpha(t) - \nabla_{\alpha} E_{tsai}$$
 (5.7)

$$\mathbf{x}_R(t+1) = \mathbf{x}_R(t) - \nabla_{\mathbf{x}_R} E_{tsai}$$
 (5.8)

The regularity of the final contours is fully handed over to the PCA shape model, which preserves smoothness in combination of the first several eigen-shapes. The accuracy of this method is fully dependent on the quality of shape modelling, and ACWE here acts only to guide the shape model to the region of interest. When the variations of the novel shape exceed the statistical space provided by the training set, the accuracy of the method is compromised.

Bresson et al. (2006) proposed a fully PDE-based segmentation approach that unifies the above methods in a variational framework. The approach aims to optimize a new energy functional:

$$E_{brssn} = \beta_1 E_{bndru}(\phi_{ac}) + \beta_2 E_{shape}(\mathbf{x}_R, \boldsymbol{\alpha}, \phi_{ac}) + \beta_3 E_{rgn}(\mathbf{x}_R, \boldsymbol{\alpha}, l_+, l_-)$$
 (5.9)

where E_{bndry} represents GAC, E_{shape} is given by equation 4.13, and E_{rgn} is the original MS functional:

$$E_{rgn} = \int_{\Omega} [(|I - l_{+}|^{2} + |\nabla l_{+}|^{2})H(\phi_{mod}) d\mathbf{x} + (|I - l_{-}|^{2} + |\nabla l_{-}|^{2})H(-\phi_{mod})] d\mathbf{x}$$
$$= \int_{\Omega} [\tilde{I}_{+}H(\phi_{mod}) + \tilde{I}_{-}H(-\phi_{mod})] d\mathbf{x}$$
(5.10)

	Variational	Rigidity of	Type of	Dimensionality
	Methods	shape model	registration	
Leventon	Geodesic	PCA	Rigid	2-D + 3-D
Chen	Geodesic	Rigid	Similarity	2-D
Tsai	Chan-Vese	PCA	Similarity	2-D + 3-D
Bresson	Mumford-Shah +	PCA +	Similarity +	2-D
	Geodesic	Geodesic	Affine	

Table 5.1: A comparison of the popular theories on the shape-based segmentation problem.

where l_+ and l_- are the smooth estimations of I inside and outside image domain Ω . The solution to the functional 5.9 is given by a set of motion equations:

$$\partial_t \phi_{ac} = \delta(\phi_{ac}) \left\{ \nabla \cdot \left[(\beta_1 g(I) + \beta_2 \phi_{mod}^2) \frac{\nabla \phi_{ac}}{|\nabla \phi_{ac}|} \right] \right\}$$
 (5.11)

$$d_{t}\boldsymbol{\alpha} = -\int_{\Omega} \nabla_{\boldsymbol{\alpha}} \phi_{mod} \left[2\beta_{2} \phi_{mod} | \nabla \phi_{ac} | \delta(\phi_{ac}) + \beta_{3} (\tilde{I}_{+} - \tilde{I}_{-}) \delta(\phi_{mod}) \right] d\mathbf{x}$$
 (5.12)

$$d_{t}\mathbf{x}_{R} = -\int_{\Omega} \langle \phi_{mod}, \nabla_{\mathbf{x}_{R}} \mathcal{T}_{sim} \rangle \left[2\beta_{2} \phi_{mod} | \nabla \phi_{ac} | \delta(\phi_{ac}) + \beta_{3} (\tilde{I}_{+} - \tilde{I}_{-}) \delta(\phi_{mod}) \right] d\mathbf{x} \quad (5.13)$$

$$\partial_t l_+ = l_+ - I - \Delta l_+ \tag{5.14}$$

$$\partial_t l_- = l_- - I - \Delta l_- \tag{5.15}$$

where $\Delta = \nabla \cdot \nabla$ is the Laplacian operator. The segmentation process presented by this set of equations follows a coarse-to-fine scheme. Firstly, the initial curve ϕ_{ac} evolves a small distance as GAC and is restricted by the shape model ϕ_{mod} as well. Then the PCA shape parameter α is estimated to find a best match between ϕ_{mod} and ϕ_{ac} within the statistical space provided by the training set, in the meantime, the curve also evolves under influence of the region term $(\tilde{I}_+ - \tilde{I}_-)\delta(\phi_{mod})$. Next step would be iterative optimization of the registration parameter \mathbf{x}_R while the curve keeps evolving driven by the region term. Lastly, l_+ and l_- are updated according to the current curve. These steps combined are considered as one large iteration of this method. The process comes to an end when the evolving curve achieves a steady state. Table 5.1 provides a comparison among the works of Leventon et al. (2000); Chen et al. (2002); Tsai et al. (2003); Bresson et al. (2006).

The segmentation process is a trade-off between prior shape model, the boundary information and the region influence. The shape model would insure the evolving curve to be of the intended shape class. The geodesic active contours compensate for the novel information when the shape model is incapable of fully depicting the shapes of ROIs. The region term can greatly accelerate the segmentation process and is less likely to be trapped in local minima. The advantage of this method is that the convergence is mathematically proven, and due its diversity, it can be applied to a very wide range of problems when well adjusted. However, the drawback would be computationally costly

due to the fact that the method is fully PDE based. In certain steps, iterative process may not be necessary. As is experimentally proven in section 4.4.3 in the last chapter, the estimation accuracy of shape parameter α of this method is equivalent (sometimes less accurate than) to Leventon's approach, which is non-iterative.

5.4 A Novel Hierarchical Segmentation Technique

Following the idea of Bresson et al. (2006), a hierarchical segmentation technique is proposed here for volumetric image segmentation. In this technique, however, some of the steps are refined for efficiency because the data size can be hundreds of times larger in 3-D than in 2-D. Firstly, the registration type applied here is similarity registration and the parameter \mathbf{x}_R is calculated using the method introduced in chapter 3. Secondly, the shape parameter $\boldsymbol{\alpha}$ is estimated using the method of Leventon et al. (2000) as is discussed in section 4.4. Lastly, the MS functional is replaced by its reduced form which is proposed by Chan and Vese (2001).

With the prerequisites introduced in the former chapters, the hierarchical segmentation technique executes the following steps:

Step 1: Evolve Φ_{as} using ASWE given by equation 2.18

$$\partial_t \Phi_{as} = \delta(\Phi_{as}) \left[\mu \nabla \cdot (g(\mathbf{x}) \frac{\nabla \Phi_{as}}{|\nabla \Phi_{as}|}) + \nu - \lambda |I - c_+|^2 + \lambda |I - c_-|^2 \right]$$
 (5.16)

Step 2: Calculate $\mathbf{x}_R = (s, \vec{q}, \vec{T})$ and register Φ_{as} to Φ_{mod} using the method introduced in chapter 3.

Step 3: Calculate α and update Φ_{mod} using the equations blow:

$$\alpha = \mathbf{V}_K^{\mathrm{T}} \mathcal{T}_{re} (\Phi_{as} - \bar{\Phi}) \tag{5.17}$$

$$\Phi_{mod} = \bar{\Phi} + \mathcal{T}_{re}^{-1}(\mathbf{V}_K \boldsymbol{\alpha})$$
 (5.18)

Step 4: Start with Φ_{mod} acquired in step 3, evolve Φ_{mod} using the equation blow:

$$\partial_t \Phi_{mod} = \delta(\Phi_{mod}) \left[\nabla \cdot (\Phi_{as}^2 \frac{\nabla \Phi_{mod}}{|\nabla \Phi_{mod}|}) \right]$$
 (5.19)

Step 5: Register Φ_{mod} back to Φ_{as} and Φ_{mod} is assigned to Φ_{as} .

Step 6: Evolve Φ_{as} using GAS given by equation:

$$\partial_t \Phi_{as} = \delta(\Phi_{mod}) \left[\nabla \cdot (g(I) \frac{\nabla \Phi_{as}}{|\nabla \Phi_{as}|}) \right]$$
 (5.20)

This technique can be understood as the interaction between the image and knowledge. The bridge that establishes the connection between the two is similarity registration. The surface represented by Φ_{as} after a limited step of evolution is delivered to the knowledge base provided by the training set. It contains both region and boundary information, plus a fraction of noise. The knowledge base represented by Φ_{mod} in its turn seeks to achieve an optimal and noiseless interpretation of the image information provided by Φ_{as} . Then the best-fit Φ_{mod} is registered back to Φ_{as} to replace it. This iterative process comes to a stop when the surface achieves a steady state. A graphical description of the hierarchical method is given in figure 5.2 and an example simultaneous segmentation of lungs from CT images in figure 5.3. Furthermore, for efficiency of implementation, step 1, 4 and 6 where variational models are involved, the narrow band numerical scheme proposed by Sethian (2001) is employed and the width of the narrow band is represented by b_s .

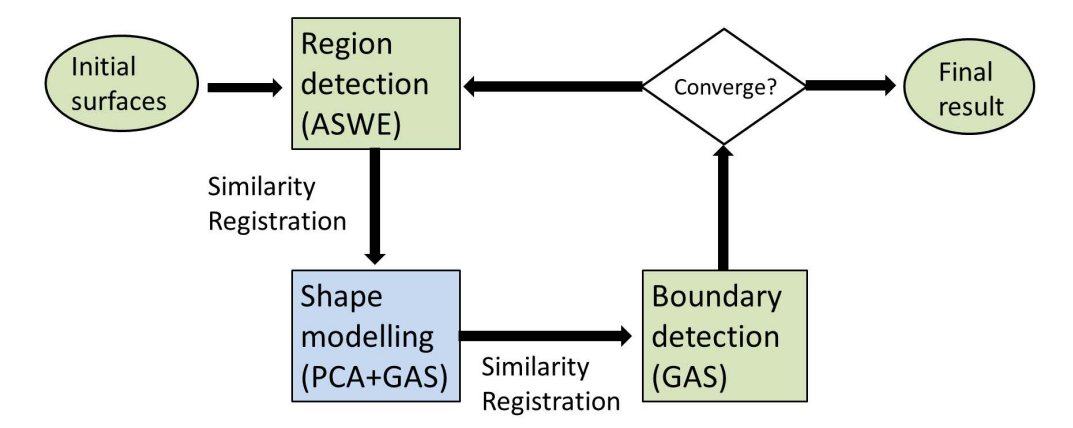


Figure 5.2: A graphical description of the proposed hierarchical method.

Based on the nature of this technique, there are several intended conditions of application:

- 1. The initial surfaces should be appropriately located.
- 2. The partition of the image should be well defined.
- 3. The ROIs to be segmented can be described by the knowledge base.

The first condition suggests that the initial surfaces are intended to be located inside the ROIs or have a major overlapping with them. The technique combines in total four mechanisms (GAS, ASWE, registration and PCA) which incur high computational cost. To reduce the efforts of computations, it is better to apply this technique at the right location. Coarse detections of the ROIs under most circumstances are straightforward while the reduction of certain local noise is where special techniques are required. The second condition requires the general partitioning of image should be the ROIs and the background. In certain images, there may be several parts that are too bright or dark.

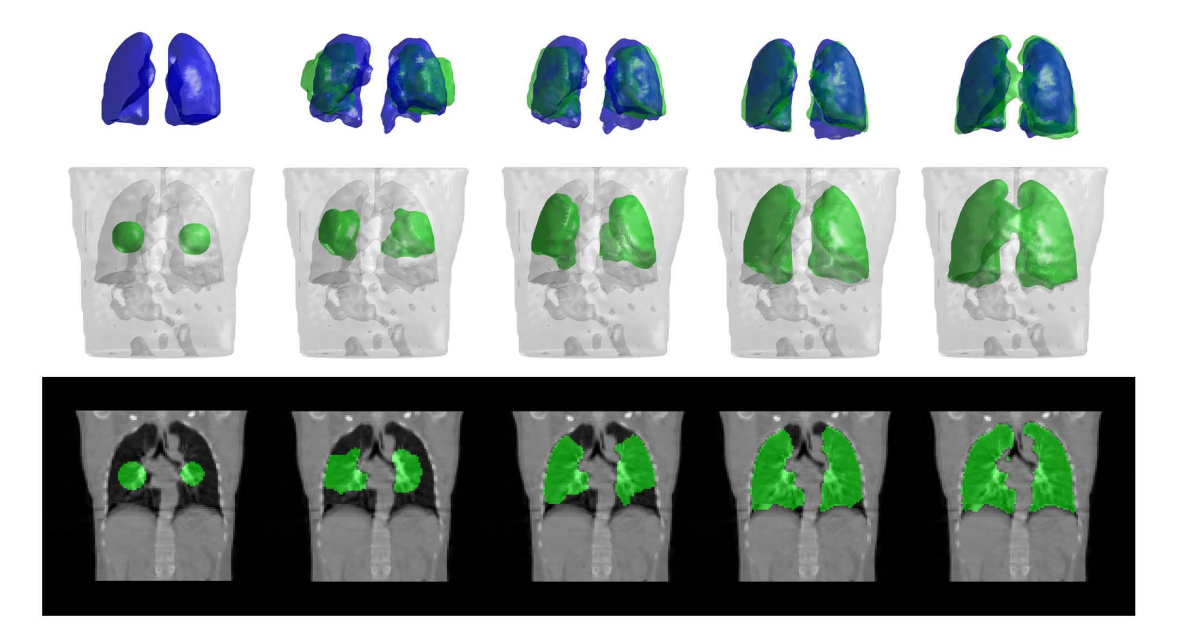


Figure 5.3: The simultaneous segmentation of lungs from volumetric CT images. The middle row gives the evolving surfaces restricted by the prior shape. The top row provides the corresponding prior shape interpretations of the surfaces extracted from the CT images. Bottom row presents typical slice views of the segmentation process.

The active surfaces may well suffer a major leakage into adjacent regions and in this case, the shape model is incapable of preventing such leakage. The shape of the ROIs should be of the same class with the training set. More on this issue will be addressed in section 5.5.2.

5.5 Experimental Results

5.5.1 An Overview

A series of experiments is presented here. The experiments can be divided into three stages. The first stage includes section 5.5.2, 5.5.3, 5.5.4, and 5.5.5. The working conditions of the proposed method are explained and some synthetic images are used to test the robustness against various types of occlusions and an increasing level of noise following the conventions in the work of Tsai et al. (2003) and Bresson et al. (2006). This stage also involves comparisons with typical methods proposed in the literature (Leventon et al. (2000) and Tsai et al. (2003)) to demonstrate the advantage of the proposed hierarchical technique. It should be pointed out that the work presented in this thesis is an improvement of both Leventon's and Tsai's methods. The models involved in both previous works have been clearly presented in table 5.1 and each model is implemented and experimented with from chapter 2 to chapter 4. The second stage includes section 5.5.6 and 5.5.7. The proposed method is applied to real world volumetric

images (low-dose CT scans) with artificial noise and synthetic tumors. In the last stage, presented by seciton 5.5.8, the robustness of the method is further proven by the segmentation of a low-dose CT scan database consisting of 33 cases. The case index which includes the patients' IDs and the disease states is provided in table B.2 in appendix B. The image size of each case is $128 \times 128 \times 128$ and the segmentation for each case is respectively performed on the left, right and simultaneously two lungs. Furthermore, the sections that involve the comparisons with previous methods are section 5.5.3, 5.5.4, 5.5.5, 5.5.7 and 5.5.8.

The parameter setting of the proposed method is $\Delta t = \epsilon = h = 1$, $\mu = 100$, $\lambda = 0.2$ (ASWE parameters, see section 5.4 and 2.5), $\xi = 50$ (GAS parameter, see section 2.2.2), $b_m = b_s = 3$ (the widths of the narrow band for lung modelling and active surfaces respectively, mentioned in section 4.3.2 and 5.4). The number of eigen-shapes for lung modelling used is K = 10 for Leventon's and Tsai's methods, and K = 3 for the proposed method. Mostly the parameter setting remains consistent in the experiments to be demonstrated. A particular parameter setting will be given in section 5.5.6 because it concerns images of extreme conditions of noise. The parameter values are chosen to well demonstrate the experimental results. Parameter optimization can improve the quality of the experiments and it will be investigated in the future works.

Just as the experiments in chapter 3 and 4, leave-one-out scheme is employed throughout the experiments in this section. Whenever the segmentation is performed, the shape corresponds to the image segmented is left out to achieve a fair evaluation of the proposed method.

The four similarity measures, E_{R1} (normalized inner product of shape's CFs), E_{R2} (Dice's coefficient), E_{D1} (average Euclidean distance), and E_{D2} (Hausdorff distance) introduced in section 4.3.3 are also adopted here for evaluation of the results. The first and second stages of experiment only involve E_{R1} and E_{D1} , because these stages are considered as test stages in this work, and two measures are sufficient to show the expected properties of the proposed method. While in practical use (the segmentation of lungs from low-dose CT images), all four similarity are employed for a thorough evaluation. Also for test stages, only the simultaneous segmentation of two lungs will be performed to reduce the redundancy of the experiments.

5.5.2 The Working Conditions of the Proposed Method

This section provides the explanations of the working conditions of the proposed method. It is pointed out in section 5.4 that the proposed method has three conditions of use, which are in short: 1. a proper initialization, 2. well-defined partition, and 3. similar shape class. Some examples are given here to show the necessity of these conditions.

Figure 5.4 presents the segmentation process of case 15 in the database of low-dose CT images using the proposed method starting from the outside the lung regions. It can be observed that the method falls into local minima and the prior shape fits itself in the wrong area. ASWE is the major force driving the prior shape and an improper initialization of evolution leads to an inaccurate result. Figure 5.5 shows that a proper initial surface gives rise to a satisfactory segmentation result.

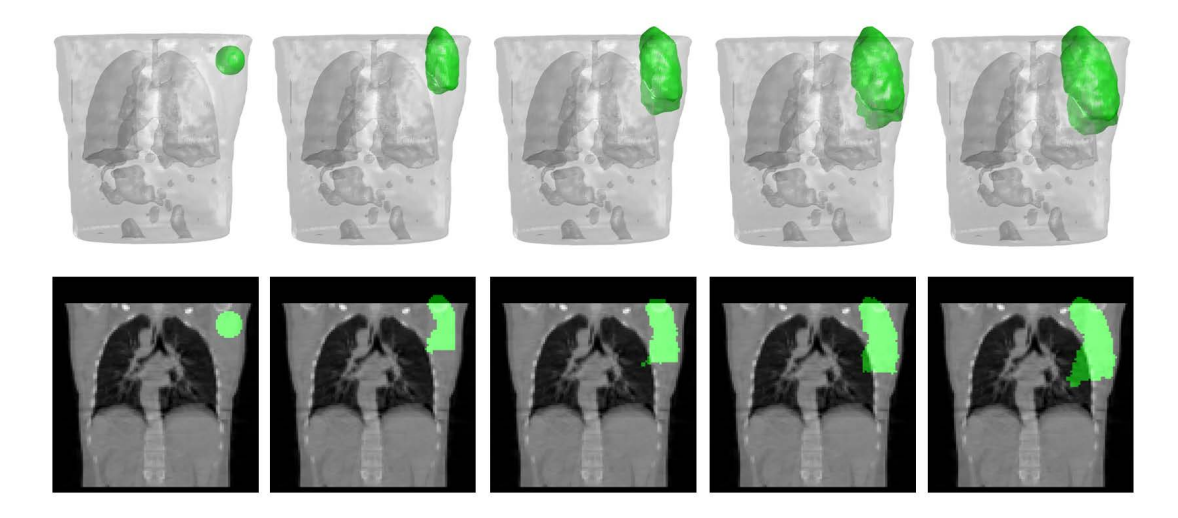


Figure 5.4: The evolution of active surfaces restricted by the prior shape starts outside the ROIs. Top row: the 3-D visualization of the evolution process. Bottom row: the corresponding slice views.

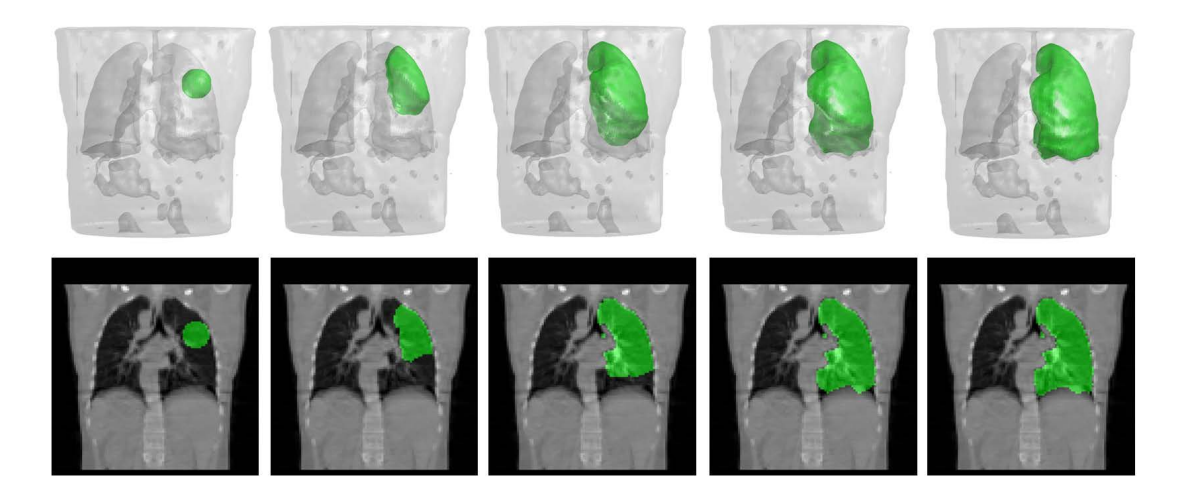


Figure 5.5: The evolution of active surfaces restricted by the prior shape starts inside the ROIs. Top row: the 3-D visualization of the evolution process. Bottom row: the corresponding slice views.

The second intended condition of use can be explained by figure 5.6. The background outside the body of the individual is enormously brightened and the optimal partition of the image becomes the human body and the background. Even though the lungs

are the ROIs and active surfaces evolve under restriction of prior shape with a proper initialization, they simply suffer a major leak into other regions of the body.

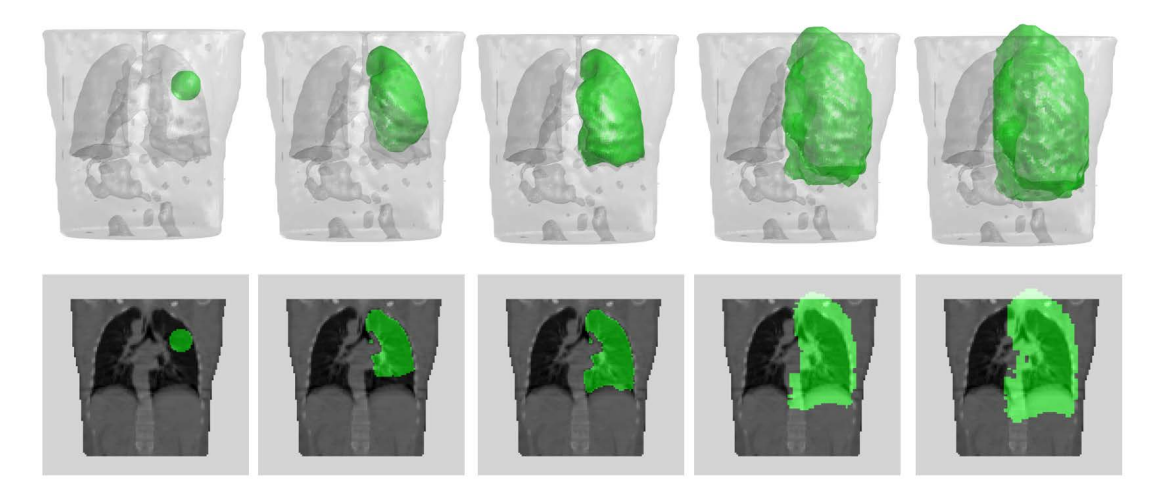


Figure 5.6: The evolution of active surfaces when the background is remarkably brightened. Top row: the 3-D visualization of the evolution process. Bottom row: the corresponding slice views.

In summary, this section demonstrates that the first two working conditions are necessary (the third is quite self-evident). The hierarchical method proposed here is in fact a delicate system which is most feasible for local optimization. In the following sections of experiments, these conditions are assumed to be fulfilled or extra schemes are proposed to achieve these conditions.

5.5.3 Synthetic Images with Occlusions

This section focuses on the robustness of the proposed method against occlusions. The images to be experimented here are synthesized using one of the mask images of lungs. The interior region is set to dark and the intensity value of exterior is set to 1000 to simulate real CT images. Two types of occlusions are synthesized here. Furthermore, the methods proposed by Leventon et al. (2000) and Tsai et al. (2003) participate in a comparison with the proposed method.

A validation experiment of the implementation of both Leventon's and Tsai's methods is presented by figure 5.7 and figure 5.8 following the work of Bresson et al. (2006). It can be observed from both figures that the ellipse in the synthesized image is accurately segmented by both methods in the presence of occlusion, achieving $E_{R1} = 0.99$ for both methods.

The first type of occlusion is inspired by Tsai et al. (2003). A cluster of solid lines puncture through the ROIs, causing several parts of the boundaries missing. Figure 5.9

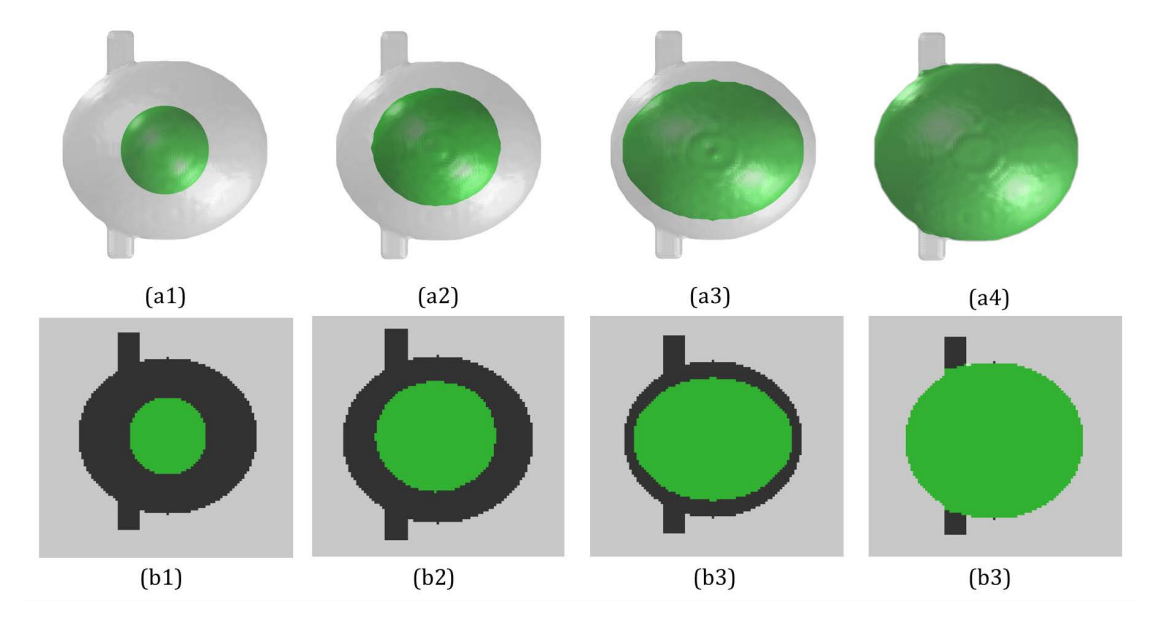


Figure 5.7: The segmentation process of a synthesized ellipse image using Leventon's method ($E_{R1} = 0.99$). The top and bottom rows are respectively the 3-D views and slice views.

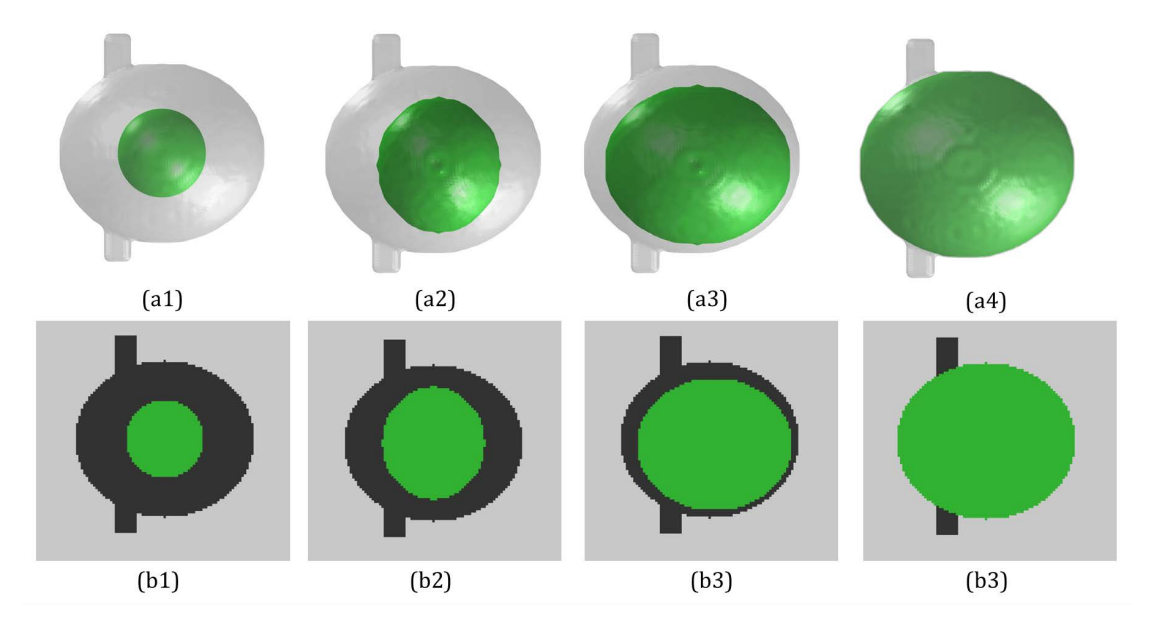


Figure 5.8: The segmentation process of a synthesized ellipse image using Tsai's method ($E_{R1} = 0.99$). The top and bottom rows are respectively the 3-D views and slice views.

presents the experiment with respect to this type of occlusion, which can also be considered as a leakage problem. A 3-D view of the image overlapped with initial surfaces for Leventon's, Tsai's and the proposed methods can be found in figure 5.9(a1). Figure 5.9(a2), (a3) and (a4) respectively present the results of these three methods. Corresponding typical slices are given in figure 5.9(b1)-(b4).

It can be observed from the figure that all three methods possess robustness against this

Experimental	E_{R1}	E_{D1}	No. of	Average time	Total
Data			iterations	of one iteration	time
Leventon's	0.94	1.68	15	6.95s	104.25s
Tsai's	0.85	1.95	5	31.31s	156.55s
Proposed	0.96	1.39	8	9.91s	79.28s

Table 5.2: A comparison concerning the accuracy and efficiency of Leventon's, Tsai's and the proposed methods for the first type of occlusion (corresponding to figure 5.9).

type of occlusion and none of them are largely affected by the line clusters. However, Tsai's method exhibits limitations of boundary accuracy mainly due to the fact that it employs no local adjustment mechanism, e.g. geodesic active surfaces. Leventon's method (figure 5.9(a2) and (b2)) produces similar result with the proposed method (figure 5.9(a4) and (b4)). Both methods present excellent boundary accuracy and the proposed method behaves a bit better at sharp corners. Nonetheless, both methods are slightly distorted by the line clusters by closely examining figure 5.9(b2) and (b4). A more detailed comparison with respect to accuracy and efficiency can be found in table 5.2.

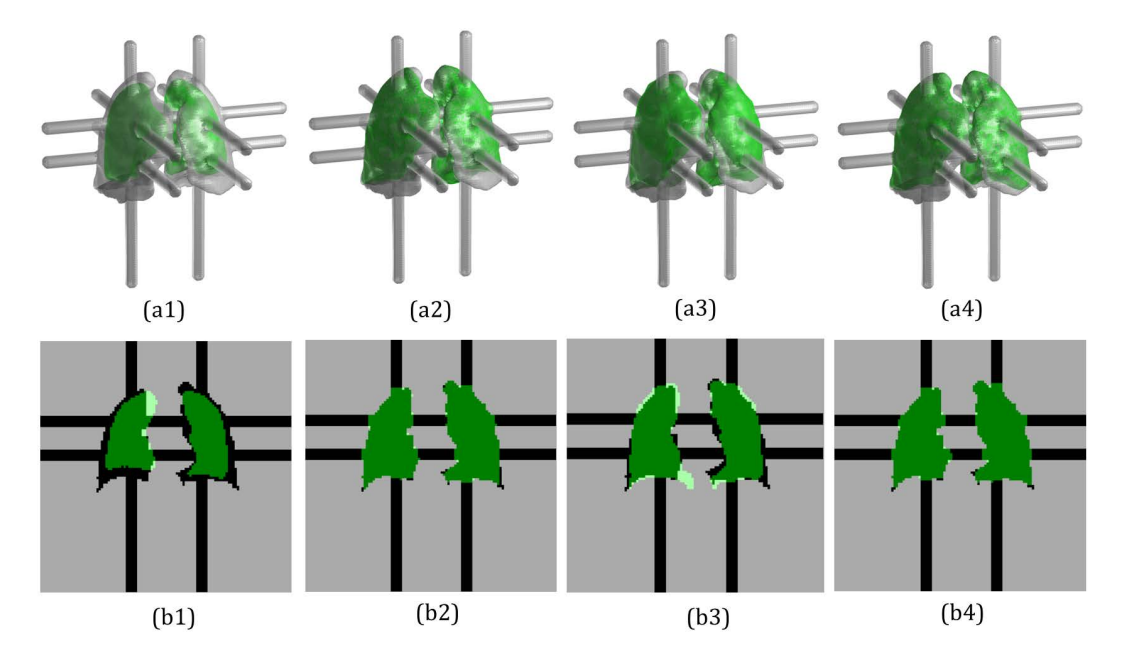


Figure 5.9: The segmentation of a synthetic image with the first type of occlusion (leakage) using Leventon's, Tsai's and the proposed method. (a1) The 3-D view of the original image overlapped with the initial surfaces for the three method. (a2) The segmentation result by Leventon's method. (a3) The segmentation result by Tsai's method. (a4) The segmentation result by the proposed method. (b1)-(b4) are typical slices corresponding to (a1)-(a4).

The second type of occlusion is to set the line clusters to the inverse intensities, as is shown in figure 5.10(a1). The initial surface is the same as the previous experiment and the results of the three methods are respectively given in figure 5.10(a2), (a3) and

(a4). Their typical slice views are demonstrated in figure 5.10(b1) to (b4). Again, these methods show their robustness against this type of occlusion with Tsai's method (figure 5.10(a2)) incapable of capturing accurate boundary, Leventon's and the proposed methods detected the boundary while slightly affected by the line cluster. Some experimental data of the three methods are provided in table 5.10 for a comparison.

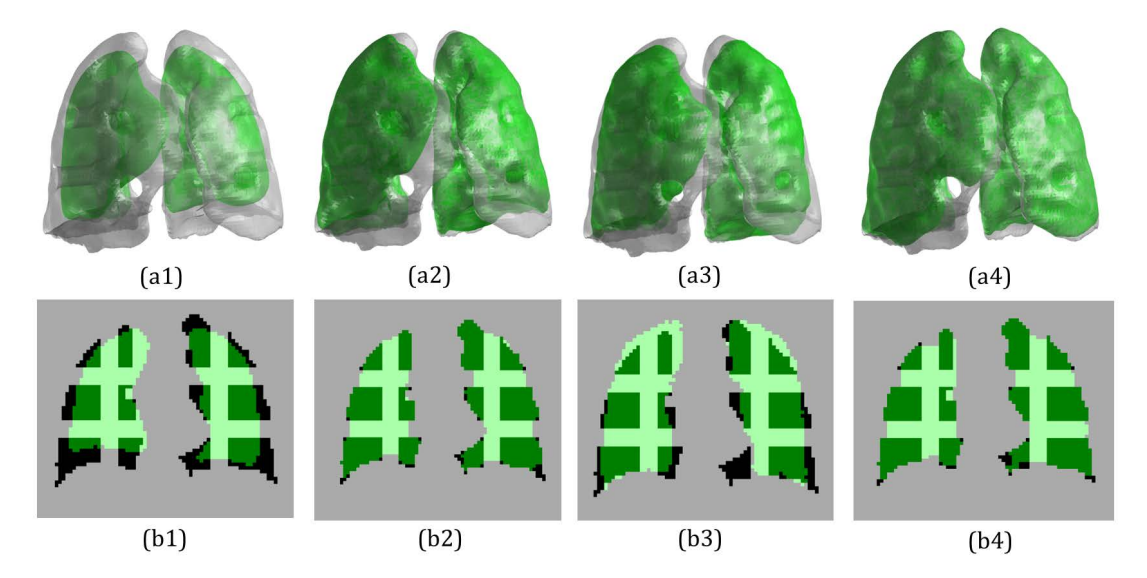


Figure 5.10: The segmentation of a synthetic image with the second type of occlusion using the three methods. (a1) The 3-D view of the image overlapped with the initial surfaces for the three methods. (a2) The segmentation result by Leventon's method. (a3) The segmentation result by Tsai's method. (a4) The segmentation result by the proposed method. (b1)-(b4) are typical slices corresponding to (a1)-(a4).

Experimental	E_{R1}	E_{D1}	No. of	Average time	Total
Data			iterations	of one iteration	time
Leventon's	0.93	1.88	17	6.21s	105.57s
Tsai's	0.82	2.13	6	31.26s	187.56s
Proposed	0.97	1.17	7	$9.97\mathrm{s}$	69.79s

Table 5.3: A comparison concerning the accuracy and the efficiency of Leventon's, Tsai's and the proposed methods for the second type of occlusion (corresponding to figure 5.10).

In summary, this section presents two types of occlusions and they are experimented with the proposed method along with two popular methods in the literature. In general, the experimental results indicates that shape-based segmentation methods are robust against occlusions. Tsai's method is based only on prior shape and region features of the image, therefore, in segmentation of shapes with large individual characteristics like lungs, it shows the limitation in achieving satisfactory boundary accuracy. Leventon's and the proposed methods produce better results and the distortions by the occlusions are controlled in an acceptable level.

Nevertheless, the experiment here shows a limited number of aspects of the occlusion problem. In this synthesized image, where the edges of regions are quite clear, Tsai's method exhibits disadvantages. However, in ultrasound images (experiments conducted by Tsai et al. (2003)), where the boundaries between regions are vague and the shape of region has less variations, the boundary information needs to be derived from the training set (the prior shape). The local detection of edges as in Leventon's and the proposed method may suffer large distortion.

5.5.4 Synthetic Images with Noise

This section presents the experiments on the segmentation of synthetic images with artificial noise. The image used here is same with that of the last section (section 5.5.3). The three methods namely, Leventon's, Tsai's and the proposed methods are to be performed on the image with an increasing level of Gaussian noise. The noise ranges from level 1 to 10 and more details about image noise information are given in the appendix A.

The first row of figure 5.11 are examples of images respectively contaminated by noise of level 1, 4, 7 and 10. The density of the white dots increases dramatically with the noise level, giving rise to large region and boundary ambiguities. The second to the fourth row are the corresponding results respectively produced by Leventon's, Tsai's and the proposed methods and they are overlapped with the ground truth. The increasing level of noise drives the results of these methods away from the accurate boundary, and blurs sharp corners of regions more than everywhere else. Therefore, observably the segmentation results in high level of noise lose thin boundaries of lungs.

The detailed results can be found in the plots presented by figure 5.12. It can be observed that all methods are affected by the noise. However, region feature enables Tsai's and the proposed methods to decrease with noise slower than Leventon's method. Most likely high levels of noise cause Leventon's method which only based on boundary information to fall into local minima. The proposed method takes advantage of both region and boundary features, therefore, it remains the most accurate among all three methods with respect to the two selected similarity measures, E_{R1} and E_{D1} . An efficiency comparison is provided by table 5.4.

Experimental	Average No.	Average time of	Average time for
Data	of iterations	one iteration	one segmentation
Leventon's	17.6	6.79s	119.50s
Tsai's	6.2	32.24s	199.88s
Proposed	7.1	10.84s	76.96s

Table 5.4: A comparison with respect to the efficiency of Leventon's, Tsai's and the proposed methods for the segmentation of noisy images (corresponding to figure 5.12).

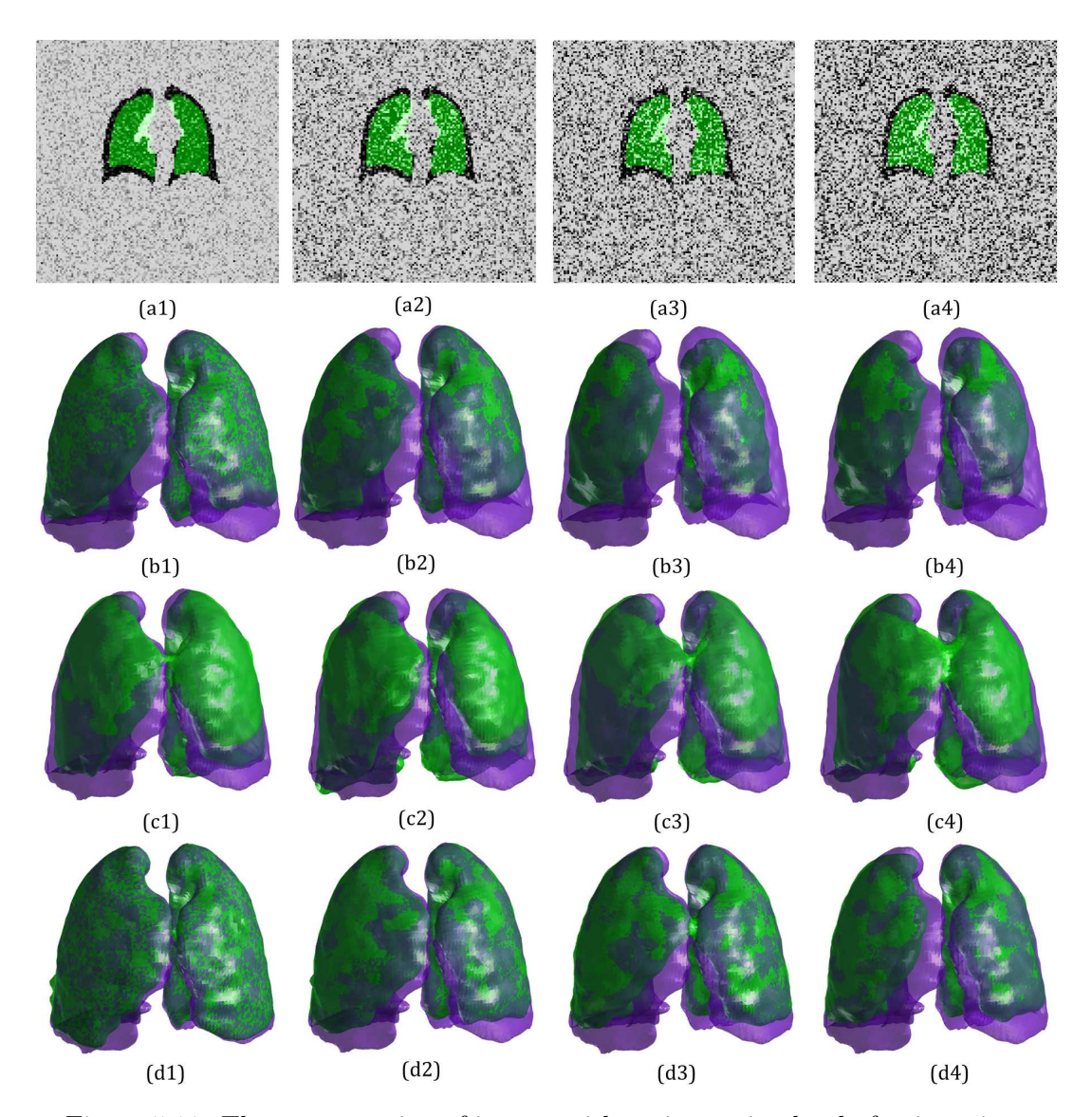


Figure 5.11: The segmentation of images with an increasing level of noise using the three methods. (a1)-(a4) are respectively the noisy images of level 1, 4, 7 and 10 with the initial surfaces overlapped. (b1)-(b4) are the 3-D views of the corresponding segmentation results by Leventon's method overlapped with the ground truth. (c1)-(c4) are the results by Tsai's method. (d1)-(d4) are the results by the proposed method.

In summary, this section presents the results of Leventon's, Tsai's and the proposed methods for segmentation of synthetic images with an increasing level of noise, from slight to severe. A slight amount of noise barely affects on all three methods. As the noise level increases to severe, the boundary-based method (Leventon's) falls into local minima, while the region-based methods (Tsai's and proposed) is capable of achieving good consistency. The proposed method stands out in this experiment due to its versatility of applying both region and boundary information.

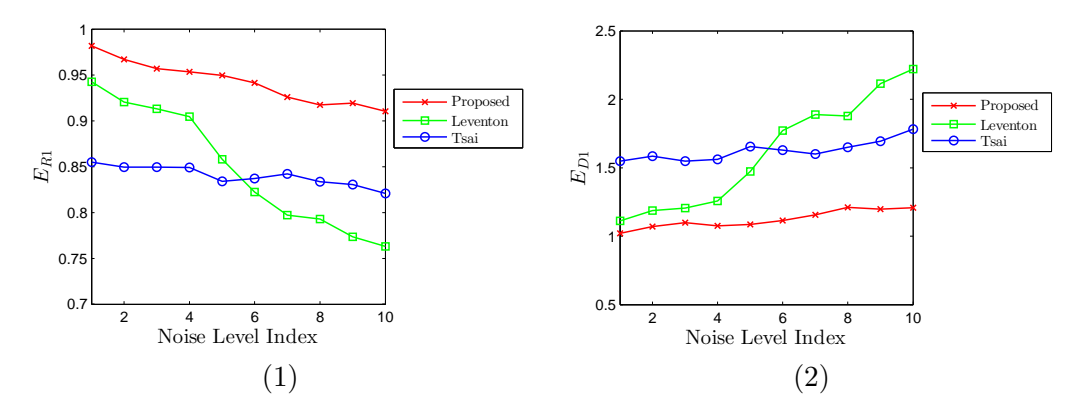


Figure 5.12: A quantitative evaluation of the three methods in segmentation of the images with increasing levels of noise using E_{R1} and E_{D1} (corresponding to figure 5.11).

5.5.5 Synthetic Images with Noise plus Occlusions

The proposed method in the previous sections delivers superior results and compensates for several drawbacks of previous method in segmentation of synthetic images with occlusions and noise respectively. It is interesting to further investigate how the proposed method behaves when the images are contaminated by noise plus occlusions. Therefore, this section focuses on this problem.

Figure 5.13(a1) to (a4) are examples of image slices with noise plus occlusions overlapped with the initial surfaces. The noise levels are same with those of figure 5.11 and the second type of occlusion shown in figure 5.10 is utilized here. Figure 5.13(b1) to (b4) are the corresponding results produced by the proposed method. It can be observed that the method achieves stable results under extreme conditions.

The plots shown in figure 5.14 present the full results of the experiment. They are compared with the results delivered by Leventon's and Tsai's methods. It can be observed that the proposed method presents more stable and accurate results than the previous two methods. This indicates even in simultaneous presence of noise and occlusions, the proposed method produces reliable results. As for efficiency, it takes 70-90 seconds from initial surfaces to achieve convergence.

In summary, this section presents an interesting experiment that further demonstrates the robustness of the proposed method. Under severe noise, the results produced by the proposed method barely change when occlusions are added. Nonetheless, the noise and occlusion types synthesized in this experiment do not cover the whole range of possible conditions and it can be improved by adding other types of noise and occlusions.

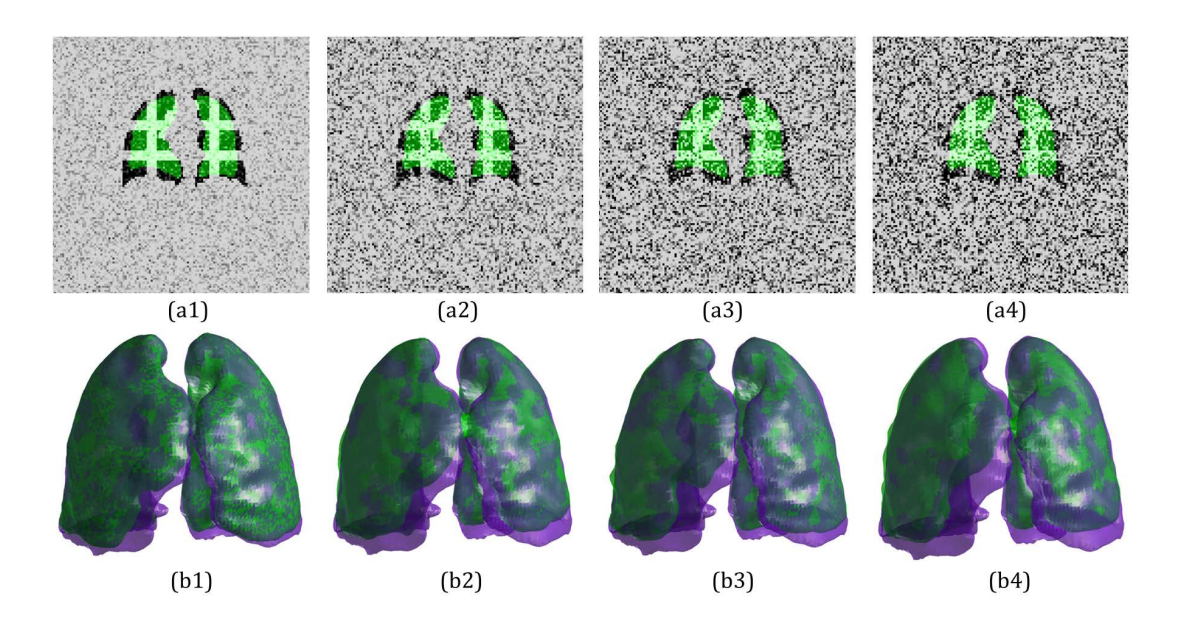


Figure 5.13: The segmentation of images with an increasing level of noise plus the second type of occlusion using the proposed method. (a1)-(a4) respectively correspond to noise level 1, 4, 7 and 10 with the initial surfaces overlapped. (b1)-(b4) are the 3-D views of the corresponding results overlapped with the ground truth.

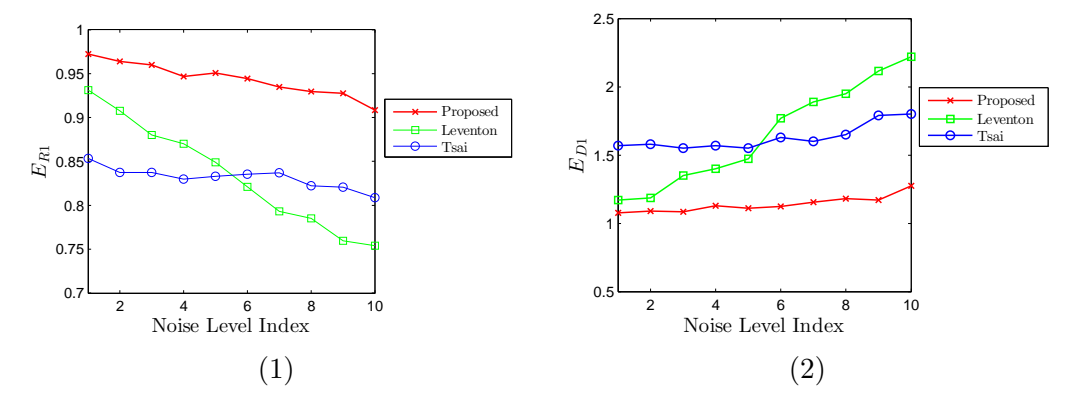


Figure 5.14: A quantitative comparison of the proposed method with Leventon's and Tsai's methods for the segmentation of the images with noise plus occlusion using E_{R1} and E_{D1} (corresponding to figure 5.13).

5.5.6 Low-dose CT Scans with Artificial Noise

In this section, the proposed method is to be tested on real CT data with manually added noise. Three cases from the database, namely case 3, 15 and 24 are selected to perform this experiment. As is discussed in section 4.4.1 that these cases are typical in terms of their shapes. Case 15 is quite average while case 3 and 24 represent two extreme conditions. Their large differences from average lungs presumably lead to difficulties in segmentation. The level of Gaussian noise ranges from level 1 to 10 and more about the noise information can be found in the appendix A. For cases with noise greater

than level 5, the parameter setting is changed to $\mu = 200$, $b_m = 1$, $b_s = 2$ (width of narrow band for lung modelling and active surfaces respectively). The initial surfaces remain consistent for each case and they are shown in figure 5.15. The convergence of the method is mostly achieved around 1.5 to 2 minutes.

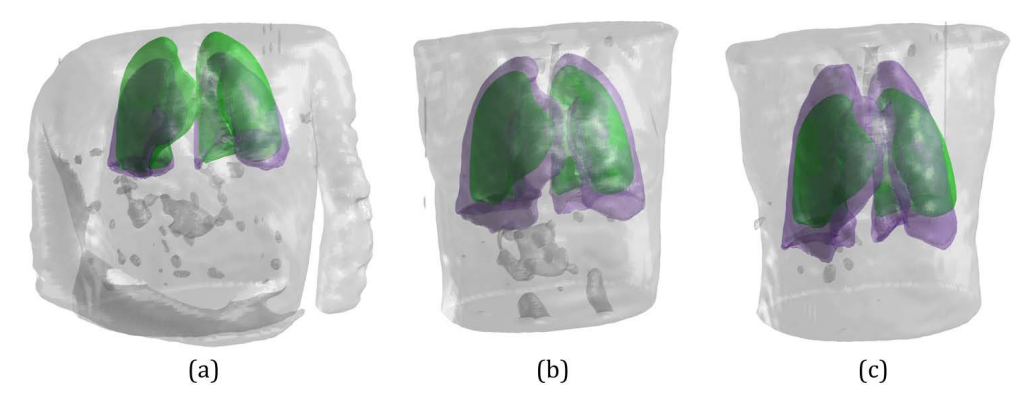


Figure 5.15: (a), (b) and (c) are respectively the initial surfaces (green) for the segmentation of case 3, 15 and 24 in the experiments of section 5.5.6 and 5.5.7, overlapped with the ground truth (purple) and raw surfaces of the bodies (grey).

Several examples of the segmentation of case 15 with increasing levels of noise are demonstrated by figure 5.16. It can be observed from the top row (the typical slice views) of the figure that the ROIs are gradually blurred in presence of noise. For noise of level 4, which is presented by figure 5.16(a2), the lungs are moderately observable, however, when the noise level increases to 7 and 10 (figure 5.16(a3) and (a4)), the lung regions almost disappear by observation. The bottom row presents the results of segmentation using the proposed method overlapped with the ground truth. The method produces smooth surfaces in lower levels of noise (figure 5.16(c1) and (c2)) and for higher levels of noise, the method is able to recover the majority of the region information (figure 5.16(c3) and (c4)).

Segmentation of case 3 is more challenging, for it is the most dissimilar with the average shapes. Several examples are presented by figure 5.17. Just like case 15, high levels of noise shown in figure 5.17 make the lung regions almost unobservable. The results overlapped with the ground truth in figure 5.17 (c3) and (c4) indicate the robustness of the method under these extreme conditions.

Another difficult case of segmentation is case 24 shown in figure 5.18. The left and right lungs of case 24 are slightly connected to each other and in presence of severe noise, which has a significant blurring effect, the front boundaries of left and right lungs merged into each other. Again, the method provides satisfactory results in low levels of noise, and stable results in high levels of noise.

Figure 5.19 shows the results of all three cases produced by the proposed method compared with Leventon's and Tsai's methods using E_{R1} and E_{D1} . The increasing severity

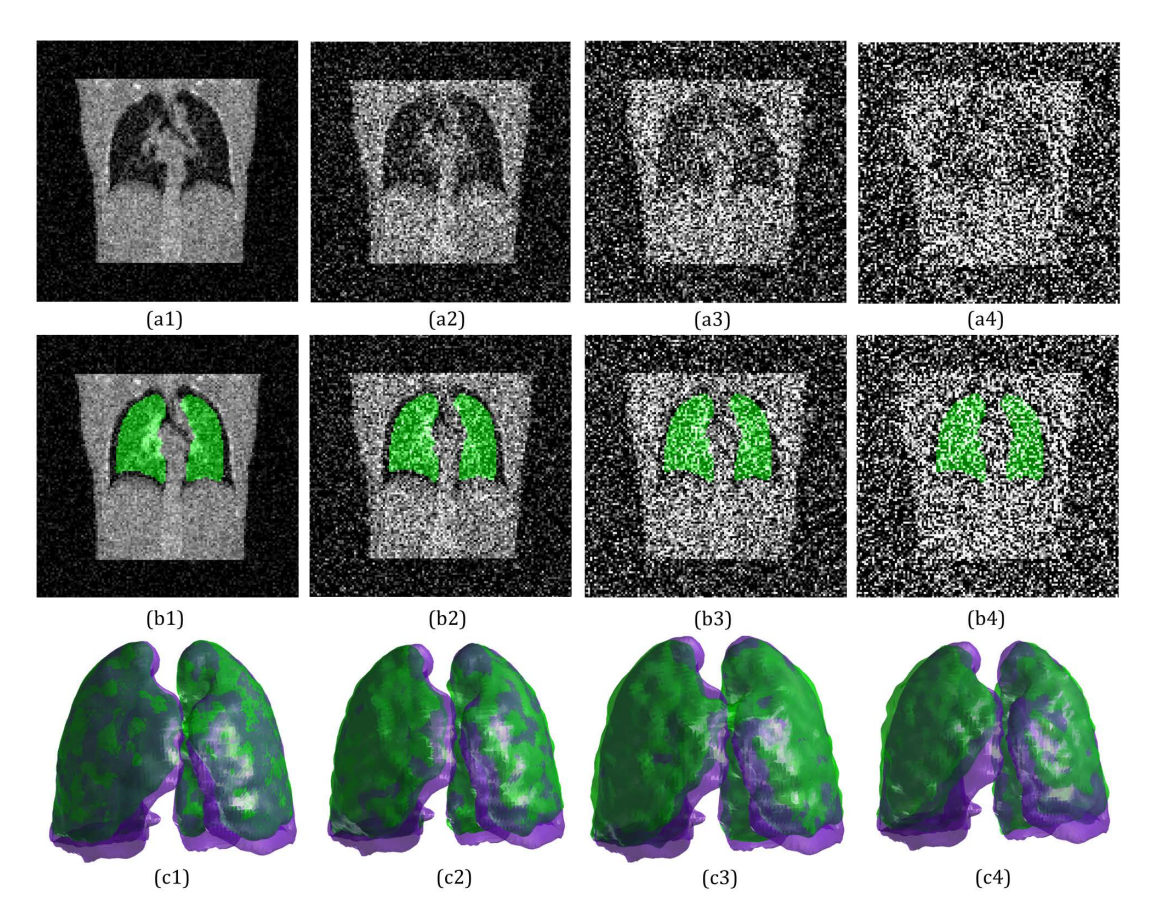


Figure 5.16: The segmentation of the low-dose CT image of case 15 from the database with an increasing level of noise using the proposed methods. (a1)-(a4) respectively correspond to noise level 1, 4, 7 and 10. (b1)-(b4) are the noisy images overlapped with the initial surfaces for segmentation. (c1)-(c4) are the 3-D views of the corresponding results overlapped with the ground truth.

of the noise drives the final surface away from the true surface due to major information loss, while the proposed method produces more accurate results than the two methods in the previous works on the whole.

In summary, this section demonstrates the segmentation of three typical cases selected from the low-dose CT database contaminated by increasing levels of noise. These cases range from normal to special, creating significant challenges of successful segmentation. The proposed method presents high stability under extreme conditions. Nevertheless, the experiment conducted here employed limited number of cases. More aspects of the method can be exhibited by wider range of cases and noise types.

5.5.7 Low-dose CT Scans with Synthetic Tumors

One of the interesting problems in thoracic CT scans is the segmentation of cancerous lungs in presence of large tumors. Real images with lung tumors are not available at hand, however, we can simulate several conditions of lung tumors in the recent work

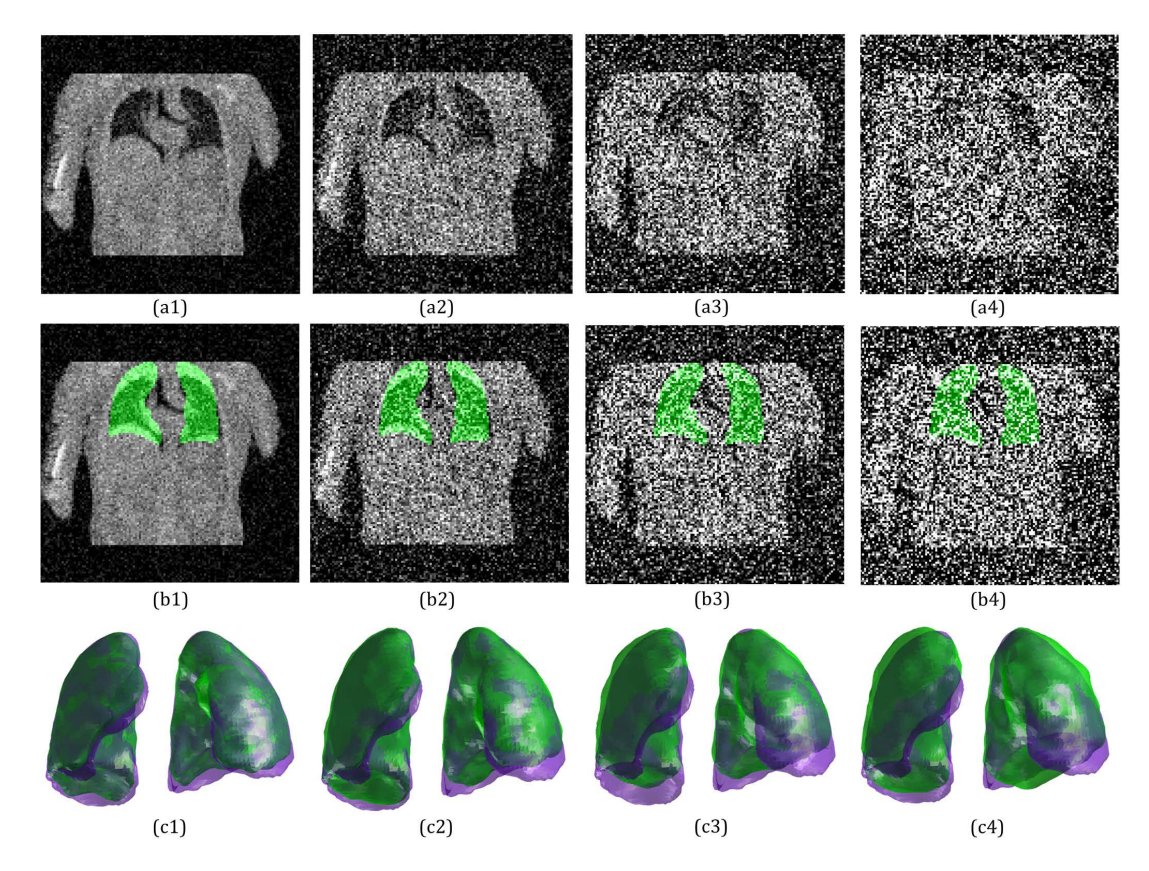


Figure 5.17: The segmentation of the low-dose CT image of case 3 with an increasing level of noise using the proposed methods. (a1)-(a4) respectively correspond to noise level 1, 4, 7 and 10. (b1)-(b4) are the noisy images overlapped with the initial surfaces for segmentation. (c1)-(c4) are the corresponding results overlapped with the ground truth.

of Sun et al. (2012). The average diameters of tumors involved in segmentation in their work are 38.8 mm (millimetre) and 53.0 mm for the left lungs and right lungs respectively. The segmentations are performed on HRCT (high resolution CT) scans of size $512 \times 512 \times 512$. The sizes of tumors are to be interpreted into voxel measurements. The average size of voxels reported by Sun et al. (2012) is 0.7mm $\times 0.7$ mm $\times 0.7$ mm, therefore, the average sizes of tumors are 56 and 76 voxels for the right and left lungs respectively. The general ratio between HRCT and low-dose CT used here is 6:1 (the $128 \times 128 \times 128$ resolution database is extended from $96 \times 96 \times 96$). Then the diameters of the synthetic tumors used in this experiment are 12 and 14 voxels for the left and right lungs respectively. The shape of synthetic tumor is consistently a sphere.

Case 3, 15 and 24 will also involve the experiment in this section. Case 3 has lungs of relatively small volumes, therefore, 5 locations of tumors are selected for the right and left lung respectively. Case 15 and 24 have larger volumes, therefore, 10 locations are selected for the right and left lungs respectively. The principle is to ensure the locations of synthetic tumors general cover the whole regions of lungs. The intensity is set to

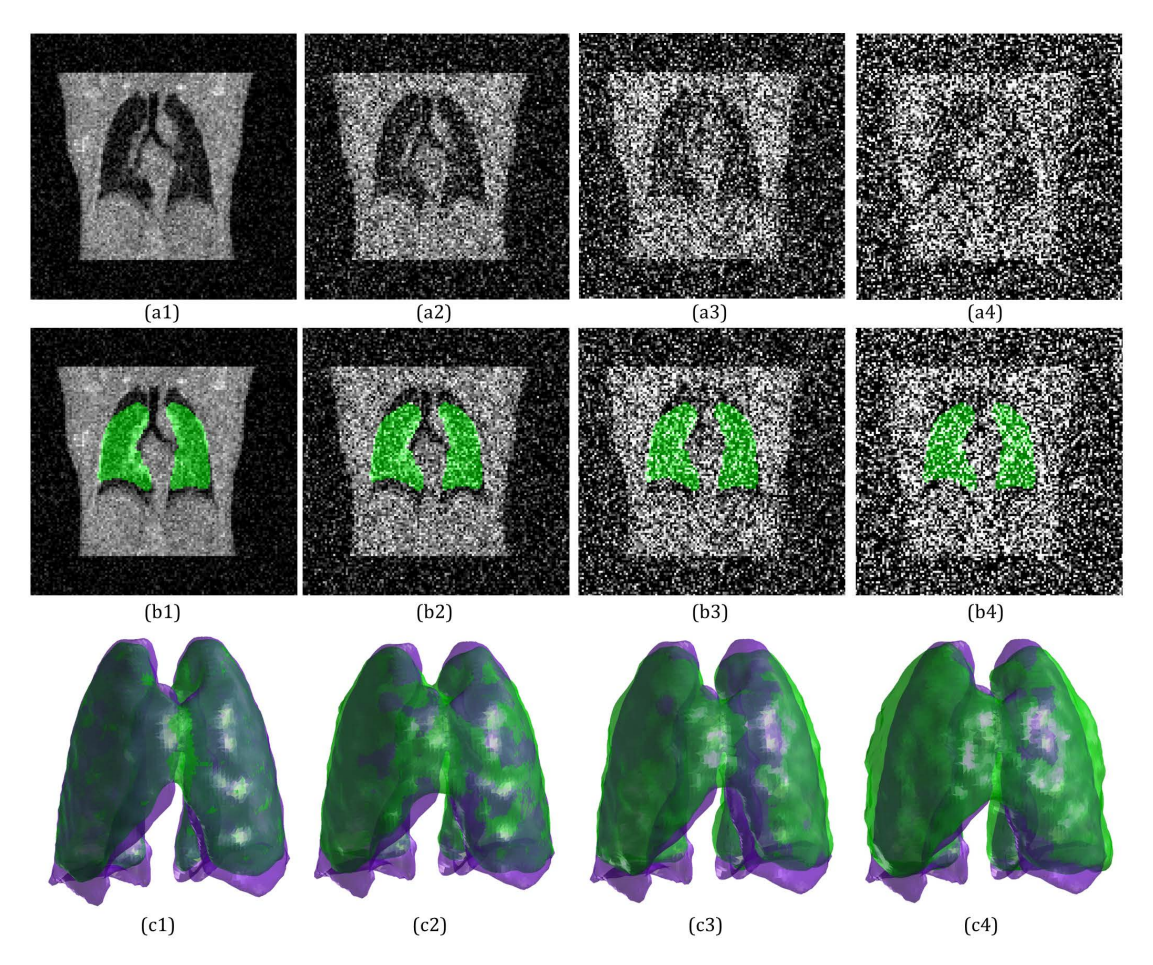


Figure 5.18: The segmentation of the low-dose CT image of case 24 with an increasing level of noise using the proposed methods. (a1)-(a4) respectively correspond to noise level 1, 4, 7 and 10. (b1)-(b4) are the noisy images overlapped with the initial surfaces for segmentation. (c1)-(c4) are the corresponding results overlapped with the ground truth.

a consistent value, 1100, which is as bright as the blood vessels. The number of low-dose CT images with tumor is in total 50. The same initial surfaces are used here as section 5.5.6 (shown in figure 5.15). The time consumed for convergence of each case ranges from 40 to 70 seconds.

Furthermore, the experiment presented in this section involves only single lung segmentation. The lungs with tumors are the regions of the most interest. In previous sections, simultaneous segmentation of lungs has been extensively demonstrated, therefore, this section focuses more on the practical use of the proposed method.

Figure 5.20 provides all the locations selected for each case. The left lungs are shown in the top row and the right lungs in the bottom row. It can be observed that the selected locations almost cover the whole area of the lungs.

Figure 5.21 provides a comparison of Leventon's, Tsai's and the proposed method. It is shown in the figure that Leventon's and Tsai's methods fail to produce satisfactory

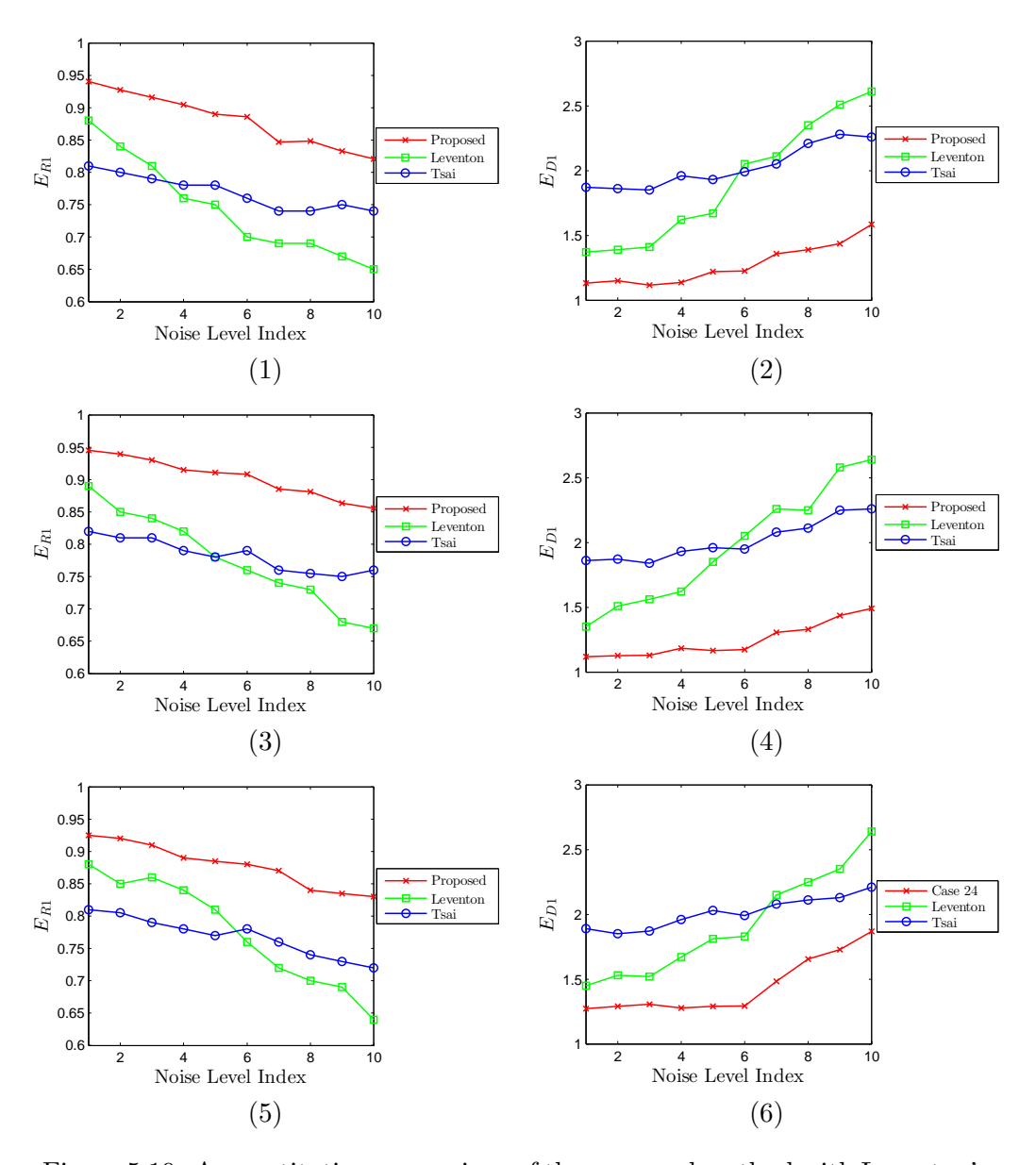


Figure 5.19: A quantitative comparison of the proposed method with Leventon's and Tsar's methods for the segmentation of the low-dose CT images using E_{R1} and E_{D1} (corresponding to figure 5.16, 5.17 and 5.18). The top, middle and the bottom rows are respectively case 3, 15 and 24.

results. The reason is that, as discussed in section 5.5.4, Leventon's method has the tendency to fall into local minima in the presence of noise and Tsai's method has no local boundary detection mechanism. However, they are not observably affected by the occlusion caused by the tumor. The proposed method following a hierarchical scheme, achieves an accurate segmentation in the presence of the tumor.

Several slice views of the segmentation of case 3 can be found in figure 5.22. The diameter of synthetic tumor is quite large and in figure 5.22(a1) and (a2), the synthetic tumors merge a little with the boundaries. The results are overlapped with the slices in figure 5.22(b1)-(b4).

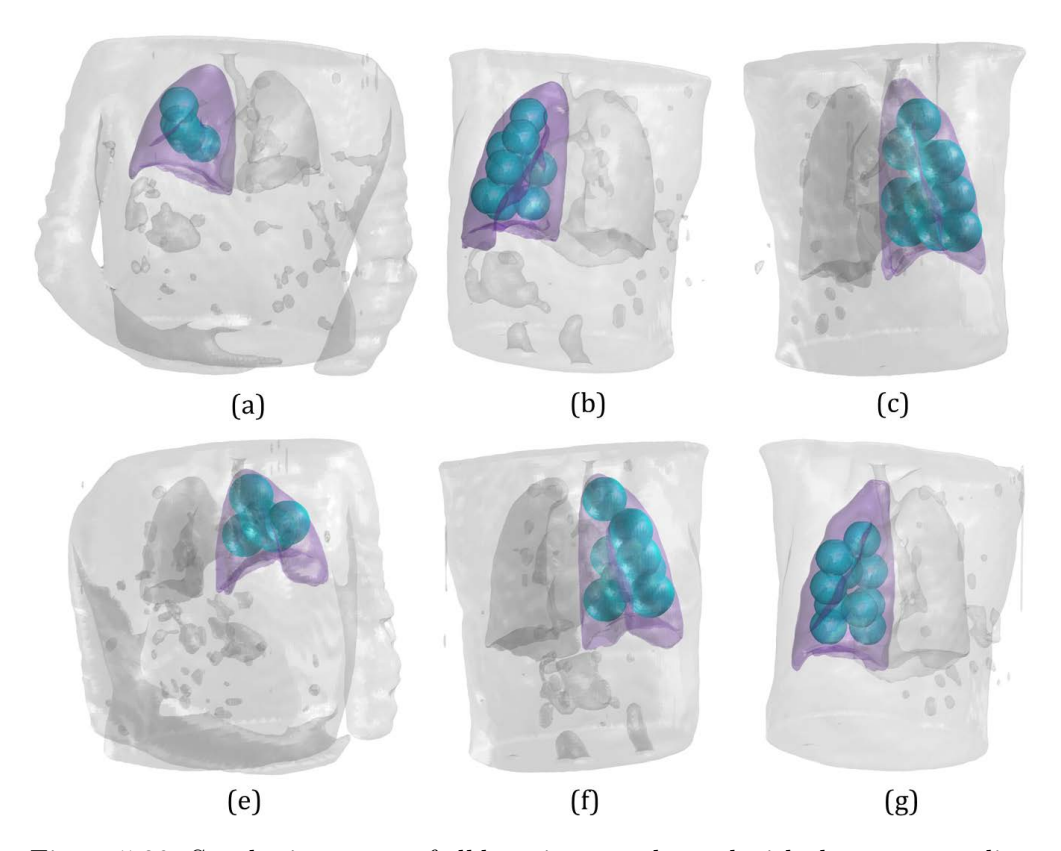


Figure 5.20: Synthetic tumors of all locations overlapped with the corresponding lungs. (a) and (e) are respectively the left and the right lungs from case 3; (b) and (f) from case 15; (c) and (g) from case 24.

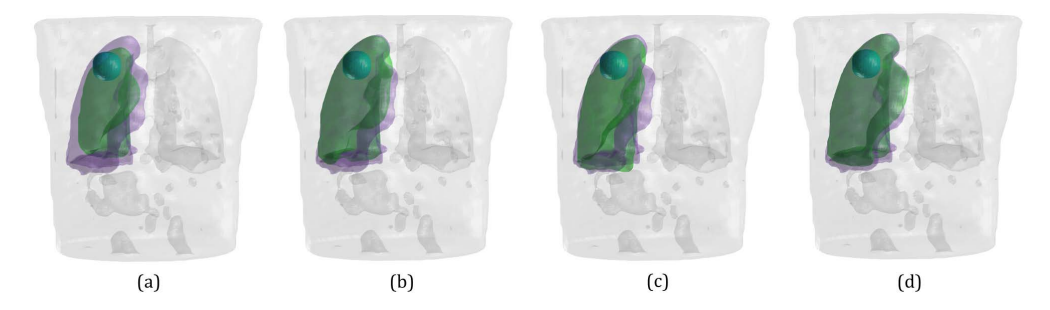


Figure 5.21: A comparison of Leventon's, Tsai's and the proposed method for the segmentation of the left lung with a synthetic tumor from case 15. (a) The overlapping of the initial surface (green), the ground truth (purple), the emphasized tumor (cyan) and the raw surfaces of the body (grey). (b), (c) and (d) are respective the results produced by Leventon's, Tsai's and the proposed methods.

Figure 5.23 presents all the results of segmentation performed on case 3. Due to the fact only 10 conditions of tumors are selected for case 3, the results are plotted separately from case 15 and 24. Both for left and right lungs, the results remain stable and are not affected by the presence of the large synthetic tumors.

Several examples of the segmentation results of case 15 for the left and right lungs can be found respectively in figure 5.24 and 5.25. The typical locations of tumors are presented

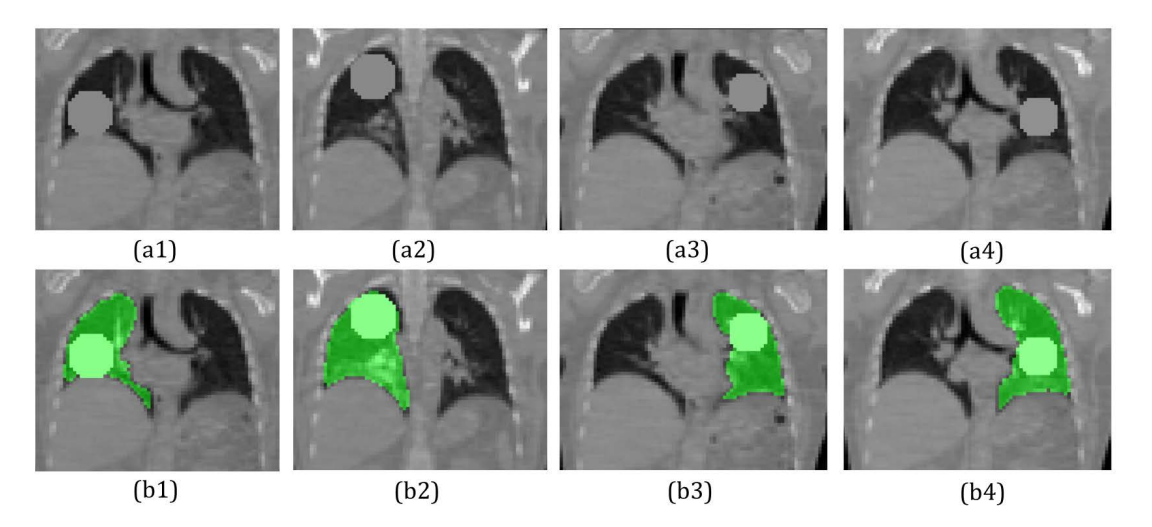


Figure 5.22: Several examples of the segmentation for case 3 with synthetic tumors viewed from typical slices. (a1)-(a4) are several selected conditions of tumor. (b1)-(b4) are the corresponding results of segmentation.

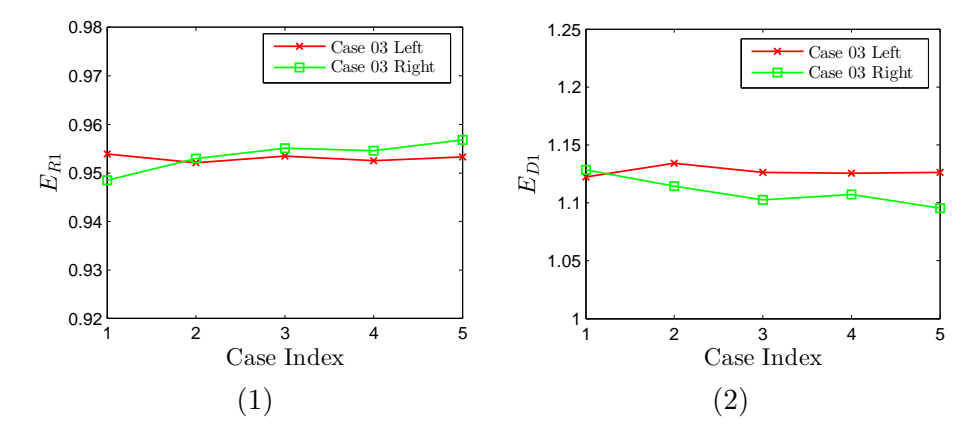


Figure 5.23: A quantitative evaluation of the proposed method in segmentation of case 3 with synthetic tumors for both left and right lungs. The case indices of the left and right lungs respectively correspond to figure 5.20 (a) and (e).

and just as case 3, some tumors merges with boundaries.

Lastly for case 24, several tumor locations and their corresponding results are given in figure 5.26 and 5.27. Case 24 is tall and thin, the tumor of average diameter in certain cases as in figure 5.26(a2) and figure 5.27(b3) touches two side of lung boundaries.

Figure 5.28 shows the results of segmentation performed on case 15 and 24. The left and right lungs are plotted respectively for each case, therefore, 4 plots are generated. Observably the proposed method is not affected by the synthetic tumors of all locations that cover the whole regions of lungs.

In summary, this section presents the segmentation of a low-dose CT database of synthetic tumors. The tumors are synthesized in accordance with recent experiments found in the literature (Sun et al., 2012). The locations of synthetic tumors are manually

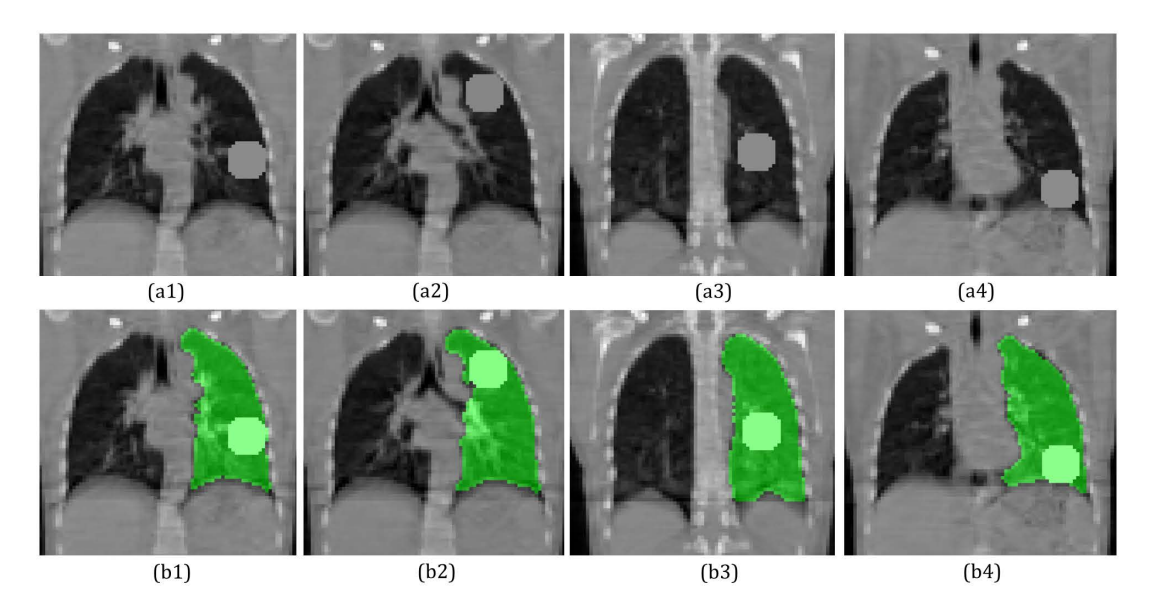


Figure 5.24: Several examples of segmentation for the left lungs of case 15 with synthetic tumors viewed from typical slices. (a1)-(a4) are several selected conditions of tumor. (b1)-(b4) are the corresponding results of segmentation.

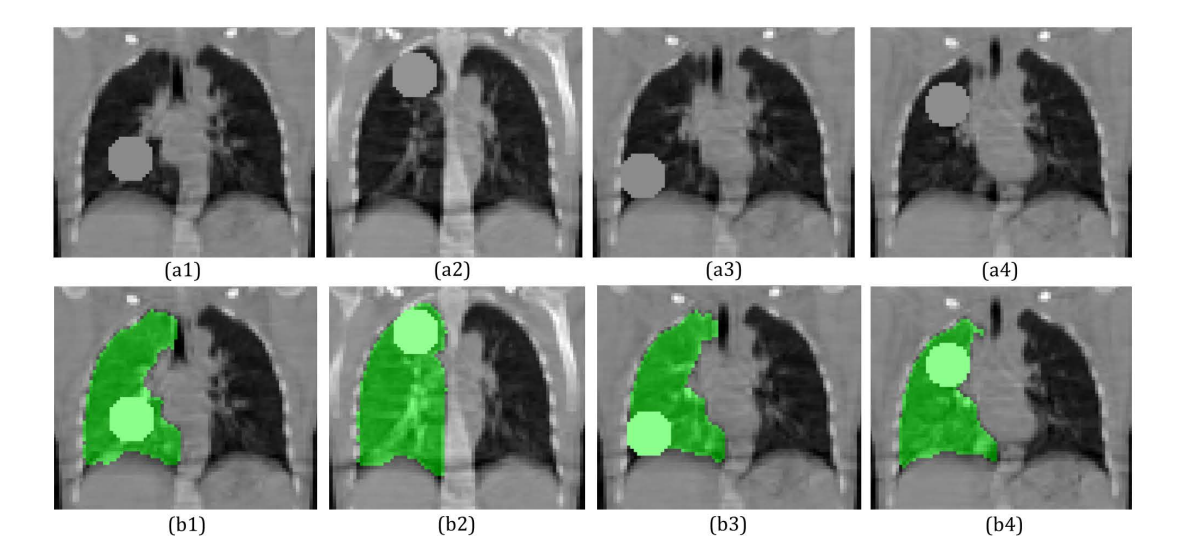


Figure 5.25: Several examples of segmentation for the right lungs of case 15 with synthetic tumors viewed from typical slices. (a1)-(a4) are several selected conditions of tumor. (b1)-(b4) are the corresponding results of segmentation.

selected on typical cases and cover almost the whole regions of lungs. Satisfactory results are produced in this experiment. Notwithstanding, the synthetic database is not as reliable as real database. The experiment will be further improved as long as sources of database of lung cancer are available.

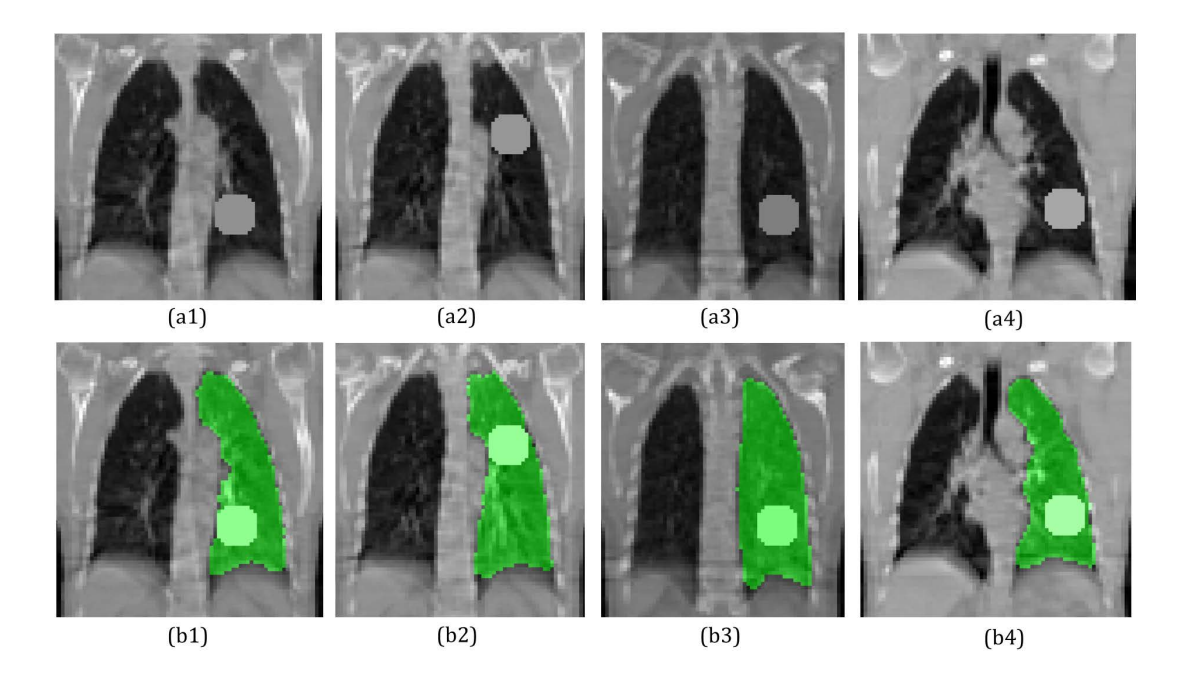


Figure 5.26: Several examples of segmentation for the left lungs of case 24 with synthetic tumors viewed from typical slices. (a1)-(a4) are several selected conditions of tumors. (b1)-(b4) are the corresponding results of segmentation.

5.5.8 A Database of Low-dose CT Scans

An application of the proposed method to the real world problem is demonstrated in this section, i.e. the segmentation of lungs from a low-dose thoracic CT scan database. The segmentation is performed on all three classes of lungs, namely the left, right and two lungs simultaneously.

Following the three intended conditions of use, an initialization scheme for the proposed method is designed specifically for the database according to the features of the low-dose CT scans. The CT images of the database typically consist of a black background, an individual body and inside the body are the lung regions to be extracted. The initialization scheme is then formulated as follows:

- Step 1: Extract the mask image of the individual body. The background is a connected and the darkest region outside body, therefore, the image is thresholded by a value of 200 and morphologically smoothed (erosion and then dilation). Then the largest connected region is detected and thus the mask image of body is found automatically inside the image.
- Step 2: Extract the raw regions of the lungs. The image is thresholded by 500 and the acquired mask merged with the body mask by an 'AND' operation. A noisy version of the lung regions along with certain small regions from other organs is thereby obtained.

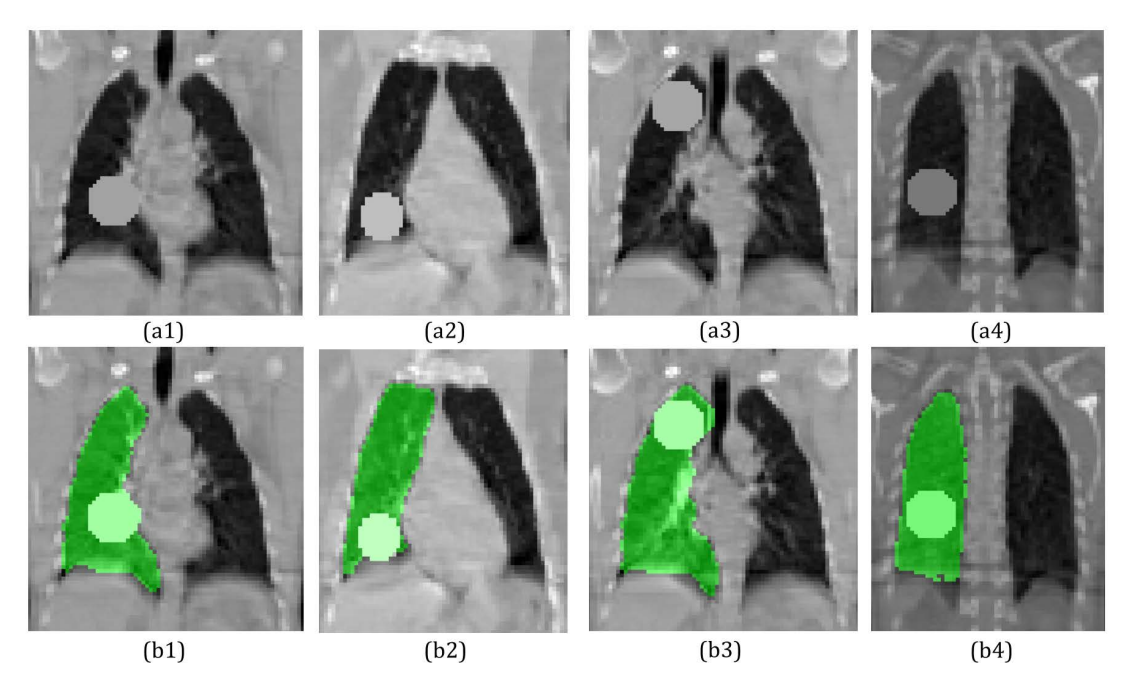


Figure 5.27: Several examples of segmentation for the right lungs of case 24 with synthetic tumors viewed from typical slices. (a1)-(a4) are several selected conditions of tumor. (b1)-(b4) are the corresponding results of segmentation.

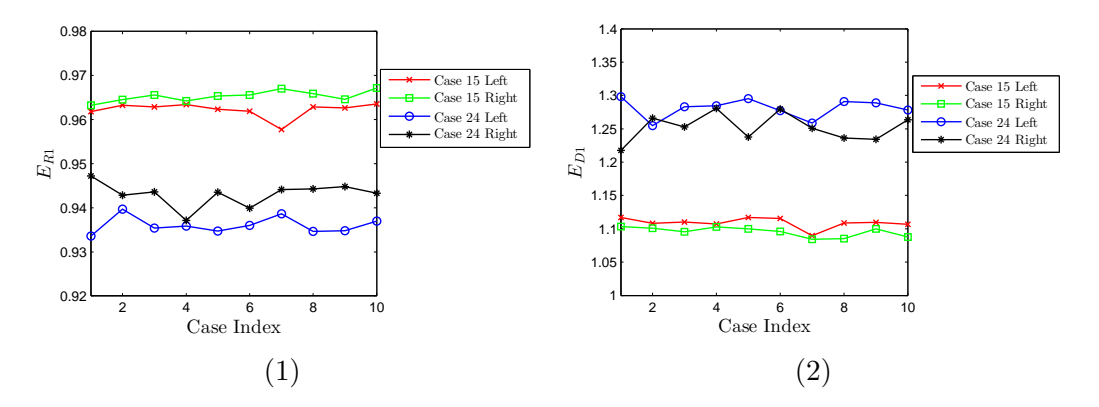


Figure 5.28: A quantitative evaluation of the proposed method for the segmentation of case 15 and 24 with synthetic tumors for both left and right lungs. The case indices of the left and right lungs of case 15 and 24 respectively correspond to figure 5.20 (b), (f), (c) and (g).

Step 3: Register the average lungs obtained from the trainings set to the lung regions obtained from step 2 with respect to translation. The registration technique introduced in chapter 3 is applied in this step. For single lung segmentation (left or right), the average lungs are labelled respectively as the left and the right lungs. They are also eroded by a distance of 2 voxels. The main purpose is to ensure that the starting point of the proposed segmentation method has a major overlap with the lung regions.

This scheme employs the simplest techniques in general image processing and it provides

the intended initial conditions for all the cases in the database. A graphical description is shown in figure 5.29. With these initial conditions, the proposed segmentation method is performed on the database. The time taken to convergence from these initial surfaces for single lung segmentation (left and right) ranges from 40 to 70 seconds, and for the simultaneous segmentation of two lungs, 60 to 100 seconds.

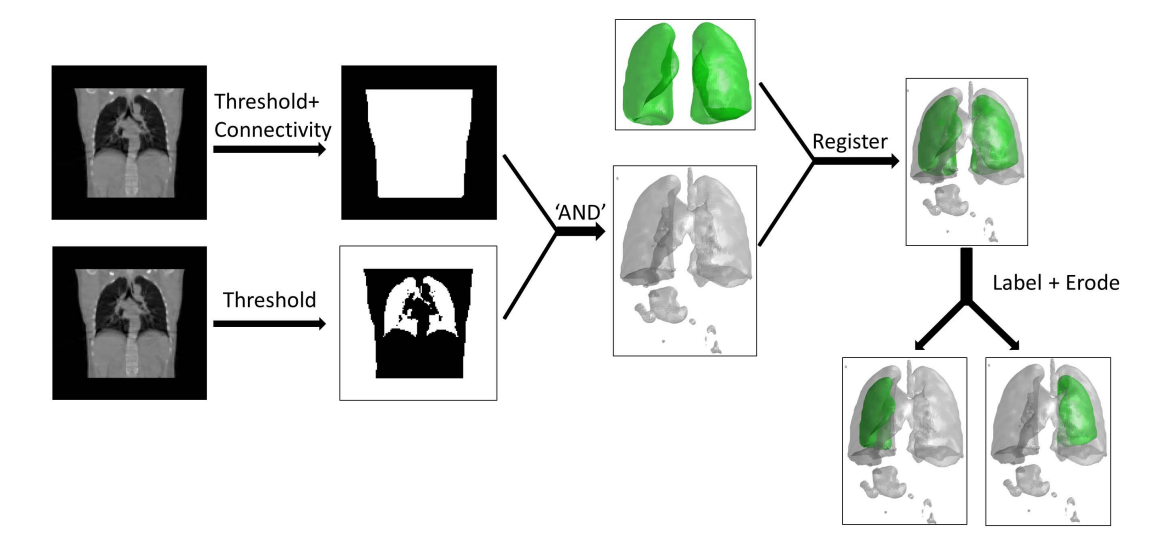


Figure 5.29: A graphical version of the initialization scheme for the segmentation of the low-dose CT database.

A comparison of Leventon's, Tsai's and the proposed methods is given in figure 5.30. Just as previous sections, Leventon's and Tai's methods provide unsuccessful segmentation results while the proposed proposed method does. Additionally, the segmentation results given by IAS introduced in chapter 2 for case 3, 15 and 24 are presented in figure 5.31. It can be observed that IAS is unable to provide satisfactory results as airways are included in the final results.

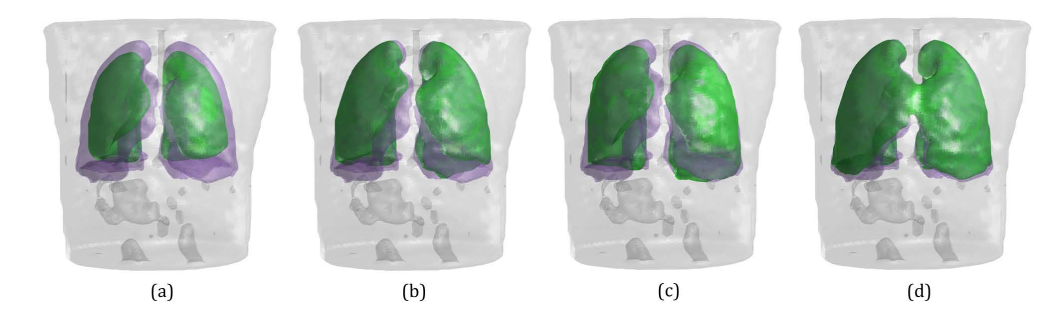


Figure 5.30: A comparison of Leventon's, Tsai's and the proposed method for the simultaneous segmentation of lungs from case 15 in the low-dose CT database. (a) The overlapping of the initial surface (green), the ground truth (purple) and the coarse surfaces of the body (grey). (b), (c) and (d) are respectively the results produced by Leventon's, Tsai's and the proposed methods.

Figure 5.32 presents the segmentation results of the low-dose CT database performed for the left, right and two lungs respectively. The proposed method on the whole produces

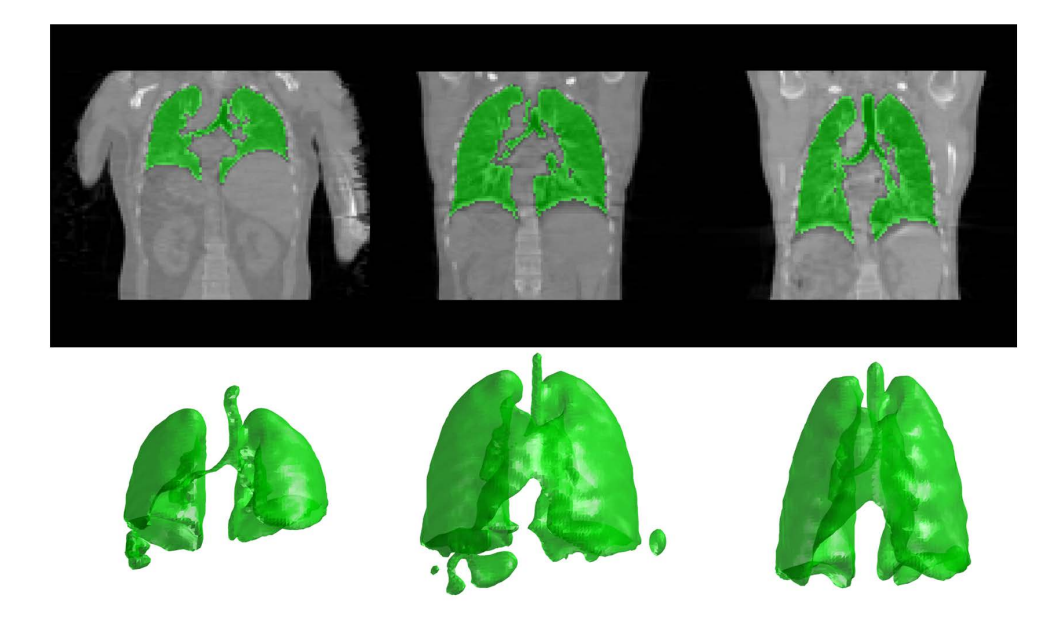


Figure 5.31: The segmentation results using IAS introduced in chapter 2 for case 3, 15 and 24. Top row from left to right are respectively the segmentation results of case 3, 15 and 24 viewed from typical slices. The bottom row are their corresponding 3-D views.

accurate and stable results. Due to the versatility of the database, certain cases exhibit lower similarity with the ground truth. These are most likely caused by the in accuracy in the modelling process. For certain rare cases, case 3 and 10 for instance, the individual shapes are largely different from the average as discussed in section 4.4.1.

Furthermore, it can be observed that the segmentation results of the right lungs are stabler than those of the left and two lungs simultaneously. This may well caused by the large variations of the left lungs as discussed in section 4.4.2.

A comparison of Leventon's, Tsai's and the proposed methods for the simultaneous segmentation of the left and the right lungs from the CT low-dose database is presented in figure 5.33. It can be observed that the proposed method achieves better results over the previous two methods.

In summary, this sections presents the segmentation of a low-dose CT scan database. It is a real world application and a specific initialization for the proposed method is given here to fully automate the segmentation process. The segmentation is performed on all three classes of lungs and the results indicate satisfactory accuracy and stability of the proposed method.

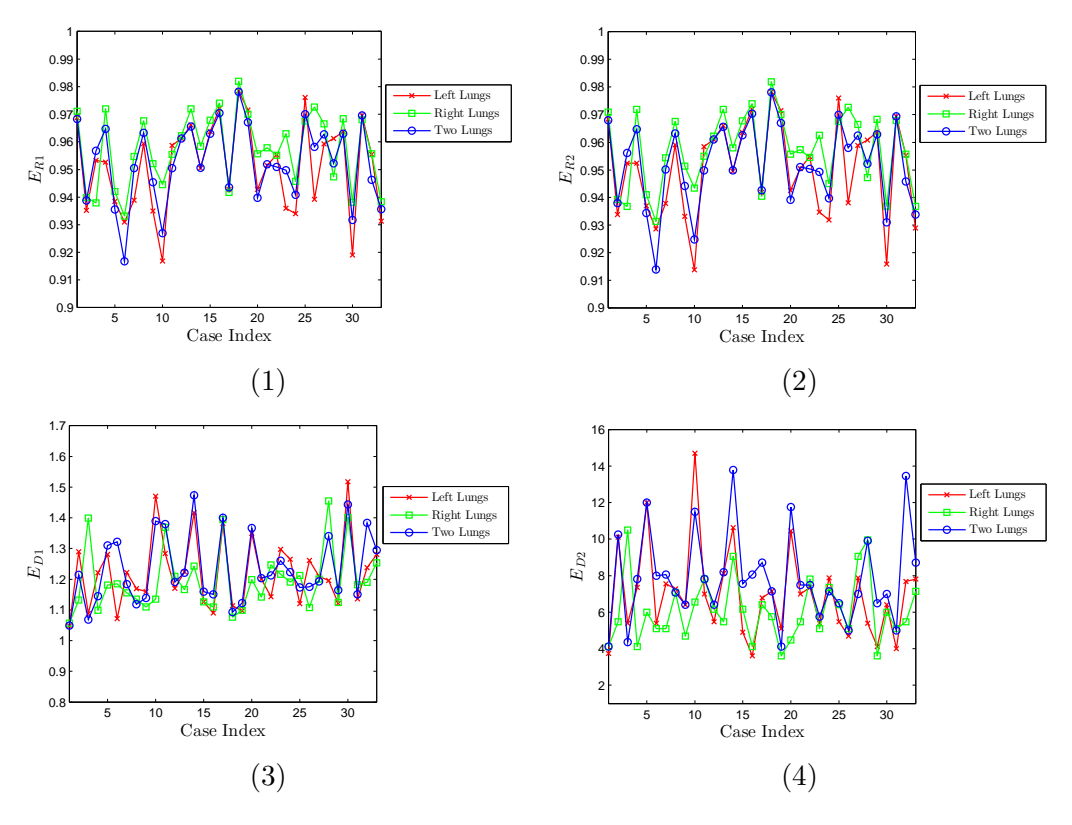


Figure 5.32: The quantified results of the proposed method measured by E_{R1} , E_{R2} , E_{D1} and E_{D2} for the segmentation of the low-dose CT database for the left, right and simultaneously two lungs.

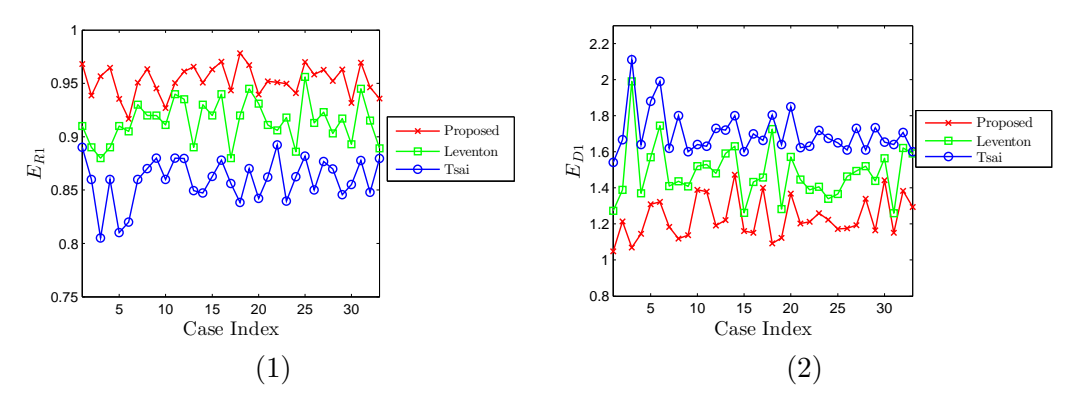


Figure 5.33: A comparison of Leventon's, Tsai's and the proposed methods for the segmentation of the two lungs simultaneously from the low-dose CT database using E_{R1} and E_{D1} .

5.6 Conclusions and Future Directions

This chapter based on the idea of Bresson et al. (2006), proposes a novel hierarchical segmentation method for the segmentation of lungs from volumetric CT images. This method is a combination of three models, which are active contours/surfaces, statistical shape modelling and similarity registration. With these models introduced in previous

chapters, this chapter puts major focus on the application of this method to volumetric images. The method employs a coarse-to-fine scheme which takes advantage of strong regions features, delicate boundary adjustments and prior shape restrictions.

An extensive amount of experiments are conducted to demonstrate the robustness of this method against noise and occlusions, including synthetic images and real world images of low-dose CT scans. Compared to previous methods introduced by Leventon et al. (2000) and Bresson et al. (2006) in the literature, the proposed method overcomes local minima and achieves satisfactory boundary accuracy. The implicit shape representation also enables the method to segment two lungs simultaneously. The method proposed here is also a suitable solution for general volumetric image segmentation in the presence of noise and occlusions.

Nevertheless, no methods are without disadvantages. The mechanism of the proposed method also involves an iterative process. Also, from the intended working conditions, the method requires a specific initialization scheme for the segmentation to be fully automated. This method in fact provides a local optimal solution to the prior-shape-based segmentation problem.

Regarding the future directions, first, the method should be applied to a database of lungs with cancer as well as fibrotic disease to test its suitability for this problem. Second, the method should be used to segment images of more shape classes. Several analyses are given on the lung class, however, it is always better to involve more shape classes to extend the scope of application of this method. Moreover, more types of noise, including salt & pepper noise, Poisson noise (shot noise), should participate in the test of robustness against noise. Last but not least, it is interesting to conduct phantom studies that quantitatively test the performance of the proposed segmentation method by gradually reducing the beam energy of the CT scanners.

Chapter 6

Shape-based Segmentation Aided by Texture Information

6.1 Inspirations and Introduction

Shape information is one of the prior knowledge that can be applied to the image segmentation. There exists another field of research that aims to model general image information, and that is texture. Compared to shapes which convey global region information, texture representation of images is derived from neighborhood pixels/voxels. The ROIs in images can be readily emphasized with well established models. As is introduced in the chapter 5, the shape-based segmentation technique requires a proper initialization to achieve an accurate segmentation result. In the segmentation of low-dose CT scans (section 5.5.8), an observation-based initialization scheme is designed specifically for this class of images by assuming the structures to be consistent, however, when the assumptions of the image structure are inapplicable, one needs to adapt more compensation schemes. The degree of automation is thus reduced.

In fact, this problem can be overcome by applying texture-based feature extraction methods when the interior voxel intensities follow a consistent pattern. This chapter introduces a supervised texture segmentation method which is used as a precursor to shape-based segmentation technique to improve the degree of automation in volumetric CT image segmentation. One only needs to understand interior region features without knowing the whole structures of the image.

Various styles of 2-D texture modelling exist in this active field of research, including the Gabor filtering (Jain and Farrokhnia, 1990; Paragios and Deriche, 2002; Sagiv et al., 2006), Fourier descriptors (Nixon and Aguado, 2008), Markov random fields (MRF) (Varma and Zisserman, 2003), local histograms (Hofmann et al., 1998), etc. The former two are based on filtering theory and the latter two statistical modelling.

Most popular among them is the Gabor filtering theory which models the texture through obtaining the responses from the selected filter banks. This process imitates human perception of texture structures and provides a rich source of information that gives rise to a satisfactory discrimination of textures (Han et al., 2011). However, the intrinsic drawbacks of the filter banks are that they involve a large amount of parameters to adjust, high computational cost (convolutions with the filters), and significant memory consumption.

Statistically-based modelling, e.g. MRF, is another powerful style of texture understanding. Varma and Zisserman (2003) proposed to apply MRF for classification purpose and by using rather a small number of parameters, the result of classification surpasses traditional filter banks. A special case of MRF, the Gaussian Markov random field (GMRF) enjoys a wide range of applications for its simplicity of parameter estimation (Rue and Held, 2004). GMRF is to be employed here for modelling of lung textures in volumetric CT images.

6.2 Previous Works

6.2.1 GMRF Texture Modelling

Chellappa and Chatterjee (1985) proposed the early idea of texture modelling using GMRF. The parameters calculated using least square estimation (LSE) are regarded as feature and then they are applied to the texture classification problem, achieving good accuracies. Later Krishnamachari and Chellappa (1997) employed GMRF for texture segmentation in a multi-resolution set-up of images. Two parameter estimation techniques are proposed, which are respectively based on Kullback-Leibler distance and local conditional distribution invariance. Segmentation results of synthetic texture and satellite images suggest the advantage of GMRF texture modelling with respect both accuracy and efficiency.

Following the works on classical GMRF, Descombes et al. (1999) introduced improved parameter estimation schemes based on LSE applied to a non-stationary framework and renormalization theory. The estimation schemes lead to successful segmentation of remote sensing data and are robust with respect to the sampling size of texture. Çesmeli and Wang (2001) instead of directly using GMRF model parameters as features, applied a 2-D array of locally excitatory globally inhibitory oscillator networks (LEGION) to the model parameters, enabling the homogeneous textures to synchronize and distinct textures to correspond to different phases. Other works on deriving texture features from GMRF parameters include Kim et al. (2006) who sought to model GMRF parameters using random spatial interaction (RSI) that is applied to the segmentation of synthetic

and real world images, and Zhao et al. (2007) who added weights to the GMRF parameters (pixels closer to the centre gain more importance) and achieved significant results on the classification of textures from QuickBird satellite images.

Until recently, Mahmoodi and Gunn (2011) combined variational model with GMRF texture feature extractions to achieve optimal segmentation of texture images using maximum likelihood estimation (MLE) of the parameters. Dharmagunawardhana et al. (2012) proposed to use local histograms of GMRF parameters as features for segmentation and later Dharmagunawardhana et al. (2014) applied isotropic GMRF, referred to as IGMRF, to discrimination of various types of lung textures (normal or diseased).

6.2.2 Volumetric Texture Modelling

Volumetric texture modelling approaches are not rich in the literature. The most likely reason is that volumetric textures are difficult to obtain in the real world, which is unlike the 2-D case, where various sources of large databases are widely available for researchers to work on.

Early research on this idea is presented by Ranguelova and Quinn (1999). This work employs volumetric GMRF to model and synthesize textures, and then achieves supervised segmentations of both synthetic and the magnetic resonance (MR) images of brain ventricles. This 3-D based method shows superiorities over conventional 2-D method for slice by slice processing.

Another volumetric texture segmentation method is proposed by Aldasoro and Bhalerao (2007). This is a multi-resolution approach based on Fourier domain filtering and is also applied to both synthetic textural images and MR images of human knees, providing a starting point that facilitate further quantitative analyses such as cartilage extraction.

Xu et al. (2006) introduces a method for classification of lung tissues. It is an extension of adaptive multiple feature method (AMFM) to 3-D. The method is successful in recognition various classes of diseased lung tissues and exhibits greater discriminative power than the 2-D version of AMFM.

6.3 Mathematical Preliminaries

6.3.1 Markov Random Fields in Volumetric Images

Let $\Omega_D \in \mathbb{Z}^3$ be a 3-D bounded discrete image domain and the neighborhood of a voxel $\mathbf{i} \in \Omega_D$ can be defined as a set $\mathcal{N}_{\mathbf{i}}$ that satisfies:

$$\mathcal{N}_{\mathbf{i}} = \{ \mathbf{i}' \in \Omega_D | d(\mathbf{i}', \mathbf{i}) \le \sqrt{3}r, \mathbf{i}' \ne \mathbf{i} \}$$
(6.1)

where $d(\mathbf{i}', \mathbf{i})$ denotes the distance between two voxels and r is an positive integer. Here, it is assumed that $\mathcal{N}_{\mathbf{i}}$ is a cube that contains a total number of $N = (2r+1)^3 - 1$ voxels. It can be noticed that N here is often an even number. An example of neighborhood system can be found in figure 6.1.

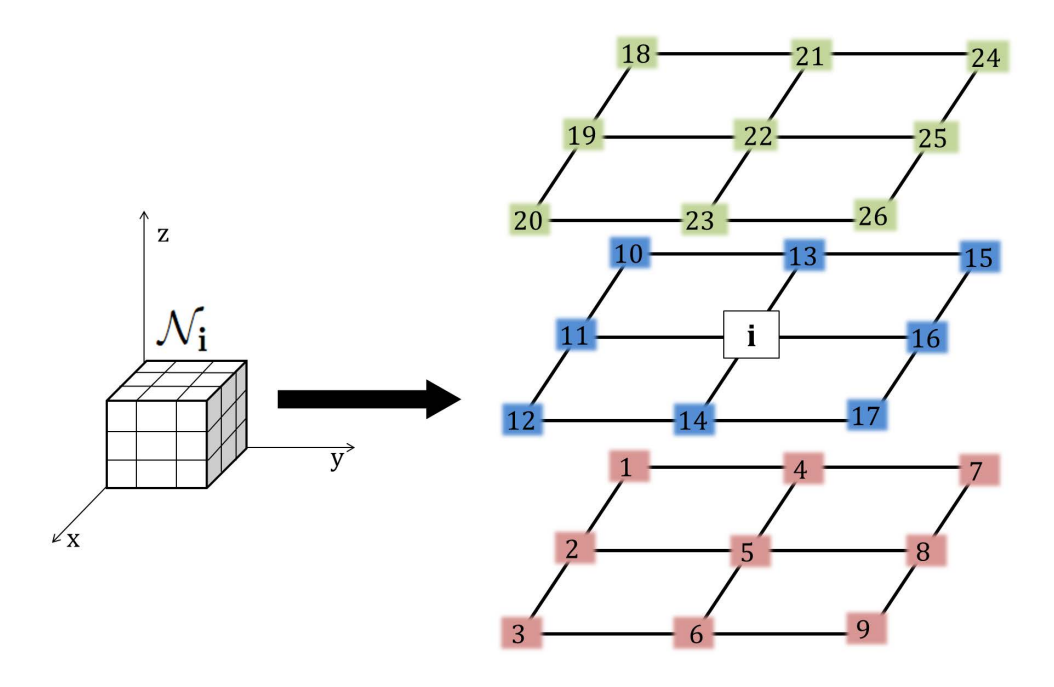


Figure 6.1: An example of the neighborhood system of voxel \mathbf{i} (r = 1, N = 26). The indexing through the neighborhood system follows a 'x-y-z' manner.

Let $X = \{X_{\mathbf{i}} | \mathbf{i} \in \Omega_D\}$ be a set of random variables and each $X_{\mathbf{i}}$ is mapped to a value (intensity) $I_{\mathbf{i}} \in \mathbb{R}^+$, then X here is a random field. $X_{\mathbf{i}} = I_{\mathbf{i}}$ denotes an event that $X_{\mathbf{i}}$ takes the value $I_{\mathbf{i}}$ and $\{X_{\mathbf{i}} = I_{\mathbf{i}} | \mathbf{i} \in \Omega_D\}$, abbreviated as X = I, the joint event. The probability of X to take the value I is represented by P(X = I), abbreviated as P(I).

X is referred to as a MRF (Markov random field) when it satisfies:

$$P(I_{\mathbf{i}}|I_{\Omega_D\setminus\mathbf{i}}) = P(I_{\mathbf{i}}|I_{\mathcal{N}_{\mathbf{i}}}) \tag{6.2}$$

where $\Omega_D \setminus \mathbf{i}$ is the set difference, which represents all the voxels in the image other than \mathbf{i} , and $I_{\mathcal{N}_{\mathbf{i}}}$ denotes the intensities of voxels in $\mathcal{N}_{\mathbf{i}}$. This equation indicates that the MRF assumes the intensity of a voxel is related only to those of its neighborhood voxels in $\mathcal{N}_{\mathbf{i}}$ and independent from every voxel else.

The assumption of MRF has wide applications in image texture modelling, which mainly studies local distribution of voxel intensities.

6.3.2 Conditional Gaussian-Markov Random Fields

One of the significant subclasses of MRF is the Gaussian-Markov random fields (GMRF). GMRF depicts image textures using a finite number of parameters in a linear manner. Using the notations introduced in the last section (section 6.3.1), the conditional probability density function (PDF) of local intensities is written as:

$$p_{\mathbf{w_i},\sigma_i}(I_i|I_{\mathcal{N}_i}) = \frac{1}{\sqrt{2\pi}\sigma_i} \exp\left(-\frac{(I_i - \mathbf{w_i}^T \vec{I}_{\mathcal{N}_i})^2}{2\sigma_i^2}\right)$$
(6.3)

where parameter $\mathbf{w_i} = (w_{\mathbf{i_1}}, w_{\mathbf{i_2}}, ..., w_{\mathbf{i_{N/2}}})^{\mathrm{T}}$ denotes the weights of the contributions by the corresponding neighborhood voxel intensities and the elements of vector $\vec{I}_{\mathcal{N}_{\mathbf{i}}} = (I_{\mathbf{i_1}} + I_{\mathbf{i_N}}, I_{\mathbf{i_2}} + I_{\mathbf{i_{N-1}}}, ..., I_{\mathbf{i_{N/2}}} + I_{\mathbf{i_{N/2+1}}})^{\mathrm{T}}$ correspond to that of $\mathbf{w_i}$. It can be noticed that the dimension of $\mathbf{w_i}$ is half of the neighborhood size of voxel \mathbf{i} . The reason is that the interaction parameters of voxels that are symmetric with respect to voxel \mathbf{i} are equal to each other (Li and Singh, 2009), i.e. $w_{\mathbf{i_{1+n}}} = w_{\mathbf{i_{N-n}}}$, where $0 \le n < N$.

Here $\mathbf{w_i}$ exhibits the parametrized relation between the selected voxel \mathbf{i} and its adjacent voxels $\{\mathbf{i}_i\}$, and the log-likelihood of $\mathbf{w_i}$:

$$\ln \mathcal{L}(\mathbf{w_i}, \sigma_i | I_{\mathcal{N}_i}) = \ln \prod_{i=1}^{N} p_{\mathbf{w_i}, \sigma_i}(I_{\mathbf{i}_i} | I_{\mathcal{N}_{\mathbf{i}_i}})$$

$$= \sum_{i=1}^{N} \ln p_{\mathbf{w_i}, \sigma_i}(I_{\mathbf{i}_i} | I_{\mathcal{N}_{\mathbf{i}_i}})$$
(6.4)

The maximum likelihood estimation (MLE) of parameter $\mathbf{w_i}$ and σ_i leads to minimizing $\ln \mathcal{L}$. The solution to this problem can be found by setting the derivatives of \mathcal{L} with respect to $\mathbf{w_i}$ and σ_i to zero, i.e. $\nabla_{\mathbf{w_i}} \mathcal{L} = 0$ and $\partial_{\sigma_i} \mathcal{L} = 0$. It is equivalent to least square estimation (LSE) and the parameters can be calculated using the following equations:

$$\mathbf{w_i} = \sum_{i=1}^{N} \left(\vec{I}_{\mathcal{N}_{\mathbf{i}_i}} \vec{I}_{\mathcal{N}_{\mathbf{i}_i}}^{\mathrm{T}} \right)^{-1} \sum_{i=1}^{N} \left(I_{\mathbf{i}_i} \vec{I}_{\mathcal{N}_{\mathbf{i}_i}} \right)$$
(6.5)

$$\sigma_{\mathbf{i}}^2 = \sum_{i=1}^N \left(I_{\mathbf{i}_i} - \vec{I}_{\mathcal{N}_{\mathbf{i}_i}}^{\mathrm{T}} \mathbf{w}_{\mathbf{i}} \right)^2$$
 (6.6)

Parameter $\mathbf{w_i}$ and σ_i can be considered as the representation of the voxel \mathbf{i} in GMRF. They are to be used to build texture features that discriminate inhomogeneous regions in the work of Dharmagunawardhana et al. (2012). However, considering the case when r = 1 in 3-D, smallest number of neighborhood voxel is 26, and later in the formulation of texture features, the number of dimension is going to increase to more than 10 times. This vastly exceeds the computational capacity of a normal workstation, therefore, a

simpler model proposed by Dharmagunawardhana et al. (2014) is employed here for 3-D case

Dharmagunawardhana et al. (2014) applied IGMRF (isotropic GMRF), which takes the following form:

$$p_{\mathbf{w_i},\sigma_i}(I_i|I_{\mathcal{N}_i}) = \frac{1}{\sqrt{2\pi}\sigma_i} \exp\left(-\frac{(I_i - \mathbf{w_i}\vec{I}_{\mathcal{N}_i})^2}{2\sigma_i^2}\right)$$
(6.7)

It can be noticed that the vector $\mathbf{w_i}$ is reduced to a scalar $\mathbf{w_i}$, which means that the neighborhood voxels in \mathcal{N}_i share a common parameter. This is a special case GMRF, also known as circular GMRF. LSE is employed here for parameter estimation. The residue in the sense of LSE is

$$\varepsilon_{\mathbf{i}} = I_{\mathbf{i}} - w_{\mathbf{i}} \vec{I}_{\mathcal{N}_{\mathbf{i}}} \tag{6.8}$$

We would like find a w_i that minimizes the residues of all voxels in the image domain:

$$\mathbf{w_{i}} = \underset{\mathbf{w_{i}}}{\operatorname{argmin}} \sum_{\mathbf{i} \in \Omega_{D}} \varepsilon_{\mathbf{i}}^{2}$$

$$= \sum_{\mathbf{i} \in \Omega_{D}} \left(I_{\mathbf{i}_{i}} - \mathbf{w_{i}} \vec{I}_{\mathcal{N}_{\mathbf{i}_{i}}} \right)^{2}$$
(6.9)

This is a simple quadratic equation and the solution can be found by setting the first order of its derivative to zero. Then w_i can be obtained by

$$\mathbf{w_i} = \frac{\sum_{\mathbf{i} \in \Omega_D} \left(I_{\mathbf{i}_i} \sum_{i=1}^N I_{\mathbf{i}_i} \right)}{\sum_{\mathbf{i} \in \Omega_D} \left(\sum_{i=1}^N I_{\mathbf{i}_i} \right)^2}$$
(6.10)

Then parameter σ_i is computed by the following equation:

$$\sigma_{\mathbf{i}} = \sqrt{\frac{1}{N} \sum_{\mathbf{i} \in \Omega_D} \left(I_{\mathbf{i}_i} - w_{\mathbf{i}} \sum_{i=1}^{N} I_{\mathbf{i}_i} \right)}$$
 (6.11)

The parameter estimation of this model is of less computational cost and it gives satisfactory results in discriminating diseased lung tissues from healthy ones. Therefore, IGMRF is to be applied to model lung texture. It is sufficient to extract regions of lungs from low-dose CT images, providing proper initializations for the shape-based segmentation technique introduced in chapter 5. This will be shown later in section 6.6.

6.4 The Texture Feature Formulation

The parameters (w_i and σ_i) of IGMRF can be regarded as an interpretation of the image information other than intensity values. It is intended that the formulated texture feature should be typical in representation of the corresponding texture class. The parameters themselves are not sufficient to play this role (Dharmagunawardhana et al., 2012, 2014), however, they can be arranged to fulfil this purpose.

Dharmagunawardhana et al. (2012) proposed a texture feature that employs the local distributions of $\mathbf{w_i}$ and σ_i . It is referred to as parameter local histogram (PL histogram). PL histogram exhibits outstanding discriminative power in texture classification. As is pointed out in the last section (section 6.3.2) that in 3-D case, the number of image voxels increases to hundreds of times larger, therefore, the smallest estimation window is to be employed in this work, which is the 26-neighborhood condition.

Let $\Omega_{D_l} = \{i, \mathcal{N}_i\}$ represent the local domain of 26 voxels that contains the neighborhood of voxel i, then the calculations of w_i and σ_i respectively becomes

$$\mathbf{w_{i}} = \frac{\sum_{\mathbf{i} \in \Omega_{D_{l}}} \left(I_{\mathbf{i}_{i}} \sum_{i=1}^{N} I_{\mathbf{i}_{i}} \right)}{\sum_{\mathbf{i} \in \Omega_{D_{l}}} \left(\sum_{i=1}^{N} I_{\mathbf{i}_{i}} \right)^{2}}$$

$$\sigma_{\mathbf{i}} = \sqrt{\frac{1}{N} \sum_{\mathbf{i} \in \Omega_{D_{l}}} \left(I_{\mathbf{i}_{i}} - \mathbf{w_{i}} \sum_{i=1}^{N} I_{\mathbf{i}_{i}} \right)}$$

$$(6.12)$$

$$\sigma_{\mathbf{i}} = \sqrt{\frac{1}{N} \sum_{\mathbf{i} \in \Omega_{D_l}} \left(I_{\mathbf{i}_i} - w_{\mathbf{i}} \sum_{i=1}^{N} I_{\mathbf{i}_i} \right)}$$

$$(6.13)$$

Each voxel in the image corresponds to a parameter vector $(\mathbf{w_i}, \sigma_i)^T$ and these two parameters give rise to two feature images. Local histograms on the local domain Ω_{D_l} are calculated and normalized respectively for the two parameters. It is suggested in the work of Dharmagunawardhana et al. (2014) and Sorensen et al. (2010) that the original information of the image, namely the intensity values to be employed in combination with the PL histograms to enhance the discriminative power. Therefore, the texture feature is formulated using the histograms both calculated according to the IGMRF parameters and intensity values. Each voxel corresponds to three histograms and they are put into one large vector $\hat{I}_{\mathbf{i}}$ (see figure 6.2). Thus, $\hat{I}_{\mathbf{i}}$ is used here as the feature vector for texture segmentation of volumetric images. Examples of typical texture patterns and their corresponding average PL histograms are demonstrated in figure 6.3.

6.5 The Probability Images for Segmentation

Sample patches from the lung regions are selected in the low-dose CT database to build up the training set of texture features for segmentation. The selection process takes

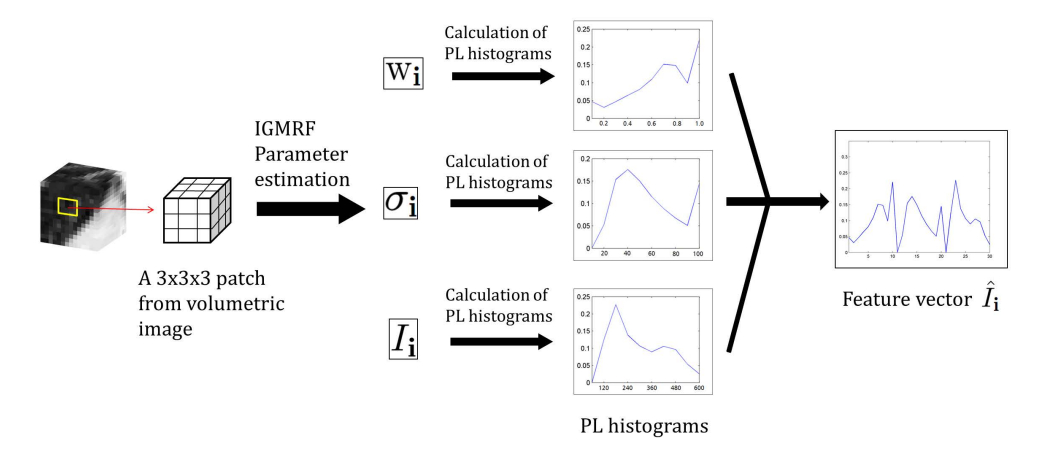


Figure 6.2: A graphical description of the texture feature formulation process.

advantage of the manually segmented mask images of lungs. When a $3 \times 3 \times 3$ moving window has a 100% overlap with the mask images, the patch in the window is stored and its corresponding PL histograms calculated. These PL histograms comprise the training set of texture features for the lung represented by $\hat{\mathbf{I}} = \{\hat{I}_i\}$.

With the established texture feature training set $\hat{\mathbf{I}}$, the probability of voxel \mathbf{i} belonging to the domain of the ROIs denoted by Ω_{ROI} can be calculated by the following equation:

$$P(\mathbf{i} \in \Omega_{ROI}|\hat{\mathbf{I}}) = \exp\left(-D(\hat{I}_{\mathbf{i}},\hat{\mathbf{I}})^k\right)$$
 (6.14)

where $D(\hat{I}_{\mathbf{i}}, \hat{\mathbf{I}})$ is the distance between $\hat{I}_{\mathbf{i}}$ and the nearest \hat{I}_{j} in the training set $\hat{\mathbf{I}}$. Each voxel corresponds to a distance value and these distance values constitute a distance image. The order k has the effect of enhancing the contrast of the posteriori probability and significantly reduce the effect of outliers. While this process can be considered as a soft classification (calculation of probabilities), the increase of k will gradually lead to a hard classification. The probability of each voxel to be inside the region of interest is calculated using equation 6.14 and thus, a probability image is generated corresponding to the image to be segmented. For representation convenience, $P(\mathbf{i} \in \Omega_{ROI}|\hat{\mathbf{I}})$ is simply written as $P_{\mathbf{i}}$. Figure 6.4 presents an example of the an original image, its distance and probability images. (See section 6.6 for more details.)

As is pointed out in section 6.1 that the role of the texture in this work is intended to increase the automation degree of image segmentation. The limitation of the method employed in section 5.5.8 is that it requires proper initialization schemes. A new type of prior knowledge is generated till this point and it can readily provide an appropriate starting point of the proposed segmentation method introduced in chapter 5. A sufficiently large k enables the probability image to reveal the ROIs. The probability images can thus generate reliable characteristic functions of the ROIs which can be used as initial surfaces for segmentation.

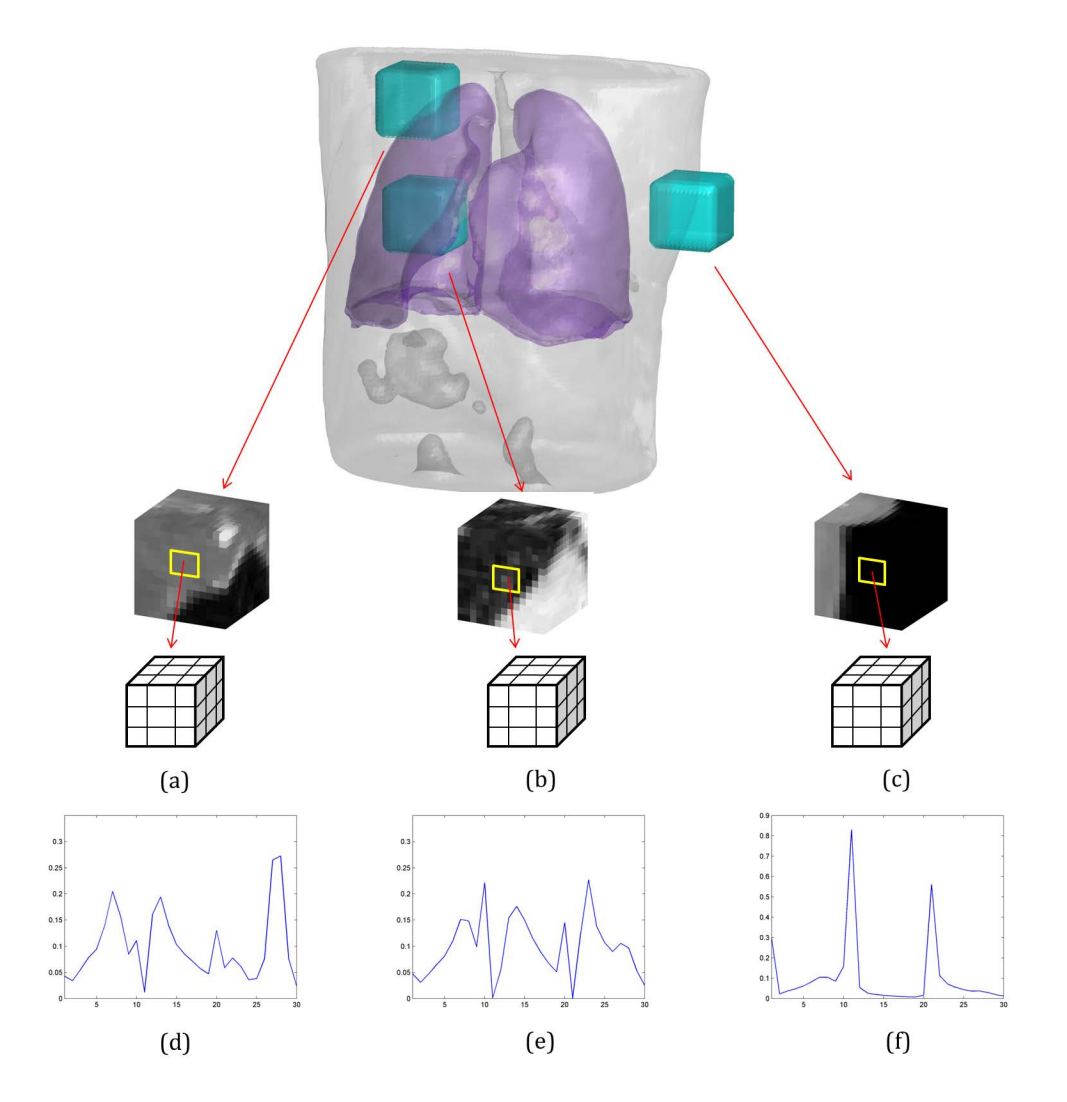


Figure 6.3: Three volumes extracted from low-dose CT scans and the corresponding average PL histograms representing their texture features. (a) A cubic volume from the body with a tip of the left lung. (b) A volume of the left lung with a tip of the heart. (c) A volume of the background with a tip of the body. (d), (e) and (f) are respectively their PL histograms.

6.6 Experimental Results

This section presents the application of the texture features to the low-dose CT images. Based on the probability images obtained using the texture features, the hard classification approach proposed in section 6.5 is described experimentally and this approach combined with the registration technique introduced in chapter 3 constitutes an initialization scheme suitable for the segmentation of lungs from low-dose CT images. The initialization scheme is validated by the databases of low-dose CT images and CT images with synthetic tumors.

Leave-one-out scheme is again employed here. Given 33 cases in the CT database, 32 among them provide sample patches, and the 'left-out' case is regarded as the novel

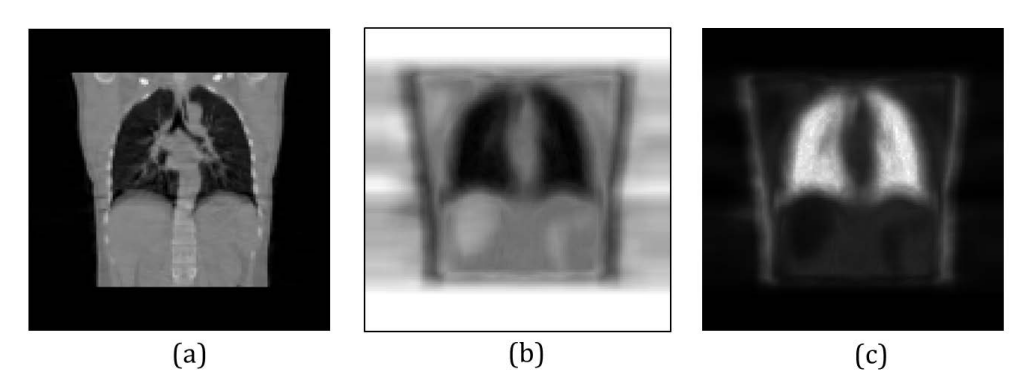


Figure 6.4: (a), (b) and (c) are respectively a slice from a volumetric CT image, its distance images $(D(\hat{I}_i, \hat{\mathbf{I}}))$ and probability images (P_i) .

data to be examined. The case index of the lung database used in the experiments is provided by table B.2 in appendix B.

6.6.1 Texture Segmentation and an Automatic Initialization Scheme

In section 6.5, the probability image corresponding to the image to be segmented can be calculated by equation 6.14. The parameter k has to be large enough for the probability image to reveal the ROIs. Here, an experimental explanation is given.

Figure 6.5, figure 6.6 and figure 6.7 demonstrate several examples of the probability images calculated using the proposed texture features. It can be observed from those figures that the increase of k from 1 to 50 gradually manifests the ROIs of the CT images. Outliers can be spotted in figure 6.5(a2) and (a3), figure 6.6(b2) and (b3), figure 6.7(c2) and (c3). When k > 10, the image remains stable and outliers vanish as presented in figure 6.5(a4) to (a7), figure 6.6(b4) to (b7), figure 6.7(c4) to (c7). Therefore k = 50 is considered here as the 'sufficiently large value'. A hard classification is thereby achieved by simply thresholding of the probability images. Let us assume the CFs (characteristic functions) of the regions extracted by texture features to be \mathcal{X}_{tex} , then we have

$$\mathcal{X}_{tex} = \begin{cases} 1, & P_{\mathbf{i}} > 0.99, \\ 0, & P_{\mathbf{i}} \le 0.99, \end{cases}$$
 (6.15)

Next, a validation experiment is conducted for the feasibility of the hard classification scheme to be applied to the initialization of the proposed segmentation method in chapter 5. The shape-based segmentation method requires a proper initialization, ideally located inside the ROIs. Therefore, the percentage of the region \mathcal{X}_{tex} overlapped with the manually segmented lung regions is used here to validate the effectiveness of the initialization scheme. The percentage represented by E_{tex} can be calculated by the

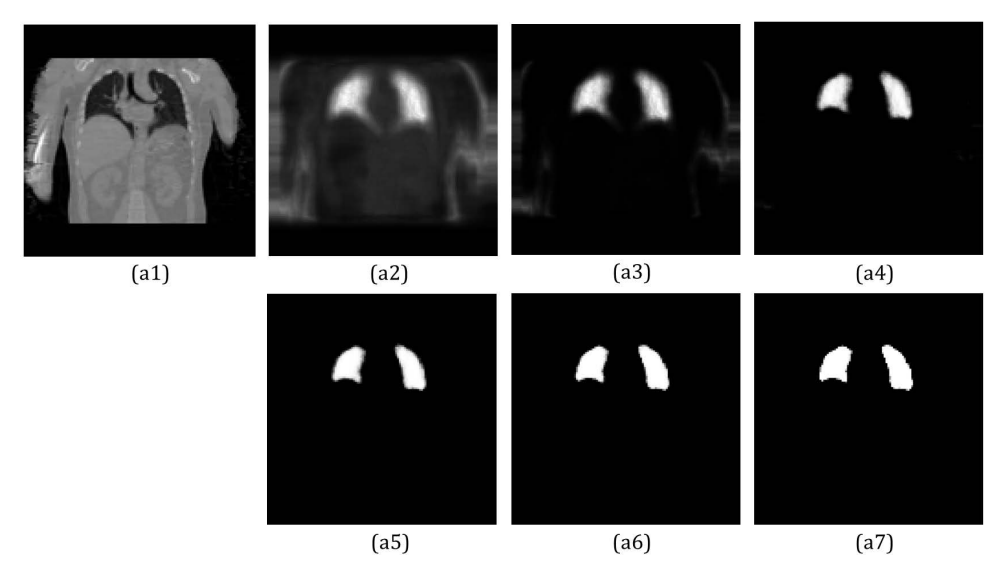


Figure 6.5: The probability images of case 3 computed using PL histograms that change with an increasing value of k. (a1) The original image slice. (a2)-(a7) respectively correspond to k = 1, k = 2, k = 5, k = 10, k = 20, k = 50.

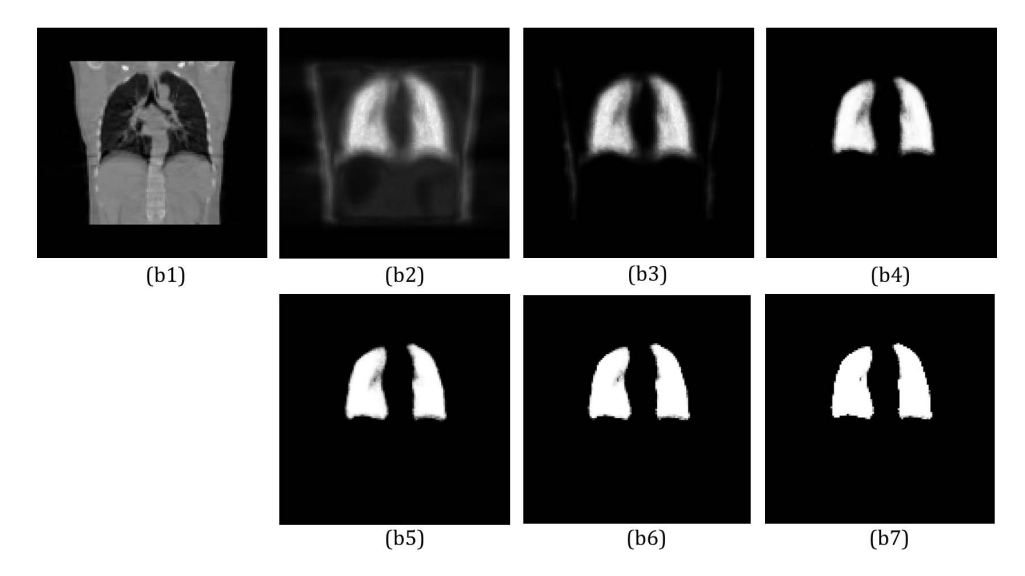


Figure 6.6: The probability images of case 15 computed using PL histograms that change with an increasing value of k. (b1) The original image slice. (b2)-(b7) respectively correspond to k = 1, k = 2, k = 5, k = 10, k = 20, k = 50.

following equation:

$$E_{tex} = \frac{\int_{\Omega} \mathcal{X}_{tex} \mathcal{X}_{ROI} \, d\mathbf{x}}{\int_{\Omega} \mathcal{X}_{tex} \, d\mathbf{x}}$$
 (6.16)

where \mathcal{X}_{ROI} represents the CFs of manually segmented lung regions regarded as the ground truth. The validation is performed on the low-dose CT database and the results are presented by figure 6.8. Within the database the proposed hard classification scheme achieves major overlapping with the ROIs, thereby proving the volumetric texture feature provides an ideal initialization for segmentation.

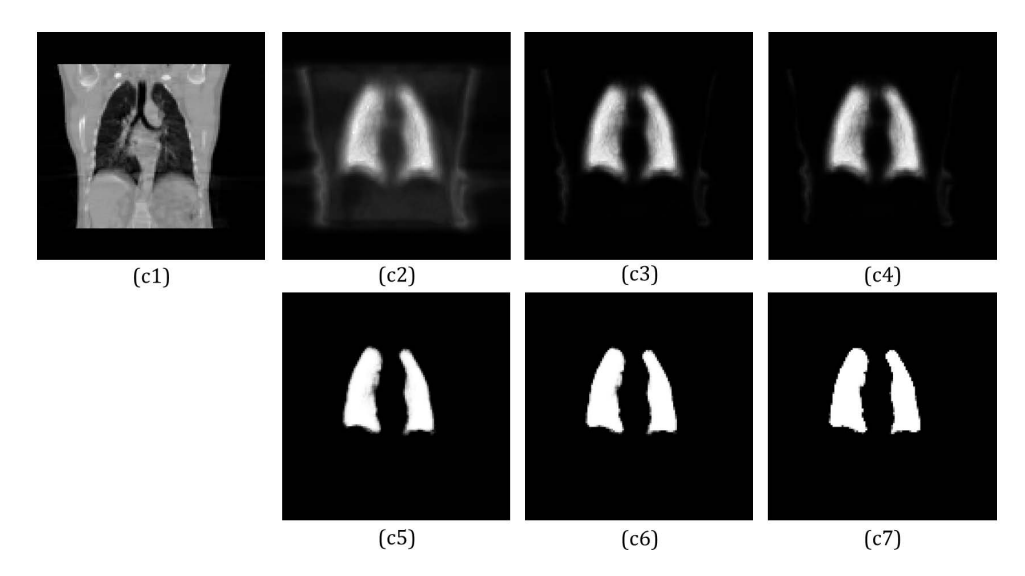


Figure 6.7: The probability images of case 24 computed using PL histograms that change with an increasing value of k. (c1) The original image slice. (c2)-(c7) respectively correspond to k = 1, k = 2, k = 5, k = 10, k = 20, k = 50.

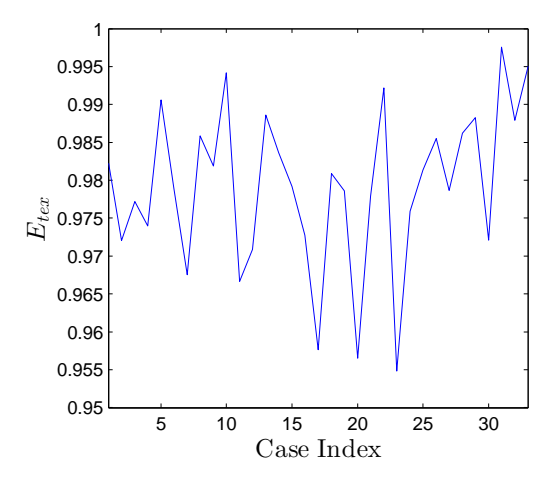


Figure 6.8: The percentage of volume obtained by the proposed hard classification method overlapped with the ground truth for the whole database.

Three examples of the initial surfaces provided by the hard classification are demonstrated in figure 6.9. They are overlapped by coarse surfaces extracted from the original CT images and the ground truth mask images. It can be observed that some dots are located outside the lung regions. This indicates that there are some areas outside the lung possess similar textures. However, these small structures are obviously unable to hamper a successful segmentation of the ROIs using the robust method introduced in chapter 5.

Therefore, a proper initialization of the shape-based segmentation method proposed in chapter 5 can be simply found by registering two lungs to the regions provided by the hard classification, and thus it is not necessary to observe the CT images to produce an

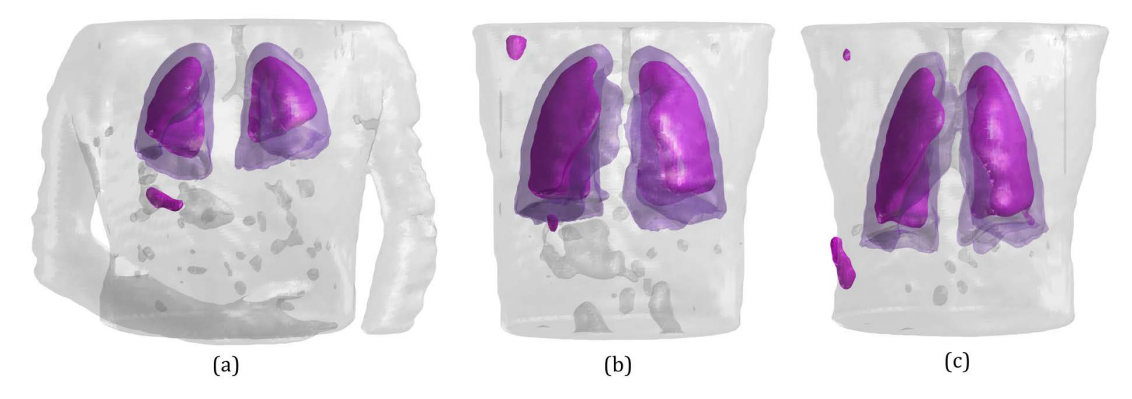


Figure 6.9: The hard classifications (magenta) of low-dose CT images of case 3, 15 and 24, overlapped with the ground truth (purple) and the coarse surfaces of the body (grey).

initialization scheme. Figure 6.10 demonstrates the process of finding proper initializations for segmentation of the right, left and two lungs simultaneously.

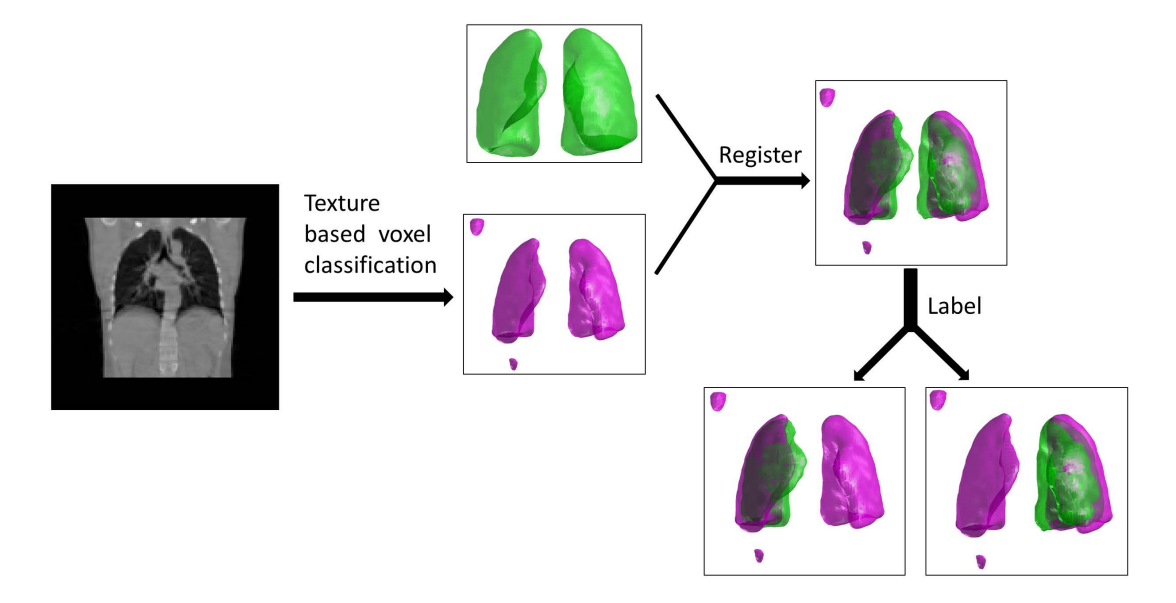


Figure 6.10: A graphical description of the initialization scheme based on the texture information.

6.6.2 The Shape-based Segmentation aided by the Initialization Scheme

With an automatic initialization scheme presented in section 6.6.1, validations of this scheme are performed in this section by applying this scheme to the low-dose CT images and CT images with synthetic tumors (built up and utilized in section 5.5.7).

Figure 6.11 gives an example of an improper initialization of Leventon's, Tsai's methods and the segmentation method proposed in chapter 5 leading to an inaccurate direction

of surface evolution. Therefore, the initialization scheme proposed here is an essential precursor to be drawn on for shape-based segmentation methods.

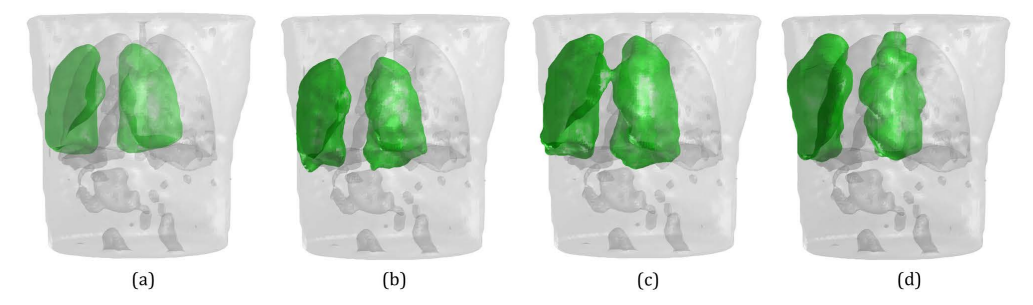


Figure 6.11: The improper initialization leads to failures of the segmentation. (a) The initial surfaces. (b), (c) and (d) are the results respectively produced by Leventon's, Tsai's and the hierarchical segmentation method proposed in chapter 5.

Figure 6.12 gives the results of the segmentation of lungs (right, left and two together) from the low-dose CT images using the initialization scheme followed by the shape-based segmentation method in chapter 5. Fluctuations can be observed due to individual variations, however, the segmentation results remain accurate and stable. The results presented in figure 6.12 are similar to those presented in figure 5.32, which indicates the effectiveness of the automated initialization scheme using the proposed texture features. However, they are not exactly the same because they are obtained using different initial conditions.

As for low-dose CT images with occlusions (synthetic tumors), the artificial database built up in section 5.5.7 is also used here to evaluate the initialization scheme. Some examples of applying the proposed supervised texture segmentation method to the images are given in figure 6.13.

It is predictable that the tumors will be excluded from the regions found by the hard classification. By registering the average lungs to the regions found by texture features, a major overlapping of the initial surfaces with the ROIs can be achieved and starting from these surfaces, a successful segmentation can be obtained (see figure 6.14). Different conditions of tumors for both left and right lungs of case 3 participate the evaluation. Figure 6.15 demonstrates similar results with those presented in figure 5.23. This indicates that the shape-based segmentation scheme assisted by the initialization method achieves satisfactory segmentation.

Other examples of segmentation process starting from the proposed initialization scheme based on the texture segmentation can be found in figure 6.16 and 6.17, which are respectively for case 15 and 24. The region and boundary information loss caused by the tumors affects the results of the texture segmentation, however, these circumstances are overcome after registering the average lungs to the regions produced by the texture segmentation. Similar results of all conditions of tumors in case 15 and 24 are presented

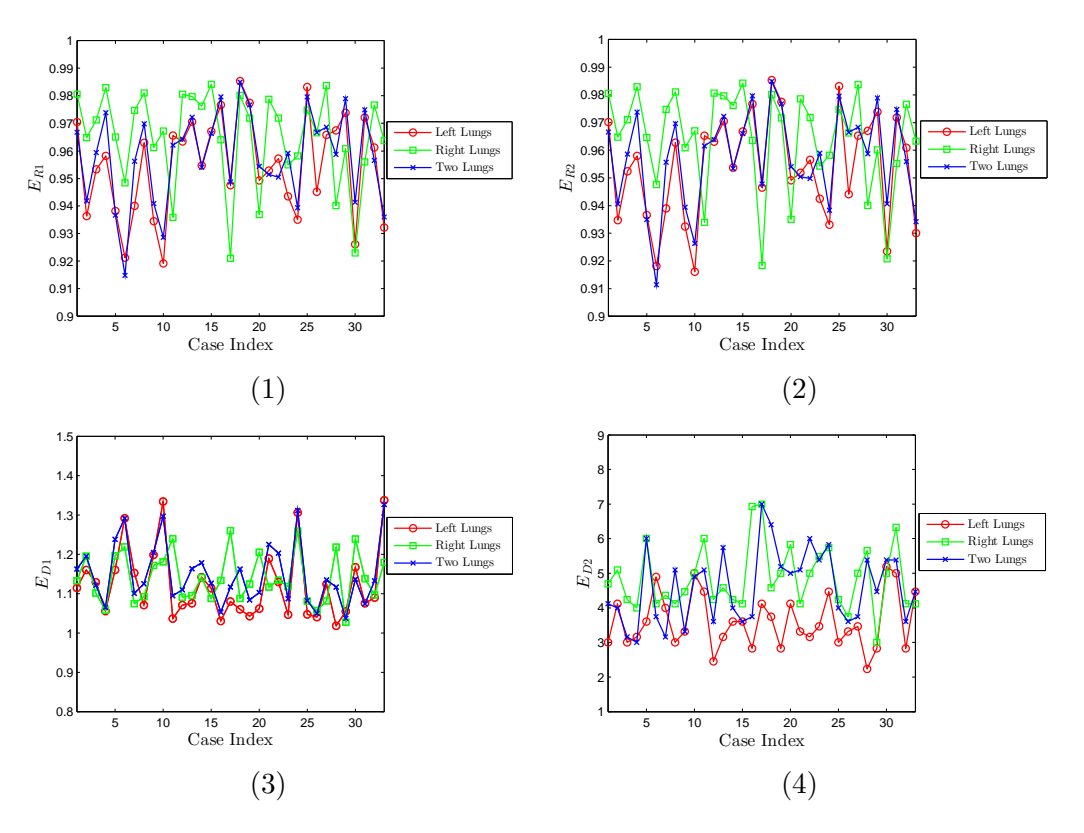


Figure 6.12: The results of the segmentation using the proposed initialization scheme followed by the shape-based segmentation method introduced in chapter 5 measured by E_{R1} , E_{R2} , E_{D1} and E_{D2} in segmentation of the low-dose CT database for the left, right and simultaneously two lungs.

in figure 6.18 compared to those demonstrated in figure 5.28. This further suggests that the combination of texture-based initialization scheme and the shape-based segmentation method is successful for the segmentation of lungs in the presence of tumors.

6.7 Conclusions and Future Directions

This chapter introduced a novel supervised volumetric texture modelling and segmentation method based on IGMRF. The part played by the texture feature in this work is to provide a proper initialization for the image segmentation method proposed in chapter 5 and thus to improve the degree of automation. With the texture feature applied to the image, a hard classification scheme is proposed to reveal the most relevant regions of the images that can be readily employed for segmentation purpose. The experiments are conducted using the same low-dose CT database in section 5.5 and the results suggest that the method is capable of providing appropriate initial surfaces for the hierarchical method proposed in chapter 5, aiding it to achieve a successful segmentation.

Notwithstanding, the method has several aspects to improve. Firstly, this method employ a special case of GMRF which involves only two parameters (w_i and σ_i). More

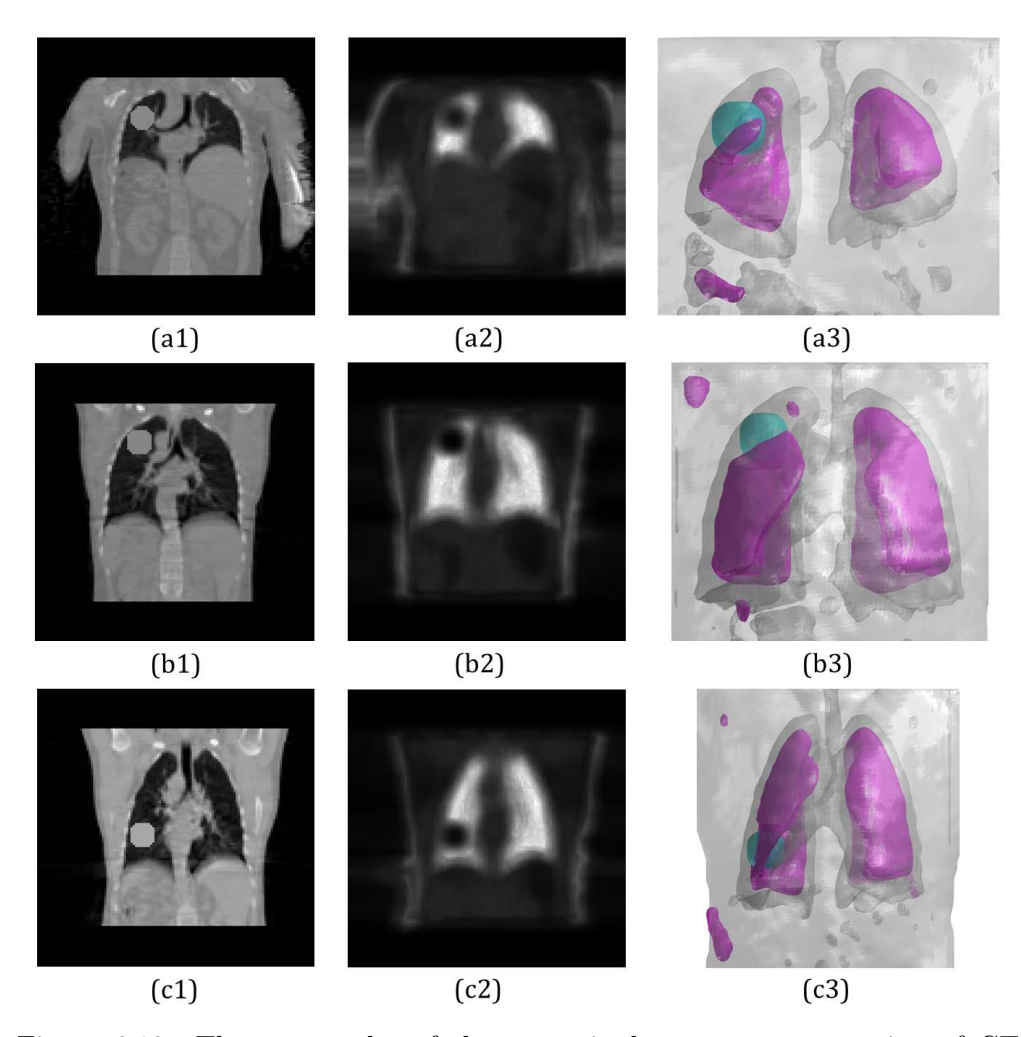


Figure 6.13: Three examples of the supervised texture segmentation of CT images with synthetic tumors using the proposed method. (a1), (b1) and (c1) are respectively the typical slices from case 3, 15 and 24. (a2), (b2) and (c2) are respectively the corresponding soft classifications (probability images). (a3), (b3) and (c3) the overlapping of the hard classification surfaces (magenta), emphasized tumors (cyan) and the coarse surfaces of the bodies (grey).

parameters possess greater potentialities to deliver higher discrimination power. Secondly, the only application of this method presented in this chapter is the lung database. It better to apply this method to more classes of synthetic and real world textures to further investigate its effectiveness. Moreover, the texture feature can be incorporated with variational segmentation framework to perform a supervised volumetric texture segmentation (Paragios and Deriche, 2002). Lastly, the method has the potentiality to perform unsupervised texture segmentation in combination with active surfaces (Dharmagunawardhana et al., 2012).

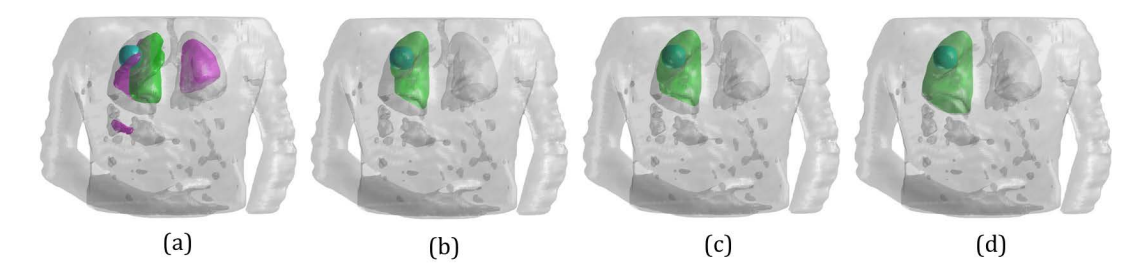


Figure 6.14: A 3-D visualization of the segmentation process of case 3 with synthetic tumors. (a) The overlapping of the regions extracted by the hard classification method (magenta), the initial surface found by the initialization scheme (green), the synthetic lung tumor (cyan) and the coarse surfaces of the human body (grey). (b)-(d) are the evolution of the shape-based active surfaces.

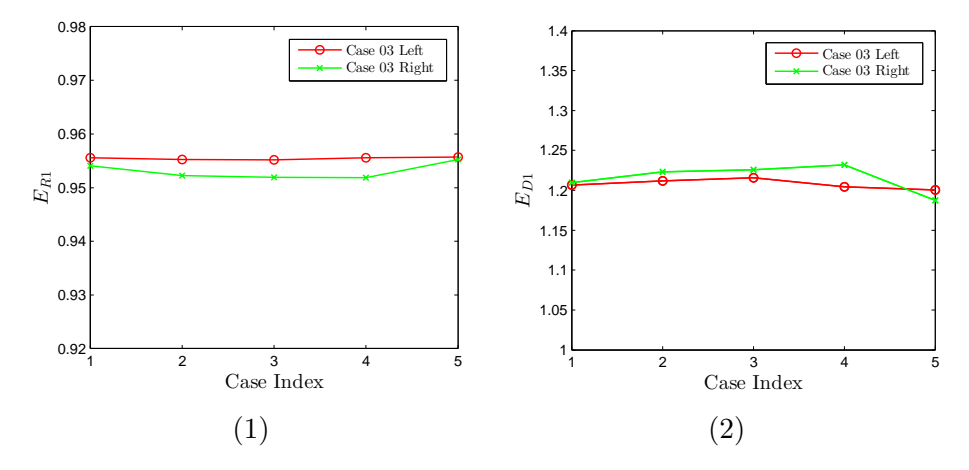


Figure 6.15: The segmentation of case 3 with synthetic tumors for both left and right lungs (corresponding to figure 6.16 and 6.17). The case indices of the left and right lungs respectively correspond to figure 5.20 (a) and (e).

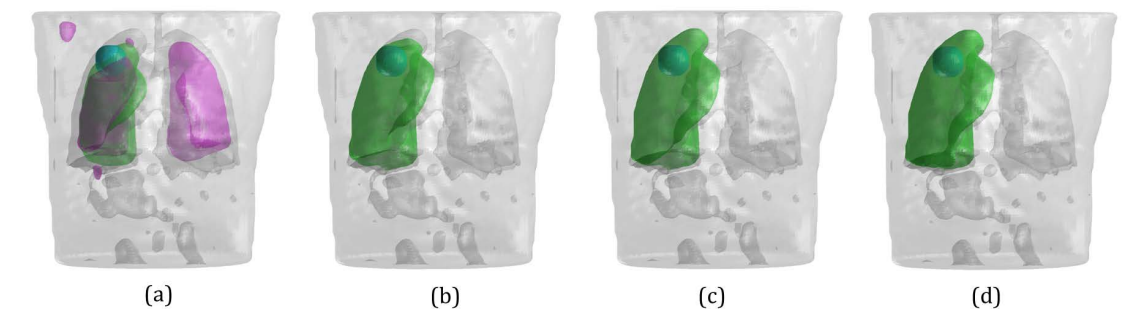


Figure 6.16: A 3-D visualization of the segmentation process of case 15 with synthetic tumors. (a) The overlapping of the regions extracted by the hard classification method (magenta), the initial surface found by the initialization scheme (green), the synthetic lung tumor (cyan) and the coarse surfaces of the human body (grey). (b)-(d) are the evolution of the shape-based active surfaces.

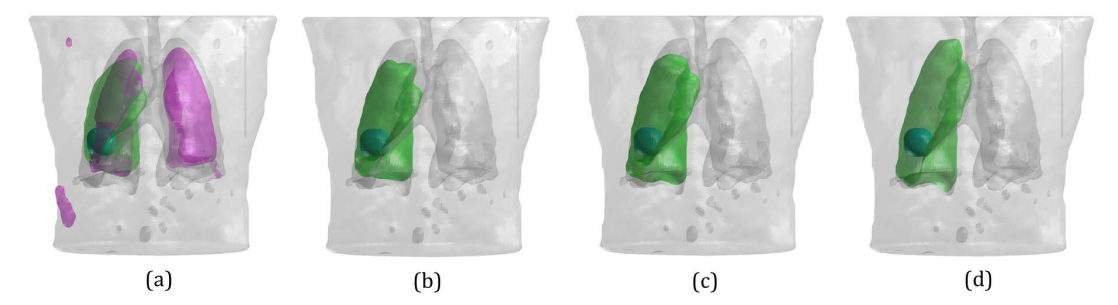


Figure 6.17: A 3-D visualization of the segmentation process of case 24 with synthetic tumors. (a) The overlapping of the regions extracted by the hard classification method (magenta), the initial surface found by the initialization scheme (green), the synthetic lung tumor (cyan) and the coarse surfaces of the human body (grey). (b)-(d) are the evolution of the shape-based active surfaces.

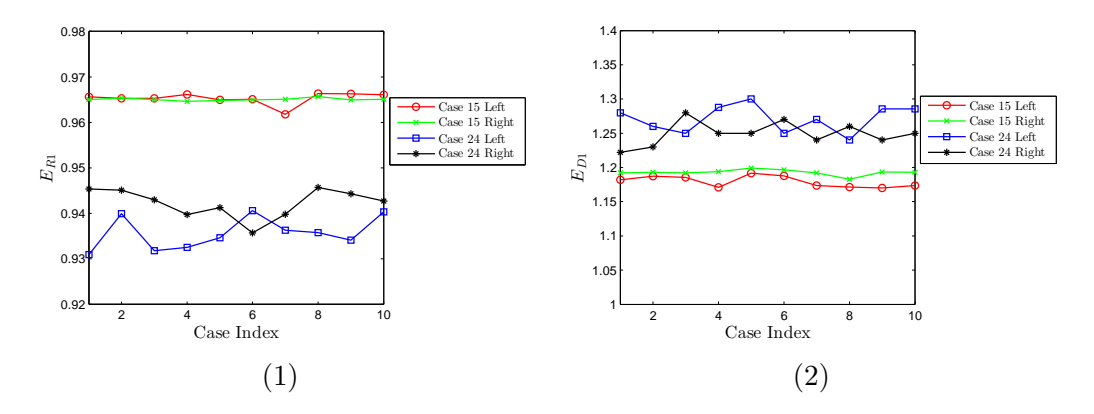


Figure 6.18: The quantitive results of the segmentation of case 15 and 24 with synthetic tumors for both left and right lungs. The case indices of the left and right lungs of case 15 and 24 respectively correspond to figure 5.20 (b), (f), (c) and (g).

Chapter 7

Conclusions and Future Works

7.1 Conclusions

This thesis describes the process of formulating an effective methodology for the segmentation of lungs from volumetric CT images based on prior knowledge. Four major models are involved, namely variational image segmentation method (active contours/surfaces), similarity registration, statistical shape modelling and supervised texture classification. Each of the models are investigated in details to verify its potentiality to become an effective part of the final segmentation mechanism through extensive experiments from test stages to real-world applications.

The necessities and challenges of extracting lungs from CT scans are discussed and a brief review of early and recent methods of lung segmentation is presented. Introducing prior knowledge into segmentation techniques enjoys a good popularity in recent years and sequential works concerning this topic are done in 2-D under variational frameworks and shown to be powerful in extraction of specific shapes from images in the presence of significant noise and occlusions. Therefore this idea is employed for the segmentation of lungs. However, shape-based segmentation in 3-D are not rich in the literature. Introducing prior knowledge into segmentation techniques in 3-D remains to be further explored.

Variational feature extraction models, namely active contours/surfaces, are considered to be advanced image segmentation methods. They are associated with mathematical optimization problems and naturally smoothed by internal force during evolution in segmentation. Their stability is mathematically supported. However, internal force is insufficient for lung segmentation under impact of bright vessels, dark airways and large anomalies, shown by experimental results in chapter 2. Therefore, prior knowledge (prior shape) is necessary for an accurate segmentation.

A bridge to associate active surfaces with the prior shape model is similarity registration, which involves calculation of optimal scale, rotation and translation parameters. A novel registration technique of two volumetric shapes represented by characteristic functions is proposed. PCA is employed to find principal axes of each shape. These principal axes provide an initial transformation which largely facilitates the calculation of rotation parameters. Geometric moments are used to estimate scale parameter. Then finding optimal rotation and translation are generalized into solving phase correlation problems which exploit fast Fourier transform (FFT). Extensive experimental results show the robustness of the proposed technique registering topologically complex volumetric shapes in the presence of severe noise.

Shape decomposition using PCA is the current state of the art. The decomposition process vastly reduce the redundancy of the training set of shapes and assists in building up deformable shape templates. Then, finding the optimal shape parameters that best approximates a novel shape becomes the chief concern. An novel hybrid optimization scheme is proposed based on the works of Leventon et al. (2000) and Bresson et al. (2006). The estimation process of shape parameters is coupled with the proposed registration technique introduced in chapter 3 for better accuracy and efficiency.

When the necessary techniques are ready to be employed after respective investigations, they are incorporated into accomplishing the task of the segmentation of lungs from the volumetric CT images with a huge amount of noise and occlusions. The proposed segmentation method, when its conditions of use are satisfied, exhibits high robustness over previous method against noise and occlusions in a series of experiments, including synthetic images for specific tests and the real-world database of low-dose CT scans.

The statistical shape model is one type of prior knowledge. Another type of prior knowledge, which is the texture information, also participates in the segmentation mechanism to enable it to achieve a higher degree of automation. Texture modelling technique proposed by Dharmagunawardhana et al. (2014) based on IGMRF is extended to 3-D. A supervised texture segmentation method that employs the novel texture feature is proposed to serve as a precursor to the proposed segmentation method. The texture segmentation method is a feasible choice for this task after the validation by CT images with synthetic tumors and the database of low-dose CT scans.

7.2 Future Directions

Each of the four models has several aspects of to improve, therefore, future directions are proposed respectively for the four models.

Active contours/surfaces have a rich amount of parameter settings. The experiments in section 2.6 provide a limited number of typical conditions. A quantitative analysis should be performed on various types of image to fully exhibit its potential applications.

The similarity registration consists of isotropic scale, rotation and translation. It is intriguing to extend the method to affine and non-rigid registrations. The shapes of lungs are versatile and in figure 4.3, where typical examples are illustrated, it can be observed that the scale difference between individual lungs are directional (in certain cases up and down, and some other cases left and right). Therefore, a directional scale estimation may well improve registration accuracy.

Statistical shape modelling is only performed on the shapes of lungs. Even though lung shapes themselves can be divided into three subclasses (left, right and two lungs), it better to apply the method to a wider range of shape classes, say heart and brain ventricles, and other anatomical structures.

The proposed hierarchical method should be also performed on a CT database of lung cancers for a further evaluation. It is interesting to apply the method to more types of volumetric images of various shape classes, say MRI brain images and ultra-sound heart images. The method follows an iterative optimization process, progressively achieving the final result, presumably this method has the capability of motion tracking. If animated volumetric images are available, the potentialities of the method can be further explored.

The supervised texture segmentation technique can be applied to the discrimination of more volumetric textures, say lung tissues with different kinds of diseases. Also, the volumetric texture feature model coupled with active surfaces can perform unsupervised texture segmentation.

Appendix A

Image Noise Information

This appendix provides the noise information of images involved in section 5.5.4 and 5.5.6. The information is to be presented using three measures that compare original image and test image defined by Gonzalez et al. (2004). The first measure is image SNR (signal-to-noise ratio) in dB:

$$SNR = 10 \cdot \log_{10} \left(\frac{\int_{\Omega} I^2 d\mathbf{x}}{\int_{\Omega} (I - I_t)^2 d\mathbf{x}} \right)$$
 (A.1)

The second is PSNR (peak signal-to-noise ratio) in dB:

$$PSNR = 10 \cdot \log_{10} \left(\frac{\max(I^2) \int_{\Omega} d\mathbf{x}}{\int_{\Omega} (I - I_t)^2 d\mathbf{x}} \right)$$
(A.2)

And the third is RMSE (root mean square error):

RMSE =
$$\sqrt{\left(\frac{\int_{\Omega} (I - I_t)^2 d\mathbf{x}}{\int_{\Omega} d\mathbf{x}}\right)}$$
 (A.3)

With preliminaries given, the noise information of the synthetic image in seciton 5.5.4 and the CT scan of case 3, 15, 24 in section 5.5.6 from level 1 to 10 are respectively given by table A.1, A.2, A.3, and A.4:

Similarity	SNR	PSNR	RMSE
measures			
level 1	15.92	16.02	158.11
level 2	12.92	13.02	223.39
level 3	11.24	11.34	271.11
level 4	10.10	10.20	308.97
level 5	9.29	9.39	339.16
level 6	8.68	8.78	363.74
level 7	8.19	8.29	385.07
level 8	7.81	7.91	402.39
level 9	7.48	7.58	417.66
level 10	7.22	7.32	430.74

measures			
level 1	8.49	23.57	154.98
level 2	5.52	20.60	218.17
level 3	2.57	17.65	306.30
level 4	0.91	15.98	371.14
level 5	-0.26	14.81	424.60
level 6	-1.14	13.94	469.53
level 7	-3.68	11.39	629.46
level 8	-4.97	10.11	729.72
level 9	-5.75	9.33	798.24
level 10	-6.29	8.79	849.34

Similarity | SNR PSNR RMSE

Table A.1: Noise information of figure 5.11 and 5.12 demonstrating the experiments in section 5.5.4.

Table A.2: Noise information of figure 5.17 demonstrating the experiments in section 5.5.6.

Similarity	SNR	PSNR	RMSE
measures			
level 1	7.16	24.16	151.50
level 2	4.19	21.20	213.13
level 3	1.23	18.24	299.65
level 4	-0.47	16.54	364.35
level 5	-1.64	15.37	417.20
level 6	-2.54	14.47	462.73
level 7	-5.17	11.84	626.31
level 8	-6.49	10.52	728.64
level 9	-7.30	9.71	800.24
level 10	-7.86	9.15	853.26

Similarity	SNR	PSNR	RMSE
measures			
level 1	7.44	23.63	152.26
level 2	4.46	20.66	214.43
level 3	1.51	17.71	301.22
level 4	-0.18	16.01	366.08
level 5	-1.37	14.83	419.50
level 6	-2.26	13.94	464.80
level 7	-4.86	11.34	626.89
level 8	-6.16	10.03	728.85
level 9	-6.97	9.23	799.69
level 10	-7.51	8.68	851.38

Table A.3: Noise information of figure 5.16 demonstrating the experiments in section 5.5.6.

Table A.4: Noise information of figure 5.18 demonstrating the experiments in section 5.5.6.

Appendix B

Case Index of the Lung Database

Case Index	Subject ID	Disease State
Case 1	BRUCI003	Emphysema
Case 2	BRUCI004	Healthy
Case 3	BRUCI007	Healthy Smoker
Case 4	BRUCI008	Healthy Smoker
Case 5	BRUCI009	Healthy
Case 6	BRUCI014	Healthy
Case 7	BRUCI015	Healthy
Case 8	BRUCI016	Healthy Smoker
Case 9	BRUCI018	Healthy
Case 10	BRUCI020	Healthy
Case 11	BRUCI021	Healthy Smoker
Case 12	BRUCI022	Emphysema
Case 13	BRUCI024	Healthy Smoker
Case 14	BRUCI028	Healthy
Case 15	BRUCI032	Healthy
Case 16	BRUCI033	Emphysema
Case 17	BRUCI036	Emphysema
Case 18	BRUCI037	Emphysema
Case 19	BRUCI038	Healthy Smoker
Case 20	BRUCI039	Emphysema
Case 21	BRUCI040	Healthy
Case 22	BRUCI041	Healthy
Case 23	BRUCI042	Healthy
Case 24	BRUCI043	Healthy
Case 25	BRUCI044	Healthy
Case 26	BRUCI045	Emphysema
Case 27	BRUCI049	Emphysema
Case 28	BRUCI051	Emphysema
Case 29	BRUCI052	Emphysema
Case 30	BRUCI062	Emphysema
Case 31	BRUCI072	Emphysema
Case 32	BRUCI076	Emphysema
Case 33	BRUCI077	Emphysema
Case 34	BRUCI085	Emphysema
Case 35	BRUCI089	Emphysema

Table B.1: The case index of the high resolution CT images referred in chapter 3.

Case Index	Subject ID	Disease State
Case 1	BRUCI003	Emphysema
Case 2	BRUCI007	Healthy Smoker
Case 3	BRUCI008	Healthy Smoker
Case 4	BRUCI009	Healthy
Case 5	BRUCI014	Healthy
Case 6	BRUCI015	Healthy
Case 7	BRUCI016	Healthy Smoker
Case 8	BRUCI018	Healthy
Case 9	BRUCI020	Healthy
Case 10	BRUCI021	Healthy Smoker
Case 11	BRUCI022	Emphysema
Case 12	BRUCI024	Healthy Smoker
Case 13	BRUCI028	Healthy
Case 14	BRUCI032	Healthy
Case 15	BRUCI033	Emphysema
Case 16	BRUCI036	Emphysema
Case 17	BRUCI037	Emphysema
Case 18	BRUCI038	Healthy Smoker
Case 19	BRUCI040	Healthy
Case 20	BRUCI041	Healthy
Case 21	BRUCI042	Healthy
Case 22	BRUCI043	Healthy
Case 23	BRUCI044	Healthy
Case 24	BRUCI045	Emphysema
Case 25	BRUCI049	Emphysema
Case 26	BRUCI051	Emphysema
Case 27	BRUCI052	Emphysema
Case 28	BRUCI062	Emphysema
Case 29	BRUCI072	Emphysema
Case 30	BRUCI076	Emphysema
Case 31	BRUCI077	Emphysema
Case 32	BRUCI085	Emphysema
Case 33	BRUCI089	Emphysema

Table B.2: The case index of the low-dose CT images referred to in chapter 4, 5 and 6.

References

- M. Al-Huseiny, S. Mahmoodi, and M. Nixon. Robust rigid shape registration method using a level set formulation. *International Symposium in Visual Computing*, pages 252–261, 2010.
- Constantino Carlos Reyes Aldasoro and Abhir Bhalerao. Volumetric texture segmentation by discriminant feature selection and multiresolution classification. *Medical Imaging, IEEE Transactions on*, 26(1):1–14, 2007.
- P.J. Besl and N.D. McKay. A method for registration of 3-d shapes. *IEEE Transactions* on pattern analysis and machine intelligence, 14(2):239–256, 1992.
- D. Breitenreicher and C. Schnörr. Robust 3d object registration without explicit correspondence using geometric integration. *Machine Vision and Applications*, 21(5): 601–611, 2010.
- X. Bresson, P. Vandergheynst, and J.P. Thiran. A variational model for object segmentation using boundary information and shape prior driven by the mumford-shah functional. *International Journal of Computer Vision*, 68(2):145–162, 2006.
- M.S. Brown, M.F. McNitt-Gray, N.J. Mankovich, J.G. Goldin, J. Hiller, L.S. Wilson, and DR Aberie. Method for segmenting chest ct image data using an anatomical model: preliminary results. *Medical Imaging, IEEE Transactions on*, 16(6):828–839, 1997.
- V. Caselles, F. Catté, T. Coll, and F. Dibos. A geometric model for active contours in image processing. *Numerische Mathematik*, 66(1):1–31, 1993.
- V. Caselles, R. Kimmel, and G. Sapiro. Geodesic active contours. *International journal of computer vision*, 22(1):61–79, 1997a.
- V. Caselles, R. Kimmel, G. Sapiro, and C. Sbert. Minimal surfaces based object segmentation. *Pattern Analysis and Machine Intelligence, IEEE Transactions on*, 19(4): 394–398, 1997b.
- Erdogan Çesmeli and DeLiang Wang. Texture segmentation using gaussian-markov random fields and neural oscillator networks. *Neural Networks, IEEE Transactions* on, 12(2):394–404, 2001.

J.M. Chambers, W.S. Cleveland, B. Kleiner, and P.A. Tukey. Graphical Methods for Data Analysis. The Wadsworth Statistics/Probability Series. Boston, MA: Duxury, 1983.

- T.F. Chan and L.A. Vese. Active contours without edges. *Image Processing*, *IEEE Transactions on*, 10(2):266–277, 2001.
- Rama Chellappa and Shankar Chatterjee. Classification of textures using gaussian markov random fields. Acoustics, Speech and Signal Processing, IEEE Transactions on, 33(4):959–963, 1985.
- T. Chen, B.C. Vemuri, A. Rangarajan, and S.J. Eisenschenk. Group-wise point-set registration using a novel cdf-based havrda-charvát divergence. *International journal of computer vision*, 86(1):111–124, 2010.
- Y. Chen, H.D. Tagare, S. Thiruvenkadam, F. Huang, D. Wilson, K.S. Gopinath, R.W. Briggs, and E.A. Geiser. Using prior shapes in geometric active contours in a variational framework. *International Journal of Computer Vision*, 50(3):315–328, 2002.
- TF Cootes, DH Cooper, CJ Taylor, and J. Graham. Trainable method of parametric shape description. *Image and Vision Computing*, 10(5):289–294, 1992.
- T.F. Cootes, A. Hill, C.J. Taylor, and J. Haslam. Use of active shape models for locating structures in medical images. *Image and vision computing*, 12(6):355–365, 1994.
- D. Cremers, S.J. Osher, and S. Soatto. Kernel density estimation and intrinsic alignment for shape priors in level set segmentation. *International Journal of Computer Vision*, 69(3):335–351, 2006.
- D. Cremers, F. Tischhäuser, J. Weickert, and C. Schnörr. Diffusion snakes: Introducing statistical shape knowledge into the mumford-shah functional. *International journal of computer vision*, 50(3):295–313, 2002.
- DM Denison, MD Morgan, and AB Millar. Estimation of regional gas and tissue volumes of the lung in supine man using computed tomography. *Thorax*, 41(8):620–628, 1986.
- Xavier Descombes, Marc Sigelle, and Francoise Preteux. Estimating gaussian markov random field parameters in a nonstationary framework: application to remote sensing imaging. *Image Processing, IEEE Transactions on*, 8(4):490–503, 1999.
- Chathurika Dharmagunawardhana, Sasan Mahmoodi, Michael Bennett, and Niranjan Mahesan. Unsupervised texture segmentation using active contours and local distributions of gaussian markov random field parameters. In *British Machine Vision Conference*, pages 88.1–88.11, 2012.
- Chathurika Dharmagunawardhana, Sasan Mahmoodi, Michael Bennett, and Mahesan Niranjan. Quantitative analysis of pulmonary emphysema using isotropic gaussian markov random fields. 2014.

J. Diebel. Representing attitude: Euler angles, unit quaternions, and rotation vectors. Technical report, Stanford University, Palo Alto, CA, 2006.

- N. Gelfand, N.J. Mitra, L.J. Guibas, and H. Pottmann. Robust global registration. In *Proceedings of the third Eurographics symposium on Geometry processing*, page 197. Eurographics Association, 2005.
- Rafael C Gonzalez, Richard Eugene Woods, and Steven L Eddins. *Digital image processing using MATLAB*. Pearson Education India, 2004.
- S. Granger and X. Pennec. Multi-scale em-icp: A fast and robust approach for surface registration. *Computer Vision-ECCV 2002*, pages 69–73, 2006.
- B. Gutman, Y. Wang, T. Chan, P.M. Thompson, A.W. Toga, et al. Shape registration with spherical cross correlation. In 2nd MICCAI Workshop on Mathematical Foundations of Computational Anatomy, pages 56–67, 2008.
- G. Hamarneh and T. Gustavsson. Combining snakes and active shape models for segmenting the human left ventricle in echocardiographic images. In Computers in Cardiology 2000, pages 115–118. IEEE, 2000.
- Shoudong Han, Wenbing Tao, and Xianglin Wu. Texture segmentation using independent-scale component-wise riemannian-covariance gaussian mixture model in kl measure based multi-scale nonlinear structure tensor space. *Pattern Recognition*, 44(3):503–518, 2011.
- LW Hedlund, RF Anderson, PL Goulding, JW Beck, EL Effmann, and CE Putman. Two methods for isolating the lung area of a ct scan for density information. *Radiology*, 144(2):353–357, 1982.
- E.A. Hoffman. Effect of body orientation on regional lung expansion: a computed tomographic approach. *Journal of Applied Physiology*, 59(2):468–480, 1985.
- E.A. Hoffman and E.L. Ritman. Effect of body orientation on regional lung expansion in dog and sloth. *Journal of Applied Physiology*, 59(2):481–491, 1985.
- E.A. Hoffman, LJ Sinak, RA Robb, and EL Ritman. Noninvasive quantitative imaging of shape and volume of lungs. *Journal of Applied Physiology*, 54(5):1414–1421, 1983.
- Thomas Hofmann, Jan Puzicha, and Joachim M Buhmann. Unsupervised texture segmentation in a deterministic annealing framework. *Pattern Analysis and Machine Intelligence*, *IEEE Transactions on*, 20(8):803–818, 1998.
- M. Holtzman-Gazit, R. Kimmel, N. Peled, and D. Goldsher. Segmentation of thin structures in volumetric medical images. *Image Processing, IEEE Transactions on*, 15(2):354–363, 2006.

Jiang Hsieh. Computed tomography: principles, design, artifacts, and recent advances. SPIE Bellingham, WA, 2009.

- S. Hu, E.A. Hoffman, and J.M. Reinhardt. Automatic lung segmentation for accurate quantitation of volumetric x-ray ct images. *Medical Imaging, IEEE Transactions on*, 20(6):490–498, 2001.
- P. Hua, Q. Song, M. Sonka, E.A. Hoffman, and J.M. Reinhardt. Segmentation of pathological and diseased lung tissue in ct images using a graph-search algorithm. In *Biomedical Imaging: From Nano to Macro*, 2011 IEEE International Symposium on, pages 2072–2075. IEEE, 2011.
- X. Huang, N. Paragios, and D.N. Metaxas. Shape registration in implicit spaces using information theory and free form deformations. *Pattern Analysis and Machine Intelligence*, *IEEE Transactions on*, 28(8):1303–1318, 2006.
- Anil K Jain and Farshid Farrokhnia. Unsupervised texture segmentation using gabor filters. In Systems, Man and Cybernetics, 1990. Conference Proceedings., IEEE International Conference on, pages 14–19. IEEE, 1990.
- W.A. Kalender, H. Fichte, W. Bautz, M. Skalej, et al. Semiautomatic evaluation procedures for quantitative ct of the lung. *Journal of computer assisted tomography*, 15 (2):248, 1991.
- M. Kass, A. Witkin, and D. Terzopoulos. Snakes: Active contour models. *International journal of computer vision*, 1(4):321–331, 1988.
- J.M. Keller, F.M. Edwards, and R. Rundle. Automatic outlining of regions on ct scans. Journal of Computer Assisted Tomography, 5(2):240, 1981.
- Dong Hwan Kim, Il Dong Yun, and Sang Uk Lee. New mrf parameter estimation technique for texture image segmentation using hierarchical gmrf model based on random spatial interaction and mean field theory. In *Pattern Recognition*, 2006. ICPR 2006. 18th International Conference on, volume 2, pages 365–368. IEEE, 2006.
- R. Kimmel. Fast edge integration. Geometric Level Set Methods in Imaging, Vision, and Graphics, pages 59–77, 2003.
- R. Kimmel and A.M. Bruckstein. Regularized laplacian zero crossings as optimal edge integrators. *International Journal of Computer Vision*, 53(3):225–243, 2003.
- T.T.J.P. Kockelkorn, E.M. van Rikxoort, J.C. Grutters, and B. van Ginneken. Interactive lung segmentation in ct scans with severe abnormalities. In *Biomedical Imaging: From Nano to Macro*, 2010 IEEE International Symposium on, pages 564–567. IEEE, 2010.
- P.J. Kostelec and D.N. Rockmore. Ffts on the rotation group. *Proc. Santa Fe Institute Working Papers Series Paper 03-11*, 60, 2003.

Santhana Krishnamachari and Rama Chellappa. Multiresolution gauss-markov random field models for texture segmentation. *Image Processing, IEEE Transactions on*, 6(2): 251–267, 1997.

- M.E. Leventon, W.E.L. Grimson, and O. Faugeras. Statistical shape influence in geodesic active contours. In *Computer Vision and Pattern Recognition*, 2000. Proceedings. *IEEE Conference on*, volume 1, pages 316–323. IEEE, 2000.
- Michael Emmanuel Leventon. Statistical models in medical image analysis. PhD thesis, Massachusetts Institute of Technology, 2000.
- Stan Z Li and S Singh. Markov random field modeling in image analysis, volume 3. Springer, 2009.
- W. Li, Z. Yin, Y. Huang, and Y. Xiong. Automatic registration for 3d shapes using hybrid dimensionality-reduction shape descriptions. *Pattern Recognition*, 44(12):2926–2943, 2011.
- L. Lucchese, G. Doretto, and G.M. Cortelazzo. A frequency domain technique for range data registration. *Pattern Analysis and Machine Intelligence*, *IEEE Transactions on*, 24(11):1468–1484, 2002.
- Sasan Mahmoodi, Muayed S Al-Huseiny, and Mark S Nixon. Similarity registration for shapes based on signed distance functions. In *Advances in Visual Computing*, pages 599–609. Springer, 2012.
- Sasan Mahmoodi and Steve Gunn. Snake based unsupervised texture segmentation using gaussian markov random field models. In *Image Processing (ICIP)*, 2011 18th IEEE International Conference on, pages 3353–3356. IEEE, 2011.
- R. Malladi, J. Sethian, and B. Vemuri. Evolutionary fronts for topology-independent shape modeling and recovery. *Computer Vision-ECCV'94*, pages 1–13, 1994.
- R. Malladi, J.A. Sethian, and B.C. Vemuri. Shape modeling with front propagation: A level set approach. *Pattern Analysis and Machine Intelligence, IEEE Transactions on*, 17(2):158–175, 1995.
- C.R. Maurer Jr, R. Qi, and V. Raghavan. A linear time algorithm for computing exact euclidean distance transforms of binary images in arbitrary dimensions. *Pattern Analysis and Machine Intelligence*, *IEEE Transactions on*, 25(2):265–270, 2003.
- T. McInerney and D. Terzopoulos. T-snakes: Topology adaptive snakes. *Medical Image Analysis*, 4(2):73–91, 2000.
- J. Montagnat and H. Delingette. Spatial and temporal shape constrained deformable surfaces for 3d and 4d medical image segmentation. 2000a.

Johan Montagnat and Hervé Delingette. Spatial and Temporal Shape Constrained Deformable Surfaces for 3D and 4D Medical Image Segmentation. Technical Report RR-4078, INRIA, 2000b.

- D. Mumford and J. Shah. Optimal approximations by piecewise smooth functions and associated variational problems. *Comm. Pure Appl. Math*, 42(5):577–685, 1989.
- Mark Nixon and Alberto S Aguado. Feature extraction & image processing. Academic Press, 2008.
- S. Osher and J.A. Sethian. Fronts propagating with curvature-dependent speed: algorithms based on hamilton-jacobi formulations. *Journal of computational physics*, 79 (1):12–49, 1988.
- N. Paragios, M. Rousson, and V. Ramesh. Non-rigid registration using distance functions. Computer Vision and Image Understanding, 89(2-3):142–165, 2003.
- Nikos Paragios and Rachid Deriche. Geodesic active regions and level set methods for supervised texture segmentation. *International Journal of Computer Vision*, 46(3): 223–247, 2002.
- J. Pu, J. Roos, C.A. Yi, S. Napel, G.D. Rubin, and D.S. Paik. Adaptive border marching algorithm: Automatic lung segmentation on chest ct images. *Computerized Medical Imaging and Graphics*, 32(6):452–462, 2008.
- Elena Ranguelova and Anthony Quinn. Analysis and synthesis of three-dimensional gaussian markov random fields. In *Image Processing*, 1999. ICIP 99. Proceedings. 1999 International Conference on, volume 3, pages 430–434. IEEE, 1999.
- Martin Reuter. Hierarchical shape segmentation and registration via topological features of laplace-beltrami eigenfunctions. *International Journal of Computer Vision*, 89(2-3): 287–308, 2010.
- Martin Reuter, Silvia Biasotti, Daniela Giorgi, Giuseppe Patanè, and Michela Spagnuolo. Discrete laplace—beltrami operators for shape analysis and segmentation. *Computers & Graphics*, 33(3):381–390, 2009.
- Martin Reuter, Franz-Erich Wolter, and Niklas Peinecke. Laplace—beltrami spectra as shape-dnaof surfaces and solids. *Computer-Aided Design*, 38(4):342–366, 2006.
- M. Rousson, N. Paragios, and R. Deriche. Implicit active shape models for 3d segmentation in mr imaging. Medical Image Computing and Computer-Assisted Intervention—MICCAI 2004, pages 209–216, 2004.
- Havard Rue and Leonhard Held. Gaussian Markov random fields: theory and applications. CRC Press, 2004.

S. Rusinkiewicz and M. Levoy. Efficient variants of the icp algorithm. In 3-D Digital Imaging and Modeling, 2001. Proceedings. Third International Conference on, pages 145–152, 2001.

- Raif M Rustamov. Laplace-beltrami eigenfunctions for deformation invariant shape representation. In *Proceedings of the fifth Eurographics symposium on Geometry processing*, pages 225–233. Eurographics Association, 2007.
- C. Sagiv, N.A. Sochen, and Y.Y. Zeevi. Integrated active contours for texture segmentation. *Image Processing, IEEE Transactions on*, 15(6):1633–1646, 2006.
- A Segal, Dirk Haehnel, and Sebastian Thrun. Generalized-icp. In *Proc. of Robotics:* Science and Systems (RSS), volume 25, pages 26–27, 2009.
- JA Sethian. Evolution, implementation, and application of level set and fast marching methods for advancing fronts. *Journal of Computational Physics*, 169(2):503–555, 2001.
- R. Shojaii, J. Alirezaie, and P. Babyn. Automatic lung segmentation in ct images using watershed transform. In *Image Processing*, 2005. *ICIP 2005. IEEE International Conference on*, volume 2, pages II–1270. IEEE, 2005.
- José Silvestre Silva, Jaime B Santos, Diogo Roxo, Paula Martins, Eduardo Castela, and Rui Martins. Algorithm versus physicians variability evaluation in the cardiac chambers extraction. *Information Technology in Biomedicine, IEEE Transactions on*, 16(5):835–841, 2012.
- Lauge Sorensen, Saher B Shaker, and Marleen De Bruijne. Quantitative analysis of pulmonary emphysema using local binary patterns. *Medical Imaging, IEEE Transactions* on, 29(2):559–569, 2010.
- M. Spiegel, D.A. Hahn, V. Daum, J. Wasza, and J. Hornegger. Segmentation of kidneys using a new active shape model generation technique based on non-rigid image registration. *Computerized Medical Imaging and Graphics*, 33(1):29–39, 2009.
- Shanhui Sun, Christian Bauer, and Reinhard Beichel. Automated 3-d segmentation of lungs with lung cancer in ct data using a novel robust active shape model approach. *Medical Imaging, IEEE Transactions on*, 31(2):449–460, 2012.
- D. Terzopoulos, A. Witkin, and M. Kass. Constraints on deformable models: Recovering 3d shape and nonrigid motion. *Artificial Intelligence*, 36(1):91–123, 1988.
- R. Toledo, X. Orriols, X. Binefa, P. Radeva, J. Vitria, and JJ Villanueva. Tracking of elongated structures using statistical snakes. In *cvpr*, page 1157. Published by the IEEE Computer Society, 2000a.

R. Toledo, X. Orriols, P. Radeva, X. Binefa, J. Vitria, C. Canero, and JJ Villanueva. Eigensnakes for vessel segmentation in angiography. In *icpr*, page 4340. Published by the IEEE Computer Society, 2000b.

- A. Tsai, A. Yezzi Jr, W. Wells, C. Tempany, D. Tucker, A. Fan, W.E. Grimson, and A. Willsky. A shape-based approach to the segmentation of medical imagery using level sets. *Medical Imaging, IEEE Transactions on*, 22(2):137–154, 2003.
- Y. Tsin and T. Kanade. A correlation-based approach to robust point set registration. Computer Vision-ECCV 2004, pages 558–569, 2004.
- Manik Varma and Andrew Zisserman. Texture classification: Are filter banks necessary? In Computer vision and pattern recognition, 2003. Proceedings. 2003 IEEE computer society conference on, volume 2, pages II-691. IEEE, 2003.
- L.A. Vese and T.F. Chan. A multiphase level set framework for image segmentation using the mumford and shah model. *International Journal of Computer Vision*, 50 (3):271–293, 2002.
- Y. Wang, K. Woods, and M. McClain. Information-theoretic matching of two point sets. Image Processing, IEEE Transactions on, 11(8):868–872, 2002.
- Ye Xu, Milan Sonka, Geoffrey McLennan, Junfeng Guo, and Eric A Hoffman. Mdct-based 3-d texture classification of emphysema and early smoking related lung pathologies. *Medical Imaging, IEEE Transactions on*, 25(4):464–475, 2006.
- P.J. Yim, J.J. Cebral, R. Mullick, H.B. Marcos, and P.L. Choyke. Vessel surface reconstruction with a tubular deformable model. *Medical Imaging, IEEE Transactions on*, 20(12):1411–1421, 2001.
- Yindi Zhao, Liangpei Zhang, Pingxiang Li, and Bo Huang. Classification of high spatial resolution imagery using improved gaussian markov random-field-based texture features. Geoscience and Remote Sensing, IEEE Transactions on, 45(5):1458–1468, 2007.